

Plasma Fluctuation Studies in the TCV Tokamak: Modeling of Shaping Effects and Advanced Diagnostic Development

THÈSE N° 4516 (2009)

PRÉSENTÉE LE 23 OCTOBRE 2009
À LA FACULTÉ SCIENCES DE BASE
CRPP ASSOCIATION EURATOM
PROGRAMME DOCTORAL EN PHYSIQUE

ÉCOLE POLYTECHNIQUE FÉDÉRALE DE LAUSANNE

POUR L'OBTENTION DU GRADE DE DOCTEUR ÈS SCIENCES

PAR

Alessandro MARINONI

acceptée sur proposition du jury:

Prof. G. Gremaud, président du jury
Dr S. Coda, directeur de thèse
Dr S. Brunner, rapporteur
Dr A. Krämer-Flecken, rapporteur
Dr C. M. Roach, rapporteur



ÉCOLE POLYTECHNIQUE
FÉDÉRALE DE LAUSANNE

Suisse
2009

È privilegio di chi gode di buona reputazione essere creduto anche quando mente

C'est un privilège de celui qui a une bonne réputation, être cru même quand il ment

It's a privilege of who has a good reputation, to be believed even when he lies

(Miguel de Cervantes)

Abstract

One of the most important issues for magnetic-confinement fusion research is the so-called anomalous transport across magnetic field lines, i.e. transport that is in excess of that caused by collisional processes. The need to reduce anomalous transport in order to increase the efficiency of a prospective fusion reactor must be addressed through an investigation of its fundamental underlying causes.

This thesis is divided into two distinct components: one experimental and instrumental, and the other theoretical and based on numerical modeling. The experimental part consists of the design and installation of a new diagnostic for core turbulence fluctuations in the TCV tokamak. An extensive conceptual investigation of a number of possible solutions, including Beam Emission Spectroscopy, Reflectometry, Cross Polarization, Collective Scattering and different Imaging techniques, was carried out at first. A number of criteria, such as difficulties in data interpretation, costs, variety of physics issues that could be addressed and expected performance, were used to compare the different techniques for specific application to the TCV tokamak. The expected signal to noise ratio and the required sampling frequency for TCV were estimated on the basis of a large number of linear, local gyrokinetic simulations of plasma fluctuations. This work led to the choice of a Zernike phase contrast imaging system in a tangential launching configuration. The diagnostic was specifically designed to provide information on turbulence features up to now unknown. In particular, it is characterized by an outstanding spatial resolution and by the capability to measure a very broad range of fluctuations, from ion to electron Larmor radius scales, thus covering the major part of the instabilities expected to be at play in TCV. The spectrum accessible covers the wavenumber region from 0.9 cm^{-1} to 60 cm^{-1} at 24 radial positions with 3MHz bandwidth. The diagnostic is an imaging technique and is therefore also well suited to investigate inhomogeneous spatial regions, where the need for an excellent spatial resolution is greatest. Additionally, it was also designed as translatable to broaden the region of study, which can extend up to the magnetic axis, in selected configurations. The translatable design combined with the flexibility of TCV in terms of plasma positioning in the vacuum vessel allows the phase contrast system to measure fluctuations across virtually the whole plasma minor radius. The diagnostic is sensitive both to radial and poloidal wave numbers, depending on the configuration.

A parallel project to the development and installation of the phase contrast imaging system was the installation of a prototype Doppler reflectometer operating in a homodyne configuration, both in X and in O mode polarization. The reflectometer was operated parasitically to assess its performance which proved to be excellent; it is now routinely available on TCV.

The theoretical part of the thesis consisted of extensive modeling of the effect of plasma shape, in particular triangularity, on turbulent transport by means of linear and nonlinear gyrokinetic simulations. This was motivated by experiments on TCV that had shown a

dramatic improvement in confinement, up to a factor of two, in inverting the sign of the triangularity from positive to negative. Negative triangularity was indeed found to have a stabilizing influence on ion scale instabilities, specifically on the so called trapped electron mode (TEM). Simulations were carried out on actual TCV shots and the variation of the heat flux with triangularity calculated by the nonlinear simulations is in fair agreement with the experimental results. Linear simulations and a simple analytical model explain, in agreement with nonlinear runs, the resulting stabilization as a result of a rather complex modification of the toroidal precessional drift of trapped particles exerted by negative triangularity.

Keywords: Tokamak, plasma physics, confinement, turbulence, imaging diagnostic, transport, heat, particle, drift, nonlinear, gyrokinetic, phase contrast

Version abrégée

Le transport généré par des phénomènes non-collisionnels à travers les lignes de champ magnétique est parmi les problèmes les plus importants dans le domaine de la recherche sur la fusion nucléaire à confinement magnétique. Le besoin de réduire ce type de transport pour pouvoir augmenter l'efficacité d'un futur réacteur à fusion doit être abordé par une investigation directe de ses causes fondamentales.

Ce travail de thèse est divisé en deux composantes: la première expérimentale, la deuxième théorique et basée sur la modélisation numérique. La partie expérimentale consiste en la conception et installation d'un nouveau type de diagnostic de fluctuations turbulentes dans l'intérieur du tokamak TCV. Une étude détaillée de nombreuses techniques possibles, dont le *Beam Emission Spectroscopy*, la Réflectométrie, le *Cross Polarization*, la Diffusion Collective et différentes méthodes d'imagerie, a été effectuée en premier. De différents critères, comme la difficulté d'interpréter les données, les coûts, l'ampleur des études de physique possibles et les performances attendues, étaient les critères utilisés pour comparer les différents diagnostics pour l'application à TCV. Le rapport signal bruit attendu et la fréquence d'échantillonnage requise sur TCV ont été estimés à l'aide d'un grand nombre de simulations linéaires, locales et gyrocinétiques des fluctuations. Le résultat de ce travail a été le choix de la méthode du contraste de phase de Zernike avec une configuration tangentielle.

Le diagnostic a été spécifiquement conçu pour fournir des informations inconnues jusqu'à maintenant sur les caractéristiques de la turbulence. En particulier, il est caractérisé par une localisation spatiale exceptionnelle et par la capacité de mesurer un large spectre, depuis l'échelle du rayon de Larmor des ions à celui des électrons, donc en couvrant la plupart des instabilités attendues sur TCV. En particulier le spectre accessible est compris entre 0.9 cm^{-1} et 60 cm^{-1} en 24 positions radiales avec une bande passante de 3MHz environ.

Le diagnostic se base sur une méthode à imagerie et est donc adapté à l'investigation des régions spatiales inhomogènes, d'où la nécessité d'une très bonne résolution est plus importante. En outre, le diagnostic a aussi été conçu pour être déplacé dans la chambre à vide pour agrandir la région de plasma accessible, jusqu'à atteindre l'axe magnétique dans des configurations particulières. La capacité de déplacement du diagnostic, combinée avec la flexibilité de TCV quant aux positions possibles du plasma à l'intérieur de la chambre à vide, permet au contraste de phase d'effectuer des mesures sur quasiment tout le petit rayon du plasma. Le diagnostic est sensible aux nombres d'onde radiaux et poloïdaux, en fonction de sa configuration.

Un projet parallèle au développement et à l'installation du système du contraste de phase était l'installation d'un prototype de réflectomètre Doppler avec une configuration homodyne, en polarisation X comme en polarisation O. Le réflectomètre a été utilisé de manière parasite sur TCV pour vérifier ses performances, qui se sont démontrées excellentes; il

est maintenant régulièrement utilisé sur TCV.

La partie théorique de la thèse a intéressé la modélisation, avec des simulation gyrocinétiques linéaires et non linéaires, de l'effet de la forme du plasma, en particulier de la triangularité, sur le transport turbulent. Cette étude a été motivée par des expériences effectuées sur TCV qui ont montré comme, en changeant la triangularité de positive à négative, le confinement de l'énergie du plasma augmente d'un facteur deux. Les simulations ont permis de vérifier que la triangularité négative a un effet stabilisant sur les instabilités à l'échelle ionique, en particulier sur les modes causés par les électrons piégés (TEM). Les simulations ont été effectuées sur des tirs réels de TCV et la variation du flux de chaleur en fonction de la triangularité calculée par les simulations non linéaires est en bon accord avec l'expérience. Les simulations linéaires et un simple modèle analytique expliquent, en accord avec les simulations non linéaires, que la stabilisations est due à la modification assez compliquée de la dérive de précession toroïdale des électrons piégés, exercée par la triangularité.

Mots clés: Tokamak, physique des plasmas, confinement, turbulence, diagnostic à imagerie, transport, chaleur, particules, dérive, nonlinéaire, gyrocinétique, contraste de phase

Contents

1	Nuclear Fusion: history and present status	1
1.1	Introduction	1
1.2	Nuclear fusion	2
1.3	Magnetic confinement, idea and historical development	4
1.4	Tokamak	6
1.5	The TCV tokamak	8
1.5.1	Auxiliary heating system	8
1.5.2	Main TCV diagnostics	13
2	Feasibility study of fluctuation diagnostics in TCV	19
2.1	Introduction and objectives	19
2.2	Motivation for development of core fluctuation diagnostics on TCV	22
2.3	Modeling predictions of turbulence characteristics in the TCV tokamak	23
2.4	Overview of main possible diagnostics	26
2.4.1	Beam Emission Spectroscopy	26
2.4.2	Electron-Positron annihilation	30
2.4.3	Reflectometry	32
2.4.4	Collective Scattering	42
2.4.5	Phase Contrast	49
2.4.6	Alternative imaging methods	56
2.4.7	Cross Polarization Scattering	62
2.5	Concluding remarks	69
3	Phase Contrast diagnostic and Doppler Reflectometer, theoretical treatment and practical realization	77
3.1	The interaction of light and plasma	77
3.2	Theoretical treatment of gaussian beam propagation	83
3.3	Imaging properties of the Phase Contrast technique	87
3.4	Imaging conditions	91
3.5	Localization Properties of the Tangential Phase Contrast technique	95

3.5.1	Basic principle	95
3.5.2	Expected localization in TCV	96
3.5.3	Spatial filter	104
3.6	Experimental set-up	106
3.6.1	Optical properties	106
3.6.2	Detector properties	110
3.6.3	Mechanical vibrations	113
3.6.4	Geometrical beam path	120
3.6.5	Lasers	129
3.6.6	Mirrors	131
3.6.7	Windows for vacuum interface	138
3.6.8	Bellows	141
3.6.9	The optical table	142
3.6.10	Detectors	146
3.6.11	Data acquisition	148
3.7	Data analysis techniques	151
3.7.1	Maximum Entropy Method	152
3.7.2	Unevenly spaced data	154
3.8	Doppler reflectometer	157
3.9	Present status	160
3.10	Appendix: Evaluation of diffracting apertures	161
4	Modeling of shaping effects on turbulent transport	167
4.1	Introduction	167
4.2	Plasma equilibrium and shape	167
4.3	Particle drifts in magnetized plasmas	169
4.4	Trapped particles instability	173
4.5	Gyro-kinetics and the GS2 code	177
4.6	The effect of plasma shape on performance	180
4.6.1	Historical results	180
4.6.2	Methodology of numerical simulations	182
4.6.3	Geometrical background	185
4.6.4	Linear simulations	186
4.6.5	Non-linear simulations	194
4.7	Investigation of instability drives	198
4.8	Impurities and additional effects	204
4.9	General dependence of the toroidal precessional drift on plasma shape	209
4.10	Conclusions	212

4.11 Appendix 1: convergence studies	212
4.12 Appendix 2: toroidal drift benchmark	218
5 Conclusions and future plans	225
5.1 Summary	225
5.2 Future plans	226
5.3 Conclusions	227

Chapter 1

Nuclear Fusion: history and present status

1.1 Introduction

From time immemorial, men interested in describing things they saw in everyday life were called naturalists because they were, indeed, observing and studying natural phenomena. In particular, even the titles of some of the earliest studies mentioned nature explicitly, for example Lucretius' *De Rerum Natura*, and were attempts at describing the laws of nature and the role of men as part of it. As centuries passed, man progressively moved his attention from the anthropocentric aspects of his description to the naturalistic ones, in the attempt to remove all superfluous aspects from his description. In this respect, the step which led from Ptolemy's description of the solar system to Copernicus' is especially remarkable. Progressively man acquired consciousness of the fact that his description was nothing but a picture of the world which could not account for everything. The concept of *model* was thus born and we now are aware of the fact that we describe reality through a model, which means a picture of the world which accounts *only* for what we can or want to observe. In particular it has been recognized how a theory is valid in a given limit and no longer appropriate in another limit; for example, if the GPS system used Newtonian mechanics its accuracy would be too poor for it to be useful, while orders of magnitude in accuracy are gained with Einstein's relativistic description. Over time, naturalists, also due to the proliferation of scientific knowledge, started specializing and concentrating on different aspects of the world, and over the past couple of centuries universities have also progressively moved from general naturalistic courses to the present courses of mathematics, physics, chemistry, more recently engineering and, very recently, computer science and biotechnologies. Along this process, another splitting mechanism was at play: empiricism and rationalism, which try to describe the world using two different approaches: the former wants to deduce a model of a given part of the world under consideration by observing how things behave and happen, while the latter aims at ex-

plaining the experimental evidence on the basis of first principles.

Plasma physics is not an exception to history: it is a description of a part of the world, actually a large part of it in terms of amount of mass in the universe, and is divided into subbranches, such as astrophysical plasmas, industrial plasmas, inertial confinement, magnetic confinement, each of which is divided into its subbranches and, of course, into theoretical and experimental approaches. In this thesis we will concentrate only on magnetic confinement plasma physics, trying nevertheless to follow, as long as we can, both an experimental and a theoretical approach.

1.2 Nuclear fusion

The branch of physics called nuclear fusion primarily owes its existence to a few milestones in experimental and theoretical physics of the 19th-20th centuries, in chronological order:

1. Radioactivity. It was first discovered in 1896 by the French scientist Henri Becquerel, while working on phosphorescent materials. For this discovery [1], in 1903 he was awarded the Nobel Prize for Physics.
2. On the electrodynamics of bodies in movement [2], in which Albert Einstein states, among other outstanding concepts, the equivalence of mass and energy
3. The Rutherford scattering[3, 4]. In 1909 Ernst Rutherford, with a gold foil experiment, showed how atoms are composed of heavy nuclei with electrons *orbiting* around them. Rutherford scattering is also sometimes referred to as Coulomb scattering because it relies on static electric, or Coulomb, forces. For this discovery, Ernst Rutherford was awarded the Nobel Prize for Chemistry in 1908.

Of course, many more discoveries and outstanding scientists such as Pierre and Marie Curie, Enrico Fermi, Ettore Majorana, Niels Bohr, Giuseppe Occhialini, Werner Heisenberg, Wolfgang Pauli, Erwin Schroedinger, Paul Adrien Maurice Dirac, James Chadwick, Jagadis Chandra Bose, George Gamow and many others were necessary to understand how a nucleus behaves and that, indeed, nuclei can be transformed into one another thus, by the way, discovering the philosopher's stone. It is a personal opinion of the author that the three aforementioned milestones were essential ingredients in discovering that nuclei can interact with each other and, sometimes, as a consequence, a new nucleus is created releasing a given amount of energy which depends on the particular reaction.

Indeed, the basic idea of nuclear fusion is to force light nuclei to react in such a way as to create a more stable nuclear configuration and releasing an amount of energy corresponding to the binding energy. Nature is such that the binding energy of nuclei is not

constant with the mass of the nucleus, it follows the experimental curve represented in Fig.1.1. Iron being the most stable nucleus, energy is released by going towards its atomic

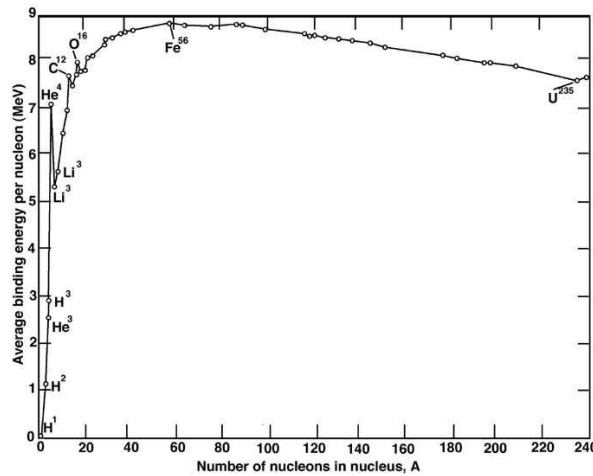


Figure 1.1: Binding energy per nucleon as a function of the mass of the nucleus.

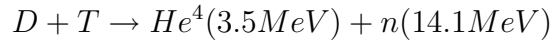
mass from the right part, i.e. by breaking heavy nuclei, or from the left part of the curve, i.e. by fusing light nuclei. The former corresponds to nuclear fission while the latter to nuclear fusion.

In order to be useful as a source of energy, a fusion reaction must satisfy several criteria. It must

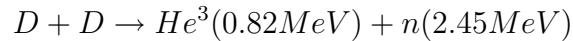
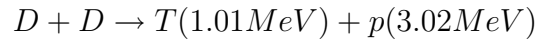
- be exothermic: This may be obvious, but it limits the reactants to the low Z (number of protons) side of the curve of binding energy. It also makes helium He^4 the most common product because of its extraordinarily tight binding, although He^3 and H^3 also appear
- involve low Z nuclei: This is because the electrostatic repulsion must be overcome before the nuclei are close enough to fuse. As the atomic number is increased, a larger kinetic energy is required for the nuclei to overcome the electrostatic repulsion.
- have two reactants: At densities less than the stellar ones, three body collisions are too improbable.
- have two or more nuclei as products: this allows simultaneous conservation of energy and momentum without relying on the emission of a photon. Indeed, if photons were emitted, being gamma photons, they would require a shell made by a heavy element, such as Pb, a few centimeters thick, to shield them and collect their energy. This would entail severe complications to the engineering design of the fusion reactor.

Considering these requirements, as well as the probability of the reaction at a given energy of the reacting nuclei, the energy released to neutrons and the ratio of the released energy

to the energy lost by bremsstrahlung processes, the most attractive fusion reaction is the following[23]



Since T is a radioactive material, safety requirements and the need to minimize neutron damages to fusion facilities suggested, at least in the case of magnetically confined plasma, the use of two other sister reactions



having a branching ratio equal to 50% (i.e. they can occur with equal probability).

The maximum of the cross section for fusion reactions is found at energies of several keV, which by far exceed the electron binding energies for almost any nucleus, thus requiring the existence of a sort of gas composed of charged particles; this gas is the fourth state of matter and is called plasma. Strictly speaking a plasma is an ionized gas, globally neutral, which is governed by collective phenomena; this is a major difference from a normal gas in which significant interactions occur only among neighboring particles. Being ionized, a plasma needs to be confined: nature chose the gravitational confinement in stars, while men, who cannot afford the mass of a star, turned to inertial or magnetic confinement.

1.3 Magnetic confinement, idea and historical development

The idea of magnetic confinement can be traced back to 1892 when Hendrik Antoon Lorentz experimentally found the law which carries his name:

$$\mathbf{F} = q\mathbf{v} \wedge \mathbf{B}. \tag{1.1}$$

In words this equation states that any particle with charge q , moving with velocity \mathbf{v} in the presence of a magnetic field \mathbf{B} , is subjected to a force in the direction orthogonal to both the magnetic field and the particle velocity, and is therefore constrained to rotate around the magnetic field line; this motion is called the Larmor motion. In other words since charged particles follow magnetic field lines, a magnetic field can be used to confine a plasma, which is indeed composed of charged particles. However the Lorentz force has a drawback: if a given surface, which is the boundary of the region where the plasma has to be confined, has a subset where the magnetic field has a perpendicular component to the surface itself, charged particles will then escape from that region following the magnetic field line.

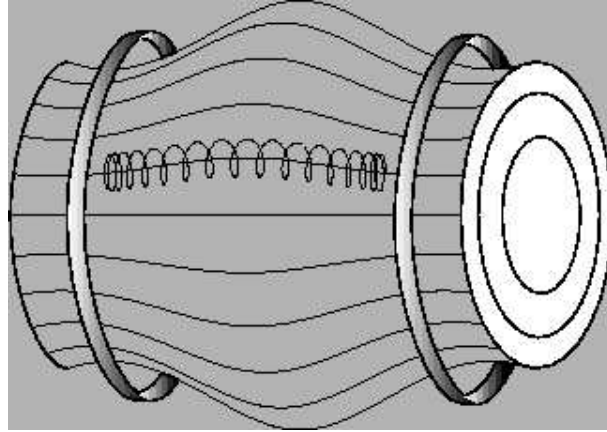


Figure 1.2: Sketch of the set-up of a linear machine. The confinement is provided by the magnetic field generated by the plasma current and, at the end points, by the magnetic mirror. The trajectory of a representative charged particle is depicted.

This is roughly the reason why linear machines, which were among the first devices adopted for fusion studies, performed poorly: particle losses at end points. In Fig.1.2 is shown a typical set-up of a linear machine. Particle losses were minimized at the end points by the so called magnetic mirrors, i.e. spatial regions where gradients in the magnetic field were externally imposed, thus producing a force directed towards the interior of the machine. To minimize particle losses at end-points linear machines require particles to have, on average, much larger perpendicular than parallel energies, where perpendicular or parallel refer to the direction of the velocity relative to the magnetic field. As this non-Maxwellian distribution is difficult and costly to achieve, linear machines were finally abandoned at the beginning of the '80s.

A solution to this problem had already been found by mathematicians in the beginning of the 20th century and is stated in the following general form[26]

Poincaré-Hopf theorem. *Let M be a compact orientable differentiable manifold. Let ν be a vector field on M with isolated zeroes. If M has a boundary, then we insist that ν be pointing in the outward normal direction along the boundary. Then we have the formula*

$$\sum_i \text{index}_\nu(x_i) = \chi(M) \quad (1.2)$$

where the sum of the indices is over all the isolated zeroes of ν and $\chi(M)$ is the Euler characteristic of M .

The theorem was proven for two dimensions by Henri Poincaré and later generalized to higher dimensions by Heinz Hopf. The only compact closed surfaces with zero Euler characteristics are the Klein bottle and the torus, thus implying that only these two surfaces do not have any point where the magnetic field has a perpendicular component.

Since the Klein bottle does not have any contained volume, only the torus is apt for magnetic confinement applications.

So in the toroidal geometry particles flowing along the magnetic field lines tend to remain inside the volume since the field lines are closed on themselves. However, due to the Maxwell-Ampere equation, the magnitude of the toroidal field is inversely proportional to the distance from the axis of symmetry; the magnetic field gradient results in a vertical drift, called the grad-B drift, which, together with curvature effects, causes a charge separation which in turn tends to expel particles from the volume. The solution is to give a perpendicular component to the magnetic field such as to make it helical: in this configuration the vertical drift averaged over a particle orbit is zero and, therefore, the particle confinement is *ideally perfect*.

There are two ways of providing this field correction: by imposing it externally through coils or letting the plasma itself generate it; the former configuration is known as stellarator while the latter as tokamak[5]. Both configurations are represented in Fig.1.3. If a plasma has to provide the helical magnetic structure it is necessary to drive a current in it. In a tokamak this is performed by discharging a transformer which drives a current in the secondary circuit, i.e. the plasma itself. Stellarators are distinct from tokamaks also because they are not azimuthally symmetric; they have a discrete rotational symmetry which is often fivefold. The major advantages of a tokamak are its axial symmetry and the simplicity of manufacturing planar coils; the primary merit of a stellarator is the absence of a net current and thus of so-called current driven instabilities. It is far beyond the scope of this thesis to deal with such instabilities which are treated in detail in [6, 7].

It is probably due to their simpler geometry that tokamaks historically received, both experimentally and theoretically, more attention than stellarators and rapidly improved their performance which was further enhanced by larger investments and, therefore, larger average sizes. Additionally, design and construction inaccuracies are argued to be the cause of lesser performances of stellarators compared to tokamaks of comparable size.

This thesis is focused, both in its experimental and theoretical parts, on the tokamak geometry, in particular on the TCV tokamak. In the following section we will give a brief overview of tokamaks and of TCV.

1.4 Tokamak

Tokamak is a russian acronym, *toroidal'naya kamera s magnitnymi katushkami*, which means toroidal chamber with magnetic coils. It was invented in the 1950s by Soviet physicists Igor Yevgenyevich Tamm and Andrei Sakharov (who had been inspired by an original idea of Oleg Lavrentyev). In 1968, at the third IAEA International Conference on Plasma Physics and Controlled Nuclear Fusion Research at Novosibirsk, Soviet scientists

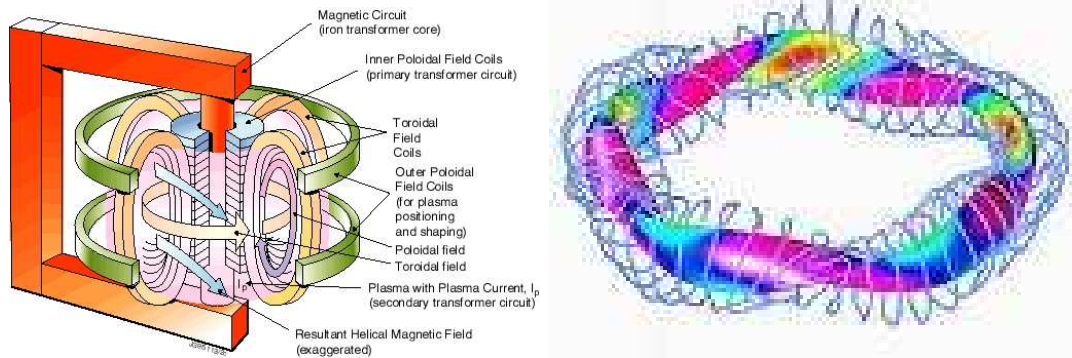


Figure 1.3: (Left) Sketch of the tokamak configuration (Right) Geometrical representation of the magnetic field coils, in light blue, and of a given plasma flux surface, in multi-color of the Stellarator W7-X.

announced the achievements of electron temperatures of over 1000 eV in a tokamak device. These astonishingly good performances were confirmed a few years later with laser scattering.

Since this performance was far superior to any obtained in other existing devices, most fusion research programs quickly switched to using tokamaks.

The basic principle of a tokamak is the following:

- A quantity of gas is injected in the vacuum vessel
- The toroidal coils are powered thus creating the confining toroidal field
- The gas is pre-ionized in one or more points of the vacuum vessel
- The central solenoid is energized and, immediately after, is powered off thus inducing a loop voltage in the plasma, which is the secondary circuit of the transformer
- Collisional processes ionize the whole plasma
- The induced current generates the poloidal field thus confining the plasma and, additionally, heating it by Joule effect
- An external, vertical, magnetic field is applied to stabilize the position of the plasma in the vacuum vessel

Ohmic heating is a consequence of Coulomb collisions whose frequency is inversely proportional to $T_e^{3/2}$, and thus becomes inefficient as the plasma temperature is raised. This forced scientists to develop other means of heating: Electron Cyclotron Resonance Heating (ECRH)[8, 9], Neutral Beam Injection (NBI)[20], Ion Cyclotron Resonance Heating (ICRH), Alfvén Heating, Bernstein Waves and Lower Hybrid (LH) waves[10, 11]. Depending on their geometrical configuration, most of the aforementioned methods also provide

current drive. An additional current is intrinsically generated in toroidal devices by the plasma itself, and so it is shared by tokamaks and stellarators, and is called the bootstrap current[12]. Roughly speaking, this current is due to the spatial pressure gradients leading to a net current parallel to the magnetic field carried by passing particles. Equating the momentum exchange between passing and trapped electrons and between passing electrons and ions, a net current parallel to the magnetic field is generated, called the bootstrap current. The bootstrap current is thus a typical effect of a toroidal machine, and is proportional to the trapped particle fraction.¹

1.5 The TCV tokamak

The *Tokamak à Configuration Variable* (tokamak having a variable configuration) is a mid-size tokamak specifically designed to study the influence of plasma shape on its confinement. Its major radius is 0.88 m and its minor radius 0.25 m. Plasmas of different shapes are realized in an almost rectangular-cross-section stainless steel vacuum vessel 0.55 m x 1.55 m whose first wall is covered with carbon tiles. Different plasmas shapes are realized through 16 independently powered coils; an overview of various plasma shapes realized in TCV is shown in Fig.1.5. A toroidal field flux of about 0.8-1.3 Wb is generated by 16 equally spaced toroidal coils, producing a toroidal field ripple lower than 1.5% over the whole poloidal section [22]. A schematic view of the TCV tokamak is represented in Fig.1.4.

Two sets of in-vessel coils vertically stabilize highly elongated plasmas. On the central column, ohmic coils, which constitute the primary circuit of the transformer, generate a loop voltage between 1 V and 10 V, resulting in a plasma current up to 1 MA. Table 1.1 contains an overview of the main parameters of the TCV tokamak. Figure 1.5 illustrates the variety of plasma shapes achieved in TCV.

1.5.1 Auxiliary heating system

The TCV tokamak has, besides a large flexibility in terms of achievable plasma shapes, the highest power density coupled to electrons, which makes TCV one of the best suited tokamaks for electron transport studies. A total of 4.3 MW is installed in the Electron Cyclotron Resonance Heating-Electron Cyclotron Current Drive (ECRH-ECCD) system; split, as depicted in Fig.1.6, in a second harmonic system, 3 MW, and a third harmonic system, 1.3 MW. In simple words the heating system makes use of the gyration motion of charged particles around a magnetic field line, motion whose frequency is given by

¹The name *bootstrap* appears in Raspe's novel *Baron Munchhausen's Narrative of his Travels and Campaigns in Russia* when the Baron, trapped upside down in a hole in the snow, tries to get out by pulling his own boots, which are outside the snow.

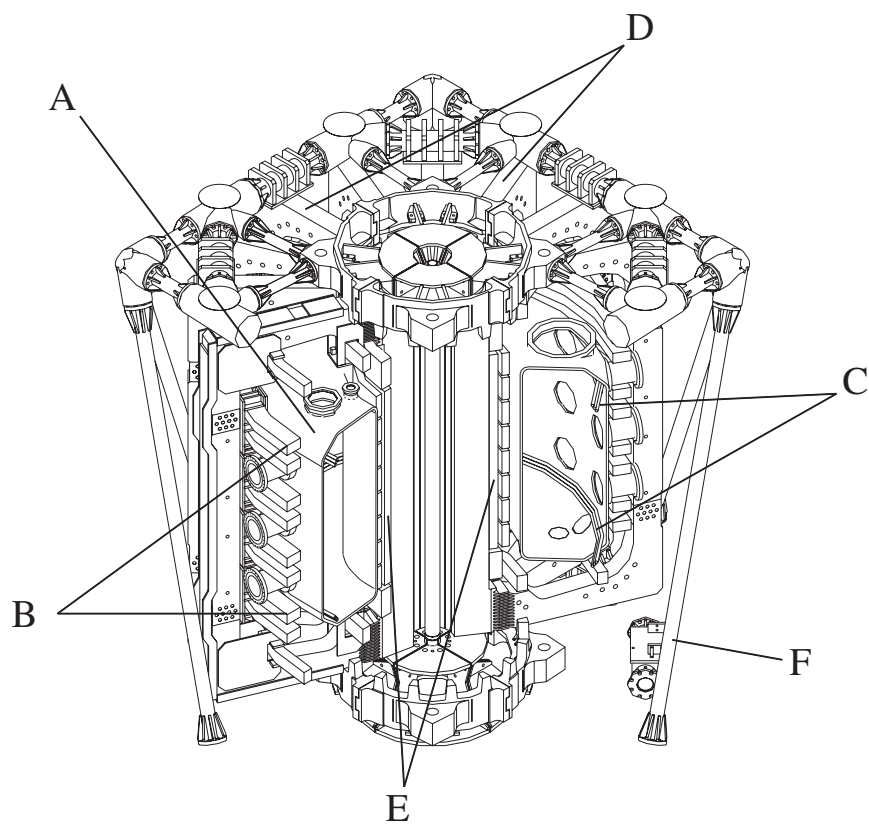


Figure 1.4: Schematic view of TCV. A) Vacuum vessel. B) Shaping poloidal field coils. C) Internal poloidal field coils used to vertically stabilize elongated plasmas. D) Toroidal field coils. E) Ohmic coils. F) Mechanical support structure. (Courtesy of Dr. Y. Camenen)

Parameter	Units	Value
Major Radius	m	0.88
Minor Radius	m	0.25
Plasma current	MA	0.2-0.5 (typ) 1 (max)
Toroidal field on axis	T	1.44 (typ) 1.54 (max)
On-axis electron density	m^{-3}	$2 \cdot 10^{20}$ (max)
On-axis electron temperature	keV	18 (max)
On-axis ion temperature	keV	1.5 (max)
Volume averaged beta	%	3 (max)
Elongation		0.9-2.8
Triangularity		-0.7 to +1
Circular plasma section	m^2	0.2
Circular plasma volume	m^3	1.1
Ohmic power	MW	0.3 (typ)
X2 EC power	MW	3
X3 EC power	MW	1.3
Pulse length	s	2 (typ) 4 (max)

Table 1.1: Overview of the TCV tokamak.

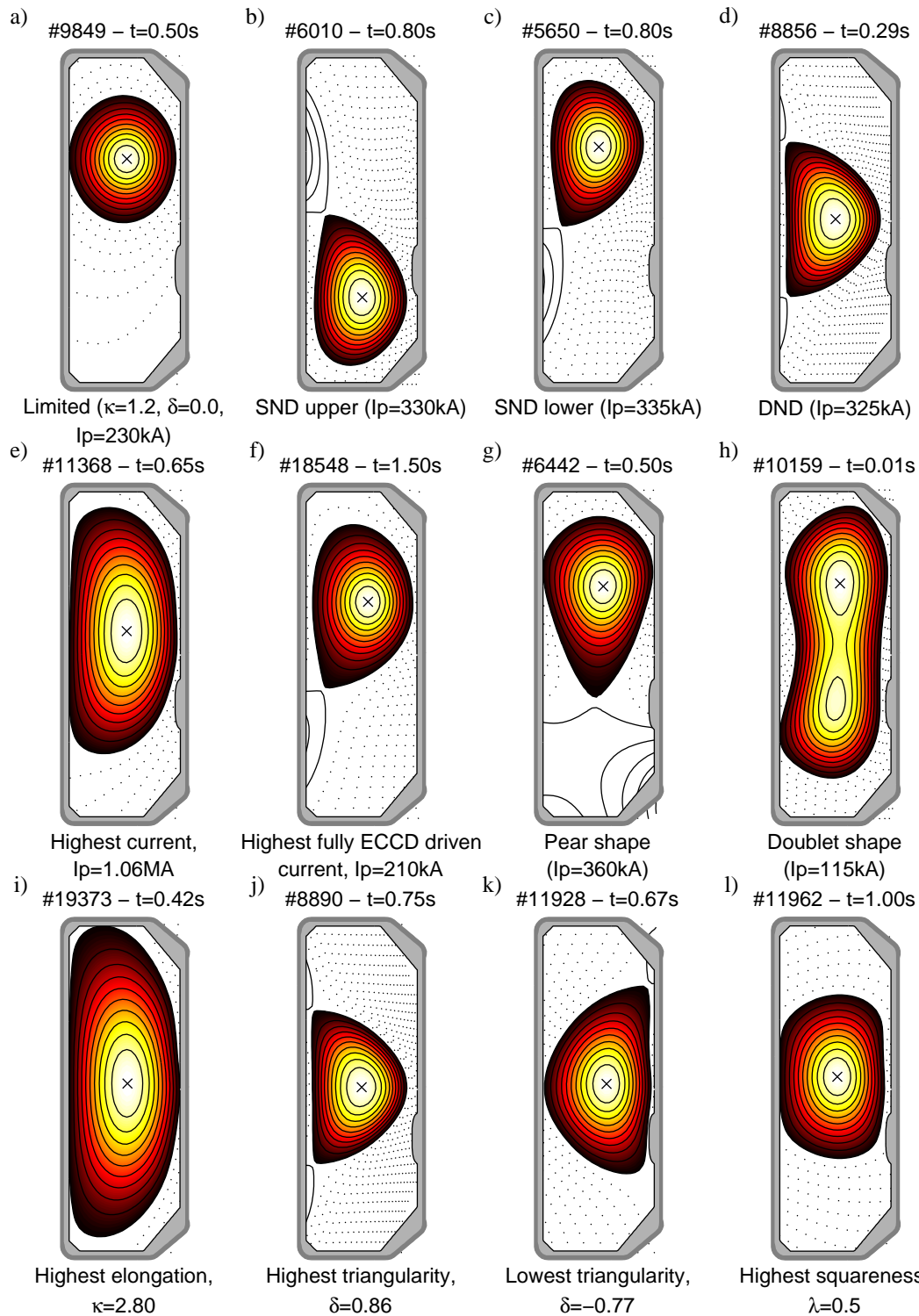


Figure 1.5: A number of representative plasma shapes obtained in the entire TCV history. Equilibria were reconstructed with the LIUQE code.

$f = qB/(2\pi m\gamma)$, where q and m are the particle charge and mass respectively, B is the magnetic field strength and γ is the relativistic factor defined as $\gamma = 1/\sqrt{1 - (v/c)^2}$, v being the particle velocity and c the speed of light. By Ampere's law, the strength of the toroidal magnetic field in a given point is inversely proportional to the distance from the torus' axis of symmetry, thus providing a unique relation between cyclotron frequency and the position in the vacuum chamber. Matching a harmonic of the cyclotron frequency with the frequency of an electromagnetic (e-m) wave injected in the plasma results in a resonance between charged particles and the wave, which provides the required heating mechanism, both for waves polarized parallel and perpendicular to the magnetic field. Considering the toroidal field of TCV, the choice of the second and third harmonic has been a compromise between a good absorption coefficient, which decreases with increasing harmonic number, and access to high density plasmas, which is enhanced with increasing harmonic number.

In TCV the second harmonic system is made up of six gyrotrons delivering 0.5 MW each at a frequency of 82.7 GHz. The power is transmitted through 30 m long waveguides and injected into the vacuum vessel through Mo mirrors steerable in the poloidal and in the toroidal plane. Losses are smaller than 7% and are minimized choosing an Extraordinary mode polarization (X-mode), in which, in the case of perpendicular injection, the electric field of the microwave is perpendicular to the plasma toroidal magnetic field. All the launchers are located on the Low Field Side (LFS), two of them on the machine mid-plane and the remaining four on the upper part, approximately 46 cm above the mid-plane. The power deposition location is controlled by varying the poloidal injection angle or, more seldom, by varying the toroidal field. Current drive is achieved through the toroidal injection angle. Access to the second harmonic X-mode is limited by the plasma right-hand cut-off frequency, which gives a maximum operational density of $4.25 \cdot 10^{19} \text{ m}^{-3}$. To heat denser plasmas the third harmonic is employed. The TCV third harmonic system is made of three gyrotrons delivering 1.3 MW through a vertical injection path. This configuration was required by the need to overcome the low coupling efficiency by allowing the beam to propagate parallel to the resonant surface, thus extending the length of resonant interaction, which is then chosen to be vertical along the whole plasma height. As a result, the localization of the absorbed power is far worse than for the second harmonic (X2) system, but the cut-off density is significantly higher being $11.5 \cdot 10^{19} \text{ m}^{-3}$.

The TCV EC system allows high coupled power densities, localized heating, a large variety of target plasmas and fully sustained ECCD driven plasma current[13].

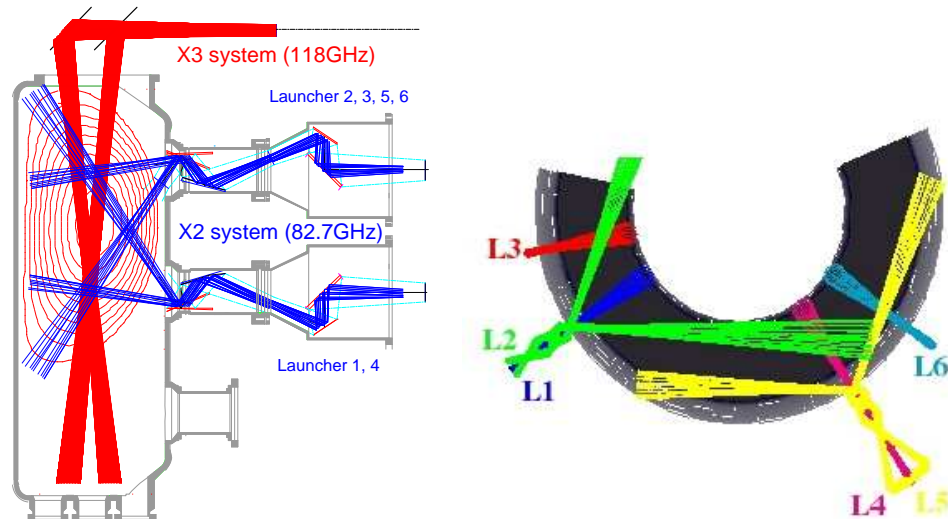


Figure 1.6: (Left) Poloidal section of the TCV X2-X3 ECRH launching system. (Right) Toroidal view of the TCV X2 ECRH launching system.

1.5.2 Main TCV diagnostics

In this section we will briefly explain the most important or most used diagnostics currently operational in the TCV tokamak, some of which have been, by the way, of paramount importance for the work described in this thesis.

Magnetics and equilibrium reconstruction

The magnetic system in TCV comprises poloidal field coils and horizontal magnetic-flux loops [17]. The former are arranged on four cross sections, toroidally separated by 90 degrees, each equipped with 38 almost evenly spaced coils mounted inside the vacuum vessel. The signals from two opposite sections are acquired and used for equilibrium reconstruction. The same signals are averaged to cancel any toroidal asymmetry and fed in real time to the plasma shape and position control system. A set of 38 flux loops is also used both for real-time control and equilibrium reconstruction. In addition, two toroidal arrays, located on the equatorial midplane, are installed for MHD mode analysis. The basic equilibrium reconstruction is thus performed with an equilibrium code, called LIUQE [14], which solves iteratively the Grad-Shafranov equilibrium equation [15, 2], in order to find the best match with the measured fields on the magnetic probes and with the measured magnetic fluxes. The LIUQE code is generally additionally constrained with the total plasma energy measured with the diamagnetic loop [18]. It can be further constrained with the sawtooth inversion radius and the pressure profile measured with the Thomson Scattering system.

Thomson scattering system

We will briefly elucidate the basic mechanism underlying the Thomson scattering before describing the system installed in TCV. Readers interested in details are addressed to [20].

When a photon of energy much less than 0.5 MeV collides with an electron, the scattering process can be described in a classical way, i.e. in the particle being accelerated by the e-m wave and radiating in all directions; this representation holds when there is negligible change in the particle momentum when colliding with a photon, which is the case when the photon energy is much less than the particle rest-mass, which is equal to 0.5 MeV for electrons.

When an e-m wave is scattered by a particle, it experiences a Doppler shift in its frequency given by

$$\Delta\omega = \mathbf{v} \cdot (\mathbf{k}_{\text{diff}} - \mathbf{k}_{\text{in}}) \quad (1.3)$$

where \mathbf{v} is the particle velocity, while \mathbf{k}_{diff} and \mathbf{k}_{in} are the scattered and incident wave vectors, respectively. By measuring the Doppler shift, the particle velocity, and thus its energy, is then calculated because the two wave-vectors are known by the geometry of the system. The total signal amplitude gives the number of scattered photons, and so the number of scattering targets, i.e. the particle density.

In a plasma both ions and electrons contribute to the total scattering but, since ions are much heavier than electrons, they undergo a much smaller acceleration and therefore irradiate much less and contribute negligibly to the total signal. This is why the Thomson scattering system is commonly used to measure electron temperature and density.

When the reciprocal of the difference in the probing wave-vectors is much shorter than the Debye length of the plasma, scattering processes from different electrons are statistically independent and one speaks of incoherent Thomson scattering. This is indeed the regime of operation for practically useful geometries that provide the best spatial resolution. The small cross section in this regime forces the use of high incident powers which are provided by lasers operated in a pulsed, Q-switched [19], way. When the reciprocal of the difference in the probing wave-vectors cannot be neglected with respect to the Debye length, the so-called coherent Thomson scattering occurs, i.e. the scattered signal is sensitive to collective phenomena, such as ions' dynamics and electrostatic waves at the relevant wavelength[20]. TCV is equipped with three Nd-YAG lasers, whose wavelength is 1.064 μm , operating in a Q-switched mode, at 20 Hz. The lasers can be operated simultaneously to increase the signal to noise (S/N) ratio, typically in plasmas whose density is lower than $8 \cdot 10^{18} \text{ m}^{-3}$, or independently, to increase the effective repetition rate to 60

Hz. Electron temperatures and densities are measured vertically, which is the beams' direction of propagation in the vacuum vessel, over 25 spatial locations in the core and 10 in the edge, sampling between $Z=-0.17$ m to $Z=0.66$ m, and are characterized by an uncertainty of about 5%.

Far Infrared Interferometer

An interferometer evaluates the phase shift induced by a medium of a given index of refraction N on an electromagnetic wave with respect to a reference beam which does not pass through the same medium. In a plasma the index of refraction is proportional to the electron density and if the frequency of the probing beam is much higher than any typical plasma frequency, the beam experiences only a phase shift and undergoes negligible absorption.

In TCV, a 14 channel far infrared interferometer is used to measure the line-integrated density along 14 parallel chords in the vertical direction. The system consists of a FIR laser emitting a continuous wave at $214 \mu\text{m}$ pumped by a CO_2 laser, and of a multi-element detector unit (InSb hot-electron bolometer). The infrared laser beam is divided into a reference beam and 14 beams passing through the plasma at different radial positions. The line integrated plasma density along each vertical beam can be determined from interferometric measurements between each beam and the reference one. The whole system is automated and its central chord serves as a real time data input for the TCV density feedback system.

The frequency response of the detectors is 750 kHz and the sampling rate is 20 kHz.

The FIR signal can be inverted with basis functions determined by the Thomson Scattering measurements, to produce the local density profile [21].

Charge Exchange Recombination Spectroscopy

The CXRS technique is based on the spectral analysis of the radiation emitted by charge exchange processes between neutral atoms and ions. Analyzing a given spectral line, it is possible to derive the density, velocity and temperature of the ions species by measuring the spectrum integral, centroid position and width, respectively.

In TCV a diagnostic, i.e. ideally non-perturbative, neutral hydrogen beam injector is used to increase the signal of the charge exchange line C^{6+} . The diagnostic beam has an energy of 50 keV and a toroidal injection angle of 11.25 degrees. Due to its low power, the injector does not perturb the plasma temperature and rotation[24]. TCV is equipped with a 40 chords toroidal High Field Side-Low Field Side (HFS-LFS) and poloidal LFS system, thus measuring toroidal and poloidal C^{6+} velocities along with temperature and

density in 8 and 4 radial positions, respectively, with a sampling frequency between 2 and 20 Hz.

Neutral Particle Analyzer

Following charge exchange processes, neutrals can escape the confining magnetic field and be detected outside the vacuum vessel. In the case of a Maxwellian distribution, the source term of the neutral flux is given by [23]

$$S(E_0) = n_0 n_i \langle \sigma_{01} v_i \rangle 2 \sqrt{\frac{E_0}{\pi T_i^3}} e^{-E_0/T_i} \quad (1.4)$$

where E_0 is the energy of the neutrals, n_0 their density, n_i is the ion density and $\langle \sigma_{01} v_i \rangle$ is the product of the charge exchange cross section with the ion velocity, averaged over the neutral distribution function. Thus a measurement of $S(E_0)$ as a function of the neutral energy gives the ion temperature, provided that the ion density is known and that the mean free path of the neutrals is much longer than the plasma minor radius. This condition is more likely satisfied at high energies because the charge-exchange cross section is generally decreasing with energy. It is also to be stressed that the measurement is intrinsically line-integrated as light is collected from the whole line of sight crossing the vacuum vessel.

In TCV a Compact Neutral Particle Analyzer (CNPA) and a Neutral Particle Analyzer (NPA) are installed[25]. The CNPA is an electro-magnetic (E||B) NPA to analyze hydrogen, deuterium or helium atoms in the energy range of approximately 500 eV to 50 keV (hydrogen). Two species can be measured at a time along a horizontally viewing chord. The nominal time resolution of the CNPA is 2.5 ms for two seconds and up to 10 μ s. The NPA is a 5-channel Neutral Particle Analyzer developed in the Ioffe Institute (Leningrad, Soviet Union), to analyze neutral fluxes of hydrogen isotopes from the plasma in the energy range of 600 eV to 8 keV. The NPA views the plasma along a fixed vertical chord, which intercepts the core of most TCV plasma configurations. It consists of 5 energy channels with electrostatic discrimination. The NPA electronics allows to operate up to 100 kHz (1 kHz for standard regime).

Bibliography

- [1] H. Becquerel, *Comptes Rendus* **122** (1896) 420
- [2] A. Einstein, *Zur Elektrodynamik bewegter Körper* (1905)
- [3] H. Geiger and E. Marsden, *Proc. Roy. Soc.* **82** (1909) 495
- [4] E. Rutherford, *Philos. Mag. (6th Ser)* **21** (1911) 669
- [5] F.F. Chen, *Introduction to Plasma Physics and Controlled Fusion. Vol 1*, Springer, 2006
- [6] P.A. Davidson, *An introduction to magnetohydrodynamics*, Cambridge University Press, 2001
- [7] D. Biskamp, *Nonlinear magnetohydrodynamics*, Cambridge University Press, 1997
- [8] R. Geller, *Peroc. 1st Int. Con. Ion Source* (1969), Salcay
- [9] H. Postma, *Phys. Lett. A*, **31** (1970) 196
- [10] T.H. Stix, *Waves in plasmas*, American Institute of Physics, 1992
- [11] D.G. Swanson, *Plasma waves*, Academic Press, 1989
- [12] R.J. Bickerton *et al.*, *Nature Phys. Sci.* **229** (1971) 110
- [13] S. Coda *et al.*, *Proceedings of 22nd IAEA fusion energy conference*, 2008 Geneva, Switzerland
- [14] F. Hofmann and G. Tonetti, *Nucl. Fusion* **28** (1988) 1871
- [15] H. Grad and H. Rubin, *Hydromagnetic Equilibria and Force-Free Fields. Proceedings of the 2nd UN Conf. on the Peaceful Uses of Atomic Energy*, Geneva, 1958
- [16] V.D. Shafranov, *Reviews of Plasma Physics*, **2** (1966) 103
- [17] J.M. Moret, *et al.*, *Rev. Sci. Instrum.* **69** (1998) 2333

- [18] J.M. Moret, F. Buhlmann and G. Tonetti, *Rev. Sci. Instrum.* **74** (2003) 4634
- [19] O. Svelto, *Principles of lasers*, Plenum Press, 1998
- [20] I.H. Hutchinson, *Principles of plasma diagnostics*, Cambridge University Press, 2002
- [21] I. Furno *et al.*, *Plasma Phys. Control. Fusion* **47** (2005) 49
- [22] J.P. Hogge, *Private communication*
- [23] J. Wesson, *Tokamaks*, Oxford University Press, 1987
- [24] P. Bosshard, *Ph.D. thesis, Ecole Polytechnique Fédérale de Lausanne*, 2723 (2003)
- [25] A.N. Karpushov *et al.*, *Rev. Sci. Instrum.* **77** (2006) 033504
- [26] M. Furuta, *Index theorem 1*, American Mathematical Society, 2008

Chapter 2

Feasibility study of fluctuation diagnostics in TCV

2.1 Introduction and objectives

One of the most important issues for magnetic-confinement fusion research is the so-called anomalous transport across magnetic field lines, i.e. transport that is in excess of that caused by collisional processes. The need to reduce anomalous transport in order to increase the efficiency of a prospective fusion reactor must be addressed through an investigation of its fundamental underlying causes. These are widely believed to be microinstabilities, i.e. instabilities that are characterized by a small spatial scale compared to the system size and are generally of a turbulent nature[1]. In the past decade considerable progress has been made in magnetic fusion research, especially in tokamaks, in improving the fusion performance, particularly through enhanced control of the plasma discharge parameters. In particular, heat transport due to ion instabilities has been substantially reduced in some enhanced-confinement regimes[2] and has also been extensively studied both experimentally and theoretically, leading to a fairly good, though incomplete, understanding of the underlying physics. By contrast, electron transport remains more anomalous and is also more poorly understood. Problems arise in both experimental and numerical investigations because of the smaller intrinsic temporal and spatial scales, requiring extensive diagnostic coverage and equivalently, on the numerical side, extensive grids and long computational times. A related problem is the appearance of numerical instabilities that hinder the convergence of the simulations. For example, the advective fluctuating $\mathbf{E} \wedge \mathbf{B}$ velocity is inversely proportional to the spatial scale of the parent fluctuation, thus implying stricter limits on the Courant–Friedrichs–Lewy (CFL) condition in numerical simulations [3].

In spite of these difficulties, numerical simulations in recent years have also begun to address the nonlinear evolution and saturation of the turbulence, and nonlinearly generated modes, such as streamers [4], zonal flows [5] and geodesic acoustic modes [6], have

been predicted to regulate the saturated turbulence and thus the overall transport. These modes present an additional challenge to experimentalists owing to their complex spatial structures. While experimental evidence for their existence has been obtained [7, 8], much remains unknown about their properties, parametric dependences and effect on the level of plasma turbulence.

Existing turbulence diagnostics can be roughly classified according to what they measure: local or line integrated measurements, low k or high k turbulence spectral regions, real or Fourier space, plasma core or edge, perturbing or not, fluctuations in temperature, density, electric or magnetic field.

Strictly speaking probing the plasma in any way results in a perturbation technique, such as with actual probes or with electromagnetic waves, of a given wavelength, which are made to interact with the plasma. Truly non-perturbing techniques are instead the ones making use of any signal self generated by the plasma itself, such as the Electron Cyclotron Emission (ECE) diagnostic used to measure electron temperature fluctuations or magnetic probes used to measure fluctuations of the total magnetic field. However, in order to be meaningful, even active diagnostics must be almost non-perturbing, in the sense that the perturbation caused to the plasma has to be negligible. This has to be verified *a posteriori* by comparing two identical discharges performed with and without the diagnostic in operation and checking that any difference is within the errorbars.

Generally speaking, diagnostics meant for plasma edge can be either material probes or instruments detecting the result of plasma-light interaction, while the core can only be investigated through electromagnetic waves since the high temperatures reached could not be tolerated by material probes, at least in fusion oriented devices.

The plasma edge has historically been measured with probes because of two main advantages over e-m waves. The first is that the spatial resolution is generally determined by the spatial extent of the probe itself, that is a few millimeters. In contrast, e-m waves tend to provide poorer resolution, of the order of a few centimeters.

In the effort to try to understand anomalous transport, it is especially desirable to directly measure the transport itself; in the case, for example, of particle transport by electrostatic fluctuations, it can mathematically be expressed in the following way

$$\Gamma_{\mathbf{n}}(t) = \langle \tilde{n}\tilde{\mathbf{v}} \rangle \propto \langle \tilde{n}\nabla\tilde{\phi} \rangle \propto \langle \tilde{n}\mathbf{k}\tilde{\phi} \rangle \quad (2.1)$$

where brackets represent *ensemble* averages, $\tilde{\mathbf{v}}$ the perturbed particle velocity, \tilde{n} the perturbed density, $\tilde{\phi}$ the perturbed electrostatic potential. Probes can simultaneously measure several physical quantities, such as e-m fields, density and temperature, thus providing an easy way to experimentally compute particle or heat transport; in this lies their second advantage. In fact no core diagnostic, except for the Heavy Ion Beam Probe (HIBP), is able to provide direct measurements of turbulent fluxes.

The working principle of the HIBP diagnostic is based on the injection in the plasma core of heavy, i.e. high atomic number, singly charged ions which, by interacting with the background plasma, are ionized, thus becoming doubly charged, and are therefore deflected to a trajectory which depends on the total magnetic field. An energy analyzer permits the derivation of the electrostatic potential at the ionization location, which is the intersection between the trajectories of the primary and of the secondary beam, while the fluctuations of the double-ionized ions' intensity at the detectors provide the fluctuating electron density. Multiple detectors allow one to estimate the cross-phase between these two quantities, thus measuring the particle transport. Finally, by varying the injection angle and the energy of the primary beam, a large portion of the poloidal section can be analyzed. In 2005 a HIBP proposal for the TCV tokamak was turned down due to cost considerations and to issues concerning the accessibility to the vacuum vessel.

Diagnostics based on the interaction between e-m waves and plasmas can be divided into local or line integrated depending on whether or not they are subject to any resonance or cut-off in the plasma. Specifically when an e-m wave propagates in a plasma, or in any other medium, it is very sensitive to what happens at the resonance, or cut-off, region due to the behavior of its index of refraction. As an example the so called Reflectometer is based on the interaction at the cut-off, while the Cross Polarization Scattering (CPS) diagnostic either at the cut-off or at the resonance layer. The working principles of these two diagnostics will be explained in detail in 2.4.3 and in 2.4.7, respectively. Conversely, when the frequency of an e-m wave is much higher than any typical plasma frequency, its amplitude is barely affected and it collects all possible information from the plasma along its trajectory; for this reason these diagnostics are called line integrated, and we further divide them into Interferometric and Coherent Scattering diagnostics. The former group tends to provide a sort of image of density fluctuations along a line, while the latter provides information on a particular angle at which the probing e-m beam is scattered, and is therefore referred to as a Fourier diagnostic, in the sense that it provides information directly in Fourier space.

In principle, diagnostics operating in direct or conjugate space provide the same information as long as the whole space, direct or conjugate, is sampled. However, this is never the case due to accessibility limitations to the vacuum vessel. In particular it is, in general, more problematic to collect information at a given, even though small, scattering angle because the unscattered and the scattered beams must be separated; the latter must be further divided into each component corresponding to each scattering angle one wants to study. More detailed comparisons are made in sections 2.4.4 and 2.4.5.

2.2 Motivation for development of core fluctuation diagnostics on TCV

One of the aims of this project is to provide means for investigating, from an experimental point of view, the physical characteristics of density fluctuations present in the core region of the TCV tokamak.

When this project was started, TCV did not have any turbulence diagnostic routinely available, except for the reciprocating Langmuir probe, which provides data on fluctuations in the Scrape-Off-Layer (SOL). The FIR interferometer (see section 1.5.2.3) is the only diagnostic providing information on core turbulence through a line-averaged electron fluctuations along 14 vertical chords at 20 kHz, which is far below the level required for detailed investigations on temporal and spatial scales of fluctuations, as well as for intensive benchmarking of numerical codes vs experiment. A novel diagnostic for core fluctuations was therefore needed and its development required a study of evaluation of the various possible techniques specifically for application to the TCV tokamak. The principal and most demanding part of such a study consists of evaluating in detail the expected performance of each diagnostic, as well as identifying all the drawbacks often hidden in their theoretical foundation. At the end of this type of evaluation effort, a set of possible options generally turns out to be feasible, and the final choice is made on the basis of expected signal-to-noise ratios, costs, difficulty of construction and variety of physics issues that can be studied and compared with theory. We will describe hereafter the feasibility study for a core fluctuation diagnostic for the TCV tokamak in relation to the most important outstanding physics issues in plasma transport at the time of the study.

Fusion oriented plasmas are characterized by spatial inhomogeneities such as Internal Transport Barriers (ITB)[2, 9, 10], which are regions of the plasma interior characterized by a transport level which is comparable to the collisional one for ions, and in some cases only slightly above this level for electrons[11].

A universally accepted theoretical explanation of ITBs has not yet been found[12, 13], and experimental information on the dynamics of plasma fluctuations in this regime is still very incomplete. The large density and temperature gradients characterizing these regions cause difficulties to diagnostics since the barrier's narrow spatial extent requires a very high spatial resolution; additionally, the WKB[14] approximation, upon which the interpretation of the experimental data from some diagnostics is based, fails in the high-gradient region. These same gradients also cause numerical instabilities in simulations to be very severe.

TCV is characterized by the strongest direct electron heating on any tokamak, while the ion heating is negligible[15]. In addition, the very low density required by the heating

method results in a collisional decoupling of the two species and thus in an extremely high ratio of electron to ion temperature, which in turn enables the study of the electron transport alone [11]. Considering all the plasma features mentioned above in terms of spatial inhomogeneities, fast phenomena, and small spatial scale micro-structures, a dedicated and novel diagnostic system with high temporal and spatial resolution is therefore required to allow a better experimental characterization and a comparison to theoretical models as straightforward as possible. The characterization of the fluctuations should involve their temporal and spatial structures, their wave-number and frequency spectra and their statistical properties. A crucial goal is to study the turbulence levels and characteristics in relation to the internal magnetic configuration, plasma shape and other parameters such as the impurity ions' concentrations. An item of particular interest and very relevant to current theoretical debates is the detailed phenomenology of ITB triggering in relation to the $\mathbf{E} \wedge \mathbf{B}$ flow shear [16], which can be deduced from Doppler spectroscopy measurements. Of course, even though understanding turbulence stabilization in structures such as ITBs is of paramount importance for fusion studies, the diagnostic should work also in any other possible configuration.

In the following we will provide an overview of all the turbulence diagnostics which have been considered in the feasibility study.

2.3 Modeling predictions of turbulence characteristics in the TCV tokamak

In this section we will briefly describe the TCV tokamak in a somehow more diagnostic related way with respect to what has been done in Chapter 1, the goal being to point out all the TCV features working in favor of some diagnostics and against other ones.

The TCV tokamak is a highly flexible machine in terms of plasma shapes and positioning in the vacuum vessel. The cross section of the vacuum vessel is approximately rectangular with dimensions 0.55 m x 1.55 m, horizontal and vertical, thus allowing plasma elongations roughly between 1 and 3. Moreover, if the elongation is less than about 2, the plasma vertical position can be chosen with some freedom thus implying that the operability of a possible diagnostic should not depend on plasma shape and on its vertical position, or, at least, should be as independent from them as possible.

Even though TCV can operate with plasmas at different heights in the vacuum vessel, for unknown reasons, probably due to tiles-Scrape Off Layer (SOL) interactions, stationary ELMy H-mode plasmas can be sustained only for $Z \geq 0.1$ m above the mid-plane, preferably at $Z = 0.23$ m (this is a commonly used position as it is symmetric between the equatorial and upper ECRH launchers). This implies, if a vertical position has to be

preferred, the need to optimize a diagnostic to operate with plasmas at $Z = 0.23$ m. Another important feature is the absence of external ion heating, which immediately implies two things. First, ion turbulence is not expected to play any significant role. Second, electron-scale turbulence, the so-called Electron Temperature Gradient (ETG) modes, are not expected to be at play in advanced scenarios. This can be understood by looking at the ETG threshold formula, derived in [17] by means of a number of linear simulations using the GS2 code. The linear threshold is given by

$$R/L_{T_e,th} = \max \left[\left(1 + Z_{eff} \frac{T_e}{T_i} \right) \left(1.33 + 1.91 \frac{s}{q} \right) (1 - 1.5\epsilon), 0.8 \frac{R}{L_n} \right], \quad (2.2)$$

where ϵ is the inverse aspect ratio, q the safety factor, s the magnetic shear and Z_{eff} the effective charge. This formula was derived for positive values of magnetic shear, whereas for negative values, the following holds [18]:

$$R/L_{T_e,th} = \left(1 + Z_{eff} \frac{T_e}{T_i} \right) \left(2 + 0.4|s| + 4.2 \frac{|s|}{q} \right). \quad (2.3)$$

In the case of density profiles that are not too steep, the linear threshold depends weakly on the density gradient and, being linear in T_e/T_i , becomes very high in an advanced TCV scenario, where T_e/T_i can be as high as 10, or even more. Additionally the Z_{eff} dependence increases the linear threshold since, in TCV, the experimental effective charge is observed to significantly increase during ECH-ECCD operations, i.e. when operating in an advanced scenario. These formulae were used at the start of this feasibility study to search for ETG modes in the entire TCV database: they were found in the core only in very few marginal conditions, while their presence in the edge is questionable due to large error-bars in kinetic profiles. Only in ohmic shots, where $T_e \simeq T_i$ and $Z_{eff} \simeq 1$, are they expected to be unstable in the core. However, in such plasmas, on the basis of a mixing length argument, their contribution to the total transport is expected to be insignificant compared to longer wavelength modes, such as Ion Temperature Gradient (ITG) and Trapped Electron Modes (TEM).

The mixed fluid-kinetic 0-D code KINEZERO [19] was also run on a large number of different TCV shots, with experimentally measured kinetic profiles, to look for ETG modes; when high k fluctuations were found, these could be due to high spectral tails of the TEM mode; therefore, on a theoretical basis, it is expected that it will be difficult to experimentally assess the existence of ETG modes in TCV, at least in advanced scenarios. As a result of this large database of simulations, the expected minimum fluctuation level, including all modes, was estimated as

$$\frac{\Delta n}{\sqrt{f}} = 2\pi \nabla n \sqrt{\sum_k \frac{1}{k^2 \gamma_k}} \quad (2.4)$$

and is shown in Fig.2.1. This equation estimates the total transport with a mixing-length argument and normalizes it to the frequency bandwidth, with the assumption that, in the low k spectral region which contributes most to the total transport, the growth rate of each mode is proportional to its real frequency. The normalization to the frequency is necessary to take into account the effect of white noise on measurements taken with different bandwidths. This level gives an estimate of the minimum acceptable Signal-to-Noise (S/N) ratio of any projected diagnostic. Another important quantity to be taken

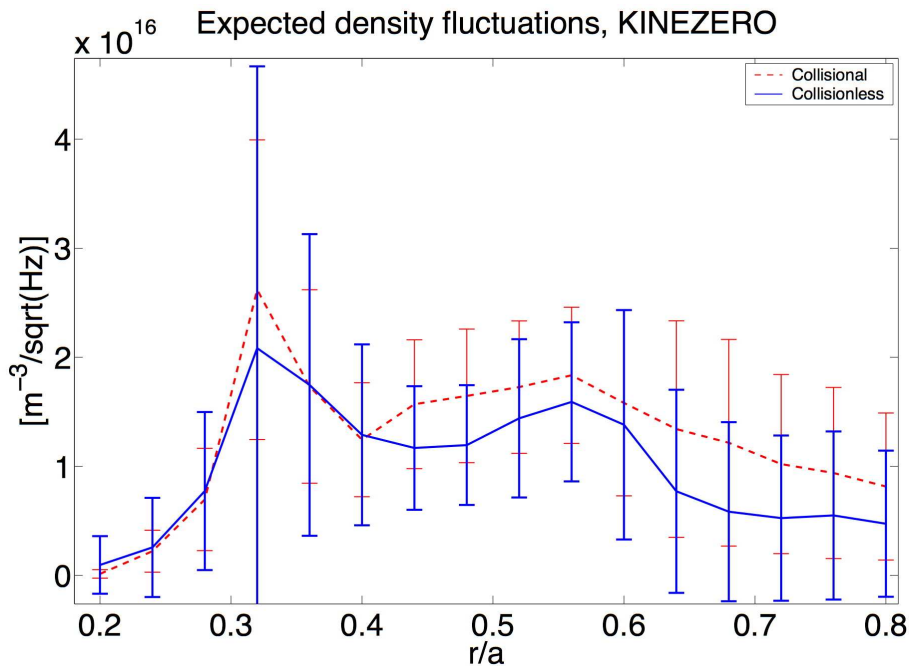


Figure 2.1: Minimum expected fluctuation density, per unit frequency bandwidth, on the basis of a set of KINEZERO collisional and collisionless simulations, as a function of the TCV normalized minor radius. Error-bars are calculated as standard deviations on the entire simulation database, while values represent the average.

into account in a feasibility study is the spectral extent of unstable modes to be detected. Ideally the experimental apparatus should be designed and built to capture any mode expected to be unstable; in practice this cannot generally be done due to the intrinsic resolution of the system which imposes lower and upper bounds. In this respect the database of simulations was also used, in particular, to deduce the shortest wavelength of fluctuations of interest to be expected in TCV.

KINEZERO is described, in detail, in [19]; for our present purposes it is sufficient to note that it relies on a number of approximations to considerably speed up the calculations, thus implying that the absolute calculated values must be treated cautiously. This is ultimately true of any turbulence code which has not been benchmarked against experiments and, as of this writing, none of the existing codes have seriously undergone such benchmarking yet. However to increase confidence in these results, we performed a set of linear

simulations using the GS2 code [20], with a Miller parametrization of the equilibrium [21], which is a local gyro-kinetic code, described in Chapter 4, which models the physics of plasma micro-instabilities more accurately than KINEZERO. The maximum expected unstable turbulent wave-number is on average smaller, with respect to KINEZERO, by about 50%, not exceeding 50 cm^{-1} . The lowest density fluctuations to be measured have been estimated to be $10^{17} \text{ m}^{-3} \text{ MHz}^{-1/2}$ at $\rho=0.44$ for an ITB shot and $6 \cdot 10^{18} \text{ m}^{-3} \text{ MHz}^{-1/2}$ at $\rho=0.72$ for an L-mode shot, where ρ is defined as the square root of the normalized volume.

2.4 Overview of main possible diagnostics

2.4.1 Beam Emission Spectroscopy

The Beam Emission Spectroscopy (BES) relies on the measurement of intensity fluctuations of the light emitted either by bulk plasma ions excited by beam ions or by beam neutrals excited by collisions with bulk plasma ions and electrons. The volume intersected by the lines of sight of the beam and of the optics is the measurement volume. Correlation lengths can be retrieved by correlating spatially separated lines of sight.

Two conflicting requirements are to be satisfied: localization of the measurement and maximization of the amount of signal collected. Concerning the first requirement, as is evident from figure 2.2, which gives a schematic view of a common BES geometrical configuration, the intersecting volume is minimized when the beam trajectory and the optical lines of sight are orthogonal to each other, while the integration length, and therefore the amount of signal collected, is maximized in a parallel configuration. Despite the better localization, a perfect perpendicular configuration is not desirable in view of the absence of a net Doppler shift which would help in discriminating the actual signal from the spurious one self-generated by the plasma. Furthermore, the beam must be as quiescent as possible in the range of frequencies of expected fluctuations since fluctuations in the beam intensity would be mistaken for actual density fluctuations.

The relevant physical processes for the BES diagnostic are the following



i.e. electron and bulk X ion impact excitation respectively, where bulk ion can be either main ions or impurities. The amount of signal emitted at the wavelength λ can be written as

$$E_\lambda = n_e n_B \langle \sigma v \rangle_v^{e,\lambda} + \sum_Z n_Z n_B \langle \sigma v \rangle_v^{Z,\lambda} \quad (2.7)$$

where n_B is the beam density and the sum extends over all the impurity species present in the plasma. For beam energies larger than 40 keV, ion excitations tend to dominate over electron excitation [24], and considering that

$$\langle \sigma v \rangle_v^{Z,\lambda} = Z^2 \langle \sigma v \rangle_v^{1,\lambda} \quad (2.8)$$

Eq.2.7 reduces to

$$E_\lambda = Z_{eff} n_e n_B \langle \sigma v \rangle_v^{1,\lambda} \quad (2.9)$$

thus implying that the presence of impurities could severely complicate the analysis since the BES signal would be sensitive to the effective charge rather than to the ion density; this in turn implies the need for an independent diagnostic to monitor the effective charge. Let us now evaluate the approximate expected performance of a hypothetical BES diagnostic in TCV.

The TCV tokamak is equipped with a non perturbing Neutral Beam Injector for Diagnostic purposes (DNBI) at an operational energy of about 50 keV, injecting hydrogen at a toroidal angle of 11.25° in the horizontal mid-plane. The beam FWHM is equal to 12 cm and has an equivalent beam current of 0.5 A.

The percentage of excited states in a hydrogen neutral beam traveling in a hot plasma has been calculated in [26, 28] taking into account all radiative and collisional processes which populate and depopulate all the excited levels. In the excited states $n=2$ and $n=3$, respectively generating the Lyman and Balmer lines, these percentages are within 0.001-0.01 and within 0.0008-0.0025 respectively, depending on plasma conditions, for densities equal to 10^{19} and 10^{20} m^{-3} . Since 50 keV is much higher than any ion temperature ever measured in TCV [29], the velocity dependence of the reaction cross section can be neglected. Considering densities of 10^{19} to 10^{20} m^{-3} and neglecting impurities we thus obtain, for the Balmer line, an expected photon rate between 1.58 and $4.95 \cdot 10^{17} \text{ ph s}^{-1} \text{sr}^{-1} \text{m}^{-2}$ and for the Lyman line 0.21 and $4.23 \cdot 10^{19} \text{ ph s}^{-1} \text{sr}^{-1} \text{m}^{-2}$. Considering an *etendue* [25] equal to 10^{-6}sr m^2 and an optical collection and transmission efficiency equal to 40% we obtain \tilde{n}/n equal to 0.81%-1.41% and 0.09%-0.12% respectively. These values have been obtained by assuming, as noise source, only photon noise at 1MHz bandwidth; in particular the beam is supposed to be quiescent, both in energy and in equivalent current, at the frequencies of interest.

Let us now briefly analyze the spatial localization. The BES diagnostic would integrate along any line of sight intersecting the beam width, and the localization would then be smeared by the random walk of a beam particle during the life time of the meta-stable excited level. This can be evaluated as the speed of a 50 keV neutral times the spontaneous radiative decay lifetime; the latter being of the order of tens of nanoseconds, and thus negligible compared to normal core fusion plasma collisional times, it results in radial shifts of the order of 1 cm. Let us consider an integration length L across the

beam width, L being the effective width L_0 composed of the actual beam full-width, $2w_0$, plus any broadening, such as the one due to radiative decay, divided by the sinus of the intersection angle between the beam and the diagnostic line of sight. Let us define ϕ

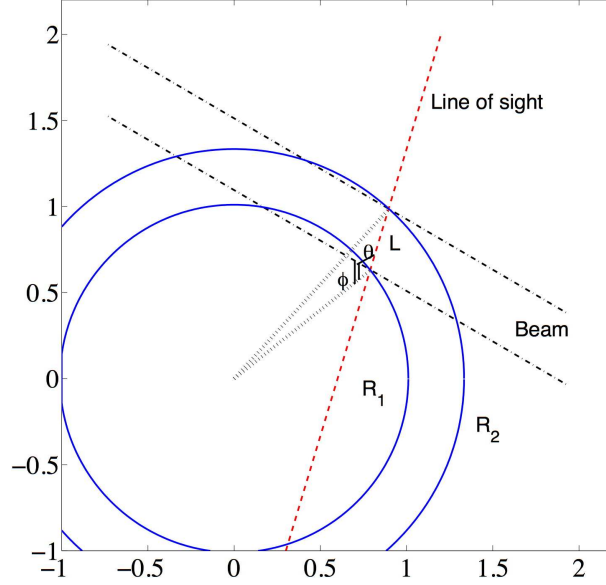


Figure 2.2: Schematic view of the BES configuration with the NBI and the two extreme radial positions sampled by a given line of sight.

as the angle between the major radius and the beam at its innermost intersection point with the line of sight (see Fig.2.2). Choosing in Fig.2.2 $\phi = \pi/2$ (which is not the case shown), allows one to sample the innermost radial position, which is one of the quantities of interest. The difference between the maximum and the minimum major radii in the intersection region is given by Carnot's theorem

$$R_2^2 - R_1^2 = L^2 - 2LR_1 \cos\left(\frac{\pi}{2} + \theta\right) \quad (2.10)$$

where θ is the angle between the beam and any given line of sight, and is positive defined, and $\phi = \pi/2$ has been assumed. This gives a normalized radial resolution equal to

$$\delta\rho = \frac{R_2 - R_1}{a} = \frac{R_1}{a} \left[\sqrt{1 + \frac{L^2}{R_1^2} - \frac{2L}{R_1} \cos\left(\frac{\pi}{2} + \theta\right)} - 1 \right] \quad (2.11)$$

When the integration length is small compared to the plasma major radius, the linear term in L/R_1 inside the square root dominates over the quadratic term, implying a strong dependence over the angle θ , i.e. whether the measurement is taken at the tangency point between the line of sight and a given flux surface. By Taylor expanding Eq.2.11 to the second order in L/R_1 we obtain

$$\delta\rho = \frac{L}{a} \sin(\theta) + \frac{L^2}{2aR_1} \cos(\theta)^2 \quad (2.12)$$

Since $L \equiv L_0/\sin(\theta)$, where $L_0 \geq 2w_0$, the radial resolution is composed of a fixed term, L_0/a , which accounts for the beam width, plus an additional term equal to $L_0^2 \cot(\theta)^2/(2aR_1)$, which accounts for the geometrical set-up.

In TCV a is equal to 0.25 m and, for core turbulence measurements, $0.9 \text{ m} < R_1 < 1.1 \text{ m}$ which gives, for $\delta\rho$, the numerical values shown in Fig.2.3, which makes clear how a good localization is achieved both with a short integration length and with a tangential configuration (near-normal to the beam). Finally, since the BES diagnostic relies on ion

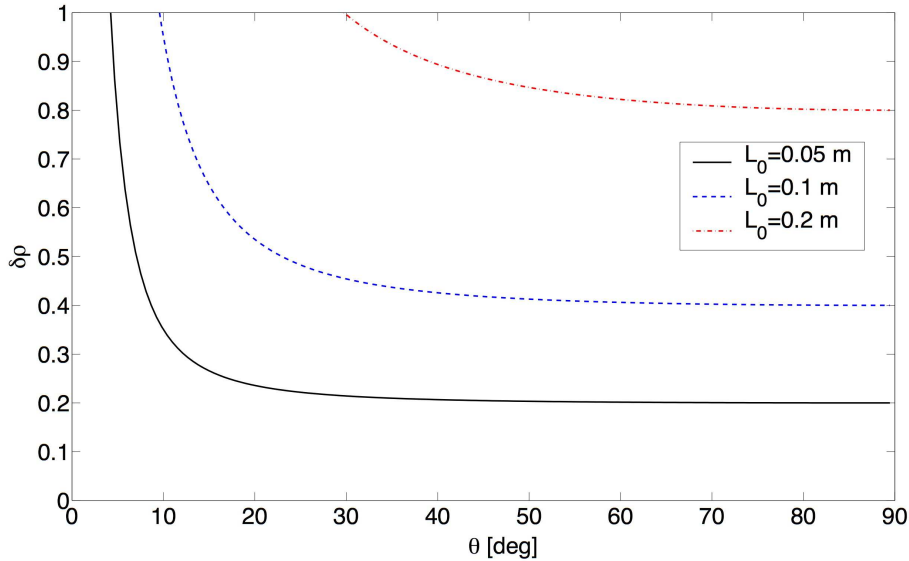


Figure 2.3: Normalized radial resolution for a number of geometrical configurations. The difference, for each value of L , in the value of R_1 in the range 0.9-1.1 m is negligible.

density fluctuations, it is sensitive to modes in the range of the ion Larmor radius: generally speaking $k_\theta \rho_i < 1$, while the minimum accessible wavenumber corresponds to a wavelength comparable with the machine size, i.e. $k_\theta \rho_i > 0.05 - 0.1$ for typical TCV ion temperature and magnetic field. As a last consideration we recall that the lines of sight must nevertheless have a finite, even though small, component along the beam in order to produce a finite Doppler shift permitting spectroscopic separation from the background plasma emission. Indeed, if we consider a line half-width σ for the bulk plasma signal equal to T_i , to discern the beam signal we need to Doppler shift it by typically 5σ ; by adopting $T_i \leq 2 \text{ keV}$ we obtain that the Doppler shift should be, at least, 0.40 nm for Lyman line and 2.14 nm for Balmer line. This translates into a relative inclination between the NBI beam direction and the lines of sight of, at least, 64 degrees for both lines; if we take as a limit 3σ instead, we obtain 70 degrees (the angle is the same as defined in Eq.2.11). These shifts need to be, of course, resolved by the spectrometer as they would produce shifts of 0.40 and 0.31 nm for the Lyman line and of 2.14 nm and 1.66 nm for the Balmer line, respectively.

2.4.2 Electron-Positron annihilation

Matter and anti-matter, when they interact, tend to annihilate, generating light whose frequency and momentum satisfy the energy and momentum conservation principles.

Considering positrons, i.e. the anti-electrons, they annihilate with electrons generating two photons of 512 keV each, plus the equivalent energy corresponding to the kinetic energy of the pre-existing electron and positron. The idea is to study electron dynamics by measuring 512 keV photons originating from plasma electrons annihilating with externally injected positrons. The Lorentz force deters positrons from being directly injected in tokamaks because of large magnetic fields, which are of the order of 1 T or more. Indeed the Larmor radius of a charged particle is equal to

$$r = \frac{p_{\perp}}{qB} = \frac{\sqrt{E^2 - m_0^2 c^4}}{qBc} \quad (2.13)$$

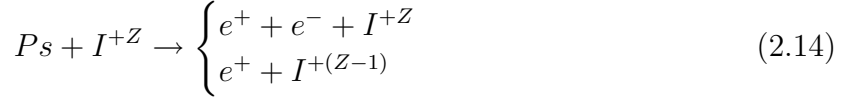
where B is the magnetic field, p_{\perp} the particle momentum perpendicular to the magnetic field, q its charge, m_0 its rest mass, c the speed of light and E the component of the total energy perpendicular to the magnetic field.

Considering a positron injected in TCV, whose field is about 1.4 T on axis, it must have an initial energy of about 42 MeV to penetrate up to the magnetic axis, i.e. to have a Larmor radius of about 10 cm. Such a high energy, corresponding to a relativistic positron, can be reached only by building an ad-hoc accelerator; therefore positrons should be injected in some sort of neutral form: for example the positronium.

The ground state of positronium exists in two different forms: the singlet state, para-positronium (p-Ps), or the triplet state, ortho-positronium (o-Ps). These two states have lifetimes equal to 125 picoseconds and 142 nanoseconds, respectively. The p-Ps lifetime is definitely too short to permit the positronium to penetrate in the plasma, while the o-Ps should have a velocity of about $4 \cdot 10^6$ m/s to reach the TCV magnetic axis. Additionally, collisions with plasma electrons and ions cause the o-Ps to convert into the p-Ps state thus causing an almost immediate loss of the positronium itself through annihilation. The cross-section was calculated in [69, 70] as $2 \cdot 10^{-17} \text{cm}^2$ for 10 eV electrons and as $5 \cdot 10^{-17} \text{cm}^2$ for 10 eV hydrogen ions. These cross sections rapidly decrease for higher energies which will thus be neglected for the purpose of this study. Considering the velocity positronium should have in order to penetrate into the TCV plasma, this translates to about 10^6 reactions/s, which is equivalent to about 0.1 reactions during the time travelled by the positron beam inside the plasma. Thus, as a rough estimate, 10% of the beam would be lost through these collisional processes.

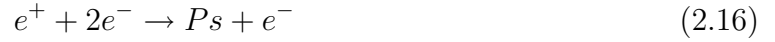
The remaining 90% of positronium atoms propagating through the plasma will undergo

collisional ionization processes with plasma electrons, bulk ions and impurities



or will annihilate after 142 ns. In the following, for simplicity, we will consider that all these atoms will react with the plasma before being annihilated.

All these reactions have been shown in [22] to be equivalent to assuming the plasma to be composed of pure hydrogen and the electron ionization rate to be equal to twice that of hydrogen. Positrons can undergo several processes: re-form positronium in collisions with neutral hydrogen, annihilate with plasma electrons and undergo three body recombination, i.e.



The latter mechanism, being a three body reaction, is rather improbable and can be neglected [23], while the two former ones will be taken into account for the estimate of the total signal collected from density fluctuations. Half of the positronium formed by collisional processes will immediately undergo annihilation while the remaining half will either annihilate, exit the plasma or be re-ionized at some distance from the recombination point. A schematic overview of all the possible reactions the Ps beam can undergo is depicted in Fig.2.4.

Let us call α the probability of the reaction o-Ps to p-Ps, β the total ionization probability of Ps, γ the annihilation with a plasma electron, δ the probability to re-form another Ps by colliding with a plasma ion (the ortho-para branching ratio is 0.5), then, having \dot{N} o-Ps per second we have a total rate of annihilations equal to

$$\begin{aligned} & \alpha\dot{N} + (1 - \alpha)\beta\gamma\dot{N} + 0.5(1 - \alpha)\beta\delta\dot{N} + 0.5(1 - \alpha)\beta\delta[\alpha + (1 - \alpha)\beta\gamma + 0.5(1 - \alpha)\beta\delta]\dot{N} + \dots \\ & = \sum_{n=0}^{\infty} \dot{N}[\alpha + (1 - \alpha)\beta\gamma + 0.5(1 - \alpha)\beta\delta][0.5(1 - \alpha)\beta\delta]^n \\ & = \dot{N}[\alpha + (1 - \alpha)\beta\gamma + 0.5(1 - \alpha)\beta\delta] \frac{1}{1 - 0.5(1 - \alpha)\beta\delta} \end{aligned} \quad (2.17)$$

The sum extending to infinity simulates an infinite plasma, even though for a finite plasma the probability of a positron being transported to the first wall and being annihilated should be used instead; in our rough estimate we will consider an infinite plasma. We have already estimated α being equal to 0.1 which, considering the values of cross sections reported in [22], is the value we will assume also for ionization and recombination processes. We will further simplify the calculation by neglecting γ compared to δ since, for typical plasma parameters, the lifetime of positrons in a typical fusion plasma is of the order of 10 s [22], therefore much longer than energy and particle confinement times.

Thus the count rate is of the order of 10% of the incoming Ps flux. The fluctuating signal, which is due to density fluctuations, scales as the spectrum of density fluctuations compared to the total density.

Both ion and electron density fluctuations will contribute to the total signal even though the major part is due to o-p Ps conversion, i.e. the first term in the above equation. This term, being a Poisson process, is affected by an intrinsic relative noise equal to $1/\sqrt{N}$. So, estimating the fluctuating core signal to a few percent, \dot{N} has to be larger than 10^4 . Additionally, this diagnostic could hardly be sensitive to the position of the event in the plasma because the higher order terms in the above equation, which constitute about a tenth of the total signal, are averaged over the whole minor radius, being due to ionization and recombination effects. Localization could not be achieved by isolating detectors with long shielding tubes in such a way as to collect only radiation coming from a given plasma region, because the measurement would be anyway line integrated along the symmetry axis of the tube, i.e. the line of sight of the detector.

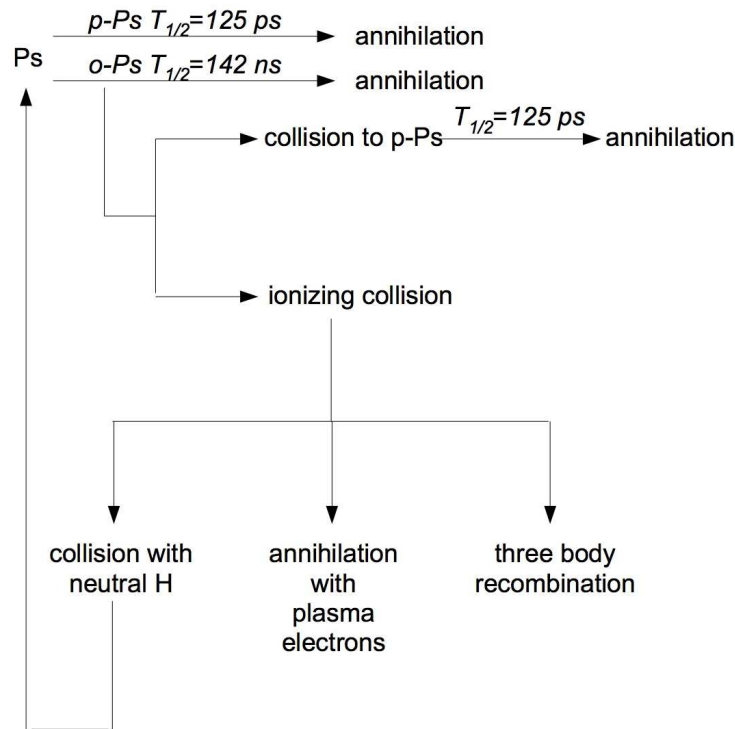


Figure 2.4: Schematic view of the different processes, considered in the text, which positrons can undergo in a plasma.

2.4.3 Reflectometry

In reflectometry experiments an electromagnetic wave is injected into the plasma and a part of it is received after reflection at the cut-off layer. The spatial location of the

reflecting layer in the plasma depends in general, in the cold plasma approximation, upon the electron density profile, the total magnetic field, the probing beam frequency and its polarization with respect to the total magnetic field.

Usually reflectometers are used to determine density profiles via radar-like techniques, or to investigate plasma density fluctuations which perturb the radial position of the reflecting layer. The received reflected wave is mixed with a reference signal thus enabling the extraction of the phase delay which is a direct measure of the wave time of flight in the plasma.

In the geometric optics approximation, the phase difference between two points can be written as

$$\Delta\phi_{A,B} = \int_A^B \mathbf{k}(\mathbf{x}) \cdot d\mathbf{x} = \int_A^B dx N(x) \frac{\omega_0}{c} \quad (2.18)$$

where N is the plasma refraction index, c is the speed of light and ω_0 is the pulsation of the injected wave which, in normal tokamak experiments, is in the range of the microwaves. Considering a pure ordinary mode propagating in the plasma perpendicularly to the total magnetic field, the refractive index is given by $N^2 = 1 - \omega_p^2/\omega^2$, where ω_p is the plasma frequency. Near the cut-off layer the WKJB approximation breaks down because k tends to zero, but it can be shown that in the case of negligible absorption and linear density gradient [27], Eq.2.18 can still be used by subtracting a fixed $\pi/2$ phase shift such that

$$\Delta\phi = \oint dx N(x) \frac{\omega_0}{c} - \frac{\pi}{2}, \quad (2.19)$$

where the integral is calculated back and forth to the cut-off.

Despite the real behaviour caused by temperature effects, the standard theory assumes the cold plasma approximation, which allows only two modes of propagation, namely X and O mode. These correspond to three different cut-off frequencies, named O-R-L, which have angular frequencies equal, respectively, to

$$\omega_{pe} \quad (O) \quad \sqrt{\frac{\omega_{ce}^2}{4} + \omega_{pe}^2} - \frac{\omega_{ce}}{2} \quad (R) \quad \sqrt{\frac{\omega_{ce}^2}{4} + \omega_{pe}^2} + \frac{\omega_{ce}}{2} \quad (L) \quad (2.20)$$

where ω_{pe} is the plasma frequency and ω_{ce} is the electron cyclotron frequency. Taking into account finite plasma temperature effects it is possible to show [34] that absorption is negligible, but a correction of the ray trajectory is necessary; this correction is obtained by replacing the electron mass with $m_e = m_e \sqrt{1 + 5/K}$ in the cold dielectric tensor, where $K = m_e c^2 / T_e$. The validity of this equation for the X mode, which is the only mode for which these effects are important, requires $K(1 - \omega_{ce}/\omega_0) \gg 1$; for a TCV eITB pulse, for example, this value can be as high as 40.

In the case of fluctuation studies we distinguish between homodyne and heterodyne detection; the former measures

$$I_r = \tilde{I}_0 \cos(\tilde{\phi}) \quad (2.21)$$

where I_r is the received intensity, expressed as a fluctuation of the amplitude, \tilde{I}_0 , and of the phase, $\tilde{\phi}$. The latter splits the received signal and shifts one component by $\pi/2$ thus obtaining

$$I_{r,1} = \tilde{I}_0 \cos(\tilde{\phi}) \quad I_{r,2} = \tilde{I}_0 \sin(\tilde{\phi}) \quad (2.22)$$

yielding fluctuations both in the reflected amplitude, which are related to the shape of the reflecting layer, and in the reflected phase, which are proportional to the time of flight.

As briefly mentioned above, in the presence of density fluctuations the cut-off layer position is modulated by a scale length L given by

$$\frac{1}{L}(t) = \frac{\partial \tilde{n}}{n_0 \partial x}(t) = \frac{\int_{-\infty}^{\infty} ik \hat{n}(k, t) e^{ik \cdot x}}{n_0} \quad (2.23)$$

which, in the case of an ideally monochromatic fluctuating spectrum, is inversely proportional to the fluctuating wave vector. The phase of the reflected wave, being proportional to the beam path, will fluctuate as well; therefore the temporal spectrum of fluctuations can be reconstructed by measuring the phase of the reflected wave.

Let us write the fluctuating permittivity as

$$\epsilon(x) = \epsilon_0(x) + \tilde{\epsilon}(x); \quad (2.24)$$

the fluctuating phase is then calculated by expanding Eq.2.19 to first order in the perturbation

$$\begin{aligned} \phi &= 2k_0 \int_0^{x_c(\omega_0)} dx \sqrt{\epsilon_0 + \tilde{\epsilon}} \simeq 2k_0 \int_0^{x_c(\omega_0)} dx \left[\sqrt{\epsilon_0} \left(1 + \frac{\tilde{\epsilon}}{2\epsilon_0} \right) \right] \\ &= 2k_0 \int_0^{x_c(\omega_0)} dx \sqrt{\epsilon_0} + k_0 \int_0^{x_c(\omega_0)} dx \frac{\tilde{\epsilon}}{\sqrt{\epsilon_0}} = \phi_0 + \tilde{\phi} \end{aligned} \quad (2.25)$$

In the vicinity of the cut-off layer, the WKBJ approximation breaks down due to the singularity in the integrand. Therefore this equation is valid when the radial fluctuation wave number, k_r , is less than $k_0/\sqrt[3]{k_0 L_\epsilon}$ [34], where k_0 is the probing wave vector and $L_\epsilon = (d\epsilon_0/dr)^{-1}$ is the scale length of the plasma permittivity at the cut-off. For TCV, the equivalent radial scale is approximately equal to 1.5 cm for an eITB, 1.7 cm at mid-radius for an H-mode and 1.9 cm at the edge of an H-mode. The wave number is thus upper bounded to approximately 3 cm^{-1} for all these three cases. Fluctuation wave numbers that far exceed this limit give contributions to the reflected phase from all the points where the shape of the zero order solution of the wave equation matches the shape of density fluctuation distribution[33].

In the case of localized measurements it is possible to derive an equation binding the radial wave number spectra of phase and density fluctuations[35]

$$\Gamma_\phi(k_r) = 2\pi \frac{k_0^2}{|k_r|} M L_\epsilon [C^2(w) + S^2(w)] \Gamma_n(k_r) \quad (2.26)$$

where the spectra, $\Gamma_{n,\phi}$, are defined as the Fourier transform of the autocorrelation function considered as a function of x_c , $w = \sqrt{2|k_x|L_\epsilon/\pi}$ is a quantity much larger than unity for tokamaks, $C^2 + S^2$ are Fresnel integrals approximately equal to 1/4 each, M is defined as

$$M = \frac{\partial \epsilon}{\epsilon \partial n_e}. \quad (2.27)$$

In the case of propagation perpendicular to the magnetic field M is equal to 1 for O mode and 4 for X mode.

Equation 2.26 gives the opportunity to recover the spectrum of density fluctuations, Γ_n , from that of phase fluctuations, Γ_ϕ , in the case of long wavelength radial fluctuations.

It has been pointed out in [41] how the interpretation of reflectometry becomes much more difficult when the poloidal component of density fluctuations' wavevector cannot be neglected compared to the radial one. In fact in this case, after reflection, the beam breaks up into a group of scattered waves propagating in different directions, among which also the specular one, that add up at the receiving antenna. Poloidally scattered components are collected at the receiving antenna due to, first, the antenna spatial extent and, second, to the plasma density profile which, being in general peaked, acts as a lens causing rays to converge. Two dimensional fluctuations would not cause any problem in the case of flat or hollow density profiles, which would by the way force the use of X-mode polarization since the dependence of its cutoff on the magnetic field preserves spatial resolution. On the contrary, since the O-mode cut-off only depends on the density profile, the spatial resolution would therefore be lost if the density profile was flat and plasma regions with a hollow density profile would be inaccessible.

In a numerical study [41] Mazzucato showed that, taking into account 2D fluctuations, there exists, along the radial direction, a surface, called virtual cut-off, where the level of fluctuations of the reflected wave amplitude is the lowest along the orthogonal direction. This suggests the possibility of reducing the problem from 2D to 1D thus enabling the use of 1D formulas.

If we call σ_ϕ the standard deviation of the phase modulation and Δk_θ the width of the poloidal fluctuation spectrum, then the variance of the scattered waves in the radial direction is equal, if $\Delta\sigma_\phi \Delta k_\theta \ll k_0$, to $\sigma_\phi^2 \Delta k_\theta^2 / (2k_0)$; so that an observer located at a distance from the (virtual) cut-off greater than the reciprocal of this spectral width will sample a complicated interference pattern and will not be able to recover the correct fluctuations. However, in this model an observer, if able to collect all the scattered rays, would see them coming from a point, the virtual cut-off, due to the bending of all the rays given by the lens effect of the plasma; in this way he could be able to recover the required spectrum adopting a 1D geometric optics model for the amplitude of the reflected electric field.

This model of reflectometry requires the following conditions:

Validity of the geometrical optics limit

$$\Delta k_r < \frac{k_0}{\sqrt[3]{k_0 L_\epsilon}}. \quad (2.28)$$

The reflecting points must be distributed over a distance shorter than the radial scale lengths of fluctuations

$$\sigma_\phi^2 < \frac{k_0^2}{L_\epsilon \Delta k_r \Delta k_x^2}. \quad (2.29)$$

Since for large fluctuations $\Delta r_c/L_\epsilon = \sigma_\phi^2/L_\epsilon \Delta k_r \Delta k_x^2$, for an extraordinary mode we obtain $\sigma_n^2 < 1/(\pi^{3/2} L_n^2 \Delta k_x^2)$; in the opposite limit of fluctuations, that is $\sigma_\phi^2 \ll 1$, this equation reads $\Delta k_r \Delta k_x^2 < k_0^2/L_n$. In TCV we can expect $\sigma_n < 10^{-2,-3}$ for the first inequality, while $\Delta k_r < 5 \text{ cm}^{-1}$ taking $L_n = 50 \text{ cm}^{-1}$ and $\Delta k_x = 1 \text{ cm}^{-1}$. These limits decrease very rapidly in case of stronger poloidal turbulence.

If these conditions are fulfilled it is indeed possible to build a reflectometer which is actually able to collect almost all the scattered waves, thus obtaining complete information on the fluctuation spectra; such a device is called Microwave Imaging Reflectometer (MIR) and is described next.

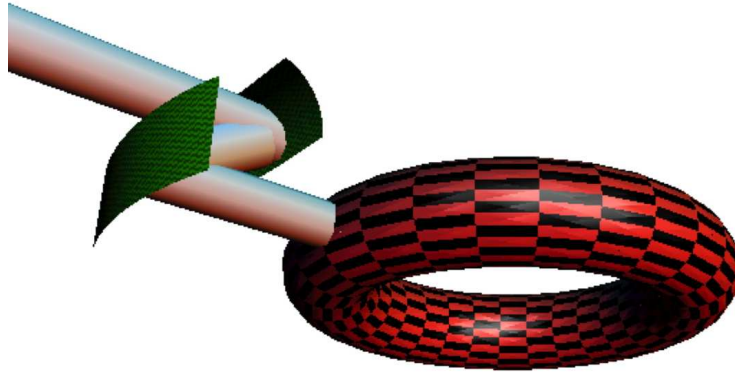


Figure 2.5: Schematic view of the Microwave Imaging Reflectometer set-up. The beam front is tailored, by two cylindrical mirrors, to approximately match the curvature of the cut-off surface, before being injected in the plasma.

The optical set-up, schematically represented in Fig.2.5, has to make use of two cylindrical lenses to tailor the beam wave front in order to make its curvature as close as possible to that of the reflecting layer. This means that the poloidal lens' focal point is on the virtual cut-off surface, while the toroidal one is at $R=0$; obviously the poloidal lens has to be translatable to search the focus of the virtual cut-off for various discharges and probing frequencies. In this way a plane image of the cut-off layer can be produced on the detection plane, where a 2D array of detectors is able to reconstruct the fluctuations profiles. In order to avoid spurious refraction effects, and considering the size of the optics,

focusing metallic mirrors are to be preferred to lenses. It has to be underlined that, even though MIR was invented to recover 1D fluctuation spectra, it is able to sample 2D spectra by means of a two-dimensional detector array on the image plane.

The advantages of MIR are the following

1. Possibility of using X or O mode (as indeed in standard reflectometry)
2. Possibility of acquiring 3D plasma fluctuations with multiple closely spaced cut-offs.

The disadvantages are

1. The considerable amount of space required by the installation (at least a couple of meters in radial direction outside the vessel)
2. The large amount of data collected (for a 10x10 array detection system at a frequency of 1MHz we obtain 10^8 words/s, which could be reasonably translated into 10^7 to $2 \cdot 10^8$ words/pulse for TCV)
3. The amount of local oscillator power needed in order to obtain a heterodyne signal
4. The instrumental selectivity allows one to investigate only fluctuations for which $k_{\perp} \rho_i < 1$, thus excluding part of the electron modes
5. The fact that, for a midplane port, it can work only for plasmas at $Z=0$ or, alternatively, for highly elongated negative triangularity plasmas which, on the low field side, offer a flat reflecting layer.

The instrumental selectivity depends on the poloidal region of the cut-off covered by the beam and on the spatial resolution; for example with a resolution of 1 cm and a region of 10 cm, the theoretical resolution is $0.63 \text{ cm}^{-1} < k_{\theta} < 3.1 \text{ cm}^{-1}$.

Considering a 10 cm wide probing wave having $k_0 = 20 \text{ cm}^{-1}$ and fluctuations dominated by $k_{\theta} \simeq 3 \text{ cm}^{-1}$, we obtain a divergence angle of the probing beam such that, travelling from the virtual cut-off to the vessel and about 1 meter outside it (the distance covers the space needed to install the mirror matching the toroidal curvature of flux surfaces), the width of the beam becomes almost equal to half a meter, which is the minimum size of the mirrors in the vertical direction.

In the following we will estimate the performance of a hypothetical future reflectometer in TCV.

Assuming $\Delta k_{\theta} = 1 \text{ cm}^{-1}$ (which is already about a factor 2 lower than the expected TCV edge turbulence wave numbers) and a level of density fluctuations equal to 1% we estimate the critical distance, beyond which it is impossible to recover correct data, to be

about 5 cm, which is the distance between the antenna and the virtual cut-off. Moreover the distance between real and virtual cut-offs is estimated, for cylindrical geometry, as

$$L = a (L_c)^b \quad (2.30)$$

where $a = 1 - 0.89e^{-0.43r_c}$, $b = 1 - 0.66e^{-0.45r_c}$ and r_c is the position of the real cut-off (all the parameters are expressed in meters)[36]. For typical TCV parameters this distance is estimated in 10 to 20 cm thus making, according to this model, the use of standard reflectometry quite unreliable.

These phenomena play a role also in the estimated correlation lengths given by the so-called correlation reflectometer, which is a set of standard reflectometers with sweepable frequencies which allow an estimate of the turbulence correlation length by spatially separating the respective cut-off layers. Indeed if we model the data taken by the reflectometer as actual data plus noise, what one obtains is a reduction of the correlation lengths estimated by the diagnostic with respect to the real turbulent value.

In [37] an attempt to quantify the signal of the correlation reflectometer with an analytical 2D non linear model is carried out and the predicted response is found to depend on the turbulence regime. In particular the authors summarize the response properties in two regimes

1. Low turbulence level, i.e. $\tilde{n}/n \ll 1$
2. High turbulence level, i.e. $\tilde{n}/n \lesssim 1$

and in the case of short poloidal correlation lengths compared to the Airy pattern. The authors find that, even with a low turbulence level, the extracted correlation lengths are a function of both the perturbed density and the effective correlation length, thus implying an intrinsic ambiguity in the deduction of the effective correlation lengths. In the case of strong turbulence, the two dimensional spectrum generates multi-scattering which eventually strongly modify the reflected spectrum in a way that is no longer related to the actual turbulence spectrum.

In competition with MIR a new imaging technique, synthetic imaging, has been proposed [38]. Briefly, it employs a numerical back projection analysis in order to recover the fluctuating electric field at the cut-off layer.

$$E(x, t) = F^{-1}\{F[E(x_0, t)e^{ik_x(x-x_0)}]\} \propto F^{-1}\{F[E(x_0, t)e^{ik_y^2(x-x_0)}]\} \quad (2.31)$$

where x is the cut-off layer radial position, x_0 the detecting plane position, F and F^{-1} stand for, respectively, Fourier and inverse Fourier transforms, $k_x = \sqrt{k_0^2 - n^2k_y^2} \simeq k_0 - n^2k_y^2/(2k_0)$, k_y being the poloidal fluctuating wave-vector. Assuming a constant

of proportionality, α , between measured frequency, Ω , and poloidal wave-vector we can rewrite the last equation as

$$E(x, t) = F^{-1}\{F[E(x_0, t)e^{i\alpha^2\Omega^2(x-x_0)}]\} \quad (2.32)$$

By varying the back-projection distance $x - x_0$ the authors could identify the presence of a virtual location in the plasma where the amplitude fluctuations strongly decrease and the phase fluctuations dominate. This plane corresponds to the image plane in a lens based optical system and, in [38], it is shown how synthetic reflectometry and MIR have similar response properties in the case of small density fluctuations.

Even though the synthetic reflectometer is by far simpler to implement than MIR, it has a few drawbacks:

1. The model is linear and cannot therefore work with high turbulence levels. Indeed in [38] the simulations find a virtual cut-off only for $\tilde{n}/n \lesssim 1\%$.
2. Fluctuating wave vectors must propagate in the poloidal direction much faster than their de-correlation time

Therefore all the reflectometry configurations considered so far seem to be limited to low turbulence levels or, in other words, to conditions treatable with linear models.

Another reflectometry configuration is the so called Doppler reflectometer, whose geometrical configuration is depicted in Fig.2.6, in which the probing beam does not propagate into the plasma orthogonally to the magnetic surfaces but at a finite angle in the poloidal direction. In this configuration the receiving horn receives the backscattered signal according to the Bragg relation

$$mk = k_0[\sin(\theta_i) - \sin(\theta_s)] \quad (2.33)$$

where m is the diffraction order, k is the fluctuating wave number and k_0 is the probing beam wave number. The most important contribution, the 0th order, corresponding to a standard Snell reflection, will propagate away from the receiving horn and will be reflected back and forth by the reflecting layer and the vacuum vessel. The backscattered field originates from a theoretically well defined wave-vector which depends only upon the probing frequency and the tilt angle of injection. Therefore, by scanning the injection angle it is possible to measure a large part of the fluctuating spectrum. This requires either a steerable launching mirror or a movable vertical position of the plasma in the vacuum vessel, or both of them.

The peculiarity of this configuration enables one to deduce the turbulence velocity, measured in the laboratory frame, thanks to the Doppler shift experienced by the back scattered field according to

$$\omega_D = \mathbf{v} \cdot \mathbf{k}_\perp \quad (2.34)$$

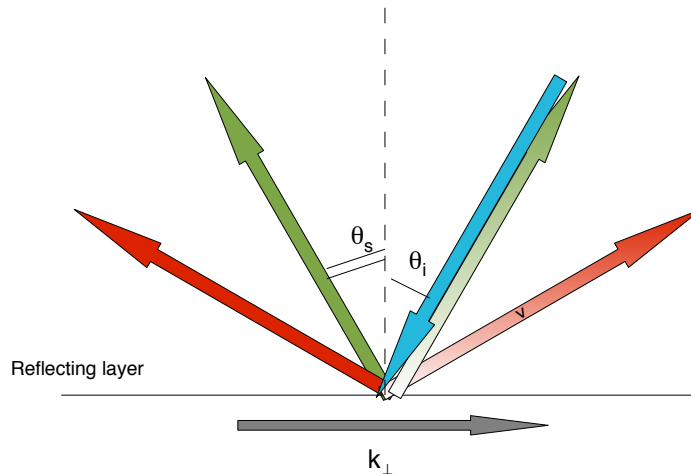


Figure 2.6: Sketch of the geometrical configuration of the Doppler reflectometer. The blue arrow represents the probing beam, solid red and green arrows the negative scattered components, gradient-colored arrows represent the corresponding positive components. Positive and negative are defined with respect to a given k_{\perp} direction on fluctuations on the reflecting layer. The vertical dashed line is the normal to the reflecting layer.

where v is the velocity of turbulence in the laboratory frame, equal to the fluid velocity plus the intrinsic turbulence phase velocity, and k_{\perp} is the fluctuation wave number selected in Eq.2.33.

The perpendicular, rather than the total, wave vector is used in Eq.2.34 because it is much larger than the parallel one since, due to the much higher parallel conductivity, fluctuations are aligned orthogonally to the magnetic field lines. Using Eq.2.33, for the case of a monostatic antenna, i.e. by choosing $\theta_i = -\theta_s$, the Doppler frequency is given by

$$\omega_D = 2v_{\perp}k_0 \sin(\theta) \cos(\alpha) \quad (2.35)$$

where α is the angle formed between the field line and the probing beam direction.

Since the Doppler shift is directly proportional to the electron velocity perpendicular to the equilibrium magnetic field, the reconstructed velocity is the sum of the fluid velocity components and the turbulence phase velocity, that is the velocity of the plasma itself with respect to the laboratory frame and the velocity of the density fluctuations with respect to the plasma frame. Even though the fluid velocity is composed of the diamagnetic and $\mathbf{E} \wedge \mathbf{B}$ drifts, only the latter is generally considered to contribute. Unfortunately the contributions of the intrinsic turbulence phase velocity and of the $\mathbf{E} \wedge \mathbf{B}$ drift are not easily separated unless an independent measurement is available: for example by reversing

the equilibrium magnetic field and/or by comparing with CXRS measurements. However it is possible to make some estimates of the main turbulence contribution to the signal by the chosen k_{\perp} so that, eventually, an estimate of the order of magnitude of the two terms is indeed possible according to theoretical models.

The k resolution of the instrument has been calculated in [39] as

$$\Delta k_{\perp} = \sqrt{2} \frac{2}{w} \sqrt{1 + \left(\frac{w^2 k_0}{\rho} \right)^2} \quad (2.36)$$

where w is the beam spot size and the effective radius of curvature of the spot $\rho = R_{plasma} R_{beam} / (R_{plasma} + R_{beam})$. As a result there exists an optimum value of w for any given ρ : considering a probing frequency in the range 70 to 100 GHz, which corresponds to the O-mode cut-off layer position over most of the TCV poloidal cross section, typical values could be about $w \simeq 1.5 - 2$ cm resulting in a resolution $\Delta k_{\perp} \geq 2$ cm⁻¹.

In present day Doppler reflectometry experiments the scattering and receiving tilt angles are chosen to be equal and in the range 18-30 degrees. These values are a compromise between the need of getting rid of the strong $m = 0$ reflection component and the desire to minimize the loss of k resolution due to the spot curvature.

The advantage of the Doppler reflectometer is the possibility of giving results no matter where the plasma is, because the probing beam does not need to propagate orthogonally to the magnetic flux surfaces as in standard reflectometry and in MIR. This also implies that the technique is flexible in terms of the choice of access port. By applying multiple probing frequencies it could be possible to estimate the $\mathbf{E} \wedge \mathbf{B}$ shear flow, which is expected to be of paramount importance in regulating the turbulence saturation level [26]. The probing frequencies should be chosen such that the respective cut-offs are radially separated by distances larger than the integration length of each probing beam; in this way the calculated plasma velocities for each probing beam, i.e. in the cut-off position of each beam, would be independent to one another.

Of course also for the Doppler reflectometer the question whether turbulence influences the backscattered signal arises: fluctuations perpendicular to the probing beam direction cause the localization of measurements to deteriorate, and complicated interference phenomena like the ones described above for standard reflectometry could make the reconstruction of $v(r)$ and $k(r)$ impossible. Nevertheless, if we assume that all these noise components result in a symmetric broadening of the k spectrum, then by performing a long enough time averaging it could be possible in principle to obtain the correct velocity value. In this frame, an investigation with a 2D full-wave code has been carried out in [39] and the result is that thanks to time averaging the required information about the velocity can be recovered, if the fluctuation level is not too high, but the spectrum could be lost.

To conclude, this section is a collection of different theories, experimental indications and numerical simulations on microwave reflectometry. The common message is the extreme complexity of the measurement in the case of high fluctuation levels, i.e. non-linear coupling of modes, when dealing with two-dimensional structures. It is beyond the scope of this feasibility study to determine which description is the best, nevertheless it is enough to say that microwave reflectometry, due to the excessive cost and complexity of MIR or to ambiguity in the measurements, does not meet all the requirements listed in the first section in terms of diagnostic flexibility in its use and of lack of ambiguity in the interpretation of experimental results.

2.4.4 Collective Scattering

In this section, collective scattering designates the scattering technique which enables one to recover some points in the density fluctuation spectrum by collecting the light scattered, by density fluctuations, at angles which satisfy the Bragg relation. The word collective means that the diagnostic is designed to measure collective electron behavior, i.e. fluctuating wave-numbers such that $k\lambda_D < 1$, where λ_D is the Debye length.

The first work on the subject dates back to 1979 by Slusher and Surko[30], in which they describe how to determine density fluctuations by coherent detection of scattered CO₂ light. A more advanced treatment of light-plasma interaction is given in Chapter 3, here we simply describe the simple interpretation of Bragg scattering.

The scattering process is characterized by the differential cross section

$$S = S_0 S(\mathbf{k}, \omega) \quad (2.37)$$

where S_0 is the Thomson cross section $(e^2/4\pi\epsilon_0 mc^2)^2$ and $S(\mathbf{k}, \omega)$ is the spectral density of plasma density fluctuations. The Fourier variables must satisfy the energy and momentum conservation laws, that is

$$\omega = \omega_s - \omega_0 \quad (2.38)$$

$$\mathbf{k} = \mathbf{k}_s - \mathbf{k}_0 \quad (2.39)$$

with the subscripts s and 0 indicating respectively scattered and incident, while their difference is equal to the fluctuating part.

In plasma physics, transport-relevant micro-fluctuations are characterized by wave-numbers of the order of a few thousand inverse meters, and real frequencies of the order of hundreds of kHz; therefore, in the case of a CO₂ laser, whose real frequencies are much higher than any plasma characteristic frequency, the fluctuating frequencies and wave-numbers

are negligible *in magnitude*, thus providing the following relations

$$\omega_s \simeq \omega_0 \quad (2.40)$$

$$|k_s| \simeq |k_0| \Rightarrow \theta_B \simeq 2 \arcsin(|k|/2|k_0|) \quad (2.41)$$

where θ_B is the so called Bragg scattering angle. According to the wave number of the injected light one can select the fluctuations' spectral region of interest, provided that a given range of Bragg scattering angles is achievable.

Assuming a Gaussian probing beam with a $1/e^2$ intensity waist equal to $2w_0$, the ideal instrumental k resolution is the standard deviation of the spatial Fourier transform of the probing beam electric field, that is $1/w_0$. Thus, for a beam waist of 5 cm a resolution of 0.2 cm^{-1} can be obtained, which might be sufficient or not depending on the range of fluctuations under investigation and the experimental apparatus. Using a heterodyne system, the spectral resolution is limited only by the beam width. However, the actual minimum spectral resolution is somewhat worse than this because the scattered signal has to be separated from the unperturbed beam. Therefore the actual limit is a function of the Bragg angle and of the machine size. Indeed, given a beam path equal to L , the condition permitting the separation of the scattered and unscattered beams is

$$L \tan(\theta_B) > 2w_0 \quad (2.42)$$

By imposing the minimum k to be equal to the intrinsic resolution $1/w_0$, in the approximation $|k| \ll |k_0|$, we obtain

$$L \geq 2w_0^2 k_0 \quad (2.43)$$

Concerning the spatial resolution, the common region between the probing and scattered lines of sight results in the following localization

$$\delta L \simeq 2 \cdot 2w_0 \cot(\theta_B) \simeq \frac{4w_0 k_0}{k} \quad (2.44)$$

which, always considering the lowest wave-vector that can be resolved, is equal to

$$\delta L \geq 4w_0^2 k_0 \quad (2.45)$$

which, exceeding tens of meters for a microwave and even a kilometer for a CO_2 laser beam, is essentially a line integrated measurement. This spatial resolution can be improved considering high wave-vectors, of the order of k_0 (Eq.2.44).

However it is possible to achieve a better result by taking into account the spatial variation of the magnetic pitch angle and assuming that fluctuations, due to the much higher parallel conductivity along magnetic field lines, satisfy the equation

$$\mathbf{k} \cdot \mathbf{B} \simeq 0 \quad (2.46)$$

so that the presence of magnetic shear allows one to select a given spatial region. Indeed the instrumental selectivity function takes the form [31]

$$F(r) = e^{-\frac{2k}{\Delta} \sin\left(\frac{\xi(r)}{2}\right)} \quad (2.47)$$

where Δ is the k resolution and ξ the variation of the magnetic pitch angle. For low wave numbers, in the case of a radial injection in TCV we obtain the selectivity depicted in Fig.2.7 whose corresponding integration length, given approximately by its width, even though represents a significant improvement with respect to Eq.2.44, is such that one would collect information roughly from the whole plasma minor radius, therefore leading to a line integrated measurement once again. Nevertheless in Eq.2.47, for a given beam

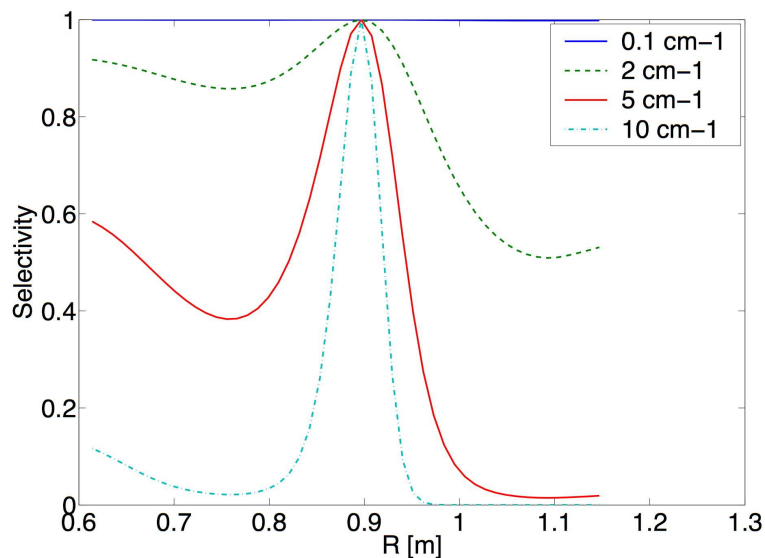


Figure 2.7: Selectivity function as a function of the TCV major radius, in meters, for a number of scattering wave-vectors, in the case of a radial propagation

and scattering angle, the only actual variable is the dependence of the magnetic field pitch angle function ξ ; it is therefore possible to obtain a better spatial localization by employing a geometrical configuration which exploits the maximum possible pitch angle variation: for example the variation along the beam path of the toroidal magnetic field instead of the poloidal one. Following the same procedure as in [32], if we take a reference frame, depicted in Fig.2.8, such that \hat{t} is parallel to the probing beam, \hat{u} is parallel to the equatorial plane and \hat{v} is such to form a right-handed reference frame, calling θ the angle between the scattering direction and the probing direction, and ϕ the angle between the fluctuation wave vector and the horizontal, we can write

$$\begin{aligned} k_u^s &= k_0 \sin(\theta) \cos(\phi) \\ k_v^s &= k_0 \sin(\theta) \sin(\phi) \\ k_t^s &= k_0 \cos(\theta) \end{aligned} \quad (2.48)$$

where k_0 is the probing wave number and k_s the scattered wave number.

Considering now two different waves originating from different spatial locations, sup-

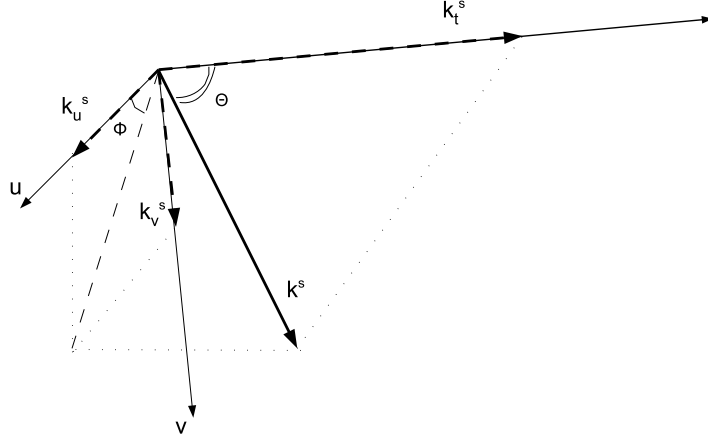


Figure 2.8: Schematic view of the scattered wave vector k^s , in the reference frame $\{\hat{t}, \hat{u}, \hat{v}\}$ described in the text.

posing that the detection system is tuned to receive the first one, it will sample also the second with a relative efficiency given by the relative angle between the two

$$F = e^{-[\sin(\frac{\phi_2 - \phi_1}{2}) \frac{2k}{\Delta}]^2} \quad (2.49)$$

The key point is to try to visualize the variation of the angle ϕ , as a function of the beam path, in a given geometrical configuration. To do this it is enough to write Eq.2.46 in the new coordinate system $(\hat{u}, \hat{v}, \hat{t})$ to obtain

$$0 \simeq \mathbf{k} \cdot \mathbf{B} = |k_0| [\sin(\theta) \cos(\phi), \sin(\theta) \sin(\phi), \cos(\theta) - 1] \cdot [B_u, B_v, B_t] \quad (2.50)$$

which implies

$$\sin(\phi) = \frac{B_t [1 - \cos(\theta)] - B_u \sin(\theta) \cos(\phi)}{B_v \sin(\theta)} \quad (2.51)$$

$$\cos(\phi) = \frac{1}{(B_u^2 + B_v^2) \sin(\theta)} \left\{ B_u B_t [1 - \cos(\theta)] \pm \sqrt{B_u^2 B_t^2 [1 - \cos(\theta)]^2 - (B_u^2 + B_v^2) \{ B_t^2 [1 - \cos(\theta)]^2 - B_v^2 \sin^2(\theta) \}} \right\} \quad (2.52)$$

Considering now a typical TCV equilibrium we calculate the spatial resolution for a tangential injection. Intuitively, also after the considerations expressed in Sec. 2.4.1, the best resolution is the one following the magnetic field line, i.e. matching the pitch angle at the tangency point. In Fig.2.9 we show two examples of the resolution obtained for a field line following beam, and a counter-field line following beam. In particular,

if in a counter-field line following configuration, the integration length is of the order of one meter, in the field line following configuration it is reduced to 20-25%; these results are in substantial agreement with [32]. As already explained in Sec.2.4.1, the tangential configuration permits a further localization due to the integration length, L , being a steep function of the plasma normalized minor radius ρ as, in the case of localization in the middle of the beam path, i.e. at the tangency point between the probing beam and the flux surface of interest, it is equal to

$$\delta\rho = \frac{R_1}{a} \left[\sqrt{1 + \frac{L^2}{R_1^2}} - 1 \right] \quad (2.53)$$

(Eq.2.11 in the case $\theta = 0$), which, for TCV is of the order of 0.5 and 0.04 for the counter and co-tangent configurations, respectively.

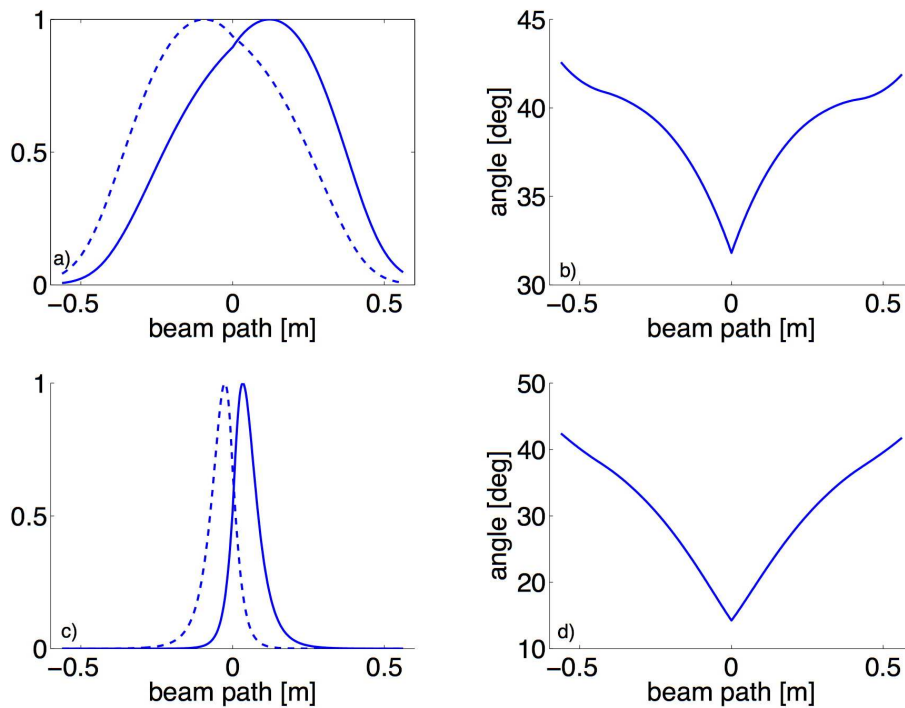


Figure 2.9: Left. Localization of the tangential collective scattering diagnostic for a typical TCV pulse. Dashed and full lines correspond to the two solutions of the angle ϕ . Right. Angle formed by the probing beam with the magnetic field line. Bottom. Field line following probing beam. Top. Counter field line following probing beam

The scattered power originating from a volume of length L in the probing beam direction of propagation from fluctuations of a given wave number generating a fluctuation amplitude \tilde{n} is given by [30]

$$P_s = \frac{1}{4} \tilde{n}^2 r_e^2 L^2 \lambda_0^2 P_0 \quad (2.54)$$

where r_e is the classical electron radius and λ_0 is the probing beam wavelength. This

power is scattered into the solid angle

$$\Delta\psi = \frac{\pi}{4} \left(\frac{\lambda_0}{\pi w_0} \right)^2 \quad (2.55)$$

This relation may be employed to determine the minimum radial resolution that can be afforded in order to collect a sufficient amount of power allowing the discrimination of signal from the detection system noise. For this purpose, assuming an effective fluctuation intensity equal to the total fluctuation intensity times the ratio of the sampled Δk to the width of the k spectrum present in the plasma, an estimation of the wave number resolution of the diagnostic is necessary.

The instrumental resolution is estimated from geometric considerations, sketched in Fig.2.10: if we call L the spatial resolution, h the distance between the scattering point and the receiving port, w_0 the beam half-waist and θ the scattering angle, we obtain

$$\tan(\Delta\theta) = \frac{\sqrt{w_0^2 + (L/2)^2}}{h - \sqrt{w_0^2 + (L/2)^2} \sin(\alpha)} \cos(\alpha) \simeq \Delta\theta \quad (2.56)$$

$$\alpha = \frac{\pi}{2} - \theta - \arctan\left(\frac{2w_0}{L}\right) \quad (2.57)$$

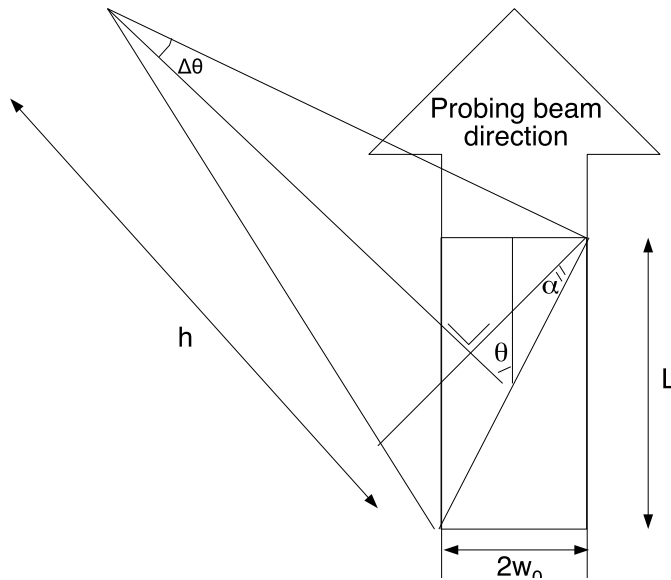


Figure 2.10: Schematic drawing of the scattering geometry and estimate of the resolution. The scale is arbitrary.

while from the Bragg relation

$$\Delta k = 2k_0 \cos\left(\frac{\theta}{2}\right) \frac{\Delta\theta}{2} \simeq \Delta\theta \left(k_0 - \frac{k^2}{8k_0} \right) \simeq k_0 \frac{\sqrt{4w_0^2 + L^2}}{2h} \cos(\alpha) \quad (2.58)$$

This instrumental broadening may be reduced to the Fourier limit ($1/w_0$) if h is sufficiently large, as per Eq.2.45. In practice a truly far-field measurement would require operating in the focal plane of a focusing optic. In the intermediate field, the resolution is given by Eq.2.58. Considering for instance a probing beam of $w_0 = 5$ cm, an integration length of 10 cm, h approximately equal to 1 m we obtain, for probing wave numbers of 60 cm^{-1} , about 3.3 cm^{-1} . Note that the contribution of the longitudinal integration to the effective spatial resolution in the radial direction, considering a scattering event around the tangency point of a magnetic surface, can be estimated to be about 1 cm; since this is less than the width of the beam, the effective radial resolution is dominated by the latter. We can therefore conclude that, in order to optimize the signal, it is worth searching for a value of L that results in similar longitudinal and transversal resolutions, i.e. equal to the beam waist. This value of the integration length, taking the tangency point is equal to

$$L = 4\sqrt{w_0 R} \quad (2.59)$$

that is about 30 cm for $R = 1$ m, i.e. TCV mid radius, and $2w_0 = 1$ cm.

Now the minimum overall level of fluctuation resulting in a signal-to-noise ratio of unity is equal to

$$\tilde{n} = \sqrt{\frac{4P_s}{r_e^2 P_0 \lambda^2 L^2} \frac{k_{max}}{\Delta k}} \quad (2.60)$$

so that if we take an equivalent noise power of $2 \cdot 10^{-13}$ W, as in the apparatus described in [42], we obtain the results in Table 2.1 where all the calculations are performed assuming

$\tilde{n} [\text{m}^{-3}]$	$P_0 [W]$	$\Delta k/k_{max} [\%]$
$3 \cdot 10^{14}$	1	3
$1 \cdot 10^{15}$	0.1	3
$3 \cdot 10^{15}$	1	1
$1 \cdot 10^{16}$	0.1	1

Table 2.1: Estimate of the minimum detectable fluctuating density for a probing wavelength of 1 mm and an integration length of 10 cm.

a probing wavelength of 1 mm and an integration length of 10 cm.

In conclusion the collective scattering is feasible and allows one to discern the shape of the k spectrum in a chosen area, since it gives the power scattered at a finite number of points. Depending on the geometry of the system, the diagnostic can provide information on k_r or k_θ in different locations of the poloidal plane by moving the plasma in the vacuum chamber. The drawback is that the plasma in the scattering region needs to be homogeneous in order to have a completely meaningful information from the diagnostic. Additionally the information provided is limited unless one can arrange for a fairly large

number of detectors in potentially difficult locations, if access to different parts of the beam and a k spectrum in each one is to be obtained. Finally, only true far-field detection can give the optimum Gaussian resolution (especially for shorter wavelengths, such as CO₂), which means that an appropriate lens must be used for each detector.

In sections 2.4.5 and 2.4.6 we will consider probing e-m waves scattered by plasma density fluctuations. The scattered electric field is considered as a function that admits a Taylor or Fourier expansion up to any order and the system is considered to be infinite. Diffraction effects will be considered, for simplicity, only in the next chapter which deals in detail with the Phase Contrast Imaging method.

2.4.5 Phase Contrast

The Phase Contrast Imaging (PCI) method is an internal reference interferometer which is capable of converting phase perturbations into amplitude ones. First proposed by Zernike[1], this method is a member of the imaging methods family, which includes the Shadowgraph, Scintillation, Central Dark Ground and Schlieren techniques, and is based on measuring the phase variation of an electromagnetic wave due to the perturbed refractive index of the physical medium it propagates through.

In the basic setup (Fig.2.11), a monochromatic laser beam is transmitted through a refractive medium located at the object plane Σ_{obj} , a lens L_1 focuses it on the so-called phase plate, whose role will be clarified hereafter and is a reflective or refractive flat optical element designed to have, usually, a depression in its central part. The undiffracted component of the beam is focused on the depression so that a phase difference between the weak diffracted component and the much stronger undiffracted one, which serves as local oscillator, is achieved. Lens L_2 refocuses the beam on the image plane Σ_{im} thus obtaining an image of the object. In order to have the best interference at the image plane between diffracted and undiffracted components, the phase shift has to be $\pm\pi/2$. When PCI is used in a plasma, the refractive index is perturbed, almost exclusively, by electron density fluctuations, see Eq.3.16. Therefore this physical quantity is what PCI is sensitive to in a fusion plasma.

When the frequency of the probing beam is much larger than the frequency of any plasma resonance or cut-off, the effect exerted by the plasma on the laser beam is a phase shift ϕ . Let us write ϕ as the sum of a static and of a fluctuating component

$$\phi = \phi_0 + \tilde{\phi}, \quad (2.61)$$

where ϕ_0 is induced by the equilibrium density profile, while its fluctuations are responsible for $\tilde{\phi}$. We will now consider as unperturbed the beam phase-shifted only by ϕ_0 and we

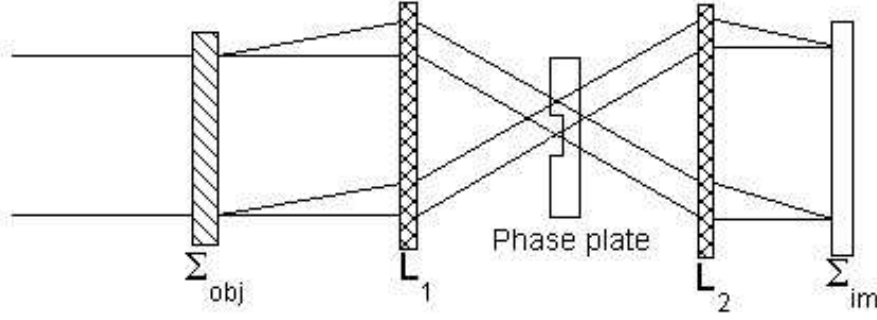


Figure 2.11: Sketch of the basic, simplified, set-up of the Phase Contrast diagnostic. The object plane is the plasma, the image plane is the detecting plane and L_1 and L_2 are the imaging optics.

will refer to it with the subscript ϕ_0 . The total scattered electric field can be expressed as

$$\mathbf{E}_{tot}(\mathbf{r}, t) = \mathbf{E}_0(\mathbf{r}, t)e^{i\phi_0(\mathbf{r}, t)}e^{i\tilde{\phi}(\mathbf{r}, t)} = E_{\phi_0}e^{i\tilde{\phi}(\mathbf{r}, t)} \simeq E_{\phi_0}[1 + i\tilde{\phi}(\mathbf{r}, t)] \quad (2.62)$$

where E_0 is the probing field, $\tilde{\phi}$ is the fluctuating phase and the last equality holds only if the fluctuating phase shift is much smaller than unity. The unperturbed field is the first term on the right hand side of the last equality of Eq.2.62, while the scattered field can be thought of as the second one. Any detector is sensitive to the power of the incident light, therefore the measured signal would be

$$P_s = |E_s|^2 = |E_{\phi_0}e^{i\tilde{\phi}}|^2 = |E_0|^2 \quad (2.63)$$

in other words, the system would not be sensitive to any first order term in the perturbed phase shift.

Looking at Eq.2.62 it is evident that the unperturbed and perturbed fields are dephased by $\pi/2$ in the phasor space, thus by applying an additional $\pi/2$ phase shift to the perturbed components, the information on the phase perturbation can be made detectable as an amplitude variation, i.e. a power modulation on a detector

$$P_s = |E_s|^2 = |E_{\phi_0}e^{i\tilde{\phi}}|^2 \simeq |E_{\phi_0}[1 + i\tilde{\phi}]|^2 \quad (2.64)$$

$$\Rightarrow \pm\pi/2 \Rightarrow$$

$$= |E_{\phi_0}[1 \mp \tilde{\phi}]|^2 = |E_{\phi_0}|^2[1 \mp 2\tilde{\phi} + \tilde{\phi}^2] \simeq |E_{\phi_0}|^2[1 \mp 2\tilde{\phi}] = P_0 + \tilde{P} \quad (2.65)$$

The same result can be seen in a slightly different way, i.e. by developing in a MacLaurin series at the end of the derivation, that is

$$E_s = E_{\phi_0}e^{i\tilde{\phi}} = E_{\phi_0} \sum_{k=0}^{\infty} \frac{(i\tilde{\phi})^k}{k!} \quad (2.66)$$

adding a $\pm\pi/2$ phase shift to diffracted components

$$\begin{aligned}
P_s &= |E_{\phi_0}|^2 \left| 1 \pm \imath \sum_{k=1}^{\infty} \frac{(\imath\tilde{\phi})^k}{k!} \right|^2 = |E_{\phi_0}|^2 |1 \pm \imath(e^{\imath\tilde{\phi}} - 1)|^2 \\
&= |E_{\phi_0}|^2 \left[3 - 2 \left(\frac{e^{\imath\tilde{\phi}} + e^{-\imath\tilde{\phi}}}{2} \pm \frac{e^{\imath\tilde{\phi}} - e^{-\imath\tilde{\phi}}}{2\imath} \right) \right] \\
&= |E_{\phi_0}|^2 [3 - 2 \cos(\tilde{\phi}) \mp 2 \sin(\tilde{\phi})] = |E_{0,\phi}|^2 [1 \mp 2\tilde{\phi} + \tilde{\phi}^2 + o(\tilde{\phi}^2)] \quad (2.67)
\end{aligned}$$

The second equation on the first line was written to explicitly express which terms take the additional $\pi/2$ phase shift \imath . Similar expressions are obtained by adding a $\pm\pi/2$ phase shift to the undiffracted component

$$P_s = |E_{\phi_0}|^2 \left| \pm\imath + \sum_{k=1}^{\infty} \frac{(\imath\tilde{\phi})^k}{k!} \right|^2 = |E_{\phi_0}|^2 [3 \pm 2 \sin(\tilde{\phi}) - 2 \cos(\tilde{\phi})] \quad (2.68)$$

which reflects the symmetry in shortening or lengthening the optical path of the undiffracted component or of the diffracted ones.

The principal advantage of the PCI technique with respect to more traditional collective scattering ones is that the former, being able to produce an image of the object of interest in real space, is not affected by difficulties in interpreting signal scattered by highly non-homogeneous regions, such as Internal Transport Barriers. The latter, on the contrary, provides information directly in Fourier space, and is therefore *a priori* not possible to discern signal originated from one particular portion of the sampling volume. For this reason, with the same port allocation requirements, it is able to extract a considerably larger variety of spatial structures.

The phase contrast method will be described in far more detail in Chapter 3; however it is enough to say here that its validity rests on the conditions expressed by the following four equations[63]

$$\frac{\omega_{pe}^2}{\omega_0^2} \ll 1, \quad (a) \quad \frac{\omega_{ce}^2}{\omega_0^2} \ll 1, \quad (b) \quad \frac{|\mathbf{k}|}{|\mathbf{k}_0|} \ll 1, \quad (c) \quad \lambda_0 r_e L n_e \ll 1 \quad (d) \quad (2.69)$$

where the subscript 0 indicates quantities referring to the probing beam, r_e is the classical electron radius, L is the integration length, n_e is the electron density, ω_{pe} is the plasma frequency and ω_{ce} is the electron cyclotron frequency.

Considering the TCV toroidal field, the second equation is satisfied to 0.01 by imposing the probing frequency to be larger than $2 \cdot 10^{11}$ rad/s. In typical TCV conditions the electron density does not exceed $3 \cdot 10^{20} \text{ m}^{-3}$, which means that the first and the fourth equations are satisfied if the probing beam has a wavelength of, at most, about $10 \mu\text{m}$ and an integration length of about 20 cm. Considering the third equation, imposing $k/k_0 \leq 0.1$ results in a maximum fluctuation wave number of 600 cm^{-1} for a CO_2 laser

beam.

One of the most important drawbacks of phase contrast is that it measures only line integrated fluctuations, which basically means that it is not possible to obtain local information unless an inversion procedure or a spatial filter is adopted. Both methods require detailed information on the magnetic field in the plasma since the former relies on assumptions on fluctuations and symmetry considerations[43], while the latter makes use of the fact that only fluctuation wave vectors perpendicular to both the magnetic field and the probing beam propagation direction are measured.

Considering the second approach one can, as in Section 2.4.4, set a reference frame such that \hat{t} is a unit vector parallel to the propagating beam direction, \hat{u} is parallel to the equatorial plane of the plasma and \hat{v} is such as to complete a right-handed reference frame $\{\hat{t}, \hat{u}, \hat{v}\}$. In such a way one can calculate, for each point of the propagation path, the angle formed by the projection of the magnetic field onto the plane perpendicular to the probing wave vector with respect to a reference direction (see Fig.2.12); this angle can be selected through an appropriate spatial filter located in a focal plane.

Fig.2.13 shows calculations for a TCV equilibrium reconstruction in the cases of toroidal

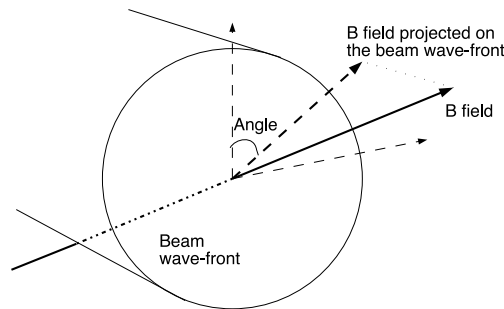


Figure 2.12: Schematic representation of a magnetic field line and its projection on the beam wave-front. The depicted angle is the one shown in Fig.2.13 and 2.14

and poloidal injection. For a poloidal configuration the position is not a single-valued function of the angle, which means that, for a given angle, there are contributions to the signal from different points in the plasma. By contrast, in the case of toroidal injection the position is a single-valued function of the angle over a large fraction of the integration path, and its derivative is small, implying that one can localize with fairly good precision the position of the interaction. This precision is enhanced when the direction of propagation makes the beam nearly tangential to the magnetic field, by matching its pitch angle. When the spatial resolution is projected onto a radial coordinate, by employing the axisymmetry of the tokamak (thus neglecting toroidal field ripple) one obtains an excellent radial localization of the measurements. Additionally, due to physical constraints, the

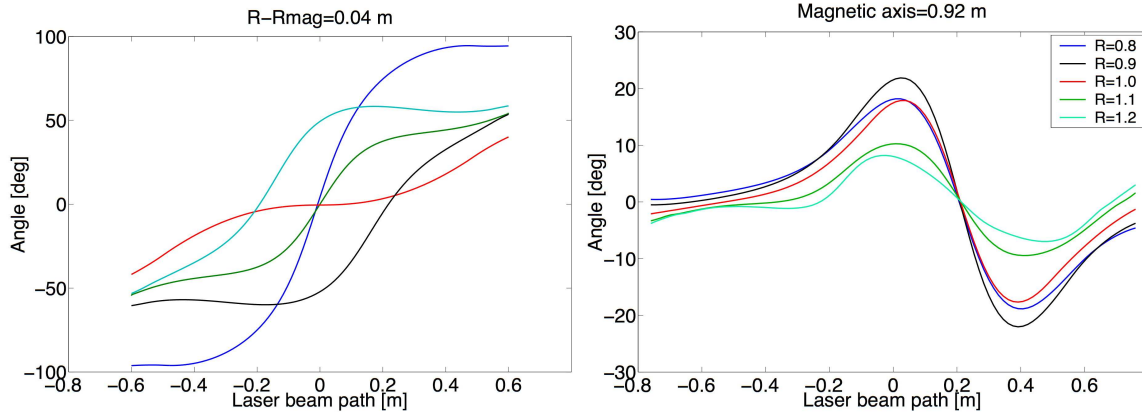


Figure 2.13: a) Angle between the component of the magnetic field perpendicular to the laser propagation direction and the reference horizontal vector in that plane, as a function of the beam path in a monotonic q profile for a number of configurations with predominantly toroidal injection. Through the magnetic axis, following the magnetic field line in black; in the midplane in blue; in the counter-field line direction in red; parallel to the midplane and above and below magnetic axis in green and light blue. b) Same as a), but for poloidal injection with a number of radial injection points. The position is not a single-valued function of the angle.

probing beam is smaller than the plasma poloidal cross section, therefore by vertically shifting the plasma in the TCV vacuum-vessel, the high resolution region can be moved across the beam cross section, so that fluctuations from most radial positions can be resolved in turn (this holds for plasmas that are not too elongated, of course). In an ideal case with a point of perfect tangency between the beam and the magnetic field, the angle function depicted in Fig.2.13 becomes degenerate at this point, i.e. all angles between 0 and π satisfy the k selection rules there.

The localization properties worsen negligibly if the equilibrium is characterized by a non monotonic q profile, as illustrated in Fig.2.14.

Let us now give a rough estimate of the achievable localization: If L is the integration length and R the radial position of interaction, in the case of a horizontal propagation and a localization at the tangency point, the radial resolution is given by

$$\delta r = R \left(\sqrt{1 + \frac{L^2}{R^2}} - 1 \right), \quad (2.70)$$

i.e. about 0.5 cm, corresponding to about $\delta r/a = 1\%$, for a core measurement in TCV and $L=10$ cm. (L is determined by the spatial filter, see Sec. 3.5.3).

In general, both in a toroidal and in a poloidal configuration, the PCI is sensitive to fluctuation wave-vectors composed of both poloidal and radial components of k_{\perp} . However, there are peculiar points along the beam path where PCI is sensitive only to the radial or to the poloidal component. For example it is easy to see that in both configurations

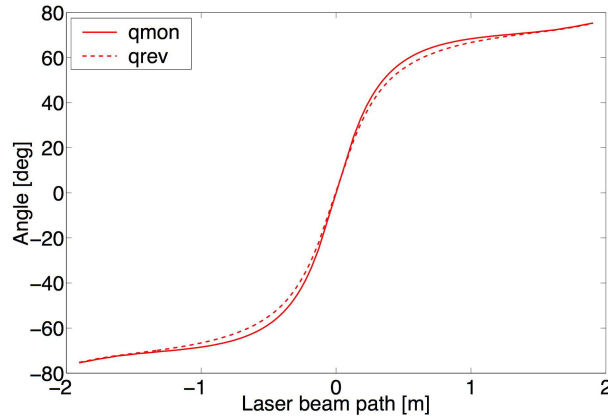


Figure 2.14: Comparison of the angle formed by the component of the magnetic field perpendicular to the laser propagation direction and the reference horizontal vector in that plane, for toroidal injection in a case of monotonic q profile, full line, and reversed, dashed line. The tangency point is chosen as the location of the minimum of the safety factor.

the points of tangency to the flux surface select only the radial component. We anticipate here that in the toroidal configuration there are points sensitive only to the poloidal component, see details in Chapter 3.

Let us now briefly see how it is possible to localize a PCI measurement. On the phase plate, or in any other focal plane of the imaging system, the spatial distribution of the scattered electric field corresponds to its spatial Fourier transform; therefore any angular position with respect to the focal point corresponds to a given orientation of the fluctuating wave vector. This angular position is nothing but the angle plotted in Fig.2.13. The localization is achieved simply by physically masking the parts of the focal plane corresponding to undesired positions along the beam path. In Chapter 3 we will give more details on how the filter is actually built.

In order to be sure to collect all the light scattered by the maximum k under investigation, one has to set the following geometric equations

$$\frac{k_{max}}{k_0} = \frac{h(1 - \alpha - \beta)}{D} \quad (a), \quad \beta = \frac{D(D - z)M^2w_0}{z_R^2h} \quad (b) \quad (2.71)$$

where D is the distance between the interaction point and the receiving mirror, β is the factor that takes into account the divergence of the gaussian beam at a short distance compared to the Rayleigh distance $z_R \equiv k_0w_0/2$, which is the distance the beam travels to increase its width by $\sqrt{2}$, h is the radius, or the half-aperture, of the receiving optical aperture, w_0 is the gaussian beam half-width at its waist, $\alpha = w_0/h$ and M^2 is the factor that takes into account the non-perfect Gaussian nature of the probing beam. Eq.2.71b expresses the intrinsic divergence of a gaussian beam at a distance z from its waist, short compared to the Rayleigh distance. Eq.2.71a imposes the aperture to be large enough to

collect the gaussian beam scattered at a distance z from its waist; the scattering angle k_{max}/k_0 and β add because they are supposed to be small; α is equal to w_0/h as only first order terms in z/z_R are retained. M^2 is equal to one for a perfectly Gaussian beam, in reality lasers are characterized by $M^2 \simeq 1.1 - 1.2$.

The PCI signal is formally expressed as

$$\tilde{\phi} = r_e \lambda_0 \int_a^b \tilde{n}_e(\mathbf{x}) dl \quad (2.72)$$

where a and b are the limits of the integration length, i.e. $b-a=L$, r_e is the classical electron radius, λ_0 is the wavelength of the probing beam and \tilde{n}_e is the density fluctuation. So that, in order to obtain a good signal to noise ratio, the key ingredients are the wavelength of the laser and the integration length, for any given turbulence level.

Assuming an experimental apparatus whose noise is such as to produce an equivalent phase variation of $5 \cdot 10^{-5}$ rad[63] and considering an integration length of 20 cm, the expected minimum detectable fluctuation is equal to $8 \cdot 10^{15} \text{m}^{-3}$ for $\lambda_0 = 10.6 \mu\text{m}$; by contrast, we obtain $3.2 \cdot 10^{16} \text{m}^{-3}$ integrating the signal over 10 cm with $\lambda_0 = 5 \mu\text{m}$. these two values translate into \tilde{n}/n of about 0.1 and 1% for a low density TCV pulse, and are comparable to the theoretical estimation of fluctuating densities obtained with a series of gyrokinetic simulations, as discussed in Section 2.3.

A limitation on the density gradient, sampled by the wave front w_0 , must be set in order to ensure the validity of the Born approximation, Eq.2.69a. This reduces to evaluating Eq.2.69d with \tilde{n}_e replaced by the spatial average variation of the electron density over the beam wave front $w_0 \nabla n_e$. This estimates gives an upper density gradient limit of 10^{23}m^{-4} , for $w_0=0.5$ cm and $1.18 \cdot 10^{22} \text{m}^{-4}$ for $w_0=4.5$ cm; conditions well satisfied in TCV eITB pulses, i.e. the ones with the highest density gradient.

Let us now examine the conditions that the diagnostic must satisfy. Firstly, to ensure the homogeneity of the wave front, the spatial dependence of the delay time in the image plane must satisfy the following condition[63]

$$\frac{\omega}{c} \frac{(M-1)^2 w_0^2}{2(Z_{\Im} - Z_{obj})} \ll 1 \quad (2.73)$$

where M is the magnification factor of the system, w_0 the beam half-width and Z_{\Im} and Z_{obj} are the positions of the image plane and of the object plane, respectively. The equation is satisfied at 0.14% for $w_0=3.5$ cm, $M=0.5$ (which is the magnification corresponding to a resolution approximately equal to a cut-off of 60cm^{-1}), a frequency bandwidth of 100 MHz and $Z_{\Im} - Z_{obj} > 2$ m, which is the shortest practical distance.

The transit phase variation of the laser light through the plasma region under investigation, $L\omega/c$, approaches one when the pulsation is about 300 MHz for an integration length of 15 cm. Thus for turbulence phenomena, which are expected at much lower frequencies,

the effect is negligible.

Other equations to be satisfied in order to have response properties compatible with the Rytov and geometric optics approximations are[63]

$$\frac{Lk}{k_0 w_0} \ll 1 \quad (2.74)$$

$$\frac{Lk^2}{\pi k_0} \leq 1 \quad (2.75)$$

$$k_0 w_0 \gg 1, \quad \frac{|x - x'|k^4}{8k_0^3} \ll 1 \quad (2.76)$$

$$\frac{|x/x_R|}{k_0^2 w_0^2} \ll 1, \quad \frac{|x'/x_R|}{k_0^2 w_0^2} \ll 1, \quad \frac{|x - x'|}{x_R} \ll 1 \quad (2.77)$$

where x and x' are the distances from the beam waist of any two points along the optical path in the plasma region, x_R is the Rayleigh distance, L the integration length, k the maximum expected fluctuation wave number.

Considering an integration length of 10 cm Eq.2.74 requires, to be satisfied to 2%, to have a cut-off equal to $k_{max} = 42 \text{ cm}^{-1}$ for a beam half-waist of 3.5 cm and a probing beam wavelength of 10.6 μm ; this value doubles if a 5 μm laser is used. Eq.2.75, expressing the Raman-Nath condition, is always satisfied up to a cut-off of 30.5 cm^{-1} for a 10.6 μm laser beam and an integration length of 20 cm, while the threshold rises to 43.1 cm^{-1} if the integration length is reduced to 10 cm, and goes up to 61 cm^{-1} if the probing k is equal to 5 μm with $L=10$ cm. The Rayleigh distance, defined as $k_0 w_0^2/2$, is at least equal to 363 m for a 10.6 μm laser with a 3.5 cm width, so that the last of Eq.2.77 is largely satisfied being no larger than $4 \cdot 10^{-3}$. The first two Eq.2.77 are satisfied even with a width reduced to 1.3 mm since in this case they are less than $7 \cdot 10^{-9}$. The l.h.s. of the second Eq.2.76 is equal to $1.1 \cdot 10^{-3}$ with a cut-off set to 60 cm^{-1} and an integration length of 20 cm, while it is equal to $2 \cdot 10^{-3}$ for a 5 μm laser beam and a cut-off equal to 120 cm^{-1} .

When operating the diagnostic with a localized measurement one should observe a Doppler shift $\mathbf{k} \cdot \mathbf{v}$, where \mathbf{k} is the fluctuation wave vector and \mathbf{v} the fluid velocity. By reversing the plasma current and the toroidal magnetic field, so as to keep the localization fixed, one could observe a difference in the absolute value of the Doppler shift for two "identical" pulses, so that the value of the $\mathbf{E} \wedge \mathbf{B}$ velocity could, in principle, be retrieved if it is indeed dominant over the diamagnetic velocity. Moreover by changing only the current, since the localization does not change significantly away from the tangency point as shown in Fig.2.13, one could use the difference in the absolute value of the Doppler shift to obtain the value of the poloidal velocity and compare it to the one given by the CXRS diagnostic. In this fashion, similarly to the Doppler reflectometry technique, one could ultimately hope to extract information about the turbulence phase velocity and compare it to theoretical calculations.

In conclusion, PCI diagnostic is feasible and allows one to obtain spatially localized images of plasma density fluctuations. These images can cover most of the poloidal cross section by vertically shifting the plasma in the vacuum vessel.

2.4.6 Alternative imaging methods

In this section we will briefly describe imaging methods alternative to the Phase Contrast and how they compare. The description is given for completeness since different authors have already treated this subject in previous works [64, 63, 66], though we will do it in a slightly different formalism.

Historically, the first two imaging techniques not relying directly on intensity fluctuations but on phase fluctuations were the Central Dark Ground (CDG) and the Schlieren techniques. The CDG consists of physically blocking the unscattered radiation and letting the scattered radiation through. The mask should ideally be of the size of the focal spot, whose diameter, for an aberration-free lens, is equal to

$$\frac{4M^2\lambda_0 f}{\pi D} \quad (2.78)$$

where λ_0 is the probing beam wavelength, f the lens' focal length, M^2 the beam mode parameter and D is the input beam diameter on the lens at the $1/e^2$ points.

The transmitted electric field, for a given phase perturbation $\tilde{\phi}$, is equal to

$$E_s = E_0 \sum_{k=1}^{\infty} \frac{(i\tilde{\phi})^k}{k!} \quad (2.79)$$

which gives an intensity equal to

$$P_s = |E_0|^2 |e^{i\tilde{\phi}} - 1|^2 = 2|E_0|^2 [1 - \cos(\tilde{\phi})] \simeq |E_0|^2 \tilde{\phi}^2 + o(\tilde{\phi}^3) \quad (2.80)$$

therefore the intensity contrast is proportional to the square of the perturbed phase, which makes the CDG much less sensitive than PCI, even though the CDG mask can be manufactured more easily than the phase plate of PCI.

The Schlieren technique, where Schlieren is a german word standing for streak, consists of letting through the unscattered component and only scattered components corresponding to positive, or negative, fluctuating wave-vectors. The result is an intensity perturbation linearly proportional to the phase perturbation but dephased by $\pi/2$. Indeed, expressing the phase perturbation as a Fourier integral

$$\tilde{\phi}(\mathbf{x}) = \int_{-\infty}^{\infty} dk \hat{\phi}(k) e^{ik \cdot \mathbf{x}} \quad (2.81)$$

by blocking, for example, the negative wave vectors, the scattered field becomes equal to

$$E_s = E_0 e^{i \int_0^{\infty} dk \hat{\phi}(k) e^{ik \cdot \mathbf{x}}} \quad (2.82)$$

so the detected power is given by

$$P_s = |E_0|^2 e^{\imath \int_0^\infty dk \hat{\phi}(k) e^{\imath k \cdot x}} e^{-\imath \int_0^\infty dk \hat{\phi}^*(k) e^{-\imath k \cdot x}} \quad (2.83)$$

since the fluctuating phase has to be real, $\hat{\phi}^*(k) = \hat{\phi}(-k)$, thus

$$\begin{aligned} P_s &= |E_0|^2 e^{\imath \int_0^\infty dk \hat{\phi}(k) e^{\imath k \cdot x}} e^{-\imath \int_0^\infty dk \hat{\phi}(-k) e^{-\imath k \cdot x}} \\ &= |E_0|^2 e^{\imath [\int_0^\infty dk \hat{\phi}(k) e^{\imath k \cdot x} + \int_0^{-\infty} d\tilde{k} \hat{\phi}(\tilde{k}) e^{\imath \tilde{k} \cdot x}]} \\ &= |E_0|^2 e^{\imath [\int_0^\infty dk \hat{\phi}(k) e^{\imath k \cdot x} - \int_{-\infty}^0 dk \hat{\phi}(k) e^{\imath k \cdot x}]} \\ &= |E_0|^2 e^{-\int_0^\infty dk \hat{\phi}(k) e^{\imath(k \cdot x - \pi/2)} - \int_{-\infty}^0 dk \hat{\phi}(k) e^{\imath(k \cdot x + \pi/2)}} \simeq |E_0|^2 [1 - \tilde{\phi}_{\pi/2}] \end{aligned} \quad (2.84)$$

where we have defined $\tilde{k} = -k$ and, after the second passage, $k = \tilde{k}$. $\tilde{\phi}_{\pi/2}$ is the fluctuating phase shifted by $\pm\pi/2$ in Fourier space. The detected power is therefore linear in the phase perturbation but dephased by $\pi/2$.

We now consider the so-called phase scintillation [67], which makes use of the phase shift cumulated by scattered components while travelling at a distance L from the scattering region.

After a distance L from the scattering region to the detection plane, the cumulated phase shift of each Fourier component, scattered at an angle θ , is equal to

$$\delta_k \simeq L k_0 [1/\cos(\theta) - 1] = L \frac{k_\perp^2}{2k_0} \quad (2.85)$$

which is then an even function in k_\perp . Let us write again the total scattered field as

$$E(\mathbf{x}) = E_0 e^{\imath \tilde{\phi}} = E_0 e^{\imath \int_{-\infty}^\infty d\mathbf{k} \hat{\phi}(\mathbf{k}) e^{\imath \mathbf{k} \cdot \mathbf{x}}} \quad (2.86)$$

adding the additional phase shift to each Fourier component and imposing the phase shift to be real, i.e. $\hat{\phi}^*(-\mathbf{k}) = \hat{\phi}(\mathbf{k})$, the Fourier integral can be rewritten as

$$\imath \int_{-\infty}^\infty d\mathbf{k} \hat{\phi}(\mathbf{k}) e^{\imath(\mathbf{k} \cdot \mathbf{x} + \delta_k)} = \imath \int_0^\infty d\mathbf{k} \hat{\phi}(\mathbf{k}) e^{\imath(\mathbf{k} \cdot \mathbf{x} + \delta_k)} + \imath \int_0^\infty d\mathbf{k}' \hat{\phi}^*(\mathbf{k}') e^{-\imath(\mathbf{k}' \cdot \mathbf{x} - \delta_{k'})} \quad (2.87)$$

where we have defined $k' = -k$. Note also that $\delta_{-k} = \delta_k$ by Eq.2.85. Its complex conjugate reads

$$-\imath \int_0^\infty d\mathbf{k} \hat{\phi}^*(\mathbf{k}) e^{-\imath(\mathbf{k} \cdot \mathbf{x} + \delta_k)} - \imath \int_0^\infty d\mathbf{k}' \hat{\phi}(\mathbf{k}') e^{\imath(\mathbf{k}' \cdot \mathbf{x} - \delta_{k'})} \quad (2.88)$$

The power on the detector is then equal to

$$\begin{aligned} P &= |E|^2 = |E_0|^2 e^{-\int_0^\infty d\mathbf{k} \hat{\phi}(\mathbf{k}) e^{\imath \mathbf{k} \cdot \mathbf{x} + 2 \sin(\delta_k)} - \int_0^\infty d\mathbf{k}' \hat{\phi}^*(\mathbf{k}') e^{-\imath \mathbf{k}' \cdot \mathbf{x} + 2 \sin(\delta_k)}} \\ &= |E_0|^2 e^{-\int_{-\infty}^\infty d\mathbf{k} \hat{\phi}(\mathbf{k}) e^{\imath \mathbf{k} \cdot \mathbf{x} + 2 \sin(\delta_k)}} \end{aligned} \quad (2.89)$$

which then results in a sinusoidal modulation of the power. This effect was experimentally confirmed by H.Weisen by starting from a phase contrast arrangement and longitudinally

shifting the position of the phase plate[65].

One can see that the phase scintillation technique can provide the same amplitude of intensity fluctuations as PCI only for a single value of k_{\perp} , the one giving $\delta_k = \pi/2$, which makes the scintillation technique inadequate for broad turbulence studies, even though it is simpler than PCI since it does not need any spatial filtering. In general, the response function is non-linear.

The Shadowgraph technique, like the phase contrast and the ones described in this section, relies on the separation between the object plane and a plane used for imaging. Since the plasma refraction index, but also the refraction index of any gas, depends on its density, denser regions act as diverging lenses thus producing less bright spots, also called shadows. On the contrary, less dense regions create brighter spots. Let us use the geometric optics approximation: a ray propagating along z , incident at position (x,y) is deflected into position (u,v) on the detecting plane

$$(u, v) = \left(x + \frac{L}{k_0} \frac{\partial \tilde{\phi}}{\partial x}, y + \frac{L}{k_0} \frac{\partial \tilde{\phi}}{\partial y} \right) \quad (2.90)$$

where L is the distance along z between the object and the detecting plane. The detected power, in the case of a uniform incident intensity is given by the energy conservation principle

$$I_d dudv = I_0 dx dy \quad (2.91)$$

which gives, in the case of small deviations of the index of refraction

$$\begin{aligned} I_0 dx dy &= I_d \left(dx + \frac{L}{k_0} \frac{d^2 \tilde{\phi}}{dx^2} dx \right) \left(dy + \frac{L}{k_0} \frac{d^2 \tilde{\phi}}{dy^2} dy \right) \\ &\simeq I_d \left(1 + \frac{L}{k_0} \nabla^2 \tilde{\phi} \right) dx dy + O(|\nabla_{x,y}^4 \tilde{\phi}|) \end{aligned} \quad (2.92)$$

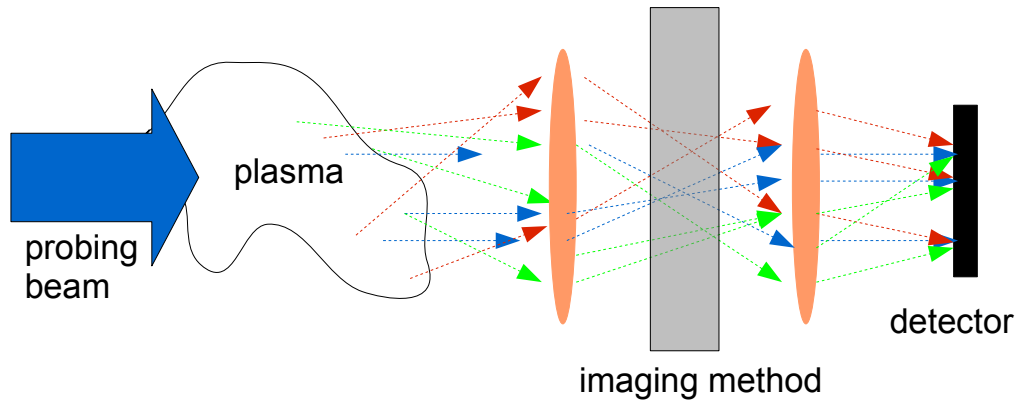
which gives, to first order in the refracting angle, a fluctuating intensity equal to

$$\tilde{I}_d = I_0 \frac{L}{k_0} \nabla^2 \tilde{\phi} = -I_0 \frac{L}{k_0} \int_{-\infty}^{\infty} d\mathbf{k} \hat{\phi}(\mathbf{k}) k^2 e^{i\mathbf{k}\cdot\mathbf{x}} \quad (2.93)$$

It can be noticed that this result is very similar to the intensity provided by the phase scintillation in the limit $k_{\perp}^2 L \ll k_0$. The two techniques are in fact different approaches to describe the same physical effect. As a result, the shadowgraphy technique shares the limitations and drawbacks of the phase scintillation method: it is non-linear and has a weak response to long wavelength fluctuations.

All these imaging methods can be combined with a spatial filter as described earlier in connection with PCI, which provides the same localization properties in all cases.

In Fig.2.15 we present a cartoon of all these methods to make their understanding more immediate.



In the focal plane

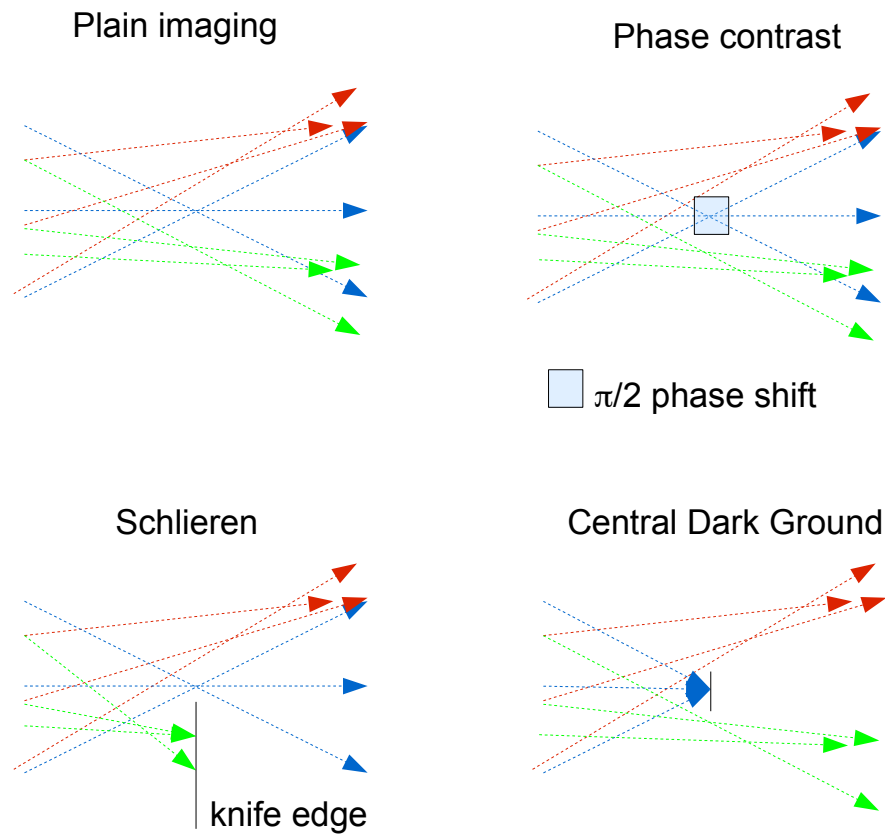


Figure 2.15: Schematic view of all the imaging methods discussed in sections 2.4.5 and 2.4.6. Blue rays correspond to undiffracted components (meaning undiffracted by fluctuations), green and red rays to diffracted components respectively corresponding to negative and positive wave-vectors (along a selected direction)

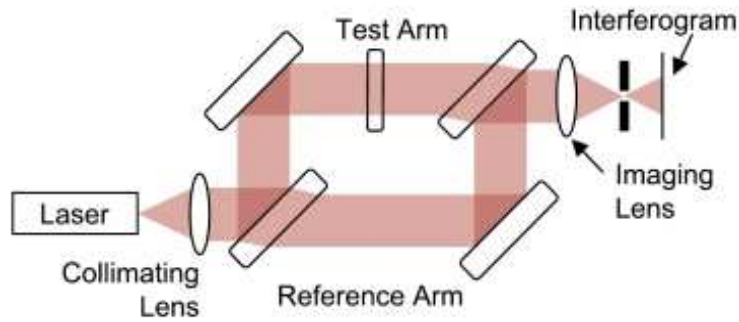


Figure 2.16: Schematic view of the optical set-up of the Mach-Zehnder interferometer.

At last we consider interferometry. Interferometry is a traditional way to observe variations of the refractive index of a transparent object. It relies on splitting a monochromatic laser beam into two parts. One part is called probing beam and propagates through the object of interest collecting changes in the index of refraction. The second part, called reference beam, is allowed to propagate freely in air or vacuum. By combining the two beams after interaction of the probing beam with the medium under consideration, the total phase shift between the two can be measured thus providing the line integral of the desired index of refraction. Interferometry can be used with a collimated probing beam to be imaged on a single detector or with an expanded beam which, being imaged on a one or two dimensional array, provides an image of the line integral of each line of sight. Interferometric measurements are not only used to measure the index of refraction but are also used to measure differences in beam paths in the same medium: the most famous use in the history of physics was the one made by Michelson to try to measure the velocity of ether. Interferometric measurements are also commonly used to determine the deviations from flatness of optical surfaces which, for high quality optics, have to be at most in the order of tens of nanometers.

In plasma physics the so-called Mach-Zehnder set-up, depicted in Fig.2.16, is commonly used to measure density profiles and, in recent years, is coupled to current profiles measurements through Faraday rotation. Let us now calculate the response properties of the Mach-Zehnder interferometer. The total electric field on the detector, after a beam splitter and a beam combiner, can be written as

$$E = \frac{E_0}{2} e^{i(\phi_0 + \tilde{\phi})} + \frac{E_0}{2} e^{i\phi_{ref}} \quad (2.94)$$

where ϕ_0 is the phase shift due to the stationary density profile, $\tilde{\phi}$ to its fluctuations and ϕ_{ref} is the phase shift of the reference beam. The beam intensity on the detector is equal

to

$$\begin{aligned} I &= \frac{|E_0|^2}{2} [1 + \cos(\phi_{ref} - \phi_0 - \tilde{\phi})] \\ &= \frac{|E_0|^2}{2} [1 + \cos(\phi_{ref} - \phi_0) \cos(\tilde{\phi}) + \sin(\phi_{ref} - \phi_0) \sin(\tilde{\phi})] \end{aligned} \quad (2.95)$$

which implies that the interferometer response is linear in the perturbation when $\phi_{ref} - \phi_0 = (n + 1/2)\pi$, where $n \in \mathbb{N}$, and quadratic when $\phi_{ref} - \phi_0 = n\pi$.

Comparing this to the response of the PCI system one can see that the interferometric imaging system has nearly identical performance. The overall image contrast is just a factor of two lower than the PCI one.

The advantages of the system are

1. Relatively easy optical set-up
2. The system responds to all wave numbers, down to zero, even though, of course, wavelengths can be uniquely identified only if they are not longer than the beam full-width or shorter than twice the spatial sampling interval (Nyquist criterion).

The disadvantages of the system are

1. The signal is sensitive to mechanical vibrations
2. ϕ_0 should be almost constant across the beam full-width
3. As all the other imaging techniques described above, in the absence of an optical filter a localization of the measurement is possible only by an Abel inversion procedure

Even though mechanical vibrations are, for TCV, significant only below a few kHz, any diagnostic should be as insensitive as possible to them, especially when looking for small fluctuations, i.e. when searching for micro-instability thresholds in physical quantities such as temperature or density gradients.

2.4.7 Cross Polarization Scattering

In Chapter 1 we described a plasma in a toroidal device, in particular in a tokamak, as a set of nested flux surfaces characterized by homogeneity, to first order, in their transport properties. It is legitimate to ask whether any perturbation of the main magnetic field can lead to any additional transport. Indeed, since charged particles follow magnetic field lines, any deviation from the equilibrium configuration will result in particles being

convected along the perturbed field line. This phenomenon is known as magnetic fluctuation. The name is a somewhat academic distinction from the so called *electrostatic* turbulence which, in turn, assumes a perfect magnetic topology and describes the anomalous transport in terms of fluctuating $E \wedge B$ drifts, which are generated by fluctuations in the electrostatic potential. In reality these are merely limiting cases and in general both the electric and magnetic field can be expected to be perturbed.

The problem of magnetic fluctuations has been investigated in a theoretical framework in the '60s and '70s and, in 1978, Rechester and Rosenbluth estimated that a relative B-field fluctuation of 10^{-4} is able to cause a stochastic magnetic topology and generate transport coefficients comparable to the ones experimentally observed [44]. These results were obtained though the assumptions of

- A fully developed chaotic field with island overlapping
- Parallel correlation lengths much shorter than the electron mean free path
- The magnetic field fluctuates over a time scale much longer than the mean collisional time

In these conditions the fluctuation of a magnetic field line, D_M , generates a particle diffusion equal to

$$D = D_M v_{\parallel} \quad (2.96)$$

where v_{\parallel} is the particle velocity along the field line and D_M is a quasilinear estimate of a spreading coefficient.

It was later shown [45] that these assumptions are not met in real plasmas and that transport coefficients do not scale linearly with the particle parallel velocity and are generally smaller than the ones predicted by Eq.2.96. From an experimental point of view one can try to directly measure fluctuations of the radial component of the magnetic field, of the plasma current density or of the plasma temperature. Additionally, since the particle transport caused by magnetic turbulence is predicted to be proportional to the particle velocity, linearly according to [44] or less than linearly according to [45], observations of suprathermal electrons provide an insight on the fluctuation level.

Historically magnetic turbulence has been analyzed only close to the edge because magnetic probes are indeed much more sensitive to perturbed magnetic fields at the edge than in the core. A number of measurements in different tokamaks have been carried out, we report here a selection

- H_{α} emission revealing plasma filaments in TFTR[54]
- Mirnov coils capturing B-field perturbations in JET[55]

These measurements showed that the dominant term generating the observed fluctuations is electrostatic[1] but, not much is known about the centre yet. For the plasma core we can cite

- The snake in JET[56]
- The runaway snake in TEXTOR[57]
- Bumpy T_e profiles in RTP and in JET[58, 59]
- Striations of H_α light emitted by ablated pellets in Tore Supra[60]

which indicate, in various and indirect ways, the presence of perturbed magnetic structures rather than actual values of magnetic field fluctuations.

Up to now the only way to investigate core magnetic fluctuations has been by means of the Cross Polarization Scattering diagnostic (CPS), which employs the mode conversion of the probing wave from X to O mode and/or vice versa caused by magnetic fluctuations. The complete three dimensional description of the CPS theory in inhomogeneous plasmas can be found in [52, 53]; here we will limit ourselves to a brief summary in one dimension. In the following we will write with the subscript "0" quantities at the probing frequency ω_0 and with the subscript "1" quantities at the scattered frequency $\omega_1 = \omega_0 + \omega$, where ω is the frequency of fluctuations. Let us consider an incident wave $E_0(x)$ propagating, with frequency ω_0 , in a plasma characterized by a conductivity tensor σ . The system is fully described by the following system of equations

$$-\nabla \wedge \nabla \wedge \mathbf{E}_0 = \epsilon\mu \frac{\partial^2 \mathbf{E}_0}{\partial t^2} + \mu \frac{\partial \mathbf{J}}{\partial t} \quad (2.97)$$

$$\mathbf{J} = \sigma \cdot \mathbf{E}_0 \quad (2.98)$$

which in frequency Fourier space becomes

$$(-\nabla \wedge \nabla \wedge + \mu\epsilon\omega_0^2 + i\omega_0\sigma\mu)\mathbf{E}_0 = 0 \quad (2.99)$$

In the presence of density or magnetic field perturbations, the tensor σ is to be replaced by $\sigma + \tilde{\sigma}$ thus giving, after a linearization in the current, a perturbed field which satisfies

$$(-\nabla \wedge \nabla \wedge + \mu\epsilon\omega_1^2 + i\omega_1\mu\sigma)\mathbf{E}_1 = -i(\omega_0 + \omega)\mu\tilde{\sigma}\mathbf{E}_0 \quad (2.100)$$

where ω_1 is the frequency of the scattered wave, and ω is the fluctuation frequency.

In the case of density fluctuations the perturbed conductivity tensor, in the cold plasma approximation, is given by $(\tilde{n}/n)\sigma$ which means that only the number of carriers is perturbed, but not their velocity.

Considering now an O-mode wave propagating perpendicularly to the magnetic field,

keeping the usual convention of the external magnetic field oriented along z, the current $\mathbf{J} = \sigma \cdot \mathbf{E}_0$ is given by the following

$$m_e \frac{\partial \mathbf{v}}{\partial t} = -e(\mathbf{E} + \mathbf{v} \wedge \mathbf{B}_0) \Rightarrow \frac{\partial \mathbf{J}}{\partial t} = \epsilon_0 \omega_{pe}^2 \mathbf{E} - \omega_{ce} \mathbf{J} \wedge \mathbf{b}_0 \quad (2.101)$$

where $\mathbf{b}_0 \equiv \mathbf{B}_0/B_0$, $\omega_{pe} = (n_e e^2 / \epsilon_0 m_e)^{1/2}$ is the plasma frequency, while $\omega_{ce} = eB_0/m_e$ is the electron cyclotron frequency. In the presence of a fluctuating magnetic field $B = B_0 + \tilde{B}$ the perturbed current $\mathbf{J} = \sigma \cdot \mathbf{E}_1 + \tilde{\sigma} \cdot \mathbf{E}_0$ satisfies

$$\frac{\partial \mathbf{J}}{\partial t} = \epsilon_0 \omega_{pe}^2 \mathbf{E}_1 - \omega_{ce} \mathbf{J} \wedge \frac{\mathbf{B}_0 + \tilde{\mathbf{B}}}{|\mathbf{B}_0|} \quad (2.102)$$

which gives for the first order perturbed current

$$-\omega_1(\tilde{\sigma} \cdot \mathbf{E}_0 + \sigma \cdot \mathbf{E}_1) + \omega_{ce}(\tilde{\sigma} \cdot \mathbf{E}_0 + \sigma \cdot \mathbf{E}_1) \wedge \mathbf{b}_0 = \epsilon_0 \omega_{pe}^2 \mathbf{E}_1 - \omega_{ce}(\sigma \cdot \mathbf{E}_0) \wedge \frac{\tilde{\mathbf{B}}}{\mathbf{B}_0}. \quad (2.103)$$

Considering the cold plasma conductivity tensor, and by approximating $\omega_1 \simeq \omega_0$, in Eq.2.103 all the terms in the scattered field cancel identically; therefore we are left with

$$\tilde{\sigma} \cdot \mathbf{E}_0 = -\frac{\omega_{ce}}{\omega_{ce} - \omega_0}(\sigma \cdot \mathbf{E}_0) \wedge \frac{\tilde{\mathbf{B}}}{|\mathbf{B}_0|} \quad (2.104)$$

the perpendicular component of this current gives rise to the so-called CPS signal, i.e. to an X-mode which can then propagate through the plasma.

Since in fusion devices, in particular in tokamaks, the level of relative magnetic fluctuations, \tilde{B}/B_0 , is small compared to the relative density fluctuations \tilde{n}/n , the net cross polarization current is expected to be small compared to the current driven by density fluctuations

$$\frac{J_{CPS}}{J_{\tilde{n}}} = -\frac{\omega_{ce}}{\omega_{ce} - \omega_0}(\sigma \cdot \mathbf{E}_0) \wedge \frac{\tilde{\mathbf{B}}}{|\mathbf{B}_0|} \frac{1}{\tilde{n}/n \sigma \cdot \mathbf{E}_0} \simeq \frac{\omega_{ce}}{\omega_0} \frac{\tilde{B}}{B_0} \frac{n}{\tilde{n}} \leq \frac{\tilde{B}/|B_0|}{\tilde{n}/n} \quad (2.105)$$

where the last two relations hold for standard tokamaks. Therefore, in order to measure the field related to the CPS current, the latter should be "protected" by appropriate instrumental shielding of the field generated by electrostatic fluctuations.

The Tore Supra team was the first to try this approach. In their pioneering work, Rax and collaborators employed O-X and X-O conversions in a vertical propagation direction. To enhance the CPS current, the receiving horn was protected by being positioned behind the O, respectively X, mode reflecting layer which was supposed to diffuse away all the unwanted signal generated by density fluctuations. They ended up with an estimation of magnetic fluctuations ranging from $5 \cdot 10^{-5}$ to 10^{-4} [46, 47]. These values are expected to lead to a chaotic field structure.

However their results have not been widely accepted mainly because, first, the receiving

horn was not completely prevented from recording small angle scattering fluctuations; second, the localization of the measurements appeared questionable. Indeed the beam can undergo mode conversion also due to multiple reflections between the reflecting layer and the vacuum chamber, even though this effect could be eliminated by modulating the incident power and looking at the phase delay of the received signal, then rejecting any delay over a prescribed threshold. The CPS diagnostic in Tore Supra was dismantled in 1999 due to the installation of a new vertical limiter with which it was incompatible.

A quite new approach has been proposed by E.Z. Gusakov and his team at Ioffe Institute of St. Petersburg. In this configuration the mode conversion takes place at the Upper Hybrid Resonance Layer (UHRL) with an extraordinary wave launched from the high field side or with an ordinary wave from the low field side[48]. The main advantage of this scheme is that most of the unwanted signal is absorbed by the plasma and is not scattered away as it was in Tore Supra.

Since the mode conversion is exploited at a resonance, the diagnostic is meant to investigate high k turbulence, whereas the cut-off scheme adopted in Tore-Supra was concerned with the low k spectral region.

Another major difference between the configuration adopted by the Tore-Supra team and the one proposed in[48] is that the CPS signal due to the ponderomotive force is not always negligible compared to the CPS signal coming from the Lorentz force. Let us illustrate this point by re-deriving the CPS signal. Let us propagate an incident wave of frequency ω_0 up to the UHR layer; at the scattered frequency we have

$$-(n + \tilde{n})e(\mathbf{v}_0 + \tilde{\mathbf{v}}) = \sigma(\mathbf{E} + \tilde{\mathbf{E}}) \quad (2.106)$$

while electrons are governed by the following

$$\frac{\partial \mathbf{v}}{\partial t} + (\mathbf{v} \cdot \nabla) \mathbf{v} = -\frac{e}{m}(\mathbf{E} + \mathbf{v} \wedge \mathbf{B}) \quad (2.107)$$

thus defining an *effective* electric field equal to the actual one minus the ponderomotive force, plus the Lorentz force

$$\begin{aligned} \mathbf{E}_{\text{eff}} &= \mathbf{E}_1 + \mathbf{v} \wedge \mathbf{B} + \frac{m}{e}(\mathbf{v} \cdot \nabla) \mathbf{v} \\ &= \mathbf{E}_1 + (\mathbf{v}_0 + \mathbf{v}_{\omega, \mathbf{k}}) \wedge (\mathbf{B}_0 + \mathbf{B}_{\omega, \mathbf{k}}) + i \frac{m}{e} (\mathbf{v}_0 + \mathbf{v}_{\omega, \mathbf{k}}) \cdot (\mathbf{k}_0 + \mathbf{k}(\omega)) (\mathbf{v}_0 + \mathbf{v}_{\omega, \mathbf{k}}) \end{aligned} \quad (2.108)$$

where $k(\omega)$ models the dispersion relation of the fluctuations while the subscripts 0, 1 and $\{\omega, \mathbf{k}\}$ stand respectively for incident, perturbed, fluctuating.

The component of the effective field at the scattered frequency is

$$\mathbf{E}_{\text{eff}} = \mathbf{E}_1 + \mathbf{v}_0 \wedge \mathbf{B}_{\omega, \mathbf{k}} + \mathbf{v}_{\omega, \mathbf{k}} \wedge \mathbf{B}_0 + i \frac{m}{e} [(\mathbf{v}_0 \cdot \mathbf{k}(\omega)) \mathbf{v}_{\omega, \mathbf{k}} + (\mathbf{v}_{\omega, \mathbf{k}} \cdot \mathbf{k}_0) \mathbf{v}_0] \quad (2.109)$$

The current component at the scattered frequency is given by

$$-\mathbf{J}_1 = en\mathbf{v}_1 + en_0\mathbf{v}_{\omega,\mathbf{k}} + en_{\omega,k}\mathbf{v}_0 \quad (2.110)$$

The continuity equation can be written in Fourier space as

$$n_0 = n \frac{\mathbf{k}_0 \cdot \mathbf{v}_0}{\omega_0} \quad (2.111)$$

In the case of an extraordinary mode converted into an ordinary mode we can thus write the CPS signal as

$$J_{1,z} = -env_{1,z} - en_0v_{\omega,k,z} = -en \frac{\sigma_{zz}(\omega_1)E_{eff}}{en} - en \frac{\mathbf{k}_0 \cdot \mathbf{v}_0}{\omega_0} v_{\omega,k,z} \quad (2.112)$$

Let us take $\mathbf{B} = B_0\hat{z}$, the wave electric field along y, and $\sigma_{z,\alpha} = i\frac{ne^2}{m\omega}\delta_{z,\alpha}$; where $\delta_{z,\alpha}$ is the Kronecker delta and the index α scans $\{x, y, z\}$. Therefore we obtain

$$\begin{aligned} J_{1,z} &= i\frac{\epsilon_0\omega_{pe}^2}{\omega_1} \left\{ [(\mathbf{v}_0 \wedge \mathbf{B}_{\omega,k} + \mathbf{v}_{\omega,\mathbf{k}} \wedge \mathbf{B}_0)_z + i\frac{m}{e}[(\mathbf{v}_0 \cdot \mathbf{k}(\omega))\mathbf{v}_{\omega,k,z} + (\mathbf{v}_{\omega,\mathbf{k}} \cdot \mathbf{k}_0)\mathbf{v}_{0,z}]] \right\} \\ &\quad - en \frac{\mathbf{k}_0 \cdot \mathbf{v}_0}{\omega_0} \mathbf{v}_{\omega,k,z} \\ &= i\frac{\epsilon_0\omega_{pe}^2}{\omega_1} \left\{ [-v_0B_{\omega,k,x} + i\frac{m}{e}[\mathbf{v}_0 \cdot \mathbf{k}(\omega)]\mathbf{v}_{\omega,k,z}] \right\} - en \frac{\mathbf{k}_0 \cdot \mathbf{v}_0}{\omega_0} \mathbf{v}_{\omega,k,z} \end{aligned} \quad (2.113)$$

or

$$\begin{aligned} J_{1,z} &= i\frac{\epsilon_0\omega_{pe}^2}{\omega_1} [\mathbf{v}_0 \wedge \mathbf{B}_{\omega,k}]_z - \frac{ne}{\omega_1} (\mathbf{v}_0 \cdot \mathbf{k}(\omega))\mathbf{v}_{\omega,k,z} - \frac{ne}{\omega_0} (\mathbf{k}_0 \cdot \mathbf{v}_0)\mathbf{v}_{\omega,k,z} \\ &= i\frac{\epsilon_0\omega_{pe}^2}{\omega_1} [\mathbf{v}_0 \wedge \mathbf{B}_{\omega,k}]_z + i\frac{\mathbf{k}_1 \cdot \mathbf{v}_0}{\mu_0\omega_1} [\mathbf{k}(\omega) \wedge \mathbf{B}_{\omega,k}]_z \end{aligned} \quad (2.114)$$

where the last equation has been derived considering the Bragg scattering condition, i.e. $k_1 = k_0 + k(\omega)$ and neglecting the displacement current in Ampere's law for low frequency fluctuations, i.e. $\mu_0 en\mathbf{v}_{\omega,\mathbf{k}} = -i(\mathbf{k}(\omega) \wedge \mathbf{B}_{\omega,\mathbf{k}})$.

The contribution of the longitudinal velocity is negligible in comparison to that of the Lorentz force in the limit of long-wavelength fluctuations which satisfy

$$\frac{k(\omega)}{\omega_{pe}} < \frac{\omega_{pe}}{c\omega_1} \quad (2.115)$$

which is typically satisfied if k is of the order of 10 cm^{-1} .

The problem with this configuration is the density limit which may not allow one to scan the entire plasma cross section. Indeed, for a given geometrical configuration, the UH layer is a function of the density profile which may result in a non monotonic profile of the resonance along the major radius, thus impairing the access to part of or the whole high field side region. For TCV, the whole horizontal midplane is indeed observable if the

central density does not exceed 10^{19}m^{-3} ; this means that ITB plasmas are well suited for this diagnostic but high density discharges, such as X3-heated H-modes, are not (see Sec. 1.5.1 for the meaning of X3 in TCV).

An estimation of the wave number can be made in this scheme by performing a time of flight measurement. The basic idea is to exploit the low velocity of the wave in the resonance region, so that expressing the time of flight as a function of the group velocity

$$t_f = \int_a^{x_s(k)} \frac{\partial k_0}{\partial \omega_0} dx + \int_{x_s(k)}^b \frac{\partial k_1}{\partial \omega_1} dx \quad (2.116)$$

and imposing the scattering condition

$$k = k_1 - k_0 \quad (2.117)$$

where k is the fluctuation wave number, x_s is the scattering position while a and b are the launching and receiving horn positions, respectively. Solving equations 2.116 and 2.117 one finds

$$\frac{dt_f}{dk} = -\frac{\partial x_s}{\partial \omega_1} \quad \Rightarrow \quad t_f \simeq t_0 - \frac{\partial x_s}{\partial \omega_1} k \quad (2.118)$$

where x_s is the UHRL radial position. Approximating the derivative with l/ω_0 , where l is the inhomogeneity radial length, one could obtain the value of k once the plasma density is known with good precision.

The radial resolution is estimated to be about 1 cm[49].

According to the reciprocity theorem[27], the CPS power is given by

$$P_{CPS} = \frac{1}{4} \int d^3r J_s(\mathbf{r}) E_r(\mathbf{r}) \quad (2.119)$$

where E_r is the field of the receiving antenna when operated in a reversed way, i.e. as an emitter. In [48] the calculation is carried out and the result is that the total CPS power is proportional to

$$S(\mathbf{k}) = |\hat{b}_{y,\mathbf{k},\omega}|^2 \left(\frac{k_x}{k_c} - \frac{\omega_{pe}^2}{k_c^2 c^2} \right)^2 + |\hat{b}_{x,\mathbf{k},\omega}|^2 \frac{\omega_{pe}^4}{\omega_{ce}^2 \omega_i^2} \quad (2.120)$$

where $\hat{b}_{x,\mathbf{k},\omega}$ and $\hat{b}_{y,\mathbf{k},\omega}$ are, respectively, the radial and poloidal Fourier components of the magnetic field fluctuations normalized to the equilibrium magnetic field, while $k_c = \omega_{ce}(R_{UHR})/c$. In Eq.2.120, the first term is due to the ponderomotive force, while the second term is due to the Lorentz force. Considering the typical magnetic field in TCV at mid-radius, and electron densities equal to 10^{18} , 10^{19} and 10^{20} m^{-3} , we estimate the term $\omega_{pe}^2/(k_c c)^2$ to be equal to 0.07, 0.7 and 7 respectively, and $k_c \simeq 6.7 \text{ cm}^{-1}$. This indicates that the ponderomotive force term is, in general, dominated by high k fluctuations; in particular it is close to zero in low-mid densities in the ITG-TEM spectral region. Indeed,

linear and non-linear simulations carried out with the GS2 code on actual TCV shots indicate that the spectral region which contributes most to the total transport is around $k_\theta \rho_i \simeq 0.2$, which implies (under the assumption $k_\theta \simeq k_r$) $k_x/k_c \simeq 0.1 - 0.03$, depending on the ion temperature. In Eq.2.120 the term due to the Lorentz force is estimated to be of the order of 0.005-0.3-6.9, for the three density values above. It follows that the numerical factors multiplying the poloidal and radial components of the magnetic field fluctuations in Eq.2.120 are, depending on plasma conditions, comparable or dominant over one another. The CPS signal is generally, therefore, an admixture of radial and poloidal components of the perturbed magnetic field.

In the derivation of Eq.2.120 we neglected the contribution to the scattered current given by $en_{\omega,k}v_0$ since, ideally, the extraordinary wave does not produce any oscillatory velocity with component along the magnetic field. However, in reality this is not true since the propagating X-mode is not a plane wave but a spherical wave which, indeed, has a small component along the external B field direction, \hat{z} . In [48] this contribution is estimated as being equal to

$$S(\mathbf{k}) = \frac{\omega_{pe}^8}{\omega_{ce}^6 \omega_i^2} |\hat{n}_{\mathbf{k},\omega}|^2 \left| \left[\frac{\tilde{k}_{iz}}{k_x - k_c} - \frac{(k_z - \tilde{k}_{iz})k_c}{(k_x - k_c)^2} \right] \right|^2 \quad (2.121)$$

where $\Re(\tilde{k}_{iz}) = k_z/2$. Estimating the ratio $k_{||}/k_{\perp} \simeq 0.01$ in toroidal plasma devices [6], the contribution from density perturbations can be rewritten as

$$S(\mathbf{k}) = \frac{\omega_{pe}^8}{\omega_{ce}^6 \omega_i^2} |\hat{n}_{\mathbf{k},\omega}|^2 * 10^{-4} \quad (2.122)$$

The factor in front of the density contribution term to the CPS signal is not always very small for TCV, due to the small value of the magnetic field strength; indeed, for the three density values taken as a reference we find it of the order of 10^{-5} , 10^{-1} and 100. The spurious signal is therefore not always negligible compared to actual magnetic field fluctuations.

This treatment, however, does not take into account the mode conversion (MC) induced by magnetic shear which couples ordinary and extraordinary waves which, in the case of a zero shear, would propagate independently. This effect is due to the fact that the probing wave experiences a magnetic field rotating in the plane perpendicular to the direction of propagation and its effect is predicted, in the cold plasma approximation, to be maximum at the UHR[51]. To perform an estimation one may simply compare the current given by the MC induced by magnetic shear (Eq.2.123a) and the current due to magnetic fluctuations (Eq.2.123b)

$$C(s)en_{k,\omega}v_{0,z} \quad (a) \qquad \frac{\epsilon_0 \omega_{pe}^2}{\omega_1} [v_0 \wedge B_{k,\omega}] \quad (b) \quad (2.123)$$

where $C(s)$ is a coefficient which accounts for the MC field. This estimation yields a contribution from the magnetic shear of up to 5%. Ultimately, the complete estimate of the fluctuation density CPS signal is to be done taking into account the electric field arising also from magnetic shear coupling and not only from beam divergence.

Considering these estimates this diagnostic does not appear especially attractive; this is not only due to the impossibility of separating the contributions of magnetic and density fluctuations to the CPS signal, but also to the impossibility of separating the radial and poloidal components of the magnetic field perturbation, since the mix is very sensitive to the target plasma. Additionally the diagnostic is almost only sensitive to high-k fluctuations which are not expected to drive considerable particle flux. Moreover, since density fluctuations contribute most to the total signal in the case of oblique propagation, the ideal target plasma has its magnetic axis located at $Z=0$ (and possibly highly elongated) allowing true perpendicular launching from an equatorial port, which is in contrast with the TCV flexibility in terms of plasma positioning in the vacuum vessel.

2.5 Concluding remarks

We try to summarize here the advantages and disadvantages of all the diagnostics explored in this chapter, to clarify to the reader why we chose the tangential PCI.

We recall how it is imperative for a modern diagnostic to be able to measure fluctuations in the following conditions

1. Excellent spatial localization
2. A good portion of the plasma cross section must be measurable
3. Data must be as independent of specific models as possible
4. The accessible spectrum must be as broad as possible

The last condition is desirable because, nowadays, numerical simulations rely on turbulence scale separation to speed up the calculations and avoid a number of numerical instabilities. This, most of the time, means considering adiabatic ions or electrons, which roughly translates into considering small or large fluctuation wave numbers, i.e. the ITG or ETG limit. It is not clear whether the results are biased by this simplification; i.e. whether the theoretical knowledge we have built up to now provides an accurate description of reality; or whether, instead, energy advection across disparate scales will induce severe modifications. Therefore ideally the same diagnostic should be able to compare small and large scale fluctuations to estimate the actual energy stored in different parts of

the spectrum. A cross diagnostic comparison is, in the opinion of the author, not sufficient because every diagnostic samples "its" fluctuations in a different way and with different calibration factors which are not always easy to compare.

In the following table we will consider only tangential configurations for BES, Collective scattering and imaging methods since no other configuration meets the localization requirements. Concerning the access to most of the poloidal cross section, we have to say that, in principle, all diagnostics meet this requirement.

Diagnostic	Loca- lization	Inter- pretation	Spectral region	Spectral identification	Structure separation	Easy set-up
BES	good	simple	low	yes	yes	moderate
EPA	poor	simple	any	not	not	yes
Refl. std	good(?)	difficult	low	not	not	yes
Refl. MIR	good(?)	difficult	low	yes	yes	not
Refl. Doppler	good(?)	difficult	high	yes	yes	yes
PCI	good	simple	any	yes	yes	not
Schlieren	good	simple	any	yes	yes	not
CDG	good	simple	any	yes	yes	not
Shadowgraph	good	simple	any	yes	yes	not
Scintillation	good	simple	any	yes	yes	not
Interferometry	poor	simple	any	yes	not	not
Interf.+ filter	good	simple	any	yes	not	not
Collective Scatt.	good	simple	high	yes	not	not
$CPS_{cut-off}$	good(?)	difficult	low	yes	yes	yes
CPS_{UH}	good(?)	difficult	high	yes	yes	yes

Table 2.2: Summary of diagnostic performance with respect to key points in diagnostic development

In Table 2.5 it appears clear that only imaging diagnostics meet all the requirements. Since the PCI is the one performing best among them, we chose to develop its tangential version for the TCV tokamak, despite considerable technical difficulties which will be described in the next chapter.

Bibliography

- [1] B. Carreras, *IEEE Trans. Plasma Sci.* **25** (1997) 1281, and references therein
- [2] J.W Connor *et al.*, *Nucl. Fusion* **44** (2004) R1
- [3] R. Courant, K. Friedrichs and H. Lewy, *Mathematische Annalen* **100** (1928) 32.
Translated into English in *IBM Journal* (1967) 215
- [4] Z. Lin *et al.*, *Phys. Plasmas* **12** (2005) 056125
- [5] R.E. Waltz *et al.*, *Phys. Plasmas* **1** (1994) 2229
- [6] N. Winsor *et al.*, *Phys. Fluids* **11** (1968) 2448
- [7] S. Coda *et al.*, *Phys. Rev. Lett.* **86** (2001) 4835
- [8] G.D. Conway *et al.*, *Plasma Phys. Control. Fusion* **47** (2005) 1165
- [9] F.M. Levinton *et al.*, *Phys. Rev. Lett.* **75** (1995) 4417
- [10] E.J. Strait *et al.*, *Phys. Rev. Lett.* **75** (1995) 4421
- [11] S. Coda *et al.*, *Phys. Plasmas* **12** (2005) 056124
- [12] X. Garbet *et al.*, *Phys. Plasmas* **8** (2001) 2793
- [13] J. Candy *et al.*, *Phys. Plasmas* **11** (2004) 1879
- [14] C. Bender and S. Orszag, *Advanced Mathematical Methods for Scientists and Engineers*, McGraw-Hill, 1978
- [15] T.P. Goodman *et al.*, *Nucl. Fusion* **43** (2003) 1619
- [16] P. Gohil *et al.*, *Nucl. Fusion* **43** (2003) 708
- [17] F. Jenko *et al.*, *Phys. Plasmas* **8** (2001) 4096
- [18] C. Bourdelle, *TTF*, Milan, Italy, 2004
- [19] C. Bourdelle *et al.*, *Nucl. Fusion* **42** (2002) 892

- [20] M. Kotschenreuther *et al.*, *Comput. Phys. Commun.* **88** (1995) 128
- [21] R. L. Miller, M. S. Chu, J. M. Greene *et al.*, *Phys. Plasmas* **5** (1998) 973
- [22] T.J. Murphy, *Plasma Phys. Control. Fusion* **29** (1987) 549
- [23] K.R. Lang, *Astrophysical formulae*, p.102, Springer-Verlag, Berlin
- [24] R.J. Fonk *et al.*, *Rev. Sci. Instrum.* **61** (1990) 3847
- [25] G. Brooker, *Modern Classical Optics*, Oxford University Press, 2003
- [26] C.D. Boley *et al.*, *Phys. Rev. Lett.* **52** (1984) 534
- [27] V.L. Ginzburg, *The propagation of electromagnetic waves in plasmas*, Pergamon Press, 1970
- [28] R.K. Janev *et al.*, *Nucl. Fusion* **29** (1989) 2125
- [29] C. Schlatter, *PhD thesis submitted, École Polytechnique Fédérale de Lausanne*, 2009
- [30] R.E. Slusher and C.M Surko, *Phys. Fluids* **23** (1980) 472
- [31] P. Devynck *et al.*, *Plasma Phys. Control. Fusion* **35** (1993) 65
- [32] E. Mazzucato *et al.*, *Phys. Plasmas* **10** (2003) 753
- [33] X.L. Zou *et al.*, *Plasma Physics Control. Fusion* **33** (1991) 261
- [34] E. Mazzucato, *Rev. Sci. Instr.* **69** (1998) 2201
- [35] E. Mazzucato *et al.*, *Phys. Rev. Lett* **71** (1993) 1840
- [36] T. Munsat *et al.*, *Plasma Phys. Control. Fusion* **45** (2003) 469
- [37] E.Z. Gusakov *et al.*, *Plasma Phys. Control. Fusion* **46** (2004) 1393
- [38] G.J. Kramer *et al.*, *Plasma Phys. Control. Fusion* **46** (2004) 695
- [39] M. Hirsch *et al.*, *Plasma Phys. Control. Fusion* **43** (2001) 1641
- [40] P.W. Terry, *Rev. Modern Phys.* **72** (2000) 109
- [41] E. Mazzucato *Nucl. Fusion* **41** (2001) 203
- [42] D.R. Smith *et al.*, *Rev. Sci. Instrum.* **75** (2004) 10
- [43] A. Lazarian, *Plasma Phys. Control. Fusion* **36** (1994) 1013

- [44] A.B. Rechester *et al.*, *Phys. Rev. Lett.* **40** (1978) 38
- [45] M. de Rover *et al.*, *Phys. Plasmas* **6** (1999) 2443
- [46] X.L. Zou *et al.*, *Phys. Rev. Lett.* **75** (1995) 1090
- [47] L. Colas *et al.*, *Nuclear Fusion* **38** (1998) 903
- [48] E.Z. Gusakov, *Plasma Phys. Reports* **28** (2002) 580
- [49] K.M. Novik *et al.*, *Plasma Phys. Control. Fusion* **35** (1993) 357
- [50] C.P. Ritz *et al.*, *Phys. Rev. Lett* **62** (1989) 1844
- [51] I. Fidone *et al.*, *Nucl. Fusion* **11** (1971) 133
- [52] X.L. Zou *Ph.D. thesis, Université Paris-Sud 11*, 1988
- [53] T. Lehner *et al.*, *Europhys. Lett.* **8** (1989) 759
- [54] S.J. Zweben and S.S. Medley, *Phys. Fluids* **B** (1989) 2058
- [55] M Malacarne and P.A. Duperrex, *Nucl. Fusion* **27** (1987) 2113
- [56] A. Weller *et al.*, *Phys Rev. Lett.* **59** (1987) 2303
- [57] R. Jaspers *et al.*, *Phys. Rev. Lett.* **72** (1994) 4093
- [58] N.Lopes Cardozo *et al.*, *Phys. Rev. Lett.* **73** (1994) 256
- [59] M.F.F. Nave *et al.*, *Nucl Fusion* **92** (1992) 825
- [60] M.A. Dubois *et al.*, *Nucl. Fusion* **32** (1992) 1935
- [61] F.M. Poli *et al.*, *Phys. Plasmas* **14** (2007) 052311
- [62] F. Zernicke, *Physica* **1** (1934) 689
- [63] S. Coda, *Ph.D. thesis, Massachusetts Institute of Technology*, 1997
- [64] H. Weisen, *Ph.D. thesis, École Polytechnique Fédérale de Lausanne*, 1986
- [65] H. Weisen, *Plasma Phys. Control. Fusion* **28** (1986) 1147
- [66] A. Mazurenko, *Ph.D. thesis, Massachusetts Institute of Technology*, 2001
- [67] L.E. Sharp *et al.*, *Plasma Phys.* **25** (1983) 781
- [68] Y.B. Kim *et al.*, *Phys. of Fluids* **3** (1991) 2050

[69] S.J. Ward *et al.*, *J. Phys.* **B 18** (1985) L525

[70] S. Hara *et al.*, *J. Phys.* **B 8** (1975) L472

Chapter 3

Phase Contrast diagnostic and Doppler Reflectometer, theoretical treatment and practical realization

3.1 The interaction of light and plasma

Let us begin this chapter by reviewing a number of physical quantities and notions routinely used in plasma physics. As mentioned in chapter 1, a plasma is a collection of charged particles that respond strongly and collectively to electromagnetic fields, typically taking the form of a gas-like cloud. The electrostatic potential of a heterogenous plasma composed of multiple charged particle species in relative thermodynamic equilibrium can be modeled by the Poisson equation with the inclusion of the Boltzmann distribution. In the proximity of a singly ionized test ion, this equation reads

$$\nabla^2\phi(\mathbf{r}) = -\frac{\rho(\mathbf{r})}{\epsilon_0} = \frac{n_e e}{\epsilon_0} e^{\frac{e\phi}{k_B T_e}} - \sum_i \frac{n_i Z_i e}{\epsilon_0} e^{\frac{-e\phi}{k_B T_i}} + \frac{e}{\epsilon_0} \delta(\mathbf{r}) \quad (3.1)$$

where δ is the Dirac delta describing the test ion at the center of the reference system. By assuming that, for each species, $e\phi \ll k_B T$, we can expand Eq.3.1 in a MacLaurin series to obtain the Debye-Huckel equation

$$\begin{aligned} \nabla^2\phi(\mathbf{r}) &= \frac{e}{\epsilon_0} \left(\delta(\mathbf{r}) + n_e + n_e \frac{e\phi}{k_B T_e} - \sum_i Z_i n_i e + \sum_i n_i Z_i \frac{e\phi}{k_B T_i} \right) \\ &= \frac{e}{\epsilon_0} \left(n_e \frac{e\phi}{k_B T_e} + \sum_i n_i Z_i \frac{e\phi}{k_B T_i} + \delta(\mathbf{r}) \right) = \frac{1}{\lambda_D^2} \phi + \frac{e}{\epsilon_0} \delta(\mathbf{r}) \end{aligned} \quad (3.2)$$

where plasma quasi-neutrality has been assumed. The solution, in spherical geometry, of the Debye-Huckel equation is given by

$$\phi(\mathbf{r}) = \frac{A}{r} e^{-r/\lambda_D} \quad (3.3)$$

The damping of the exponential function is governed by the so-called Debye length, λ_D , which accounts for charge screening effects due to the cloud of oppositely charged particles disposed around the test particle by electrostatic attraction. (This solution does not hold for distances smaller than the average distance between charged particles because the statistical averaging behind the Boltzmann distribution does not hold: in this case the Coulomb potential is the solution of the equation). The statistical averaging in Eq. 3.1 is meaningful only if the number of particles in the Debye sphere is large, i.e.

$$\frac{4}{3}\pi\lambda_D^3 n_e \gg 1 \Rightarrow \frac{4}{3}\pi \frac{\sqrt{(\epsilon_0 k_B T)^3}}{\alpha^{3/2} e^3 \sqrt{n_e}} \gg 1 \quad (3.4)$$

where α is a numerical factor taking into account the ions' contribution to the Debye length ($\alpha = 2$ if $T_e = T_i, \forall i$). Eq.3.4 means that the mean kinetic energy has to be far larger than the average Coulomb interaction between charged particles, which goes like $e^2/\bar{r} \sim e^2 \sqrt[3]{n_e}$. If Eq. 3.4 is violated the plasma cannot be considered as a gas anymore and the Boltzmann distribution cannot be used. Choosing the most unfavourable conditions, i.e. temperature ~ 10 eV which is about the ionization energy of hydrogen and density $\sim 10^{21} \text{ m}^{-3}$, the aforementioned criterion is amply satisfied, as the value is larger than 600; in real tokamaks its value is as high as 10^5 , allowing the use of the ideal gas state equation, i.e. neglecting interactions between particles and their volume in the Van Der Waals equation for real gases. Indeed real gases also behave as ideal gases at small pressures compared to the atmospheric pressure.

The Debye length is of fundamental importance in plasma diagnostics as it governs the collective behavior of the plasma. Indeed the Fourier transform of Eq. 3.3 is a Cauchy-Lorentz function

$$\hat{\phi}(\mathbf{k}) \propto \frac{1}{1 + (\mathbf{k}\lambda_D)^2} \quad (3.5)$$

which states that particle correlations in wave-number space are significant only for wavelengths much longer than the Debye length, beyond which a large number of particles contributes in phase; this mechanism saturates after a few Debye lengths, where particles are completely shielded and do not respond to the test particle movements anymore. In the opposite limit particles are uncorrelated, even though their reciprocal distance is small, because their kinetic energy far exceeds the reciprocal potential energy of interaction. The first limit gives rise to coherent or collective scattering, see Chapter 2, while the latter to incoherent scattering, e.g. Thomson scattering used to measure temperature and density fluctuations.

We can now proceed to analyze the interaction between a plasma and an externally launched electromagnetic wave.

Let us treat the plasma as an homogenous conducting medium, i.e. where currents can

flow, governed by Maxwell's equations in vacuum

$$\nabla \wedge \mathbf{E} = -\frac{\partial \mathbf{B}}{\partial t} \quad \nabla \wedge \mathbf{B} = \mu_0 \mathbf{J} + \epsilon_0 \mu_0 \frac{\partial \mathbf{E}}{\partial t}; \quad (3.6)$$

all the electromagnetic properties of the plasma are then expressed by the current density \mathbf{J} and by the vacuum permeability and permittivity μ_0 and ϵ_0 .

Let us now assume the plasma to be homogenous in time and space

$$\mathbf{X}(\mathbf{x}, t) = \int_{-\infty}^{\infty} d\mathbf{k} d\omega_0 \hat{\mathbf{X}}(\mathbf{k}, \omega_0) e^{i(\mathbf{k} \cdot \mathbf{x} - \omega_0 t)} \quad (3.7)$$

where X stands for \mathbf{E} , \mathbf{B} or \mathbf{J} , and let us further assume the fields to be small enough to produce a current linearly dependent on the fields themselves

$$\hat{\mathbf{J}}(\mathbf{k}, \omega_0) = \underline{\sigma}(\mathbf{k}, \omega_0) \cdot \hat{\mathbf{E}}(\mathbf{k}, \omega_0) \quad (3.8)$$

where $\underline{\sigma}$ is the plasma conductivity tensor.

We can then write Eq.3.6 as

$$\mathbf{k} \wedge \mathbf{k} \wedge \hat{\mathbf{E}} + \omega_0^2 \epsilon_0 \mu_0 \hat{\mathbf{E}} + i\omega_0 \mu_0 \underline{\sigma} \cdot \hat{\mathbf{E}} = 0 \quad (3.9)$$

which can be re-cast into

$$\left[\mathbf{k}\mathbf{k} - \left(k^2 - \frac{\omega_0^2}{c^2} \right) \bar{\mathbf{I}} + i\omega_0 \mu_0 \underline{\sigma} \right] \cdot \hat{\mathbf{E}} = 0 \quad (3.10)$$

introducing the dielectric tensor $\underline{\epsilon} = \bar{\mathbf{I}} + i\underline{\sigma}/(\omega_0 \epsilon_0)$, assuming the medium to be isotropic and considering \mathbf{k} directed along the z axis, we can write the dispersion relation as

$$\det \begin{bmatrix} -k^2 + \frac{\omega_0^2}{c^2} \epsilon & 0 & 0 \\ 0 & -k^2 + \frac{\omega_0^2}{c^2} \epsilon & 0 \\ 0 & 0 & \frac{\omega_0^2}{c^2} \epsilon \end{bmatrix} = 0 \quad (3.11)$$

which gives solutions for transverse and longitudinal polarizations. If the medium is not isotropic, it is in general not possible to separate propagating waves into longitudinal and transverse as they are always mixed, furthermore the refractive index is a function of the wave direction of propagation.

Let us now consider a plasma fluid treatment, i.e., ignoring the details of the distribution function, of waves propagating at phase velocities much larger than ion and electron velocities in the plasma. We are then allowed to neglect particle motion thus assuming the so-called *cold plasma approximation*, which consists of assuming that all the particles are at rest unless directly accelerated by the fields.

The equation of motion of a charged particle in a purely monochromatic field reads

$$-i\omega_0 m \hat{\mathbf{v}} = q(\hat{\mathbf{E}} + \hat{\mathbf{v}} \wedge \mathbf{B}_0) \quad (3.12)$$

where we neglected the second order term in the Lorentz force $\mathbf{v} \wedge \mathbf{B}$. By adopting $\mathbf{B}_0 = B_0 \hat{\mathbf{z}}$ we can solve for $\hat{\mathbf{v}}$ to obtain

$$\hat{\mathbf{v}} = \frac{iq}{\omega_0 m} \left[\frac{1}{1 - \Omega^2/\omega_0^2} \left(\hat{E}_x + i \frac{\Omega}{\omega_0} \hat{E}_y \right), \frac{1}{1 - \Omega^2/\omega_0^2} \left(\hat{E}_y - i \frac{\Omega}{\omega_0} \hat{E}_x \right), \hat{E}_z \right], \quad (3.13)$$

where Ω is the cyclotron frequency.

If the plasma is composed of ions and electrons, we can neglect the ion inertia and write the current density as

$$\mathbf{J} = -en_e \mathbf{v}_e = \underline{\sigma} \cdot \mathbf{E} \quad (3.14)$$

where

$$\underline{\sigma} = \frac{i\epsilon_0 \omega_{pe}^2}{\omega_0} \frac{1}{1 - \Omega_{ce}^2/\omega_0^2} \begin{bmatrix} 1 & -i\Omega_{ce}/\omega_0 & 0 \\ i\Omega_{ce}/\omega_0 & 1 & 0 \\ 0 & 0 & 1 - \Omega_{ce}^2/\omega_0^2 \end{bmatrix} \quad (3.15)$$

where $\omega_{pe} = \sqrt{n_e e^2 / \epsilon_0 m_e}$ is the electron plasma frequency and $\Omega_{ce} = eB_0 / m_e$ is the electron cyclotron frequency.

The wave equation reads

$$\left(\nabla^2 - \frac{1}{c^2} \frac{\partial^2}{\partial t^2} \right) \mathbf{E} = \mu_0 \frac{\partial(\underline{\sigma} \cdot \mathbf{E})}{\partial t} + \frac{\nabla \rho}{\epsilon_0} \quad (3.16)$$

where ρ is the charge density distribution. Let us now assume that the density is given by

$$n(\mathbf{x}, t) = n_0(\mathbf{x}) + \tilde{n}(\mathbf{x}, t) = n_0(\mathbf{x}) + \int d\mathbf{k} d\omega \hat{n}(\mathbf{k}, \omega) e^{i(\mathbf{k} \cdot \mathbf{x} - \omega t)} \quad (3.17)$$

if the broadband density fluctuation spectrum satisfies

$$\omega \ll \omega_0 \quad (3.18)$$

we can write to zeroth-order in ω/ω_0

$$\frac{\partial(\underline{\sigma} \cdot \mathbf{E})}{\partial t} \simeq \underline{\sigma} \cdot \frac{\partial \mathbf{E}}{\partial t} \quad (3.19)$$

if, furthermore, the spatial inhomogeneities of the plasma density satisfy

$$|\mathbf{k}| \ll |\mathbf{k}_0| \quad (3.20)$$

we can neglect the last term in equation 3.16 to finally write the wave equation as

$$\left(\nabla^2 - \frac{1}{c^2} \frac{\partial^2}{\partial t^2} \right) \mathbf{E} = \mu_0 \underline{\sigma} \cdot \frac{\partial \mathbf{E}}{\partial t} \quad (3.21)$$

Let us now consider the following limiting case in Eq.3.15

$$\omega_0 \gg \Omega \quad (3.22)$$

then Eq.3.21 reduces to

$$\left(\nabla^2 - \frac{1}{c^2} \frac{\partial^2}{\partial t^2}\right) \mathbf{E} = 4\pi r_e n_e \mathbf{E} \quad (3.23)$$

where $r_e = e^2/(4\pi\epsilon_0 m_e c^2)$ is the classical electron radius.

Eq.3.23 is of the form

$$\left(\nabla^2 - \frac{1}{c^2} \frac{\partial^2}{\partial t^2}\right) \mathbf{E}(\mathbf{x}, t) = U(\mathbf{x}, t) \mathbf{E}(\mathbf{x}, t) \quad (3.24)$$

which admits solutions of the form

$$\mathbf{E}(\mathbf{x}, t) = \mathbf{E}_0(\mathbf{x}, t) + \int d\mathbf{x}' dt' G(\mathbf{x} - \mathbf{x}', t - t') U(\mathbf{x}', t') \mathbf{E}(\mathbf{x}', t') \quad (3.25)$$

where $\mathbf{E}_0(\mathbf{x}, t)$ is the solution if the homogenous equation and the associated Green function satisfies

$$\left(\nabla^2 - \frac{1}{c^2} \frac{\partial^2}{\partial t^2}\right) G(\mathbf{x} - \mathbf{x}', t - t') = \delta_3(\mathbf{x} - \mathbf{x}') \delta(t - t') \quad (3.26)$$

and is given by

$$G(\mathbf{x} - \mathbf{x}', t - t') = -\frac{1}{4\pi|\mathbf{x} - \mathbf{x}'|} \delta\left(t - t' - \frac{|\mathbf{x} - \mathbf{x}'|}{c}\right) \quad (3.27)$$

therefore the solution of Eq.3.23 is given by

$$\mathbf{E}(\mathbf{x}, t) = \mathbf{E}_0(\mathbf{x}, t) - r_e \int d\mathbf{x}' \frac{n_e(\mathbf{x}', t - |\mathbf{x} - \mathbf{x}'|/c)}{|\mathbf{x} - \mathbf{x}'|} \mathbf{E}\left(\mathbf{x}', t - \frac{|\mathbf{x} - \mathbf{x}'|}{c}\right) \quad (3.28)$$

If we now write the total electric field as the sum of the incident field \mathbf{E}_0 , plus the field \mathbf{E}_1 generated by electrons accelerated by the incident field, plus the field \mathbf{E}_2 generated by electrons accelerated by \mathbf{E}_1 and so on

$$\mathbf{E}(\mathbf{x}, t) = \sum_{i=0}^{\infty} \mathbf{E}_i(\mathbf{x}, t) \quad (3.29)$$

we recognize that Eq.3.28 is nothing but the equation above in the non-relativistic limit, where all the terms $\mathbf{E}_{1,2,\dots,n}$ are found by iterating the integral 1,2,...,n times over the incident field calculated at the appropriate retarded time. The total field has to be finite in magnitude, which implies that $\lim_{n \rightarrow \infty} E_n = 0$, therefore we can think of solving the problem with a perturbation approach. If we assume that all the terms in the series are monotonically decreasing, we can stop the solution to the n^{th} term if the $(n+1)^{th}$ one is negligible in comparison: in the case where only the first term is important we obtain the so-called *first order Born approximation*.

The Born approximation involved in replacing the total wave function \mathbf{E} by the incident wave function \mathbf{E}_0 , is valid whenever the scattered wave is small compared to the incident wave, i.e.

$$|\mathbf{E}_0 e^{i(\mathbf{k}_0 \cdot \mathbf{x} - \omega_0 t)}| \gg \left| \int d\mathbf{x}' \frac{\mathbf{E}_0}{|\mathbf{x}' - \mathbf{x}|} e^{i[\mathbf{k} \cdot \mathbf{x}' - \omega_0(t - |\mathbf{x}' - \mathbf{x}|/c)]} n_e(\mathbf{x}') r_e \right| \quad (3.30)$$

where $\mathbf{k} = \sqrt{\epsilon}\mathbf{k}_0$. Let us now develop the condition $|k| \ll |k_0|$. By assuming a Fourier decomposition of the perturbed density fluctuation, Eq.3.28, in the first order Born approximation, states that the first order scattered field can be written as

$$\mathbf{E}_1(\mathbf{x}, t) = r_e \sum_{\mathbf{k}} e^{-i[\omega_0 \pm \omega(\mathbf{k})]t} \int d\mathbf{x}' E_0 \frac{1}{|\mathbf{x}' - \mathbf{x}|} e^{i\mathbf{k}_0 \cdot \mathbf{x}'} e^{i(\omega_0 \pm \omega(k))|\mathbf{x}' - \mathbf{x}|/c} \hat{n}_{\mathbf{k}} e^{\pm i\mathbf{k} \cdot \mathbf{x}'} \quad (3.31)$$

where the $\mathbf{k} = 0$ component corresponds to the first term in the r.h.s. of Eq.3.39, while all the others to the second term.

In the far-field detection limit we can approximate $|\mathbf{x}' - \mathbf{x}|$ by the constant x_0 in the denominator of the integrand, the average distance between the interaction region and the detecting plane, and if we also consider an infinite integration domain, the integral simplifies further as the exponential function reduces to the delta function, and we are left with the Bragg selection rule to first order for the scattered frequency, ω_1 , and wave number, \mathbf{k}_1 :

$$\mathbf{k}_1 = \mathbf{k}_0 \pm \mathbf{k} \quad \omega_1 = \omega_0 \pm \omega. \quad (3.32)$$

By writing

$$(\mathbf{k}_1 - \mathbf{k}_0) \cdot (\mathbf{k}_1 - \mathbf{k}_0) = \mathbf{k}^2 \quad (3.33)$$

imposing the condition $k_1 \simeq k_0$ we find

$$1 - \cos(\theta_{B,\mathbf{k}}) = \frac{k^2}{2k_0^2} \quad (3.34)$$

or

$$1 - 2\sin^2(\theta_{B,\mathbf{k}}/2) = 1 - \frac{k^2}{2k_0^2} \quad (3.35)$$

which then implies that the Bragg scattering angle θ_B is equal to

$$\theta_{B,\mathbf{k}} = 2 \arcsin \left(\frac{|\mathbf{k}|}{2|\mathbf{k}_0|} \right) \quad (3.36)$$

therefore electrons contribute in phase to the first order scattered field only at the Bragg scattering angles, at any other angle the averaged contribution is zero and the information on the perturbed density is lost.

Fluctuation wave numbers have a finite, though small, component along the beam direction because the integration volume is not infinite: if the integration length along the probing direction is L , the associated broadening in wave vector space is approximately equal to $2\pi/L$ and the simultaneous existence of positive and negative scattering orders for a given fluctuating \mathbf{k} cannot exist unless the following condition is satisfied

$$\frac{k}{k_0} \leq \frac{\delta k_z}{k} \Rightarrow L \leq 2\pi \frac{k_0}{k^2} \quad (3.37)$$

which is called the *Raman-Nath* condition. In the opposite limit, called the *Bragg* regime, only one scattering order exists.

Considering the line integral along the probing beam propagation direction, this reduces to

$$\lambda_0 r_e \int dx n_e(x) \ll 1 \quad (3.38)$$

provided that $\omega_{pe} \ll \omega_0$.

In the case that all these approximations are valid we can write the cumulated phase shift between two arbitrary spatial points, \mathbf{a} and \mathbf{b} , as

$$\phi = k_0 \int_{\mathbf{a}}^{\mathbf{b}} \bar{N}(\mathbf{x}) \cdot d\mathbf{x} \simeq k_0 \int_{\mathbf{a}}^{\mathbf{b}} dx \left(1 - \frac{\omega_{pe}^2}{2\omega_0^2} \right) = k_0 |\mathbf{b} - \mathbf{a}| - \int_{\mathbf{a}}^{\mathbf{b}} dx \lambda_0 r_e n_e(x) \quad (3.39)$$

whose fluctuating component is then given by

$$\tilde{\phi} = \lambda_0 r_e \int_{\mathbf{a}}^{\mathbf{b}} dx \tilde{n}_e(x) \quad (3.40)$$

which, by virtue of 3.38, is necessarily much smaller than 1 rad.

3.2 Theoretical treatment of gaussian beam propagation

The phase contrast principle was first proposed in 1932 by the dutch physicist Frits Zernike [1] who, for this study, was awarded the Nobel prize for physics in 1953. In 1930, Zernike was conducting research into spectral lines and discovered that the so-called ghost lines, that occur to the left and right of each primary line in spectra created by means of a diffraction grating, have their phase shifted from that of the primary line by 90 degrees. It was at a Physical and Medical Congress in Wageningen in 1933 that Zernike first described his phase contrast technique in microscopy, which was later extended by himself to test the surface figure of concave mirrors. His discovery lies at the base of the first phase contrast microscope, built during World War II.

Before describing the phase contrast principle, let us first recall a few definitions and theorems [2]. A system of curves filling a spatial region without intersecting is called a *congruence* if one and only one curve passes through each point of the region. The congruence is said to be *normal* if there exists a family of surfaces which cut all the curves orthogonally. If each curve of the congruence is a straight line, then the congruence is said to be *rectilinear*.

Let us additionally recall that light rays are defined as the orthogonal trajectories to the geometrical wave-fronts S , the solution of the eikonal equation. The following theorem of Malus and Dupin holds

Theorem. *A normal rectilinear congruence remains normal after any number of reflections and refractions*

whose corollary is that the optical path length between any two orthogonal surfaces, i.e. wave-fronts, is the same for all rays. The Malus-Dupin theorem is also known as the principle of equal optical path and implies that the orthogonal trajectories, i.e. geometrical wavefronts, of a set of normal congruences generated by successive reflections and refractions are all *optically parallel* to one another.

Let us consider rays in a homogeneous medium: if they are all generated by a point, the cutting surfaces are spherical and the rays are said to form a *homocentric pencil*. After a reflection or a refraction, it is in general not true that the normal congruence will remain a homocentric pencil and, therefore, the cutting surfaces are not spherical anymore. This is in general due to the shape of the refracting surface or to the refractive index being dependent on the rays' wavelength, if their spectrum is not monochromatic. The deviation from a sphere of the wave-fronts is generally called *aberration*.

Let us now consider a point $P(\mathbf{r})$ in a physical medium characterized by the refractive index $n(\mathbf{r})$; if there exists a point $Q(\mathbf{r})$ where an infinite number of rays departing from P converge, then Q is defined as the *sharp image* of P and the points P and Q are said to be conjugate.

From the definition of image and the Malus-Dupit theorem it follows that

Theorem. *In any aberration-free imaging system, the optical path length of all rays originating from any point in the object plane is equal*

This theorem is at the basis of any imaging system.

Let us recall, from chapter 2 Sec.4.5, that in the case of small phase shifts, scattered and unscattered components are dephased by $\pi/2$; the Phase Contrast principle consists of introducing an additional $\pi/2$ phase shift which makes the scattered signal linear in the scattered phase shift (Eq.2.61)

$$P_s = |E_{\phi_0}|^2 [1 \pm 2 \sin(\tilde{\phi})] \quad (3.41)$$

This formula was derived by assuming an infinite plane wave; we will now relax this approximation by taking into account the formalism of diffraction theory. To propagate, in vacuum, the electric field of an e-m wave from a given point $P_0 \equiv \{x_0, y_0, z_0\}$ to another point $P \equiv \{x, y, z\}$, we can consider only the time-independent part of a strictly monochromatic scalar field

$$V(\mathbf{r}, t) = E(\mathbf{r})e^{-i\omega_0 t} \quad (3.42)$$

which allows us to solve the problem by considering only the Helmholtz equation

$$(\nabla^2 + k_0^2)E(\mathbf{r}) = 0 \quad (3.43)$$

where $k_0 = \omega_0/c$. The solution is given, in the approximations formulated by Kirchhoff and later formalized by Sommerfeld, by the Fresnel-Kirchhoff integral

$$E(x, y, z) = \frac{i}{\lambda_0} \iint dx_0 dy_0 \frac{E(x_0, y_0, z_0)}{r} e^{-ik_0 r} \cos(\theta) \quad (3.44)$$

where r is the distance between the two points and θ is the angle formed by the vector PP_0 and the direction of propagation, which is assumed to be along the z axis. It can be noted how Eq. 3.44 is the mathematical expression of the Huygens principle, with each wavelet originating in the plane $z = z_0$ de-phased by $\pi/2$ with respect to the incident beam.

In the paraxial approximation, i.e. when the wave is supposed to propagate at small angles θ , we then write the distance, r , between any two points as

$$r = \sqrt{(x - x_0)^2 + (y - y_0)^2 + (z - z_0)^2} \simeq (z - z_0) + \frac{(x - x_0)^2 + (y - y_0)^2}{2(z - z_0)} \quad (3.45)$$

which, in a cosine directors picture, translates into the following order conditions, in the Taylor development, to neglect higher order contributions to the cumulated phase

$$\frac{1}{8} z \frac{k_{\perp}^4}{k_0^3} \ll 1, \quad \frac{1}{8} z \frac{k_{\perp}^4}{k_0^3} \ll \frac{1}{2} z \frac{k_{\perp}^2}{k_0} \Rightarrow \frac{1}{4} \frac{k_{\perp}^2}{k_0^2} \ll 1 \quad (3.46)$$

the Fresnel-Kirchhoff integral, neglecting first order terms in the amplitude of each wavelet, then becomes

$$E(x, y, z) = \frac{ie^{-ik_0(z-z_0)}}{\lambda_0(z-z_0)} \iint dx_0 dy_0 E(x_0, y_0, z_0) e^{-ik_0(\mathbf{x}_{\perp} - \mathbf{x}_{\perp,0})^2/2(z-z_0)} \quad (3.47)$$

searching for self-similar solutions the normalized electric field can then be written as

$$E(x, y, z) = \sqrt{\frac{1}{\pi w(z)^2}} e^{-ix_{\perp}^2 k_0/[2q(z)]} e^{-i(k_0 z + \psi(z))} \quad (3.48)$$

with the complex beam parameter q defined as

$$\frac{1}{q(z)} \equiv \frac{1}{R(z)} - i \frac{\lambda}{\pi w(z)^2} \quad (3.49)$$

the beam half-width given by

$$w(z) = w_0 \sqrt{1 + \left(\frac{z}{z_R}\right)^2} \quad (3.50)$$

the wave-front radius of curvature expressed as

$$R(z) = z + \frac{z_R^2}{z} \quad (3.51)$$

and the Gouy phase shift $\psi(z)$ equal to

$$\psi(z) = \arctan\left(\frac{z}{z_R}\right) \quad (3.52)$$

where $z_R \equiv k_0 w_0^2/2$ is the Rayleigh distance, which is the distance a gaussian beam travels from its waist to increase its width by $\sqrt{2}$.

More general possible solutions of the paraxial equation are expressed, in cartesian coordinates, as Hermite-Gaussian modes [25]

$$E_{nm}(x, y, z) = \sqrt{\frac{1}{\pi w(z)^2}} \sqrt{\frac{e^{-i2(n+m+1)\psi(z)}}{2^{n+m} n! m!}} e^{-ik_0 x_{\perp}^2/[2q(z)]} \times \\ e^{-ik_0 z} H_n\left(\frac{\sqrt{2}x}{w(z)}\right) H_m\left(\frac{\sqrt{2}y}{w(z)}\right) \quad (3.53)$$

which, being mutually orthogonal, form a basis for the expansion of a general solution of the paraxial approximation

$$E(x, y, z) = \sum_{n,m} c_{n,m} E_{n,m} \quad (3.54)$$

Laser beams are usually generated in the first, symmetric, “00” mode which, therefore, will be the only solution treated in this thesis. This is the mode described by Eq.3.48, i.e., the lowest order TEM₀₀ collimated Gaussian beam. This means assuming all the coefficients $c_{n,m}$ in Eq.3.54 to be zero but $c_{0,0}$. In particular for a gaussian beam of power P_0 and half-width w_0 , the electric field at the waist, $z = 0$, in the plane perpendicular to its propagation direction can be expressed as

$$E(\mathbf{x}_{\perp}) = \sqrt{\frac{2P_0}{\pi\epsilon_0 w_0^2}} e^{-(x_{\perp}/w_0)^2} \quad (3.55)$$

whose Fourier transform is

$$\hat{E}(\mathbf{k}_{\perp}) = \int d\mathbf{x}_{\perp} E(\mathbf{x}_{\perp}) e^{-i\mathbf{k}_{\perp} \cdot \mathbf{x}_{\perp}} = \sqrt{\frac{2\pi P_0 w_0^2}{\epsilon_0}} e^{-(k_{\perp} w_0/2)^2} \quad (3.56)$$

The gaussian beam will pass through an aperture stop, which in general is the smallest optic the beam passes through or is reflected by, supposed to be circular with radius a . If the gaussian beam passes through an aperture, Eq. 3.47 holds but needs to be evaluated over the surface area of the opening. The relative widths of the beam and of the aperture essentially determine to what extent the beam will be diffracted. Ideally one should have

an aperture much larger than the Gaussian width to minimize diffraction and an aperture as small as possible for port accessibility: the best compromise is shown in Sec. 3.10 to consist of an aperture approximately equal to the full Gaussian width.

3.3 Imaging properties of the Phase Contrast technique

Let us derive, in a similar fashion to [3], the imaging properties of the Phase Contrast technique. Let us model the imaging system as an ABCD matrix [4], which expresses, in the paraxial approximation, the distance of a ray from the optical axis, r , and its inclination with respect to it, θ , at the output plane of a generic optical element, namely o , as linear functions of the corresponding parameters at the input plane, i :

$$\begin{bmatrix} r_o \\ \theta_o \end{bmatrix} = \begin{bmatrix} A & B \\ C & D \end{bmatrix} \begin{bmatrix} r_i \\ \theta_i \end{bmatrix} \tag{3.57}$$

If we consider propagation in a medium characterized by a refractive index n and length L , followed by a focusing optic of focal length f , the corresponding ABCD matrix is given by

$$\begin{bmatrix} 1 & 0 \\ -\frac{1}{f} & 1 \end{bmatrix} \begin{bmatrix} 1 & \frac{L}{n} \\ 0 & 1 \end{bmatrix} = \begin{bmatrix} 1 & \frac{L}{n} \\ -\frac{1}{f} & 1 - \frac{L}{fn} \end{bmatrix} \tag{3.58}$$

which has a determinant of unity. Since an imaging system can be modelled by a set of successive propagations-focusing optics, the overall ABCD matrix, by Binet's theorem, is equal to

$$\begin{bmatrix} M & 0 \\ C & 1/M \end{bmatrix} \tag{3.59}$$

where C depends on the details of the optical system whose transverse magnification is M .

It is possible to recover the electric field distribution at the image plane

$$E(M\mathbf{x}_\perp, z_{im}, \omega_s) = \frac{1}{M} e^{i\frac{\omega_s}{c} \left(z_{im} - z_{obj} + \frac{(M-1)^2 x_\perp^2}{2(z_{im} - z_{obj})} \right)} E(\mathbf{x}_\perp, z_{obj}, \omega_s) \tag{3.60}$$

where ω_s is the scattered frequency and the subscripts im and obj indicate the image and the object plane, respectively. This equation can be derived by applying the Fresnel-Kirchhoff integral at each lens and free-space propagation. The phase shift term represents the cumulated phase shift, in the paraxial approximation (see Eq. 3.45), by a ray connecting points \mathbf{x}_\perp in the object plane and $M\mathbf{x}_\perp$ in the image plane.

As the Phase Contrast is an imaging technique, it is desirable that the phase shift does

not depend on the spatial position in the object plane; therefore the following condition is required

$$\frac{\omega(M-1)^2 w_0^2}{2c(z_{im} - z_{obj})} \ll 1 \quad (3.61)$$

where we considered $|x_\perp| \leq w_0$ and ω is the maximum frequency of the fluctuations; we stress that this equation does not imply a negligible phase shift, rather a phase shift that does not depend on transverse coordinates in the object plane. Therefore we will consider a new temporal coordinate such that the equivalent time delay is zero and will thus be omitted in the following equations.

We will consider furthermore spatial variations of the phase shift induced by the stationary bulk plasma density to be negligible; consequently we will subtract the uniform phase offset induced by the bulk density, since it is irrelevant for the image.

Let us now denote as $T(\mathbf{x}_\perp)$ the phase contrast transfer function introduced by the phase plate, and by $\hat{T}(\mathbf{k}_\perp)$ its spatial Fourier transform. We assume the scattered electric field to induce a small phase perturbation by writing

$$E_s(\mathbf{x}_\perp, t) = E_0(\mathbf{x}_\perp, t)[1 + \imath\tilde{\phi}(\mathbf{x}_\perp, t)] \quad (3.62)$$

The total signal at the image plane can be written as

$$E(M\mathbf{x}_\perp, t) = \frac{1}{M} e^{\imath k_0(z_{obj} - z_{im}) - \omega_0 t} \{T(\mathbf{x}_\perp) \circ A_a E_0(\mathbf{x}_\perp, t)[1 + \imath\tilde{\phi}(\mathbf{x}_\perp, t)]\} \quad (3.63)$$

where A_a accounts for diffraction effects due to the clear aperture of all the optical elements in the optical system and \circ stands for the convolution integral in the \mathbf{x}_\perp plane.

The signal intensity at the image plane is

$$I(\mathbf{x}_\perp, t) = \frac{1}{2} c \epsilon_0 |E(M\mathbf{x}_\perp, t)|^2 \quad (3.64)$$

which can be expanded to first order in $\tilde{\phi}$ to obtain

$$\begin{aligned} I(M\mathbf{x}_\perp, t) &= \frac{c}{2M^2} \epsilon_0 |T(\mathbf{x}_\perp) \circ A_a E_0(\mathbf{x}_\perp, t)|^2(\mathbf{x}_\perp, t) + \\ &\quad \frac{c}{M^2} \epsilon_0 \Im\{[T(\mathbf{x}_\perp) \circ A_a E_0(\mathbf{x}_\perp, t)][T(\mathbf{x}_\perp) \circ A_a E_0(\mathbf{x}_\perp, t)\tilde{\phi}]^*\}(\mathbf{x}_\perp, t) \\ &= I_0(M\mathbf{x}_\perp, t) + \tilde{I}(M\mathbf{x}_\perp, t) \end{aligned} \quad (3.65)$$

where I_0 is the dc intensity while \tilde{I} is the fluctuating signal.

The phase contrast signal collected at detector N is then given by

$$S(M\mathbf{x}_{\perp, N}, t) = \int_{\Sigma_N} M d\mathbf{x}_\perp I(M\mathbf{x}_\perp, t); \quad (3.66)$$

whereas the signal actually measured by the acquisition system at the time instant t_k is the integral of the signal collected at previous time instants weighted by the detector time

response function.

Let us consider a generic phase plate whose transfer function in real space reads

$$T_{PP}(\mathbf{x}_\perp) = C(\mathbf{x}_\perp)e^{i\varphi(\mathbf{x}_\perp)} = A(\mathbf{x}_\perp) + iB(\mathbf{x}_\perp) \quad (3.67)$$

where A and B can be smooth or discontinuous functions of the position on the phase plate surface. Eq.3.65 can be re-written as

$$I_0(M\mathbf{x}_\perp, t) = \frac{\epsilon_0 C}{2M^2} |(A + iB) \circ (A_a E_0)|^2(\mathbf{x}_\perp, t) \quad (3.68)$$

$$\tilde{I}(M\mathbf{x}_\perp, t) = \frac{\epsilon_0 C}{2M^2} \{ [B \circ (A_a E_0)] [A \circ (A_a E_0 \tilde{\phi})] - [A \circ (A_a E_0)] [B \circ (A_a E_0 \tilde{\phi})] \}(\mathbf{x}_\perp, t) \quad (3.69)$$

From Eq.3.69 we can infer that the fluctuating signal will be identically zero if either A or B is identically zero, which implies that no phase shift is introduced by the phase plate. Another particular mathematical case for zero fluctuating signal is $A \equiv KB$, K being a constant.

Let us now consider the phase plate depicted in Fig. 3.1; its transfer function is given by

$$\hat{T}_{PP}(k_x, k_y) = H(|k_x| - k_c) - H(|k_x| - k_m) + i\sqrt{\rho}[1 - H(|k_x| - k_c)] \quad (3.70)$$

where H is the step function, k_c is the low cut-off limit, k_m is the high cut-off limit and

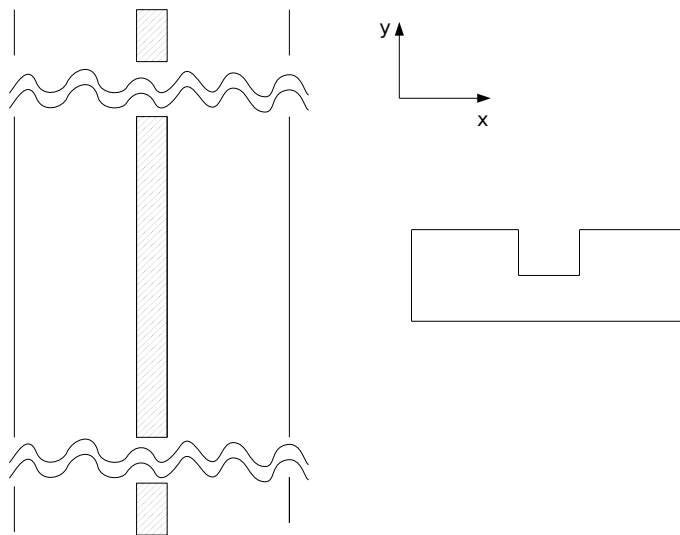


Figure 3.1: (Left) Schematic top view of the reflective phase plate considered in the calculations. the phase groove is depicted as a full region. Squiggly lines model an infinite length. (Right) Lateral view

ρ is the phase groove reflectivity. This model of the phase plate is equivalent to assuming a phase plate large enough to collect the whole scattered spectrum and a low-pass filter,

possibly in another focal point of the imaging system, to cut all the components above the Nyquist frequency of the detector array, k_m . This model is also appropriate in the case where the detectors are made of a linear array and sample only a band of the probing beam which is narrow compared to the curvature of an arbitrarily shaped phase plate. In real space this translates into

$$T_{PP}(x, y) = \frac{\sin(k_m x)}{\pi x} \delta(y) - (1 - \nu\sqrt{\rho}) \frac{\sin(k_c x)}{\pi x} \delta(y) \quad (3.71)$$

If we define a the aperture width, the fluctuating signal is given by

$$\begin{aligned} \tilde{I}(M\mathbf{x}_\perp, t) = & \frac{c\epsilon_0\sqrt{\rho}}{2M^2} \times \\ & \left[\int_{-a}^a dx' \frac{\sin[k_c(x-x')]}{\pi(x-x')} E_0 e^{-(x'/w_0)^2} \int_{-a}^a dx' \frac{\sin[k_m(x-x')] - \sin[k_c(x-x')]}{\pi(x-x')} E_0 e^{-(x'/w_0)^2} \tilde{\phi}(x') \right. \\ & \left. - \int_{-a}^a dx' \frac{\sin[k_c(x-x')]}{\pi(x-x')} E_0 e^{-(x'/w_0)^2} \tilde{\phi}(x') \int_{-a}^a dx' \frac{\sin[k_m(x-x')] - \sin[k_c(x-x')]}{\pi(x-x')} E_0 e^{-(x'/w_0)^2} \right] \end{aligned} \quad (3.72)$$

If one considers an infinite phase plate, the term $\sin(k_m x)/(\pi x) = \delta(x)$ and the above expression reduces to Eq.2.148 of [3]. Let us now consider spatially homogenous fluctuations such that

$$\tilde{\phi}(\mathbf{x}_\perp, t) = \hat{\phi}(\mathbf{k}, t) \cos(\mathbf{k} \cdot \mathbf{x}_\perp + \phi_0) \quad (3.73)$$

if we consider only the center of the gaussian beam and, for simplicity $\phi_0 = 0$, we can write an approximate transfer function in Fourier space (i.e. the ratio between the measured signal and the phase fluctuation, with proportionality constants dropped) as

$$\begin{aligned} T(\mathbf{k}) = & \int_{-a}^a dx \frac{\sin(k_c x)}{\pi x} e^{-(x/w_0)^2} \int_{-a}^a dx \frac{\sin(k_m x) - \sin(k_c x)}{\pi x} e^{-(x/w_0)^2} \cos(\mathbf{k} \cdot \mathbf{x}) + \\ & - \int_{-a}^a dx \frac{\sin(k_c x)}{\pi x} e^{-(x/w_0)^2} \cos(\mathbf{k} \cdot \mathbf{x}) \int_{-a}^a dx \frac{\sin(k_m x) - \sin(k_c x)}{\pi x} e^{-(x/w_0)^2} \end{aligned} \quad (3.74)$$

Let us consider, as already done in [3], the following two dimensionless parameters $Q = k_c w_0/2$ and $\alpha = w_0/a$; we will further assume a fixed phase plate aperture, independently of Q and α . In general the aperture width, i.e. a , is constrained by the geometry of the problem, that is by the space available in the vessel ports. Instead k_c and k_m are given by the phase plate and are therefore constrained, in the case peculiar dimensions are needed, by manufacturing processes. In Fig.3.2 we show the response properties as a function of Q for $\alpha = 1.2$ and $k_m = 50/w_0$, it can be noted how the signal increases for increasing values of Q , saturating at $Q \simeq 1.8$. Lowering Q at fixed α means smoothing the transfer function, as the phase plate shifts “only“ the non-fluctuating component, but also means eliminating part of the Local Oscillator (LO) power thus reducing the signal. In Fig.3.3 it is shown how lowering α at fixed Q translates into progressively reducing the diffraction effects as the gaussian beam is less and less truncated, while by increasing α we approach the limit of a truncated plane wave characterized by an Airy-pattern. Larger values of α at fixed Q mean smaller values of k_c , thus implying a loss of LO power which explains the

decrease in the overall response for $\alpha \leq 1.4$. Smaller values of α at fixed Q imply larger values of k_c , cutting off the long-wavelength response and potentially not allowing access to spatial scales of interest. As a last consideration, we observe that the transfer function is a high-pass filter because, the phase contrast being an internal reference technique, the reference and the probing beam experience the same phase shift induced by the stationary density profile, which is therefore unmeasurable. This concept was anticipated in Chapter 2, Sec. 4.5 when we wrote the approximate response function with respect to the beam scattered by the stationary density profile, E_{ϕ_0} , instead of the actual probing beam, E_0 .

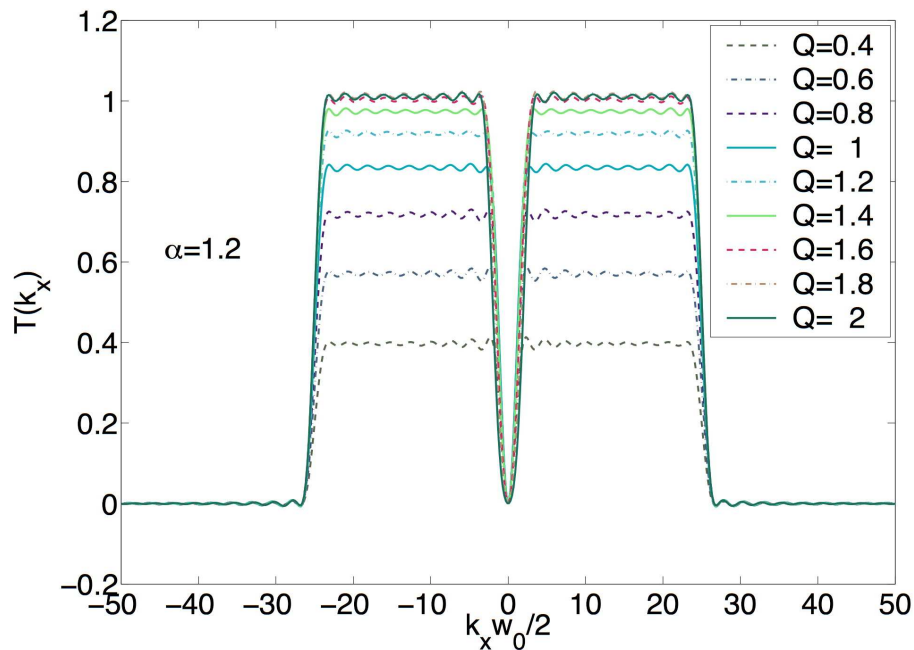


Figure 3.2: Phase contrast transfer function, in the case of truncated gaussian beam and spatial homogenous fluctuations, for a number of values of Q . A fixed high-cutoff $k_m = 50/w_0$ was assumed.

3.4 Imaging conditions

In this section we will briefly evaluate which conditions the phase plate needs to satisfy to guarantee the existence of an image. Looking at Eq.3.65 we can ask ourselves what the required shape of the phase plate is for the system to have an actual transfer function, i.e. to have a fluctuating intensity which can be written as the convolution product of the fluctuating phase and the transfer function

$$\tilde{I}(\mathbf{x}_\perp, t) \propto T(\mathbf{x}_\perp) \circ \tilde{\phi}(\mathbf{x}_\perp, t) \quad (3.75)$$

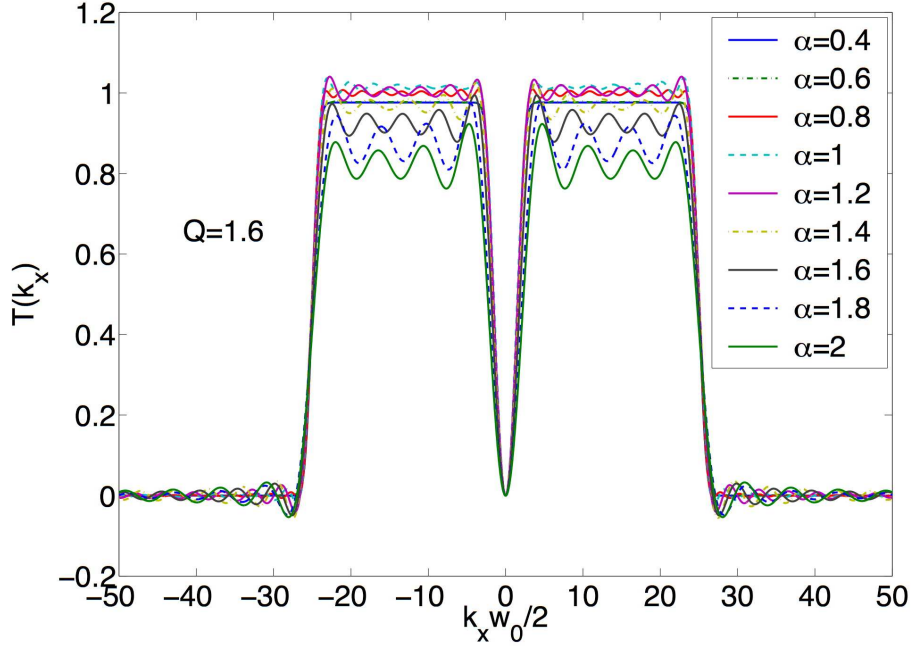


Figure 3.3: Phase contrast transfer function, in the case of truncated gaussian beam and spatial homogenous fluctuations, for a number of values of α . A fixed high-cutoff $k_m = 50/w_0$ was assumed.

with the following properties

$$\hat{T}(\mathbf{k}_\perp) = \hat{T}(-\mathbf{k}_\perp) \quad (3.76)$$

$$\hat{T}(\mathbf{k}_\perp) = 0 \quad \text{for} \begin{cases} |\mathbf{k}_\perp| - k_c \leq 0 \\ |\mathbf{k}_\perp| - k_m \geq 0 \end{cases} \quad (3.77)$$

By assuming again the phase plate geometry of Fig.3.1, an infinite aperture and a plane wave, we obtain

$$\hat{T}(k_x, k_y) = C[H(k_x + k_m) - H(k_x + k_c) + H(k_x - k_c) - H(k_x - k_m)] \quad (3.78)$$

whose inverse Fourier transform is

$$T(x, y) = C \frac{\sin(k_m x) - \sin(k_c x)}{\pi x} \delta(y) \quad (3.79)$$

where C is an arbitrary constant. Let us now consider, for simplicity, the case of a plane wave and infinite aperture; from Eqs.3.67 and 3.69 we derive

$$B_0 A(x) - A_0 B(x) = C \frac{\sin(k_m x) - \sin(k_c x)}{\pi x} \quad (3.80)$$

with

$$A_0 = \int_{-\infty}^{\infty} dx A(x) \quad B_0 = \int_{-\infty}^{\infty} dx B(x) \quad (3.81)$$

Eq.3.80 gives an infinity of solutions of which the most obvious is

$$A(x) = \frac{\sin(k_mx) - \sin(k_cx)}{\pi x} \quad B(x) = \frac{\sin(k_cx)}{\pi x} \sqrt{\rho} \quad (3.82)$$

which is the usual phase plate with phase groove reflectivity equal to ρ (see Eq.3.71).

Another choice is given by

$$A(x) = \frac{\sin(k_mx)}{\pi x} \sqrt{\frac{\rho}{2}} \quad B(x) = \frac{\sin(k_cx)}{\pi x} \sqrt{\frac{\rho}{2}} \quad (3.83)$$

where the presence of the factor $\sqrt{\rho/2}$ permits us to normalise the phase groove reflectivity to ρ . By Fourier transforming we obtain

$$\hat{T}_{PP} = \sqrt{\frac{\rho}{2}} \{H(k_m + k_x) - H(k_m - k_x) + \imath[H(k_c + k_x) - H(k_c - k_x)]\} \quad (3.84)$$

which means that diffracted components are shifted just by $\pi/4$, instead of the usual $\pi/2$. Even though the transfer function is symmetric, its value is reduced by the factor $\sqrt{2}$ with respect to the usual phase contrast.

At last we examine another solution

$$\hat{T}_{PP}(k_x, k_y) = \imath\sqrt{\rho}[H(k_x + k_c) - H(k_x - k_c)] + H(k_x - k_c) - H(k_x - k_m) \quad (3.85)$$

which means measuring only half of the scattered spectrum and the whole unscattered beam. Eq.3.69 becomes, for a perturbation with wave number greater than k_c ,

$$I_0(M\mathbf{x}_\perp, t) = \frac{\epsilon_0 E_0^2 \rho}{2M^2} \quad (3.86)$$

$$\tilde{I}(M\mathbf{x}_\perp, t) = \frac{\epsilon_0 E_0^2 \sqrt{\rho}}{2M^2} T(x) \circ \tilde{\phi} \quad (3.87)$$

where

$$T(x) = \frac{\sin(k_mx) - \sin(k_cx)}{2\pi x} \delta(y) \quad (3.88)$$

the transfer function is then given by

$$\hat{T}(k_x, k_y) = \frac{H(k_m + k_x) + H(k_m - k_x) - H(k_c + k_x) - H(k_c - k_x)}{2} \quad (3.89)$$

which is equal to the response of the phase contrast divided by two, in intuitive agreement with the argument that only half of the scattered spectrum is collected. Let us evaluate the signal also in the case of a gaussian beam and infinite aperture; the unscattered signal is equal to

$$I_0(M\mathbf{x}_\perp, t) = \frac{\epsilon_0 E_0^2}{2M^2} \left\{ \rho \text{Erf}^2(Q) + \frac{1}{4} [\text{Erf}(Q') - \text{Erf}(Q)]^2 \right\} \quad (3.90)$$

while the fluctuating signal can be written as

$$\tilde{I}(M\mathbf{x}_\perp, t) = \frac{\epsilon_0 E_0^2 \sqrt{\rho}}{2M^2} \times \left[-\text{Erf}(Q') \frac{\text{Erf}(Q_+) + \text{Erf}(Q_-)}{2} + \text{Erf}(Q) \frac{\text{Erf}(Q'_+) + \text{Erf}(Q'_-)}{2} \right] \quad (3.91)$$

where $Q = k_c w_0/2$, $Q_\pm = (k_c \pm K)w_0/2$, $Q' = k_m w_0/2$, $Q'_\pm = (k_m \pm K)w_0/2$ and we assumed again $\tilde{\phi}(x) = \hat{\phi}(K) \cos(Kx + \phi_0)$. Taking the limit $k_m \rightarrow \infty$, $\text{Erf}(Q') = \text{Erf}(Q'_\pm) = 1$ and Eq.3.91 is one half of Eq.2.141 of [3].

Let us now numerically integrate the case of a gaussian beam and finite aperture of half-width w_0 equal to a and a phase plate such that $Q = 1.5$ and $Q' = 15Q$, which is the Nyquist limit for a thirty element linear detector. Let us consider three purely sinusoidal perturbations with wave-vectors such that $kw_0/2 = \{0.175 \ 15.75 \ 26.25\}$, respectively below k_c , between k_c and k_m and above k_m . The normalised phase contrast response is plotted in Fig.3.4

If we now take a set of one hundred sinusoidal modes with random phases, amplitudes and

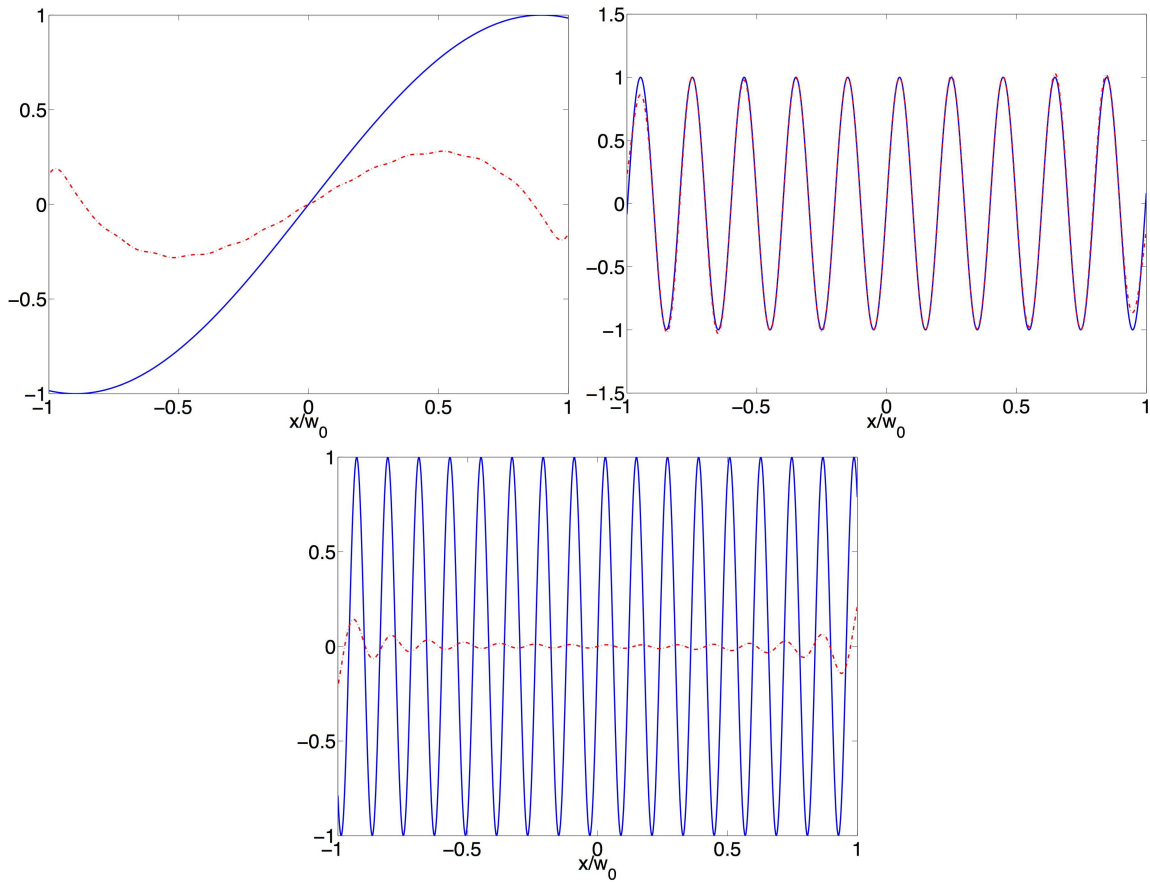


Figure 3.4: Pure sinusoidal input (blue-full) and normalised PCI response (red-dashed) for three wave numbers respectively below lower cut-off, in passband and above cut-off, from left to right.

wave-vectors, resulting in the spectrum plotted in Fig.3.5a, the PCI signal distribution becomes closer and closer to the real spatial distribution as the phase plate becomes wider and wider to collect all the scattered components: in Fig.3.5b,c,d we show the reconstruction for $k_m w_0/2 = \{22, 80, 200\}$.

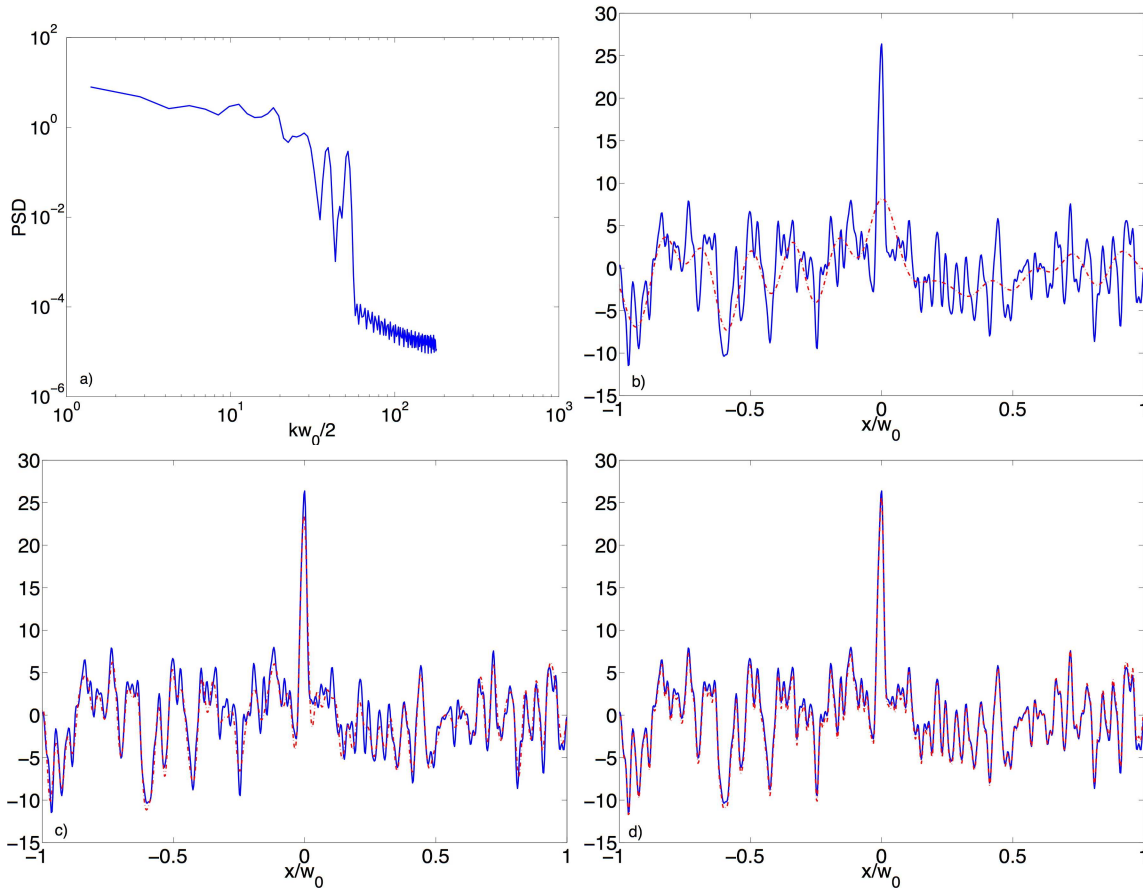


Figure 3.5: a) Power spectral density of randomly distributed input sinusoids. (b,c,d) Real space representation of (a) (blue-full) vs. normalised Phase Contrast response (red-dashed) with phase plates such that $k_m w_0/2 = \{22, 80, 200\}$, respectively.

3.5 Localization Properties of the Tangential Phase Contrast technique

3.5.1 Basic principle

It is widely accepted, in view also of some experimental evidence [6], that in magnetized plasmas fluctuations are aligned along the magnetic field, i.e. the parallel wave vector is much smaller than the perpendicular one. Thus, since the phase contrast technique, being intrinsically line-integrated, is sensitive only to fluctuations perpendicular to the laser

beam direction of propagation, one can only measure fluctuations which lie in a plane perpendicular to both the magnetic field line and to the beam direction. This identifies, at each location along the beam path, a precise angle formed by the measured fluctuation wave vector with a given reference vector in the beam wave-front plane [7]. Since this angle can be selected by spatial filtering on a focal plane, if it is a single-valued, monotonic and steep function of a linear coordinate along the laser beam path, it is indeed possible to select an effective integration length which is much shorter than the whole path travelled by the laser beam inside the plasma. We will treat this point in greater detail in the following section.

Let us try to understand this concept with an idealized example. Let us consider a current-free plasma (we are not concerned here with MHD equilibrium) and a tangential injection parallel to the mid-plane. If the probing beam direction is parallel to the toroidal field direction, before the tangency point between the probing beam and the flux surface, the projection of the magnetic field line on the beam wave-front will always be on the mid-plane, forming an angle of 0 degrees with the horizontal direction. After the tangency point, the aforementioned projection will always form an angle equal to π ; in these two regions the Phase Contrast technique is sensitive only to vertical scattering wave vectors. At the tangency point, the probing beam and the toroidal field are exactly parallel, resulting in a degenerate point for the projection; therefore the technique is sensitive to the entire scattering wave vector spectrum in the wave-front plane. The resulting projection is depicted in the right part of Fig. 3.6. The selected fluctuating wave vector is orthogonal to the direction of the projection and is thus vertical.

3.5.2 Expected localization in TCV

If we now consider a real equilibrium, the poloidal field will somehow smear out the discontinuity at the tangency point, resulting in a smooth curve. However, as we seek as steep a function as possible, the tangential launching should have a slight vertical component in order to match the pitch angle of the magnetic field. In Fig.3.7 we show, for a real TCV equilibrium, two different integration lengths resulting from selecting a region close to the tangency point or away from it.

As we have already noticed, this steepness is primarily caused by the spatial variation (curvature) of the toroidal field direction and is therefore only weakly affected by the plasma current profile, as can be seen in Fig. 3.8. In fact, in the case considered, a difference in magnetic shear (defined as the logarithmic gradient of the safety factor normalized to the minor radius) of about 0.85 results in a variation of only a few centimeters in the integration length, which in turn translates into a difference of a few millimeters in radial

resolution.

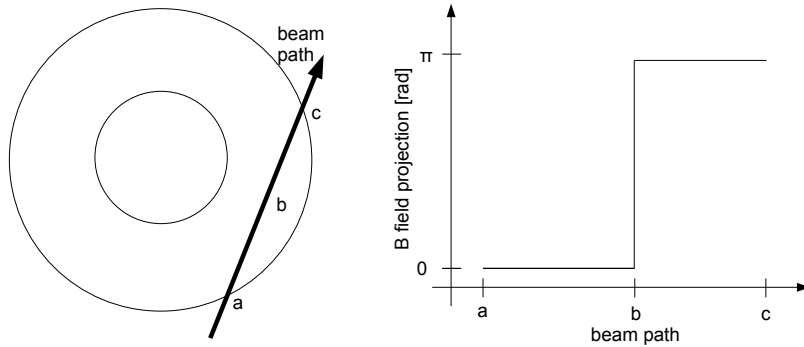


Figure 3.6: Angle between the projection of the magnetic field line onto the wave front and the outgoing horizontal direction as a function of the position along the beam path in the idealized case of a current-free plasma and tangential injection parallel to the midplane. Points a and c stand for the beginning and the end of the plasma, while b stands for the tangency point between the probing beam and the magnetic field line, assumed to be in the counter-clockwise direction.

The actual localization is better understood in terms of a radial plasma coordinate, which for us is the normalized square root of the plasma volume. In addition to the steepness of the angle as a function of the linear beam coordinate, a second effect contributes to the radial localization of the measurement: at the tangency point between the magnetic surface and the probing wave vector, a significant fraction of the laser beam path stays close to the tangency flux surface; in other words, the linear beam coordinate is also a steep function of ρ since at the tangency point, according to Eq.2.12, $\delta\rho \propto L^2$, where L is the integration length. The two effects combined result in the angle being an extremely steep function of ρ at this location, as shown in Fig. 3.9. Here, the different curves refer to different vertical (a) and horizontal (b) plasma positions in the vacuum vessel; it is clear that by displacing the plasma in the vacuum vessel, a good resolution can be achieved at virtually all values of ρ .

The steep behavior remains even if the tangency point does not happen to occur on the mid-plane, as can be seen in Fig.3.10a which refers to several vertical plasma positions in the vacuum vessel, even though the best resolution region then moves along the beam path.

It is interesting to see now the actual resolution as a function of ρ in terms of ρ itself. To do this, we adopt a spatial filter with an angular resolution of 60 degrees (see Sec.3.5.3), which allows marginal resolution near the cut-off wave number. We will see in the next section that this value could be made smaller for larger wave number cut-offs, resulting

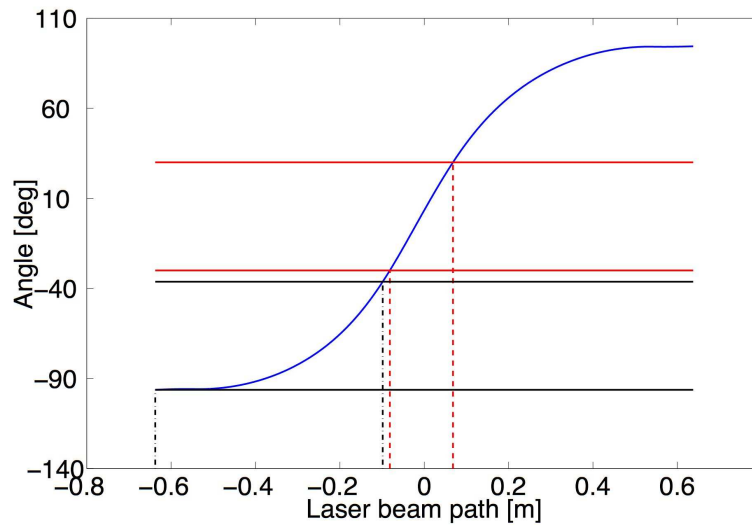


Figure 3.7: Selected fluctuation wave-vector direction, with respect to the horizontal, as a function of the distance along the beam path. The two boxes delimited by the black dash-dotted and red dashed vertical lines show, respectively, examples of poor and good spatial resolution. The width of each region is limited by diffraction.

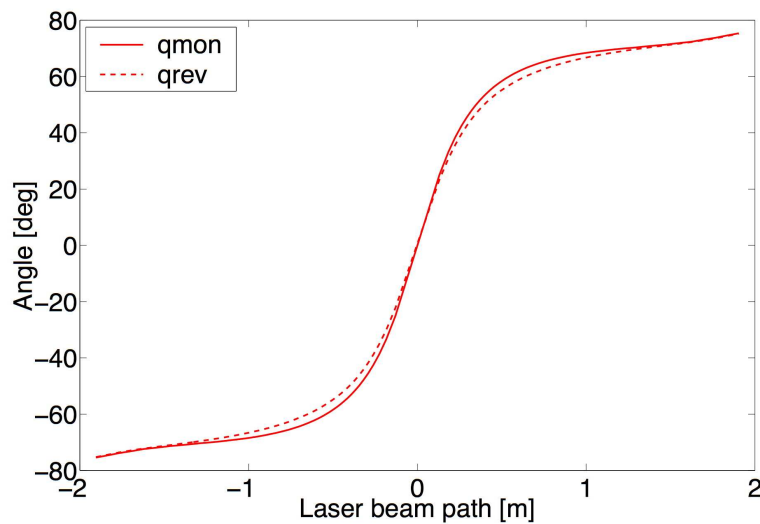


Figure 3.8: Effect of the current profile on the selected fluctuation wave-vector direction, illustrated by a comparison of two model q profiles: a monotonic profile (solid line) and a profile with central negative shear (dashed line). At the tangency point the shear is equal to 0.01 and -0.85 respectively. The resulting difference in the integration length is approximately 3.4 cm, translating into a negligible difference in radial resolution.

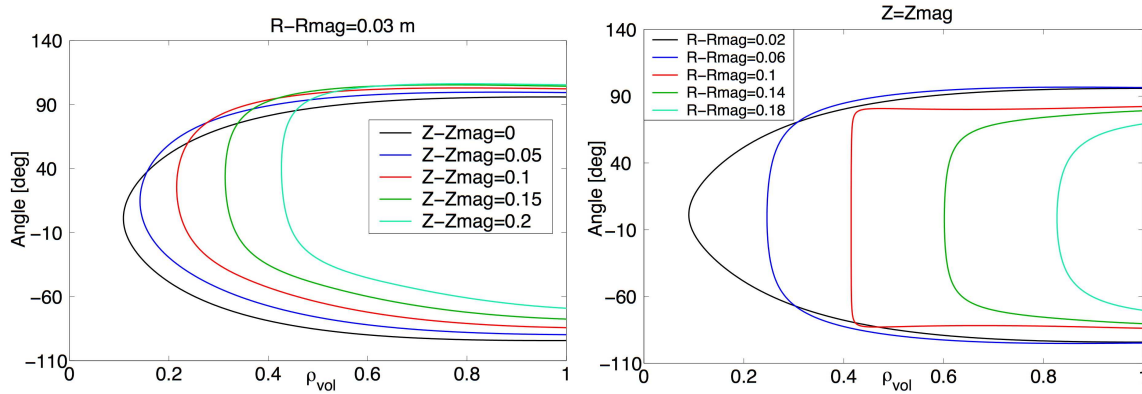


Figure 3.9: (Left) Direction of possible measurable fluctuations, expressed as an angle relative to a fixed direction in the laser wave-front plane, as a function of ρ for a vertical scan in the poloidal section. At the mid-path point the laser beam passes through the mid-plane (solid black) and vertically shifted from it by 5 (dotted blue), 10 (solid red), 15 (dashed-dotted darkgreen) and 20 (solid lightgreen) cm. (Right) Same as (left) but in the case of a horizontal scan from 2 cm on the LFS of the magnetic axis with 4 cm steps. The case $R - R_{mag} = 0.1$ was chosen to match almost exactly the magnetic field pitch angle at the tangency point.

in even better resolution.

In Figs.3.10 and 3.11 we show the resolution for the same cases plotted in Fig.3.9; the resolution $\Delta\rho$ at the tangency point is in the range $0.01 \div 0.05$.

We already mentioned how, at the tangency point, where the beam is tangent to the magnetic surface but not necessarily to the magnetic field line, the sampled fluctuations are radial, i.e. a purely radial k_ρ is selected; however, it is interesting to see whether the poloidal component could be measured in other regions of the beam path and, more important, to which extent the tangential PCI suffers from a mixing of radial and poloidal wave vectors as a result of the finite spatial resolution of the measurements and of the selected direction (the wave vector in the lab frame being fixed and determined by the spatial filter). Indeed, while the spatial filter selects a given wave-number direction in the laboratory frame, its poloidal projection onto the physically meaningful radial and poloidal directions will generally change at different locations along the beam. This direction is always purely radial at the tangency point, as shown in Figs.3.12(a,b) and 3.13(a,b). The finite, though short, integration length also results in some degree of wavenumber mixing between radial and poloidal components, depicted as an uncertainty in Fig. 3.12(c); this is calculated as the difference between the maximal and minimal components of k_ρ along the integration length corresponding to each point.

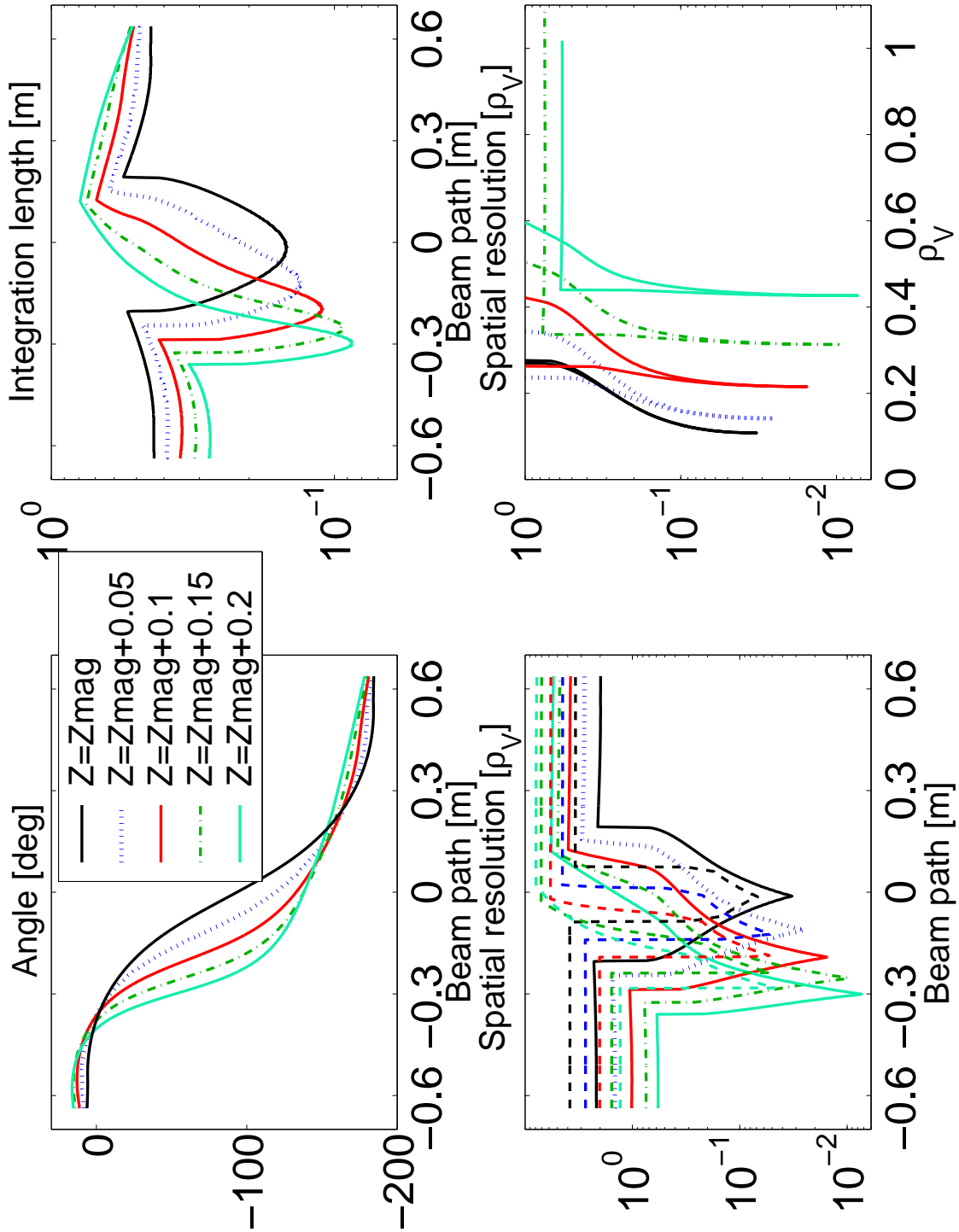


Figure 3.10: a,b,c) As a function of the distance along the laser beam path (in meters), the angle of the chosen fluctuations, the integration length and the spatial resolution are shown for a scan in the vertical distance between the laser beam and the plasma midplane at the half-way point along the beam path. d) Spatial resolution expressed as ρ_V as a function of ρ_V itself. Calculations refer to the central ray of a beam which, at the half-way point, is shifted 4 cm towards the LFS with respect to the magnetic axis and to a minimum $k_{\perp} = 0.9 \text{ cm}^{-1}$, corresponding roughly to $k_{\perp}\rho_i = 0.45$. In box (c) the dashed lines represent the virtual resolution, expressed as the poorest resolution over the beam full-width.

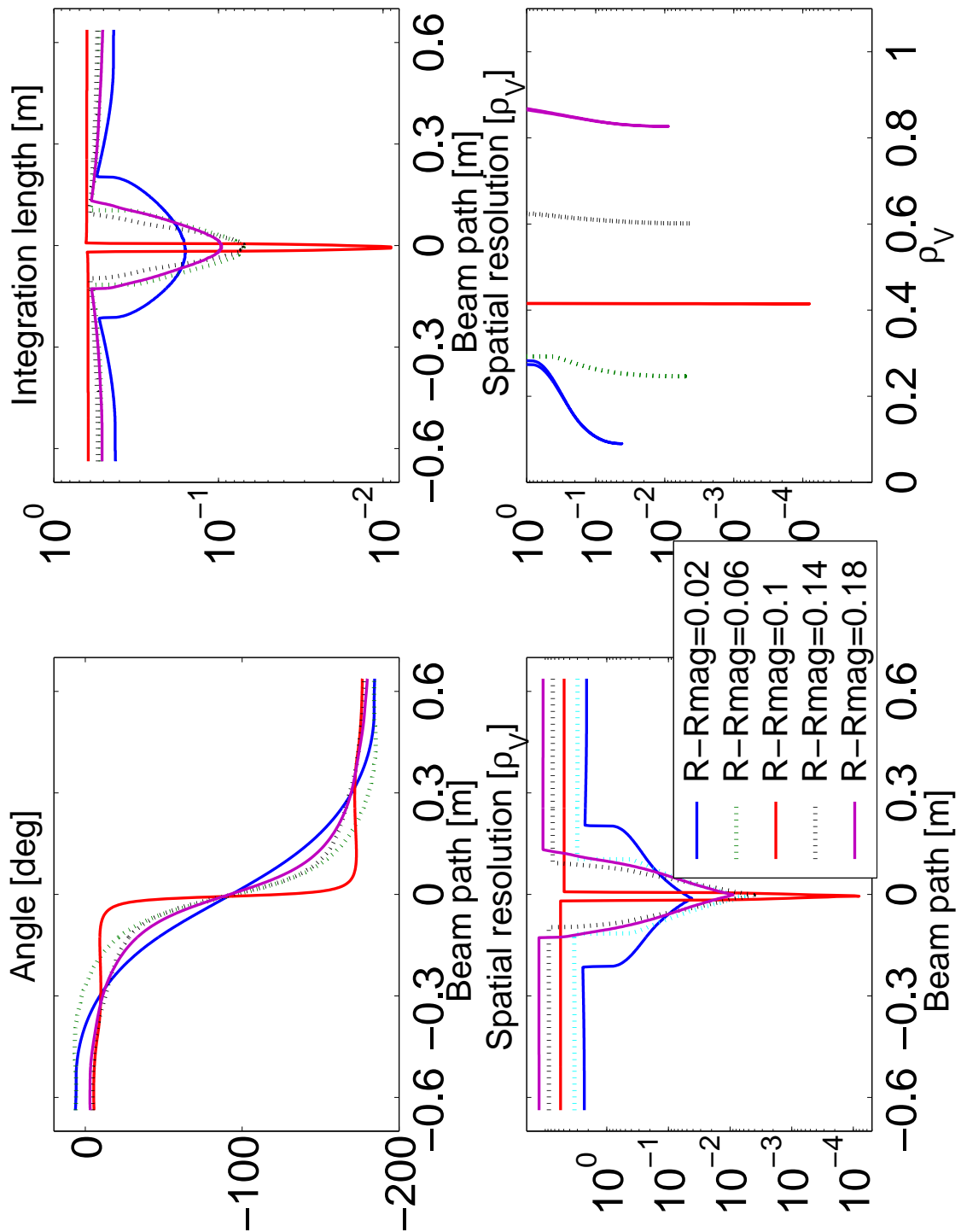


Figure 3.11: Same as figure 3.10 but for a radial scan.

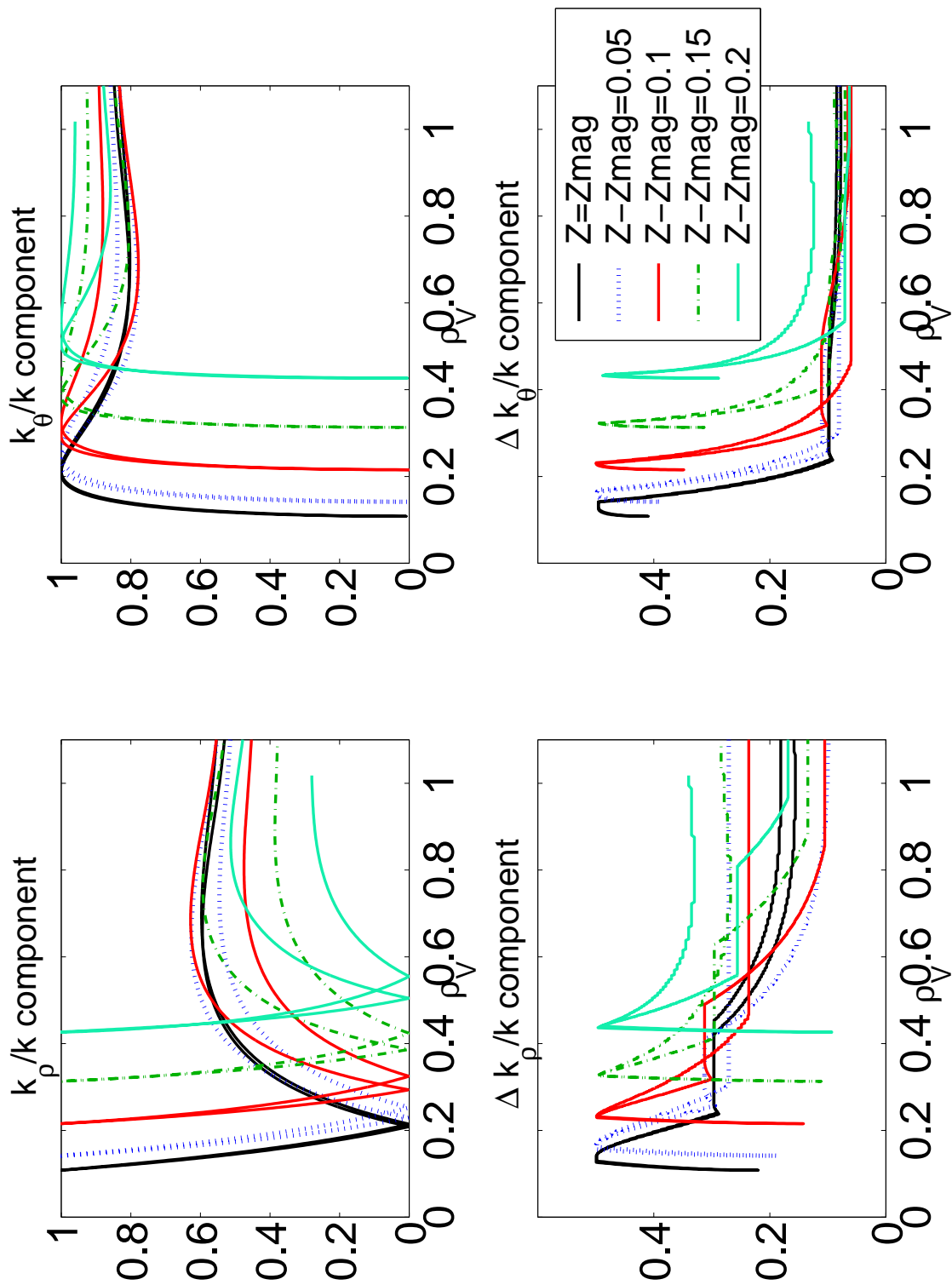


Figure 3.12: Radial and poloidal k components, and their uncertainties as functions of ρ_V for the same configuration of Fig.3.10. Uncertainties are computed as $\Delta(k_{\rho,\theta}/k)$ along the integration length.

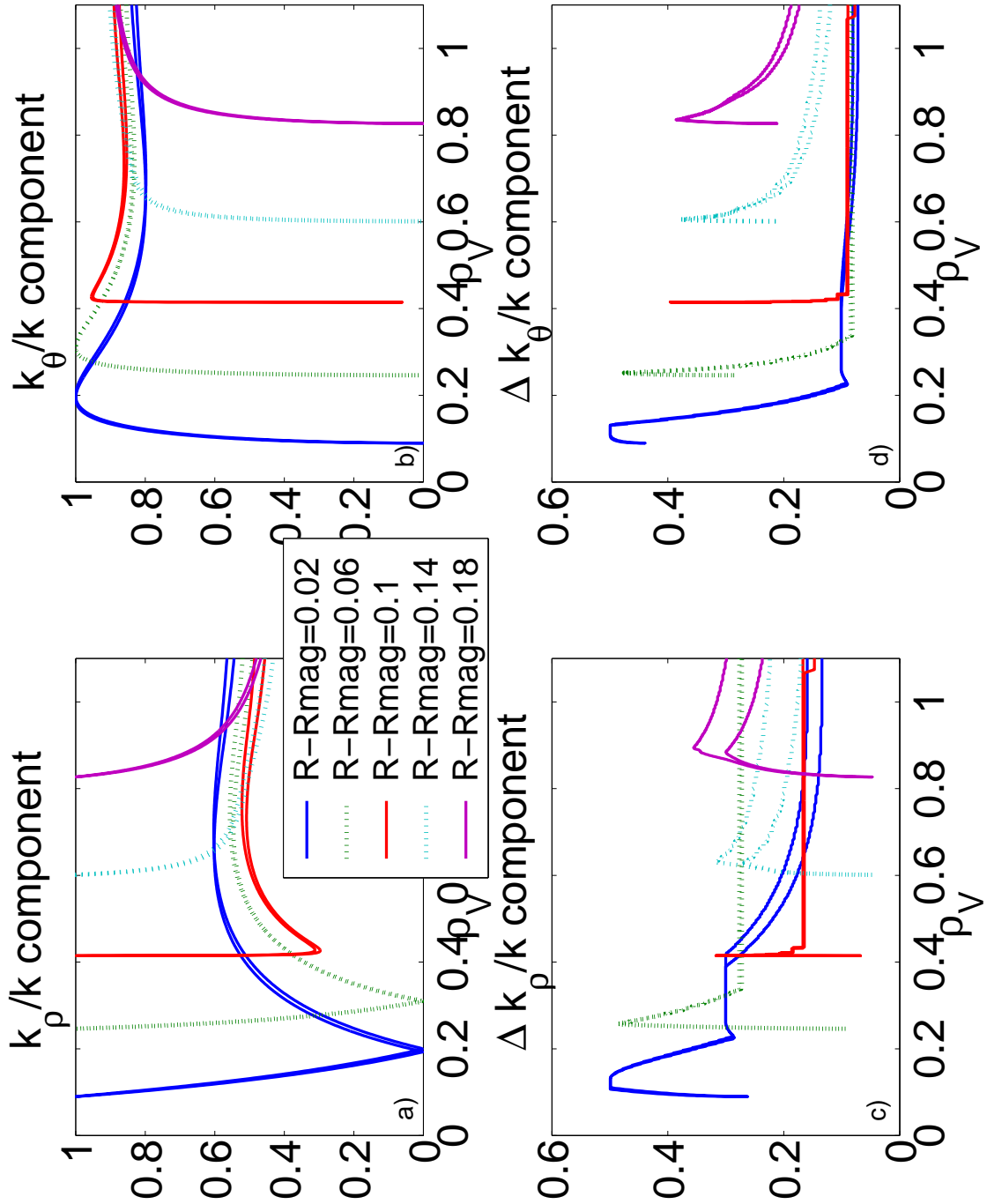


Figure 3.13: Same as Fig.3.12 but for a radial scan. The case $R - R_{\text{mag}} = 0.1$ was chosen to match almost exactly the magnetic field line pitch angle at the tangency point.

3.5.3 Spatial filter

The previous section explains how it is possible to localize measurements by selecting a particular range of fluctuation directions; in this paragraph we will describe in detail the required procedure.

An optical imaging system is usually made of focusing elements, lenses or mirrors, and thus usually possesses at least one focal plane. The spatial distribution of the electric field in the focal plane corresponds to its spatial Fourier transform. In particular, the azimuthal angular position of each scattered wavelet in the focal plane corresponds to the direction of the generating scattering wave-vector in the plane of the beam wavefront; and the radial position is linear in the diffracting angle, i.e. in the ratio of magnitudes of the scattering wave-vector to the probing beam wave-vector. Since, as was explained in Sec.3.5.1, in the tangential, field-line following configuration, the orientation of the scattering wave-vector unambiguously corresponds to a particular position along the beam path, a spatial selection can be made by filtering on the focal plane of the imaging system. The filtering is done by positioning in a focal plane a mask which allows only part of the radiation to reach the detector plane (Figure 3.14). According to the direction along which the filter is aligned, one obtains the desired angle and thus the location from which the signal originates. Because of the finite dimensions of the focal spot, dictated by diffraction, the spatial filter must have a finite width, which translates into the angular range illustrated in Figure 3.7. This angular width is a function of the wave number and is the angle subtended, on the focal plane, by the diffraction spot centered on that wave number as seen from the focal point (filter center). In case of a gaussian beam with half-width w calculated at the e^{-2} point on the focusing optics, the resulting resolution angle $\Delta\alpha$ is given by

$$\Delta\alpha = 2 \arctan \left(\frac{M^2 2}{kw} \right) \quad (3.92)$$

where $M^2 \simeq 1$ is the correction factor which accounts for a non-ideal gaussian nature of the probing beam and is defined such as the half divergence of a gaussian beam of wavelength λ and half-waist w_0 is $\theta = M^2 \lambda / (\pi w_0)$. Thus, the achievable resolution improves with k ; the worst-case scenario is given by the lower-cutoff wave number, which in an optimized configuration is given by $k_{cutoff} \simeq 3/w_0$, giving a resolution of approximately 60 degrees.

Two possible configurations may be considered for the spatial filter, as depicted in Figure 3.14. In the first one, on the left part of Fig.3.14, the resolution is optimized for all wave numbers as the filter width is just large enough to accommodate the spot size, thus is not uniform over the spectral range since it shrinks for higher k values. This distorts the spectral response since the interaction region is different for different wave numbers. In the second configuration, on the right of Fig.3.14, the achievable resolution is artificially

decreased linearly with k ; thus the angle bandwidth, and consequently the integration length, is constant over the whole spectral range.

For the PCI diagnostic we chose to manufacture both types of filters depicted in Fig.3.14

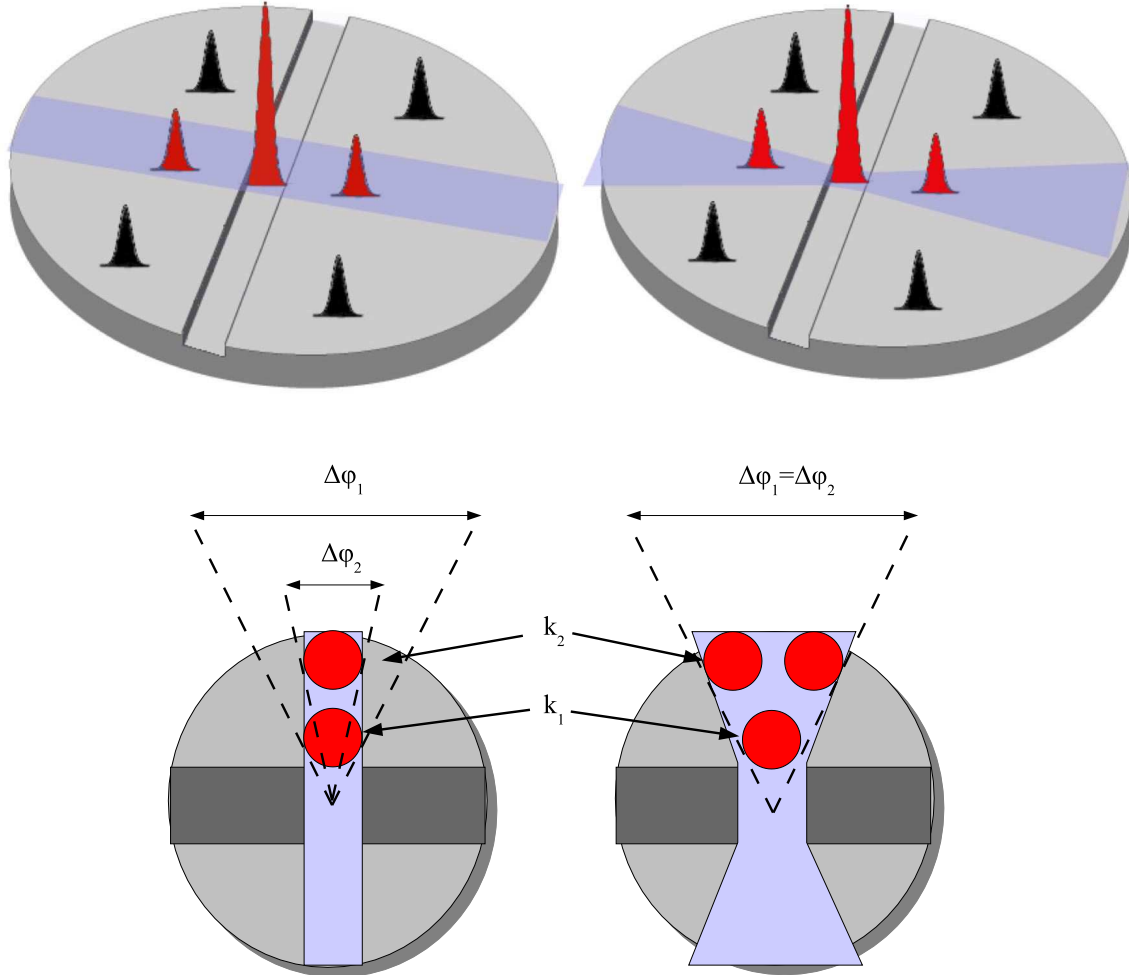


Figure 3.14: Fluctuation direction selection by means of a spatial filter, depicted as a light blue band, superimposed on the PCI phase plate, in gray. (Top) Only the undiffracted component and diffracted ones impinging on the filter, all depicted in red, are sampled by the system; other diffracted components, in black, are not selected. (Bottom) Schematic view of both configurations explaining the effect of the filter shape on spatial resolution. The maximum resolution at each wave-vector is indicated; on the left this varies with the wave vector whereas the configuration on the right features uniform resolution.

for each of the two values of the optical magnification planned for the optical system (see following sections) and for each of the phase groove widths of the two phase plates available at CRPP. The filter itself is made of stainless-steel, black chrome-plated to reduce specular reflectivity, with a diameter of 50.6 mm and 0.5 mm thickness. The required width tolerance per unit slit length is $1\mu\text{m}/\text{mm}$, which is a standard value for slits. The

minimal width of the filters is chosen at $1/e^2$ of power with an accuracy of 0.02 mm on the full width. An example of the resulting design is shown in Fig.3.15.

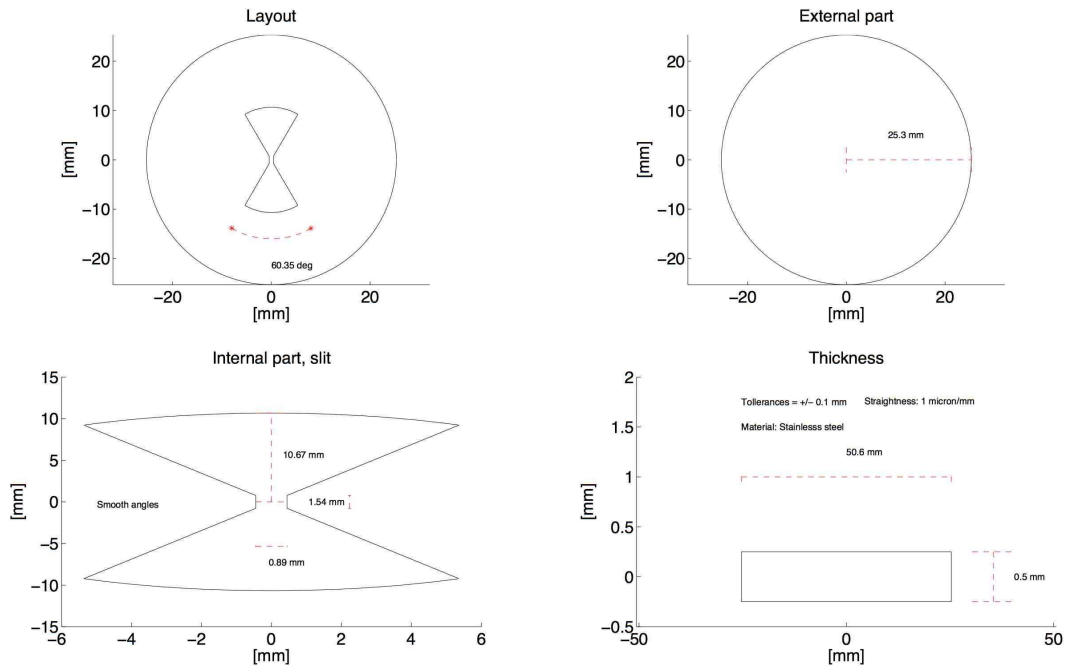


Figure 3.15: Example of the uniform response spatial filter to be used in the low magnification case with a phase groove width of 0.4 mm.

3.6 Experimental set-up

In this section we will describe in detail the experimental apparatus installed on the TCV tokamak; in particular we will consider the optical design and all the constraints imposed by the TCV torus and its hall. Additionally we will describe most of the optical and mechanical parts which compose the PCI diagnostic on TCV. First we will briefly overview optical properties of mirrors and lenses as well as a few details concerning radiation detectors.

3.6.1 Optical properties

Usually formulae used in optics refer to perfect surfaces of a given kind, e.g. spherical for lenses or flat for windows and non focusing mirrors; however, optics' surfaces are manufactured within a given tolerance which, in general, depends primarily on the size of the optic and on the substrate material. Tolerances are specified on the uniformity of the shape and on its cosmetic appearance. The maximum allowable deviation of an optical surface from its ideal shape is described by a parameter called Surface Accuracy, which

can be described in several ways:

Surface Flatness

It is the deviation for a planar surface such as a window or a mirror. When a test plate, which is a clear flat reference, is held in contact with the optic under examination and they are both illuminated, a contour map is visible as light and dark bands called Newton's rings or fringes. Due to the air gap between the surfaces, each ring corresponds to the vertical distance between the test plate and the surface under inspection. Since the air gap is very small, the surface flatness is defined in terms of wavelength: e.g. 1/4 wave or $\lambda/4$. The spacing between rings is equal to one-half the wavelength of the illumination source, i.e. 1/4 wave = 1/2 ring. Monochromatic laser green light at 546.1 nm or red light at 632.8 nm are generally used for illumination. Typically, only values less than 1/4 wave are considered to designate precision optics and values less than one tenth to be high precision.

Sometimes surface flatness is also measured by a parameter called *roughness*, which is quantified by the vertical deviation of a real surface from its ideal form. If this deviation is large, the surface is rough; if it is small the surface is smooth. This deviation can be measured in several ways

$$R_a = \frac{1}{n} \sum_{i=1}^n |z_i|$$

$$R_{RMS} = \sqrt{\frac{1}{n} \sum_{i=1}^n z_i^2}$$

$$R_v = \min_i z_i$$

$$R_p = \max_i z_i$$

$$R_t = R_p - R_v$$

$$R_{sk} = \frac{1}{nR_{RMS}^3} \sum_{i=1}^n z_i^3$$

$$R_{ku} = \frac{1}{nR_{RMS}^4} \sum_{i=1}^n z_i^4$$

of which the most common is the average definition, R_a .

When the surface under examination is not flat, e.g. a parabolic mirror, air gaps should be regular and map the height of the surface $z = z(x, y)$ on the $\{x, y\}$ plane. Irregularities are used to define how the surface deviates from the required shape; such deviations are also known as *Surface Figure*.

Surface quality

Surface Quality refers to the cosmetic features of an optical element in terms of visually permissible defects on the element's surface, and is quantified by the so called Scratch-Dig specification. During the grinding and polishing stages of fabrication, small defects can occur, such as scratches and digs. A scratch is any mark or tear and a dig is any pit or divot on the element's surface. The specification used for the maximum allowable flaws is denoted by a combination of numbers, the scratch number followed by the dig number; for example 60-40. The lower the number, the higher the level of quality. For example, a 60-40 value is common for research and industrial applications, whereas a 10-5 value represents a high quality standard for laser applications. These values do not actually correspond to a specific number of defects, but rather reflect the quality of an optical surface by means of comparisons. Developed in response to the need for an accessible, inexpensive product for inspection personnel, this is often employed as an easy to use reference tool. Although this tool reflects Scratch and Dig evaluation as defined by the U.S. Military Specification for the Inspection of Optical Components, *MIL-O-13830A*, it is not certified to national or international standards.

There is no direct correlation between scratch number and the actual size of a scratch on an optical element's surface. As a common reference, the scratch number relates to the "apparent" width size of an acceptable scratch. However, there is some ambiguity since this also includes the total length and number of allowable scratches. Dig numbers do relate to a specific size of dig. For example, a 40 dig number relates to a 400 μm diameter pit. Coating quality is also held to the same Scratch-Dig specification as the surface of an optic. Surface Quality inspection typically includes additional criteria, such as staining and edge chips. Overall cosmetic inspection also includes defects within the material, such as bubbles and inclusions, including striae. Imperfections of this nature can contribute to scattering in systems involving lasers and image defects. Inspection of surface accuracy and quality is limited to the component's clear aperture.

Clear aperture

The size of an optical element, such as mirrors, lenses and windows, does not correspond to the actual reflecting or refracting surface usable. In fact, surface quality and accuracy are specified over a smaller area centered on the optics, which is referred to as Clear Aperture. Outside the clear aperture, the optics may not behave as specified due to imperfections in the polishing and/or in the coating procedure. Standard values of clear apertures are typically between 80% and 90% of the diameter, if circular, or of the linear dimension, if other than circular, of the optical element. Values beyond 90% are generally not to be trusted.

Edge treatment

There are several terms associated with the treatment of edges. The most basic is a cut edge, which is literally what it means: a large sheet of glass is either "cut" using a scribe and break technique or cored for circular pieces, which can leave sharp edges. The next edge type is swiped or seamed edges which means that all the sharp edges are removed. The final type is a ground edge which provides an even mounting surface and gives a uniform cosmetic appearance to the perimeter of the optic. The better the treatment of the edge, the less likely it is that it may become chipped in handling. Edge chips are not permitted within the optics' clear aperture. Edge chips are typically defined for optical windows and mirrors to have maximum values of 0.25 to 0.5mm. Bevels are clean ground edges used to prevent edge chips or simply as protective chamfers. Bevels are generally defined as maximum face widths at 45° , with a standard tolerance of $\pm 10^\circ$.

Surface figure requirement

All the errors in each optical element contribute to the total deterioration of the image. A useful criterion to account for this *global* effect is the Rayleigh quarter-wave criterion, which allows a maximum deviation, also called Optical Path Difference (OPD), of one quarter of a wavelength between any point in the image plane and the ideal spherical wave front. Optical elements are usually specified either as root mean squared (rms) or peak-to-valley (p-v), which is between 3.5 and 5 times larger than the corresponding rms value. The total OPD generated by an optical system made of N optical elements is equal to

$$OPD_{rms} = \sqrt{\sum_{i=1}^N [OPD_{i,rms} A_i \Delta n_i \cos(\theta_i)]^2} \quad (3.93)$$

where OPD_i is the surface figure of each optical surface, θ_i the impinging angle, A_i the ratio between the largest surface illuminated by a single point in the object plane to the total surface of the optical element, Δn is the change in the refractive index across each optical surface. The assumption behind this formula is that optical irregularities are assumed to be directly proportional to the surface of the element. The sum is to be calculated over the optics after the interaction of the probing beam with the plasma; irregularities in the optics before the plasma deteriorate the gaussian nature of the probing beam but do not affect the signal.

Considering the surface figure values of all the optical elements and assuming the worst case scenario in the conversion from p-v values to rms values, the PCI has an OPD equal to $\lambda/1288$ for configuration $\mathfrak{A}1$ and $\lambda/166$ for configuration $\mathfrak{A}3$ (see Sec.3.6.9), which largely satisfies the Rayleigh criterion. The inclusion of a cylindrical lens in front of the image plane to enhance the signal on the detector array deteriorates the OPD leading to $\lambda/70$ in configuration $\mathfrak{A}1$ and $\lambda/10$ in configuration $\mathfrak{A}3$, which would then be at the limits

of validity of the Rayleigh criterion.

3.6.2 Detector properties

Sensors used to detect optical radiation are classified in two main groups: photodetectors and thermal detectors. To the first group belong all the detectors based on a direct interaction of radiation with the material lattice; this interaction is detected through changes in associated electrical circuits. To the second group belong all the detectors responding to heating effects caused by incident radiation; once the detector is heated, its temperature change induces some measurable physical parameter change, e.g. a change in the electrical resistance of a conductor or of a superconductor heated above its critical temperature.

The temperature change required by a thermal detector causes a slower response with respect to photodetectors, whose time response generated by pair-hole production-recombination is much faster. Typical response times are \simeq ms for thermal detectors and \simeq μ s for photodetectors.

Since the PCI is expected to measure fluctuations up to a few MHz, only photodetectors are of interest and we will therefore describe only them in the following.

Photoconductive detectors

In a photoconductive (PC) device, incident radiation impinging on a semiconductor releases energy to electrons, raising them into the forbidden energy band, thus enhancing the electrical conductivity of the material. This basic principle is effective only if the incident photon has an energy larger than the energy gap in the semiconductor and lower than the energy required for the photoelectric effect, above which electrons are expelled from the material and cannot contribute to the enhancement of its electrical conductivity. This translates into a spectral response of the material which is therefore not sensitive to radiation whose wavelength is longer than that corresponding to the energy gap or shorter than that corresponding to the photoelectric critical energy. When a bias voltage and a load resistor are used in series with the semiconductor, a voltage drop across the load resistors can be measured when the change in electrical conductivity varies the current flowing through the circuit.

Photovoltaic detectors

In a photovoltaic (PV) device, impinging radiation is absorbed at a p-n junction, producing an electron-hole pair which, in turn, is detected as a voltage. The basic fabrication

technique consists of joining a positively and a negatively doped semiconductor to form a p-n junction, i.e. a diode. The depletion zone in the contact has a width, d , which depends on the total biasing voltage, Φ [5]

$$d = \sqrt{\frac{2\epsilon_0\Phi}{e} \left(\frac{1}{n_p} + \frac{1}{n_n} \right)}, \quad (3.94)$$

n_p and n_n being the doping concentrations in the p and in the n region, respectively. The total voltage is given by

$$\Phi = \frac{k_B T}{e} \ln \left(\frac{n_p n_n}{n_i^2} \right) + \Delta V \quad (3.95)$$

where ΔV is the external biasing voltage, T the temperature and n_i the intrinsic carrier concentration, given by

$$n_i^2 = 4 \left(\frac{2\pi k_B T}{h^2} \right)^3 e^{-E_g/k_B T} (m_h^* m_e^*)^{3/2} \quad (3.96)$$

where m_e^* and m_h^* are the effective masses of electrons and holes, respectively.

If radiation is absorbed outside the depletion region, electrons and holes recombine before being separated by the depletion field and no detection occurs. In the depletion region, since no dopants exist, the incident photon must have an energy larger than the entire energy gap of the substrate material.

Let us now compare PC and PV detectors.

The minimum incident flux a detector can discern depends on the noise level of the detector. In particular if we define the Signal to Noise Ratio (SNR) as

$$SNR = \frac{\Re\Phi}{I_n} \quad (3.97)$$

where I_n is the noise current, Φ the incident power (not necessarily absorbed) and \Re the detector responsivity, we can define the Noise Equivalent Power (NEP) as the incident power which produces a SNR equal to one, in a root mean square sense. The responsivity of a photovoltaic detector is also expressed in terms of quantum efficiency η by

$$\eta = \Re \frac{h\nu}{e} \quad (3.98)$$

where ν is the light frequency.

It was mentioned that detectors are sensitive to particular spectral regions and are characterized by response time constants, therefore the NEP is a function of incident light wavelength and frequency. The NEP depends also on additional parameters such as operating temperature, optimum bias, detector area and noise-equivalent bandwidth. To compare different detectors the *normalized detectivity*, D^* , is defined as

$$D^* = \frac{\sqrt{A_d \Delta f}}{NEP} \quad (3.99)$$

and is customarily quoted in units of $\text{cm}\sqrt{\text{Hz}}/\text{Watt}$.

Several kinds of noise are active in a photo-detector:

- Johnson
- Shot
- Generation-recombination
- $1/f$
- Temperature fluctuation of the background blackbody radiation

Noise powers add and are uncorrelated, therefore their variances add as well, i.e.

$$\Delta N_{total} = \sqrt{\sum_i \Delta N_i^2} \quad (3.100)$$

in general in a PC detector the dominant sources of noise are Johnson, $1/f$, G-R and preamplifier noise; in a PV these are shot noise of the reverse saturation current, photon noise, Johnson noise of the detector resistance and of the load resistance, $1/f$ and preamplifier noise.

In general preamplifier noise can be reduced by selecting Field Effect Transistors (FETs) and by cooling the preamplifier to cryogenic temperatures.

The shot-noise can be written as[5]

$$I_{N,shot} = \sqrt{2e\bar{I}\Delta f} = \sqrt{2e\mathfrak{R}\bar{\Phi}\Delta f} \quad (3.101)$$

the generation-recombination noise current can be expressed by[5]

$$I_{N,G-R} = 2G\sqrt{e\mathfrak{R}\bar{\Phi}\Delta f}; \quad (3.102)$$

the $1/f$ noise is important only at frequencies lower than a few hundred Hz and is therefore filtered by ac amplifiers.

The Johnson noise in each resistor, of resistance R , is given by[5]

$$I_{N,J} = 2\sqrt{\frac{k_B T \Delta f}{R}} \quad (3.103)$$

By combining all the intrinsic noise forms in the D^* parameter and adding shot noise due to the Local Oscillator (LO) power, we can write the minimum detectable phase shift, i.e. the phase shift giving $\text{SNR}=1$, in the approximately constant response spectral region (see Fig.3.2) of the PCI as[3]

$$\tilde{\phi}(\mathbf{x}_\perp) = \frac{1}{C} \sqrt{\left(F_d + \frac{P_{cr}}{\rho P_d(\mathbf{x}_\perp)} \right) \frac{W_0 \Delta f}{P_d(\mathbf{x}_\perp)}} \quad (3.104)$$

where $P_d(\mathbf{x}_\perp) = 0.5A_d\epsilon_0c|E(\mathbf{x}_\perp)|^2$ is the dc power incident on the detector area A_d when the reflectivity of the phase groove ρ , is equal to one; P_{cr} and W_0 are given by

$$P_{cr} = \frac{\eta A_d}{2h\nu D^{*2}} \quad W_0 = \frac{h\nu}{2\eta}, \quad (3.105)$$

$F_d = 1$ for PV detectors and $F_d = 2$ for PC ones, and

$$C = \int_{-a}^a dx e^{-(x/w_0)^2} \frac{\sin(k_c x)}{\pi x} \quad (3.106)$$

Eq.3.104 is valid to 5-10% accuracy when $a = w_0$ and $k_c = 3/w_0$.

3.6.3 Mechanical vibrations

Introduction

In chapter 2 it was stressed how the Phase Contrast is superior to standard interferometry also because, since both the probing and the reference beam pass through the medium under analysis, it is insensitive to mechanical vibrations. Indeed, its insensitivity concerns the signal, in the sense that no contribution to the signal is due to vibrations as it is in standard interferometry. However, the signal itself is sensitive to the alignment of the whole optical system, in particular to the focusing of the unscattered beam on the phase groove; in particular, it was shown in section 3.3 how the transfer function depends on the low-pass wave-vector k_c , i.e. on the phase groove width. Any misalignment would interfere with the correct functioning of the system up to a complete loss of the signal when the beam is focused outside the phase groove and, therefore, to the absence of the required $\pi/2$ phase shift between scattered and un-scattered components. If mechanical vibrations interfered with the alignment they would have to be eliminated or, at least, reduced. If the PCI diagnostic did not require any optics mounted on the vessel, it would be largely insensitive to mechanical vibrations; examples are the PCI diagnostic on the TCA tokamak[8] and on the Alcator C-MOD tokamak [9]. In the opposite case, the PCI requires a closed loop active stabilization system, such as the one on the DIII-D tokamak[3], which we took as reference for our design.

Measurements of TCV vibrations

Four accelerometers were installed on the TCV tokamak to study how the torus vibrates. Three accelerometers were installed in sector 15, central lateral port, in the 3 directions: radial, r , toroidal, ϕ , and poloidal, θ ; to estimate the noise level, the fourth one was positioned on a concrete column at a distance of about seventy centimeters from the torus.

The acquisition system sampled at a rate of 50 kHz, while the accelerometer specifications indicate a linear response up to 5 kHz, which was the highest frequency analyzed. The absolute calibration stated in the specifications was assumed, i.e. 100 mV/g, g being the earth gravity acceleration. To work properly, these accelerometers need a flat and rigid support oriented in the direction of the vibrations to be measured.

Data showed good reproducibility: in Fig. 3.16 we compare two similar stray shots (standard power supply test shots without plasma) for all the channels; indeed they are comparable both in the rms values and in Fourier space. The typical Fourier transform of the

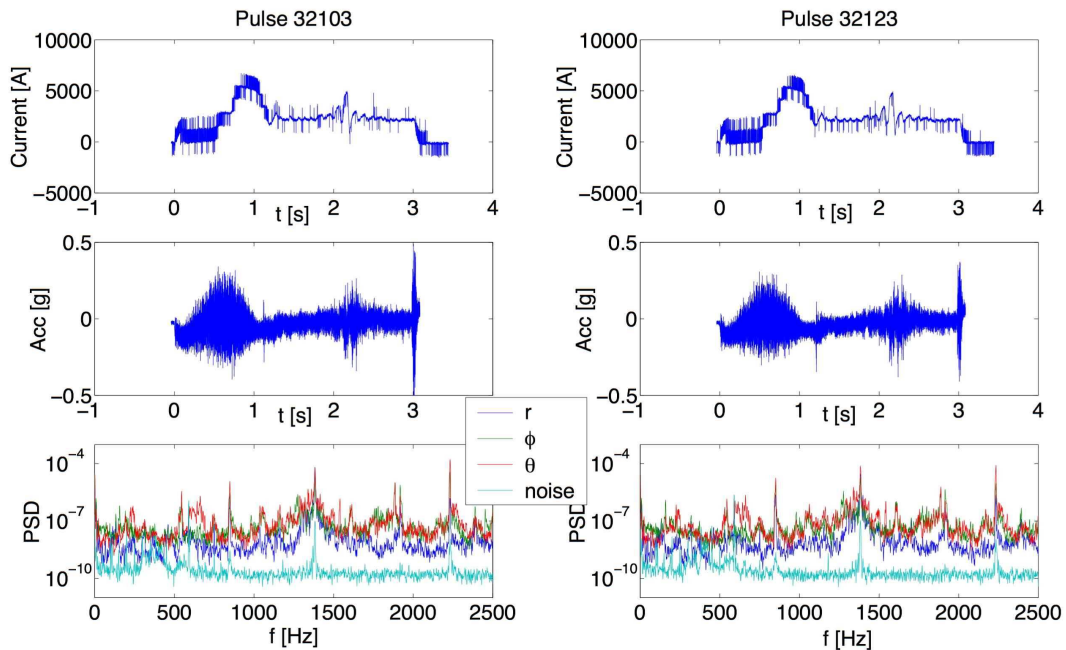


Figure 3.16: Comparison of two different stray pulses in terms of current (top), radial acceleration (center) and Fourier power spectral density of all the accelerometers (bottom).

signals of the four accelerometers sampled during an actual TCV plasma shot is shown in Fig. 3.17, where a dominant peak at about 1.3 kHz is evident. This high frequency mode is due to the rectification of the 3 phase current in the alternator, $\simeq 12 \cdot 110$ Hz, and is present in the noise-test accelerometer as well. This suggests that this vibration is due to electromagnetic pick-up of the accelerometer itself and/or of its cable. Two additional configurations were tested to address this point. The first one had one accelerometer on the torus in the ϕ direction; two (one shielded in an iron box) were mounted on the concrete column used for the noise-test, and the last one was mounted on the opposite side of the column. The results of a typical pulse are shown in Fig. 3.18, where the level of vibration on the torus is still higher, as expected, than elsewhere.

It can be noted how the vibration of the shielded accelerometer is higher than the non-shielded one located at the same position, probably due to a more rigid support provided by the box itself, and that the two non-shielded accelerometers on two sides of the column

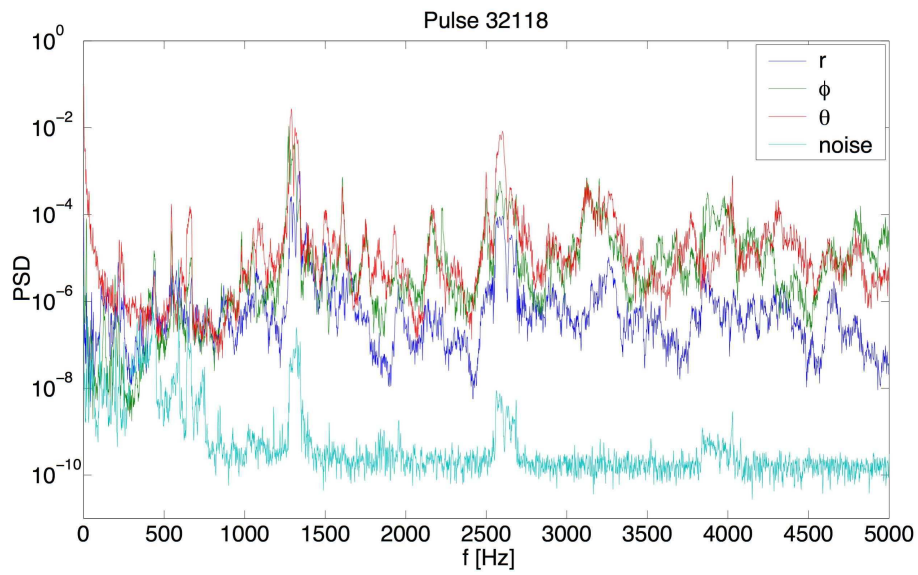


Figure 3.17: Power spectral estimates of accelerometer data.

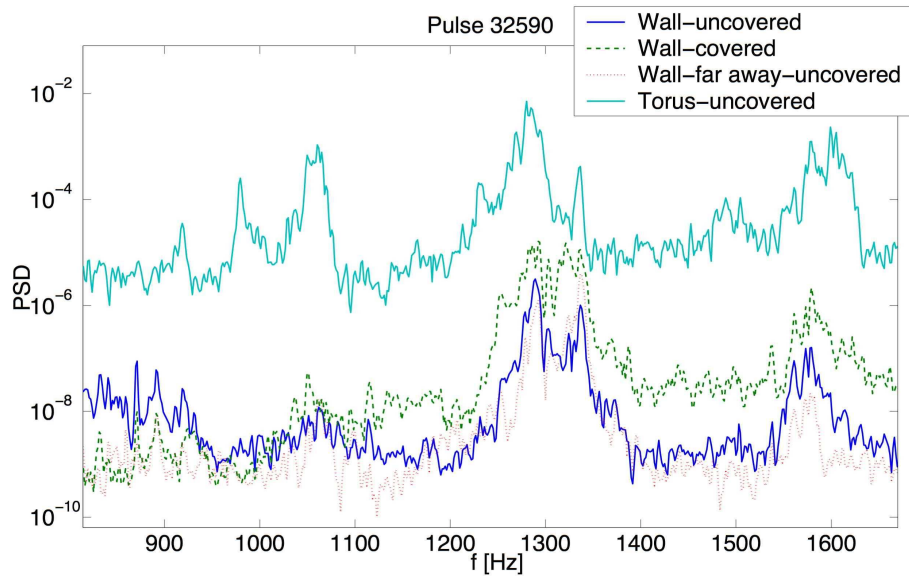


Figure 3.18: Power spectral estimates of accelerometer data in the second configuration described in the text.

have almost the same behavior; this would exclude the hypotheses of EM pick-up of the accelerometer because the one facing the tokamak should collect a larger signal than the one on the opposite side.

The second test configuration had two accelerometers on the torus in the ϕ direction, one shielded in the iron box and one outside; in addition, a third measurement involved a 60 Ohm resistance (equal to the impedance of the accelerometer) connected to the cable in order to measure the pick-up of the cable itself. The fourth accelerometer was again on the concrete column. The result is shown in Fig. 3.19, demonstrating that the EM pick-up of the cable is negligible, while the shielding box reduces the signal somewhat.

To summarize, the signal measured by the accelerometers at all frequencies can be con-

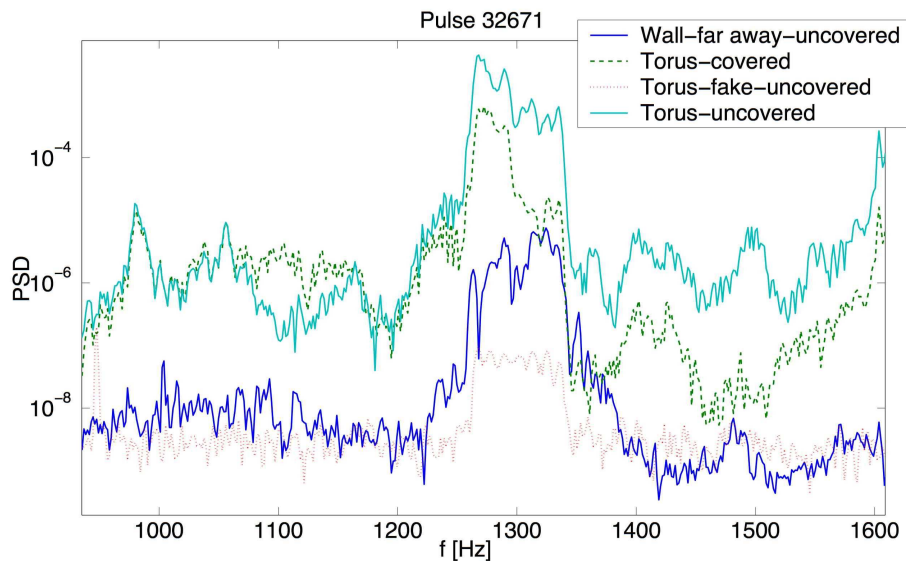


Figure 3.19: Power spectral estimates of accelerometer data in the third configuration described in the text.

sidered as actual vibrations and may be used to estimate the spatial displacement. As will be explained in the next section, the stabilization network response decreases strongly with frequency, so that high-frequency vibrations cannot be actively compensated; this is the reason why we focused on determining the nature of the 1.3 kHz peak. It is therefore important to estimate the actual spatial displacement at all frequencies. This task can be simply performed by filtering the signal and integrating twice over time. In Fig.3.20 we show how vibrations in the range 500-5000 Hz contribute negligibly to the total spatial shift. Additionally, in Fig.3.21 it is shown how the predominant contribution to the total spatial displacement comes from vibrations at 20 Hz. Indeed, by estimating the spatial displacement in the frequency ranges 0-200 Hz and 1200-1400 Hz, we find the following ratios for the accelerometers of configuration 1 (displacement in low-band divided by displacement in high-band): $r = 5.3 \cdot 10^3$, $\phi = 8 \cdot 10^2$, $\theta = 2.8 \cdot 10^3$ and noise= $2.6 \cdot 10^5$. The estimated SNR stays close to 100 also in the low frequency range. A test with a

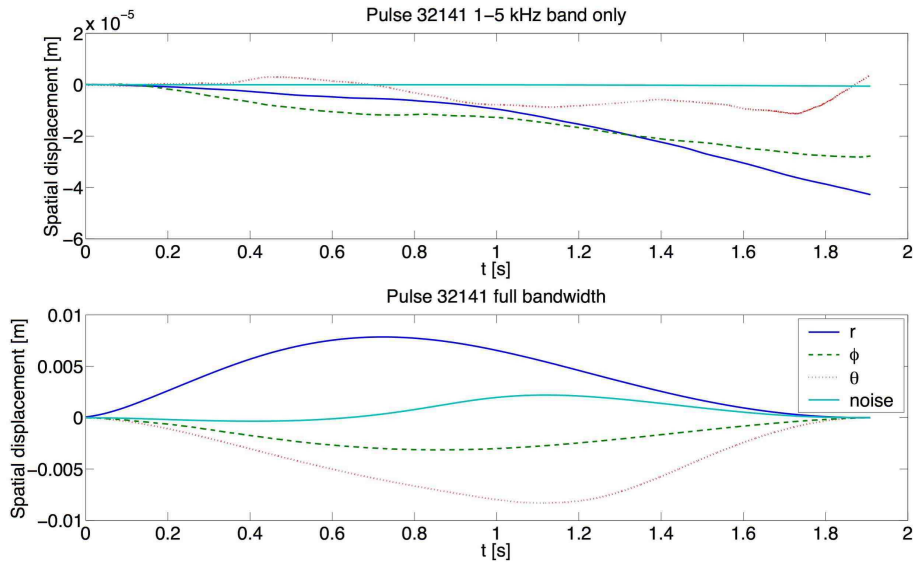


Figure 3.20: Reconstructed spatial displacement due to the whole signal and to the high frequency components only.

visible laser beam was performed on a few TCV pulses by reflecting the laser beam by a mirror mounted to the TCV vessel. After about ten meters from the reflection point, the spatial shift was composed by a steady shift of about one centimeter, due to the torque on the vessel generated by plasma current induction, plus fluctuating vibrations of the order of a few millimeters. By estimating the equivalent steady state shift on the basis of the accelerometers data and their positions at the measurements, one finds shifts of the order of 2 to 3 cm.

Design criteria for the active stabilization system

The goal of the active vibration stabilization system is to keep the focal spot on the phase plate inside the phase groove. Standard systems which address similar problems detect the position of a reference beam on a quadrant detector which is aligned in such a way as to have the beam centered on it when it is in the nominal position which, in our case, is the position of the phase groove on the phase plate. As the beam vibrates, the detector communicates the beam position to an appropriate electronic system which steers a number of mirrors which, in turn, realign the beam in the correct position. Since we need to stabilize the focal spot position on the phase plate plane, the idea is to have two rotatable mirrors, one rotating along the horizontal direction, X, the other along the vertical direction, Y.

The vibration frequency response illustrated in the last section appears very similar to the one measured on the DIII-D tokamak, especially regarding the presence of a dominant peak at 20 Hz. This led to the choice of a similar compensating circuit in terms of electronics, scanning mirrors and position sensing detector. In particular, since a visible

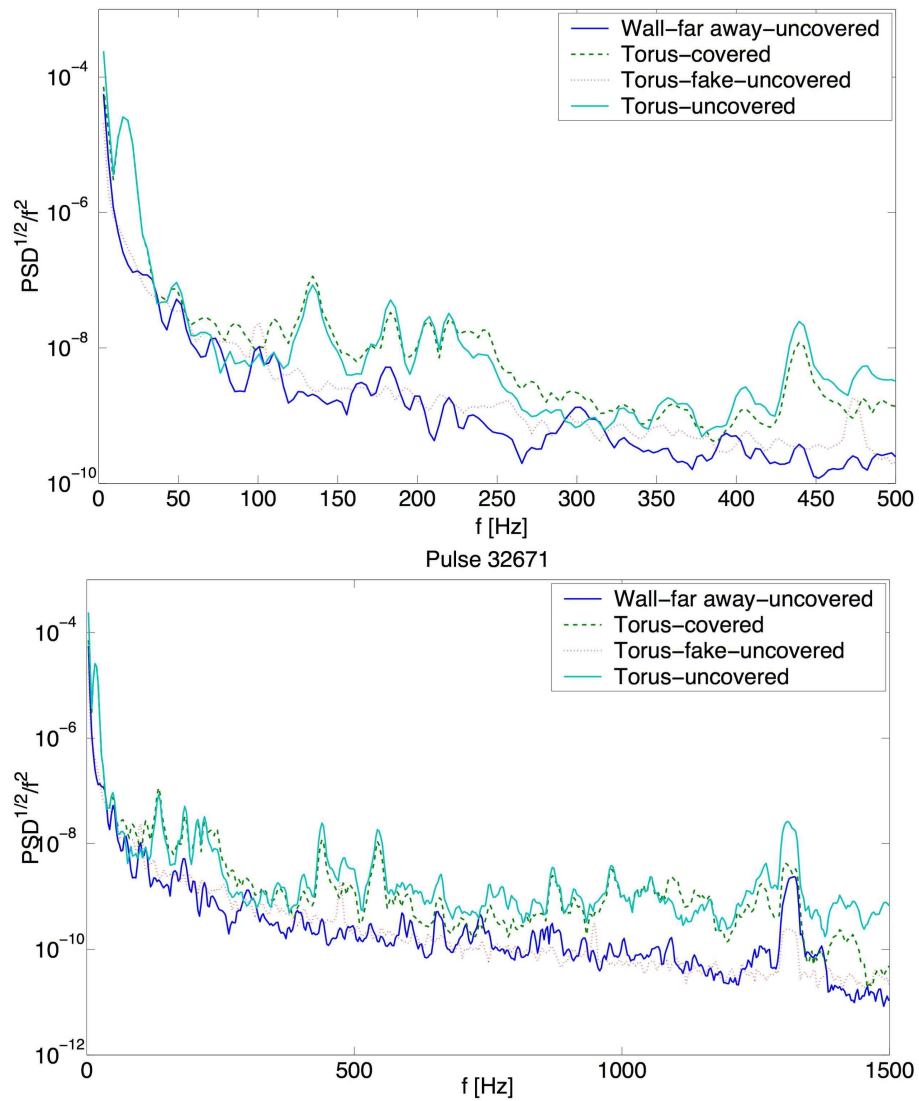


Figure 3.21: (Top) Estimated PSD of spatial displacement in the low frequency band. (Bottom) Detail of the low frequency region.

system was proven to perform poorly on the DIII-D tokamak, possibly due to power flickering of the visible laser which induced artificial vibrations, the choice of the position sensing detector fell on the 10.6 μm wavelength; although this is more expensive than visible technology, the detection system operates on the probing beam and is therefore expected to be more appropriate. The geometry adopted is a quadrant of four square HgCdTe photoconductive detectors, arranged in two rows and two columns, manufactured by *Infrared Associates Inc.* (Florida). The area of each detector is 4 mm², while spacing between detectors is 50 μm . Detectors need to be operated at 77 K; they are characterized by a normalized sensitivity $D^* \geq 2 \cdot 10^{10} \text{cmHz}^{1/2}/\text{W}$, and a field of view of 60°, and are protected by a doubly anti-reflectively coated ZnSe window. All the details concerning the optical path from the first scanning mirror to the position sensing detector are deferred to Sec.3.6.4.

The four signals exiting the quadrant detector are fed as input to the analyzing circuit board executing standard differences and sums to find the correct drive for the scanning mirrors as

$$X = \frac{X_2 - X_1}{X_2 + X_1} \frac{L}{2} \qquad Y = \frac{Y_2 - Y_1}{Y_2 + Y_1} \frac{L}{2} \qquad (3.107)$$

where $\{X, Y\}$ is the coordinate of the centroid of the beam spot on the position sensing detector surface (measured from the detector center), and L is the size of the detector's sensitive surface in mm. The circuit board OT-301DL coupled to the display OT-302 were manufactured by *On-Trak Photonics, Inc.* (California) and were bought, second hand, from *G2 Technology*.

A compensation circuit is necessary to adjust the frequency response of the position sensing detector and of the scanning mirrors; it was built on the design performed for the PCI diagnostic on the DIII-D tokamak[3]. Steering mirrors are then driven by second-hand drivers *AX-200* manufactured by *GSI Group, Massachusetts*.

We describe now the most delicate part of the active-stabilization system: the scanning mirrors. These mirrors can be mounted on several kinds of motors, such as galvanometers or piezoelectric devices; the former device type was preferred because of its superior overall performance, which can be evaluated by two important requirements to be satisfied: rotation range to compensate for large deviations, and rotation speed to compensate for fast deviations. These two requirements compete with each other as the former is inversely proportional to the latter via mirror inertia. Indeed, mirror inertia depends on the weight of the mirror and mainly on the size around the rotation axis. The size of the mirror depends on the distance from the phase plate and, in general, on details in the optical design; we mention here that our scanning mirrors are positioned around a secondary image formed after the focus-relay lens (see Sec.3.6.4) which, by definition, is the position with a minimum beam size, thus minimizing the size of the mirrors and,

therefore, their inertia. Once the size of the reflecting surface has been fixed, the inertia is directly proportional to the mirror weight, which is a linear function of the substrate density and volume. To minimize the inertia, exotic substrate materials and volumes were considered: in particular GSI proposed a Be substrate with an elliptically shaped reflecting surface whose thickness was quadratically decreasing as a function of the distance from the center of the mirror. However, despite their much better performance, their price was considerably higher, about 10 times, than standard octagonal flat quartz mirrors, which were eventually chosen.

3.6.4 Geometrical beam path

In chapter 2 it was shown how a tangential configuration is far better, in terms of spatial localization, than the standard vertical configuration already employed on the tokamaks TCA, DIII-D, Alcator C-Mod and on the stellarator LHD. Additionally, it was even shown that the probing beam has to be launched in a field-line following direction, otherwise the benefits of a tangential scheme would be lost. The goal is then to design an optical path allowing such a geometrical configuration.

Considering the tangential launching, a tangentially viewing port would have been an ideal option but, since on TCV no such ports are available, the beam needs to be steered from the radial to the tangential direction. The vacuum vessel has a major radius of 0.88 meters, a minor radius of 0.25 meters and is divided into sixteen sectors; as a result, therefore, to accomplish a near-tangential measurement near the magnetic axis, the launching and the receiving port have to be separated by three sectors. Indeed, a two sector separation would allow access to the edge only whereas a four sector separation would allow access only to the high field side of the poloidal section in the high resolution region. Furthermore it is shown in Sec.3.3 how, to measure long wavelength fluctuations, which, on the basis of mixing-length arguments, are generally the most relevant ones in terms of the amount of transport they generate, the beam waist needs to be of the order of the wavelength of the fluctuations. Extensive linear runs performed with the codes GS2 and KINEZERO showed that the modes which contribute most to the total transport are located in the region $k_\theta \rho_i \simeq 0.1 - 0.5$ which, considering typical ion Larmor radii in TCV, translates into $0.5 \leq k_\theta \leq 3 \text{ cm}^{-1}$. If one considers, as optimal, a value of $Q = k_c w_0 / 2$ between 1.4 and 1.6, this translates into a minimum beam half-waist in the range $1 \leq w_0 \leq 6 \text{ cm}$.

In Chapter 1 we mentioned that TCV can operate with plasmas at different vertical positions, even though ELMy H-mode plasmas tend to be robust and stationary only in the upper part of the vessel, especially with the magnetic axis located at $Z=23 \text{ cm}$. This nat-

usually leads one to design the beam path with the tangency point, i.e. the best resolution region, at that height. Moreover, the ports need to favor a field-line following launch, thus the vertical angle between the launching and the receiving port has to be as close as possible to the pitch angle of the magnetic field lines. The only two possibilities were the use of the upper-lateral port in sector 12 and the mid lateral port in sector 15, the latter being in use for the Bolometry diagnostic; or the upper-lateral port of sector 14 and the mid-lateral port of sector 1, respectively free and occupied by the glow antenna. No ports were available in the top and bottom parts of the vessel. The upper-lateral port of sector 14 is of difficult access due to the presence, immediately underneath, of a diagnostic neutral beam which considerably restricts the available space around it; moreover, the access to the port itself is additionally restricted by the presence of a cross-bar for the mechanical support of the machine. Despite these difficulties this was the only option available, and therefore the upper-lateral port in sector 14 and the mid-lateral port in sector 1 were assigned to the PCI project, while the glow antenna was moved to the bottom-lateral port in sector 1.

Let us now describe the lateral ports of TCV. Since TCV is equipped with a number of shaping poloidal coils, access to the vacuum vessel is achieved through a 30 cm long tunnel, whose diameter is equal to 15 cm if cylindrical, and 31.5 cm times 16 cm if rectangular. The access to the vacuum vessel itself is accomplished by a circular hole of 13 cm diameter in every port. The tangential configuration forces a net deviation of the probing beam from a purely radial direction by about 60 degrees. Such a deviation cannot be realized by one single mirror, if the probing beam is larger than a few centimeters. Additionally, considering the space availability, the beam full-width is constrained to nine to ten centimeters.

One of the key requirements was to be able to intersect or at least approach the magnetic axis which is located at a major radius of about 89 cm, depending on the plasma. Since the geometrical configuration of TCV ports does not allow the beam to pass through the average axis position without mirrors located in the vacuum vessel beyond the plasma facing surface formed by the carbon tiles, it was decided to design the system as translatable. Depending on the plasma positioning in the vacuum vessel, the mirrors can penetrate beyond the surface of the tiles to let the probing beam approach, at the tangency point, a major radius of 88-89 cm.

The launching and receiving ports are not identical and the reduced available portion of the receiving port, due to the cross-bar, combined with the larger effective width of the beam in the receiving port, due to plasma diffraction, induce asymmetries in the configuration of the two ports and in the positioning of their mirrors. In particular, these asymmetries resulted in two different penetration lengths which entail different launching and receiving angles on the two front mirrors, causing different orientations of the mir-

rors as functions of the radial positions of the launching and of the receiving port. It is anyway desirable to have independent translation stages for the two ports in view of the possibility of intermediate plasma vertical positioning in the vacuum vessel, resulting in different distances of the LCFS from the tiles at the height of the two ports, which in turn imply different innermost safe radial positions of the two front mirrors beyond the tile level.

To ensure the correct alignment of the system, one could either oversize the mirrors to accommodate the beam in its various trajectories, or design rotatable mirrors, or adopt both solutions at once. In the former case, the required amount of oversize, for a given port access, results in an unacceptable reduction of the beam waist, while the latter choice results in a slight oversize (a few mm) to accommodate the beam in the case with the largest impact angle. To minimize the over-sizing of the mirrors and ensure the correct alignment, a sufficient and necessary condition is to tilt only the two front mirrors.

The best geometrical configuration is obtained by positioning all the in-vessel mirrors, in both the launching and the receiving port, in such a way as to be positioned with their normals in the same plane (or in parallel planes); this choice leads to two advantages. First, the elliptical beam foot-print on the mirrors has one axis equal to the beam waist, which is obviously the minimum dimension achievable. If the mirrors are elliptical, their surface is minimized and has to be equal to the foot-print area plus the clear aperture; this optimizes the space occupied by the mirrors in the two ports, thus maximizing the beam waist, and minimizes the cost of the mirrors themselves. Second, the problem having been reduced from three to two dimensions, the two front mirrors need to rotate around only one axis. If we express the normal to the reflecting surface of each mirror in cylindrical coordinates $\{r, \phi, z\}$, in a reference system centered on the machine axis, we can write for the launching port

$$\mathbf{n}_i = \{\cos(\alpha_i), \sin(\alpha_i) \cos(\theta_i), \sin(\alpha_i) \sin(\theta_i)\} \quad (3.108)$$

where α_i is the angle formed by the normal to the i^{th} mirror with the toroidal direction, and θ_i the angle formed with the vertical direction (Since the system is translatable in a tunnel, the mirrors are here constrained to be aligned in the radial direction). Similarly for the receiving port

$$\mathbf{n}_i = \{\cos(\beta_i), \sin(\beta_i) \cos(\psi_i), \sin(\beta_i) \sin(\psi_i)\} \quad (3.109)$$

with $\psi \rightarrow \theta$ and $\beta \rightarrow \alpha$. In each port the normals to the mirrors lie in the same plane if $\theta_i = \theta$ and $\psi_i = \psi \forall i$, by construction. The launching and the receiving ports are separated by an azimuthal angle of $3/8\pi$ in the toroidal direction; therefore the normals to all mirrors in both ports lay in the same plane if, for example, the launching port is rotated around the vertical axis by $3/8\pi$ and then around the radial axis of the receiving

port by an angle equal to ψ . Indeed the triple product, which, when equal to zero, is a necessary condition for the three normals to be aligned in a plane, between two mirrors of the launching port (mirror number 1, steerable, and number 2, fixed) and one steerable mirror of the receiving port is equal to

$$\mathbf{n}_1 \cdot (\mathbf{n}_2 \wedge \mathbf{n}_3) = -\sin(\beta_1) \sin(\alpha_1 - \alpha_2) \sin(\theta - \psi) \quad (3.110)$$

which, since α_1 and β_1 are not fixed being the angles of the two steerable mirrors, is zero if and only if $\theta = \psi$. The triple product being equal to zero is a necessary condition for the normals to the three mirrors to be aligned in a plane. The condition $\alpha_1 - \alpha_2$, if the front mirror was not steerable, is a spurious condition implying the two mirrors are parallel. In the TCV system the normals to the mirrors in the launching port are not in the same plane as the ones to the mirrors in the receiving port. This was due to a flaw in the design which caused a misalignment of about one degree.

Even though the system can be two dimensional in one particular configuration, the translational degree of freedom of each port renders the problem inherently three-dimensional. If the two sliding directions were parallel, the beam could be made to impinge on the center of each mirror just by changing α_1 and β_1 but, since they are not, the relative distance between the two mirrors changes as a function of the relative position. Therefore the beam starting from the center of the front mirror in the launching port will not always impinge on the center of the receiving mirror or of the following ones. As the system is conceived, the distance between the impact point on the receiving mirror and the center of the mirror itself is only a function of the radial position of the receiving port; since this has the shorter of the two strokes, the displacement is limited. The solution to this problem was to oversize the mirrors in the receiving port.

The translatability of the two ports, which requires the presence in each of a bellows, a sliding rod for support, as well as a screw to rotate the front mirror, further reduces the available space for mirror positioning and, in turn, the width of the beam as well. A MATLAB graphical routine was written to simulate the beam trajectory in the vacuum vessel as aid to the actual design performed with the CAD-like software CATIA V5. The MATLAB routine was used to quickly evaluate possible alternatives without modifying the heavy design in CATIA. All the conflicting requirements listed above and all the mechanical constraints which needed to be satisfied resulted in lengthy iterations between the design in CATIA and the design in MATLAB, which lasted several months in total. The final configuration of the launching port comprises three fused silica mirrors, of which two are in vacuum, one ZnSe window for vacuum interface (described in Sec.3.6.7), a screw which allows a rotation of the front mirror by up to 4 degrees and a bellows with a linear stroke of 100 mm. The screw was designed to provide twice the amount of rotation needed to guarantee an engineering safety margin.

The receiving port contains two fused silica mirrors, both in vacuum, one ZnSe window for vacuum interface, a screw which allows a rotation of the front mirror by 11 degrees, which is about four times the design requirement, and a bellow with a linear stroke of 70 mm. The rotation range is far larger than needed because there were no mechanical constraints on the screw positioning in the receiving port, contrary to the case of the launching port. Both screws were fitted with micrometric actuators which provide 20 mm linear translation; the end of the actuator is connected with the front mirror at a given distance from the mirror axis of rotation, thus allowing the front-mirror to rotate.

The actual total rotations of both mirrors as functions of the position of the micrometric actuators were measured with the *Accutrack* system, manufactured by *Atracsys* (Switzerland). This is a localizer employing the signal of four LEDs mounted on a pen. After an initial calibration, the combined positions of the LEDs permit one to calculate the position of the pen end point. The orientation of the two front mirrors, around their respective rotation axes, with respect to a plane parallel to the radial direction passing through the center of the respective port was deduced by a least square fit calculated over one hundred measurements carried out every millimeter step of the actuator; the results for the two ports are shown in Fig.3.22.

In the receiving port, the end part of the actuator is connected to the front mirror

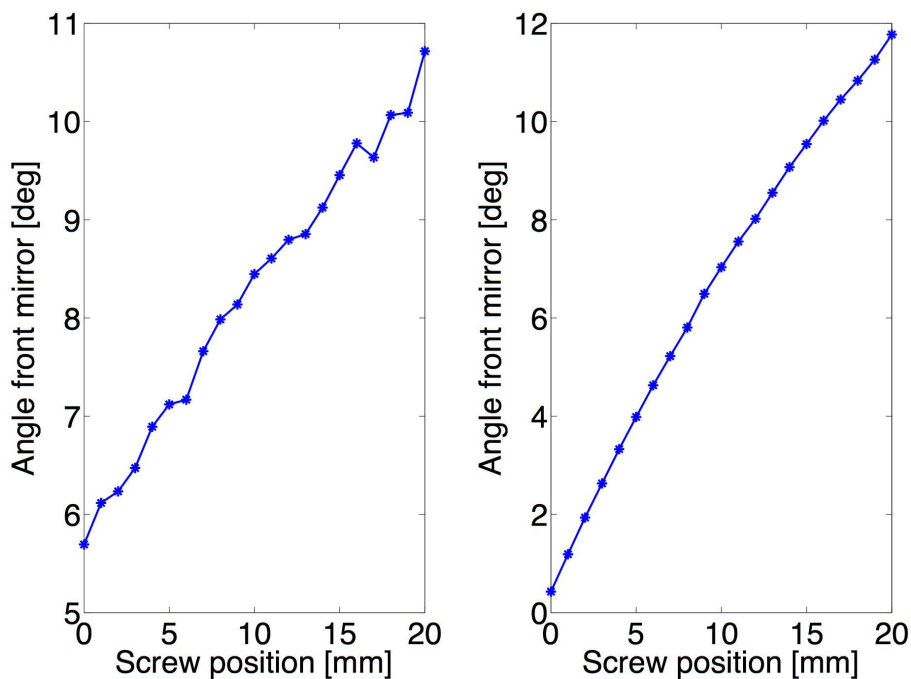


Figure 3.22: (Left) Angle, with respect to the radial direction passing through the center of the port, of the front mirror in the launching port vs the position of the actuator. (Right) Same for the receiving port.

through an electrically insulating zirconium pin. This choice was dictated by the ne-

cessity to avoid mechanical forces induced by a varying poloidal magnetic field, during the current ramp-up, in the loop formed by the front mirror support, the screw and the external flange (see Fig.3.24). Mechanical vibrations are expected to interfere with the equilibrium position of the pin and the guiding groove along which it slides, therefore a spring is used to connect the groove to the support of the front mirror. Zirconium has a compression strength of 2000 MPa and a bending strength of 700-1100 MPa, depending on the material phase. The pin is 13 mm long with a circular section 4.75 mm in diameter; the contact point with the guide is 13 mm from the clamp of the screw, which is then the distance between the applied force of the spring and the clamp. By applying De Saint Venant's theory of elasticity[16] we find that the maximum force the screw can be allowed to exert is 566-889 N, for the two extreme values of the bending strength, or 188-295 N if a safety margin of 3 is required. The spring's length and type were chosen after having tested the mechanical response to an applied perturbation of the groove position of a number of springs with different elastic constants and lengths.

The receiving port configuration was designed to let the beam exit the port in a purely radial direction. This requirement was dictated by the fact that any other exiting angle would have been problematic, or impossible, due to the aforementioned restrictions in the access to the port itself. A purely radial exiting beam has the additional advantage of being insensitive to the radial position of the port itself, therefore allowing a fixed position of the mirror outside the vessel which redirects the beam to the optical table. This was achieved at the expense of a steeper impact angle on the last mirror, named M5 in Fig.3.24, which is therefore quite large.

The design of the beam path outside the vacuum vessel was performed, first, with dedicated MATLAB routines, benchmarked with the commercial ZEMAX code and, finally, again with CATIA V5 to check the results and to appropriately design mechanical supports for all the optical elements required outside the optical table.

The PCI system requires a large optical table to accommodate focusing optics which expand the laser beam to the desired width, as well as the optics composing the imaging system, the phase plate, the CO₂ and visible lasers for alignment along with their respective safety interlock systems, the position sensing detector accompanied by the vibration active stabilizing system, and the detector array with its pre-amplifiers. The acquisition system is located under the optical table. On the basis of the amount of space required by the whole system compared to the available space outside the torus assigned to standard TCV operations, we were not allowed to install the optical table on the same floor as the tokamak. The only alternative was to install the optical table on a floor located four meters underneath TCV, which entailed a significant lengthening of the optical path; this, in turn, caused three major difficulties. The first concerns the alignment, which has to

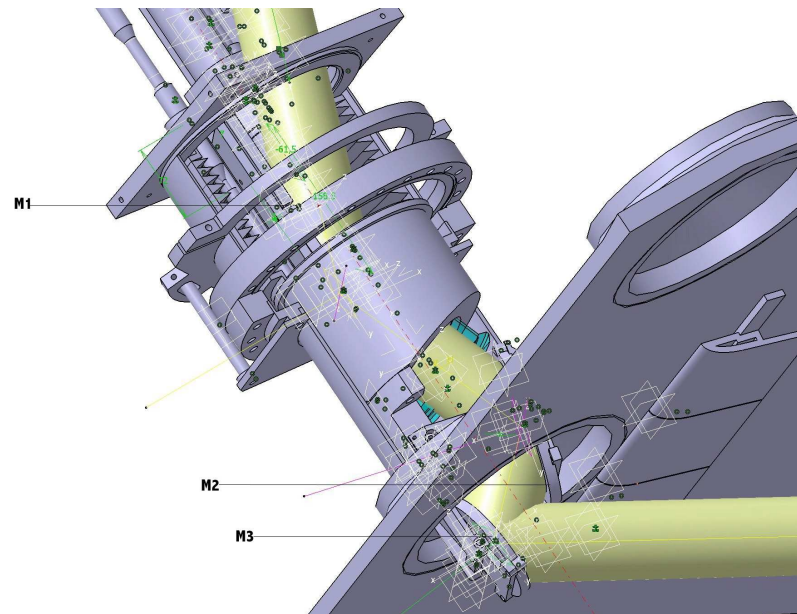


Figure 3.23: CATIA drawing of the launching port. In the picture the beam trajectory is depicted in yellow, the ZnSe window in green, mirrors are indicated as M1 M2 and M3. The bellow and the rotating screw are also visible.

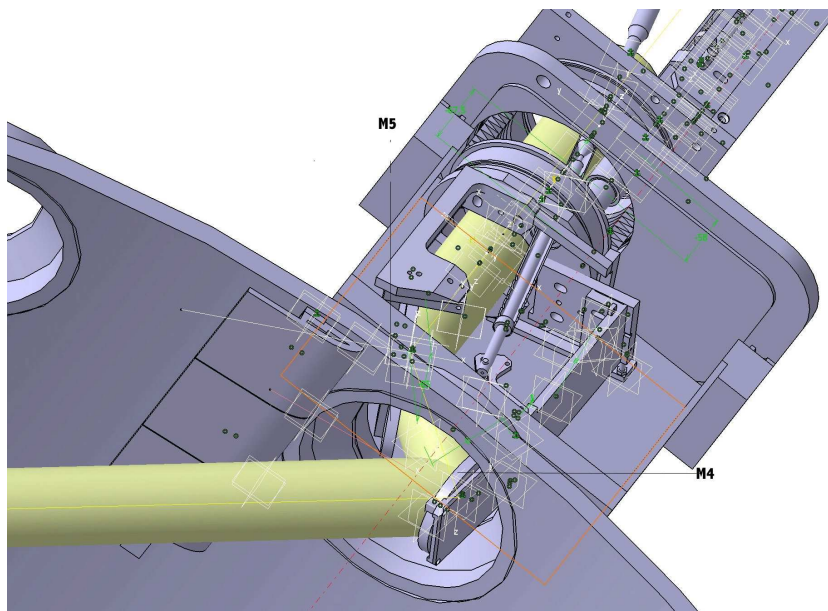


Figure 3.24: CATIA drawing of the receiving port. In the picture the beam trajectory is depicted in yellow, mirrors are indicated as M4 and M5. The bellow and the rotating screw are also visible.

be performed with, at least, one person on each floor. The second is the fact that the beam has to pass through the floor; the existing concrete floor slabs had existing vertical cylindrical holes, 8 cm in diameter and 40 cm high - a choice then had to be made whether these were sufficient or larger holes were needed. The last difficulty concerns the optical path from mirror M5 to the detectors. Indeed, since the phase contrast was designed to be sensitive also to electron scale fluctuations, all the optical elements have to be designed to collect all the scattered light. In the paraxial approximation, the half-width of a scattered beam in free space propagation is described by

$$w(z) = w(0) + z\theta \quad (3.111)$$

where θ is the scattering angle and z is the distance along the beam path. Considering a CO₂ probing beam laser of 3.5 cm half-width, and fluctuations wave-vectors $\leq 60 \text{ cm}^{-1}$, Eq.3.111 translates into a doubling of the beam waist after 3.5 m. Now, the price of an optical element, flat or focusing, increases considerably more than linearly with its linear size while its optical properties generally deteriorate; additionally, aberrations considerably increase with the oblique angle of propagation with respect to the optical axis of the system. Since PCI is highly sensitive to optical aberrations, the lengthening of the optical path after plasma scattering caused severe difficulties in the optical design.

The design of an optical system with the desired characteristics, in view of all the constraints in terms of available space outside the receiving port and the considerable distance between TCV and the optical table, including a minimization of aberrations, number and size of optical elements and their cost, required a detailed evaluation of several alternatives. These include long focal length lenses, combinations of tilted parabolic and/or spherical mirrors, large off-axis paraboloids and telescopic arrangements of several kinds. Only two configurations turned out to be feasible, and we describe them hereafter.

- Telescope with 2 lenses + existing CRPP parabolic mirror

The idea is to use a telescope made by two lenses to relay the beam exiting from the receiving port to the parabolic mirror which will then focus it on the phase plate. The parabolic mirror, used in a previous experiment at the CRPP, has a focal length of 1.91 m and a clear aperture of 13 cm.

The ABCD matrix of a telescopic device made by two lenses reads

$$\begin{bmatrix} \frac{f_1(f_2-l_3)+l_2l_3-f_2(l_2+l_3)}{f_1f_2} & \frac{-l_1[-l_2l_3+f_2(l_2+l_3)]+f_1[-(l_1+l_2)l_3+f_2(l_1+l_2+l_3)]}{f_1f_2} \\ -\frac{f_1+f_2-l_2}{f_1f_2} & \frac{f_1(f_2-l_1-l_2)+l_1(-f_2+l_2)}{f_1f_2} \end{bmatrix} \quad (3.112)$$

where f_1 and f_2 are the focal lengths of the first and the second lens, respectively, l_1 is the distance between the object plane and the first lens, l_2 is the distance between the

two lenses and l_3 is the distance between the second lens and the parabolic mirror.

Let us now find the conditions under which the beam is imparted neither a convergence nor a divergence by the telescope. By definition of the ABCD matrix this is found by imposing the element C equal to zero; Eq.3.112 then gives the familiar telescope expression $l_2 = f_1 + f_2$ and reduces to

$$\begin{bmatrix} -\frac{f_2}{f_1} & f_1 + f_2 - \frac{f_2 l_1}{f_1} - \frac{f_1 l_3}{f_2} \\ 0 & -\frac{f_1}{f_2} \end{bmatrix} \quad (3.113)$$

In this way it would be as if the parabolic mirror was positioned just outside the receiving port without constraints on free space available. It is of interest to minimize the size of the beam on the parabolic mirror, because this allows more flexibility on the positioning of the phase plate on the optical table and permits the use of the central part of the parabolic mirror, which is certainly the best part in terms of overall reflectivity and surface figure. The minimum size is obtained in the point where an image is formed, which is found by imposing $B=0$, yielding

$$l_3 = f_2 \frac{f_1^2 + f_1 f_2 - f_2 l_1}{f_1^2} \quad (3.114)$$

and Eq.3.113 reduces to

$$\begin{bmatrix} -\frac{f_2}{f_1} & 0 \\ 0 & -\frac{f_1}{f_2} \end{bmatrix} \quad (3.115)$$

The quantity $-f_2/f_1$ is the transverse magnification of the system, up to the parabolic mirror, and can be chosen at will; an opportune choice may permit reducing the large scattering angles, resulting in turn in reduced aberrations in the imaging system after the parabolic mirror, as the angles are multiplied by the reciprocal of the magnification.

In our case this design requires $f_{1,2} \simeq 3$ m and both lenses need to be larger than 10 cm in diameter. The system is not very sensitive to the position of the object plane, i.e. to the spatial localization of PCI: indeed a displacement δl_1 changes the beam width on the parabolic mirror by $f_2 \delta l_1 \theta_0 / f_1$, where θ_0 is the scattering angle from the plasma. The drawback of the system, which is the reason why it was discarded, is the difficult alignment of the first lens which has to be mounted just outside the receiving port and, in case of even a small misalignment with the beam, would cause severe aberrations limiting the system performance.

The next configuration, even though more expensive than the one above, was the final choice

- Large parabolic mirror + relay lens for focus

This design is based on propagating the beam from the receiving port to an off-axis paraboloid large enough to collect all the light scattered by the plasma. Since the optical

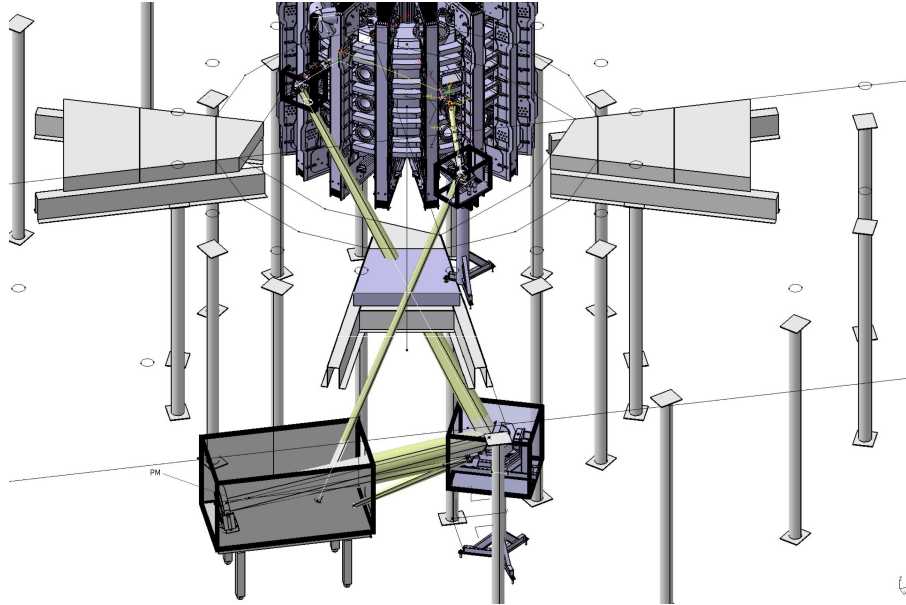


Figure 3.25: CATIA drawing of the beam path outside the vacuum vessel. In the picture the beam trajectory is depicted in yellow, the parabolic mirror is indicated as PM. The optical table is also visible. The entry port is on the right and the exit port on the left.

axis of the parabola has to be colinear with the optical axis of the propagating beam, two intermediate flat mirrors need to deviate the beam to an almost horizontal propagation direction. Such a set-up, depicted in Fig.3.25, requires a distance of about 10 m between the object plane and the off-axis parabolic mirror, whose clear aperture needs to be at least 31 cm to collect all the light scattered by high wave-vectors allowing room for mechanical vibrations.

The presence of the relay lens for focus is due to the focal lengths of parabolic mirrors being directly proportional to their size. The focal length of such a wide parabola is larger than three meters, which would then force the phase plate and, at least, the first lens after it, to be larger than 6 cm. Since, usually, these are routinely manufactured smaller than 5 cm, we chose to introduce a relay lens for focus to shorten the overall focal length and, therefore the dimensions of the phase plate and all the lenses after it.

Along the optical path, the laser beam is enclosed in plexiglas tubes and boxes to protect the optics from dust and the beam from acoustic perturbations.

The complete design is described in detail in Sec.3.6.9.

3.6.5 Lasers

In the previous sections it was mentioned that PCI is designed to operate with a monochromatic probing beam at $10.6 \mu\text{m}$. The reason for a monochromatic coherent source is explained in Sec.3.1 while the choice of $10.6 \mu\text{m}$ is dictated by a compromise between two conflicting sets of requirements. The validity of the Born and Raman-Nath approx-

imations as well as the first order paraxial approximation, which are at the basis of the theoretical approach in Sec.3.1, are more easily satisfied at short wavelengths, which are also beneficial in reducing plasma refraction effects (see Eq.3.15). Additionally, the smaller the maximum scattering angle to be analyzed, the better is the optical system in terms of aberrations and of size of its optical elements, as they are minimized. However, longer wavelengths have several advantages as they are less sensitive to damages and imperfections of the optical elements; also reflectivity tends to be much higher at long than at short wavelengths (see for example Fig.3.26). Additionally, focal spot sizes are larger at long wavelengths, thus simplifying the construction of the phase groove and the spatial filter. At last, sensitivity to plasma fluctuations is linear in the probing wavelength, as stated in Eq.3.40, therefore, longer wavelengths are more appropriate to detect small phase shifts. The choice of the CO₂ laser at 10.6 μm is therefore a compromise.

The PCI diagnostic makes use of an rf excited carbon dioxide laser manufactured by *Edinburgh Instruments, Ltd.* (UK). The laser was used for the PCI diagnostic on the TCA tokamak; it is cooled by an external closed loop water chiller and, even though its nominal output power is 8 W, it produces at this point an average output power of about 6.5 W, reached after approximately two hours of operation. Power oscillations during the transient phase are generally between 3.5 and 8 W. The output electric field is specified to be a pure linearly polarized TEM₀₀, with a nominal power full-width at the output coupler of 1.3 mm at the e^{-2} points and a nominal divergence of 9 mrad. The output wavelength was measured, with a diffraction grating, to be $10.61 \pm 0.005 \mu\text{m}$. The output power can be modulated by modulating the rf source. From dc to 10 kHz the power output follows the input modulation uniformly; in the region 10-100kHz the laser can be modeled by an RC circuit with time constant equal to $9.5 \pm 0.2 \mu\text{s}$; above 100 kHz significant deviations occur, whose modeling was not attempted. The maximum modulation frequency is 500 kHz, above which no power is coupled in output. The CO₂ laser is foreseen to safely operate with the shutter *LS-10-12*, manufactured by *Lasermet* (UK). The laser shutter is integrated in the TCV safety system that manages the access to the TCV zone during daily operations. Additionally, the TCV safety system has the capability to switch off the rf power supply in case of shutter failure.

The visible laser is a laser diode manufactured by *Scitec Instruments* (UK). It generates 100 mW CW power in the transverse TE₀₀ mode. The nominal wavelength is 632 ± 5 nm, the beam diameter at the output coupler is less than 5 mm and its divergence was measured to be less than 2.5 mrad; power stability is declared to be less than 5% over 2 hours. The beam was found to be slightly elliptical and the TE₀₀ mode contaminated by higher-order modes generating patterns of characteristic size 1-2 mm. The power supply of the visible laser is also under the control of the TCV safety system.

3.6.6 Mirrors

In this section we will describe the mirrors used in the optical design.

Mirrors need to satisfy strict surface accuracy requirements as the PCI is sensitive to optical aberrations, i.e. to differences in the optical path between the different scattered components. Let us start with the in-vessel mirrors.

The in-vessel mirrors are flat and elliptically shaped because they are positioned in a cylindrical tunnel at an angle with respect to the axis of symmetry. The required flatness was λ at 632 nm over a clear aperture equal to 90% of the elliptical axis, which required a mirror thickness of, at least, 10 mm. Five mirrors in total are installed in the vessel, four of which are in vacuum. The environment of the TCV vacuum vessel required the substrate to be made of fused silica which, to simplify the order, was also chosen as a substrate material for the mirror not in vacuum.

Except for the two front mirrors, which require a special coating, all the mirrors are coated with about 200 nm of Al protected by about 50 nm of SiO₂ deposited up to 0.37 millimeters from the edge; even though this is the actual reflecting surface of the mirrors to be used when calculating diffraction effects, only 90% of it is to be considered as useful for the scattered beam, because the required flatness is specified only on that inner portion of the mirror. The two front mirrors required a special coating which we describe hereafter. All the mirrors were bought from *DoricLenses Inc.* (Quebec).

Front mirrors are more heavily exposed to four damaging phenomena

- Plasma ion sputtering
- Erosion by neutrals
- Erosion and deposition from glow discharge cleaning
- Erosion and deposition from boronization.

The other two in-vacuum vessel mirrors are expected to be much less affected by these phenomena as they are positioned further behind the line of the plasma-facing tiles and because their reflecting surfaces both face the external part of the vessel.

Detailed calculations of the impact of the first two phenomena were performed in collaboration with G. de Temmerman of Basel University. The results of a Scrape-Off-Layer (SOL) simulations performed with the SOLPS5 code of a high density TCV shot, namely shot 10452 [10], was provided to the TRIDYN code [11] to estimate, in the extreme positions the front mirrors can reach, the erosion and deposition on different coatings. In particular, ion species considered in the calculations were $D^0, D^+, C^0, C^{1,2,\dots,6+}$. The results of the calculations imposed the use of a high Z material such as Ag, Au or Mo; in particular, protected Al would have been severely damaged after one single shot with the

mirrors positioned in the innermost position.

The ITER project foresees the use of Mo mirrors to withstand the impact of charge exchange neutrals, whereas Au is not considered due to nuclear transmutation caused by neutron impact. To add further experimental data to studies of the performances of such mirrors in a tokamak environment, we decided to use Mo for our front mirrors. Mirrors fully manufactured in molybdenum, or in Al coated with Mo, did not meet the required optical specifications; therefore we finally chose fused silica mirrors coated with Mo. The process consists of depositing on the fused silica substrate a sufficiently thick layer of Mo such that light does not interact with the substrate underneath the coating. The complex refraction index for a number of layers can be found in [12]; considering the values for Mo [13] we obtain a penetration length at $1/e$ points in power plotted in Fig.3.26a. The

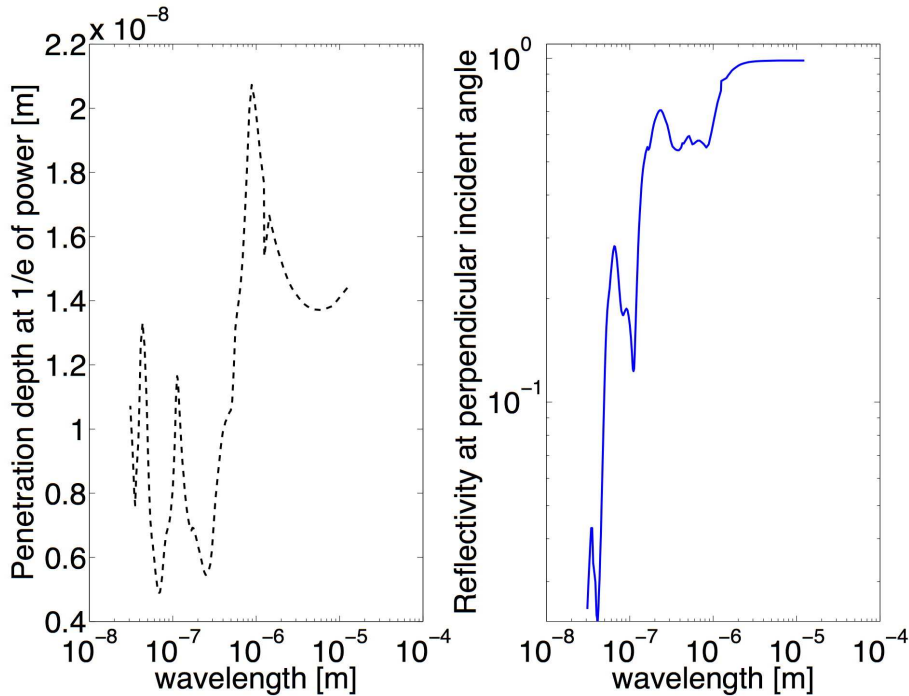


Figure 3.26: (Left) Expected penetration length into a Mo layer as a function of incident light wavelength. (Right) Expected Mo reflectivity at $10.6 \mu\text{m}$ for perpendicular incident light.

penetration length at $10.6 \mu\text{m}$ is equal to about 14 nm, thus 99% of the incident power is expected to be reflected after 64 nm; adding a safety margin of three we designed the coating to have a thickness of 200 nm. Once we assume that no power is transmitted through the reflecting Mo layer to the underlying substrate, we can make use of Snell's law to evaluate the reflection coefficient for incident light polarized parallel and perpendicular to the plane of incidence. As a function of the incidence angle, Snell's law

$$\sin(\theta_i) = \frac{1}{N} \sin(\theta_r) \quad (3.116)$$

allows one to calculate the Fresnel coefficients of a given material. The reflection coefficients at $10.6\ \mu\text{m}$, calculated for Mo, are plotted in Fig.3.27. The coating was performed

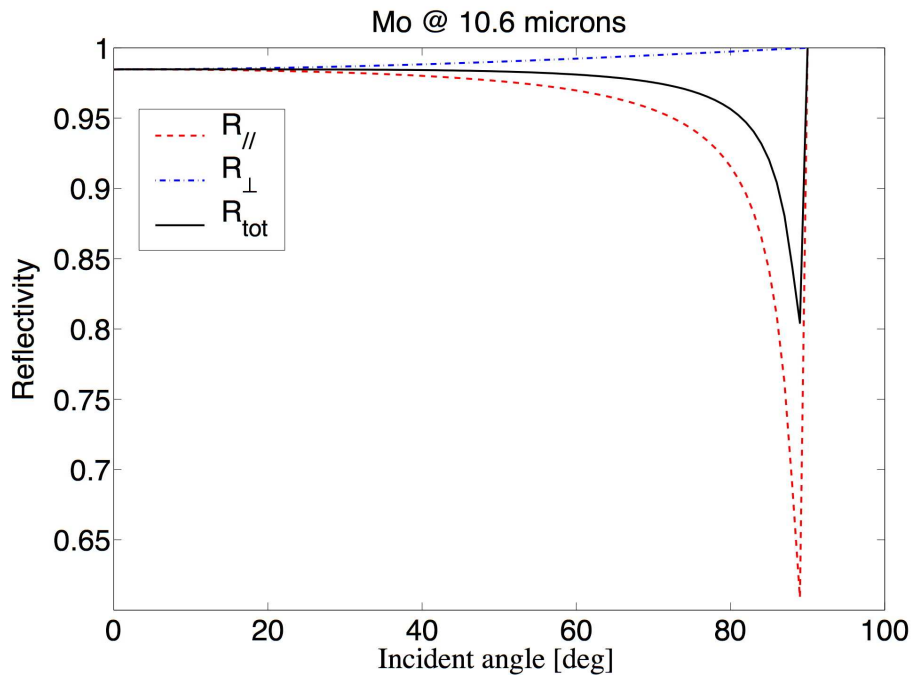


Figure 3.27: Expected Mo reflectivity at $10.6\ \mu\text{m}$, as a function of the incident angle, for light polarized parallel and perpendicular to the plane of incidence; unpolarized light is also reported as *tot*.

by *HELIA Photonics Ltd.* (Scotland).

Molybdenum is not suitable for continued operation at temperatures above $500\ ^\circ\text{C}$ in an oxidizing atmosphere, unless protected by an adequate coating. Since the baking temperature in TCV is about half that value, we did not expect any problem on this side; indeed tests at $300\ ^\circ\text{C}$ for several hours did not show any effect on the mirrors. However, even though from Fig.3.27 we expect a reflectivity larger than 98% at intermediate angles of incidence, the measured reflectivity was about 80%. An investigation was performed in collaboration with the *Interdisciplinary Centre for Electron Microscopy* of the *Ecole Polytechnique Fédérale de Lausanne* to investigate whether a possible contamination of the coating might have taken place. Measurements were done on a test mirror, coated in the same coating run as the two front-mirrors, employing the Energy Dispersive X-ray Spectroscopy (EDX or EDS) technique at a pressure of about 100 to 200 Pa. Monte-Carlo calculations estimate the thickness of the sampled volume in about 150 nm which, being smaller than the coating thickness, designed to be 200 nm, validated the use of this technique. Indeed, an analysis of the coated surface doesn't show the presence of Si, while this appeared clearly when a scratch in the coating was analyzed. This indicates that the coating thickness is indeed larger than 150 nm.

The atomic composition of the coating was determined to be approximately 60% Molybdenum and 40% Oxygen, meaning that Mo underwent oxygenation processes, most likely with atoms present in the coating vacuum chamber. The mirrors were sent back to Helia Photonics for a re-coating with a new procedure, after the first coating was removed by plasma etching. Even though the new procedure proved to be slightly better than the first one, reflectivity increased only to 85%.

Even though Mo is a high Z element, suited to withstand high ion sputtering rates,

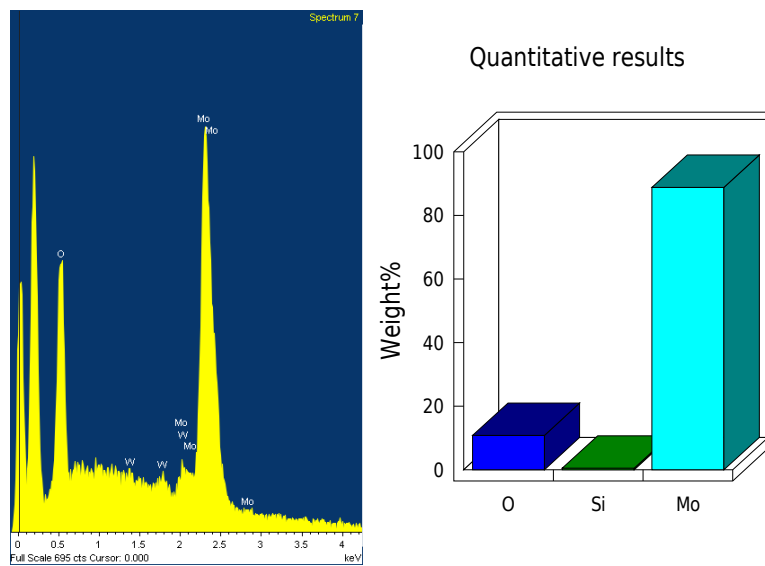


Figure 3.28: EDX report on the test mirror coated with Mo. The fraction of Oxygen is clearly significant. The weight ratio shown translates into an atomic ratio of 60% Mo and 40% O.

its sputtering threshold is only a few tens of eV[28], depending on the bombarding ions. TCV routinely runs glow discharges with singly ionized helium atoms accelerated by a potential difference of 400 V. The ion sputtering threshold is therefore by far insufficient to protect the mirrors, which need to be somehow actively shielded. This is usually performed with the use of mechanical shutters; however, since in our design, especially in the launching port, there is no room for shutter movements, alternative solutions had to be considered. The first option was to manufacture three rings, slightly larger than the torus access hole diameter, to be spaced a few millimeters apart and oppositely charged, with a total zero charge deposited on the rings, in such a way as to create the potential barrier depicted in Fig.3.29. The negative part would repel electrons so as not to short-circuit the glow current, while the positive part would repel incoming ions and protect the mirror. If the distance between rings is smaller than 3 cm, the voltage drops to zero 5 cm away from the center; the central ring could then be positioned 5 cm beyond the first wall to

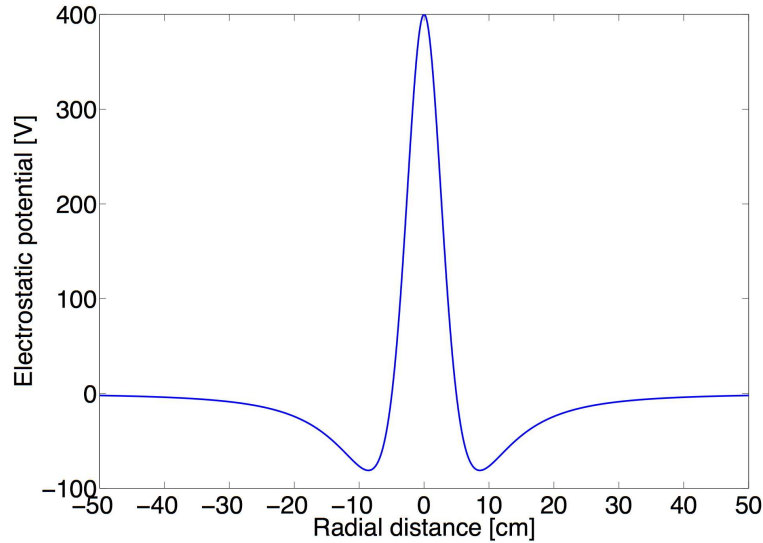


Figure 3.29: Radial profile of the electrostatic potential generated by three rings charged to $-V/2$, V , $-V/2$. The profile does not depend on the distance between rings, provided the latter is smaller than 3 cm.

preserve the ground voltage on the first wall. This option was rejected due to the risk of short-circuiting the glow current and thus of possible damages to the vacuum vessel.

The second solution relied on the fact that the mirror substrate, being a glass, is an insulator, so if the metallic mirror clamps are insulated from the reflecting surface, the latter is left at a floating potential and is therefore subjected to ion sputtering only under the sheath potential, which is below the Mo ion sputtering threshold. Two possible solutions were considered: to deposit an insulating $\text{Al}_2\text{O}_3/3\text{TiO}_2$ coating on the clamps and on the mounts to completely insulate the entire mirror, or, during the Mo coating, to mask the zones of the mirrors which would have been clamped in TCV; the first solution, which would have had to be performed by *Plasma and Thermal Coatings Ltd.* (Wales), was much more expensive and was therefore rejected. The geometrical configuration of the front mirrors is depicted in Fig.3.30. The mirror clamps are connected to the vacuum chamber, and thus are at the same electrostatic potential, while a gap separates each of them from the Mo coating; this gap assures electrical insulation of the coating provided that it is larger than the ion sheath thickness. According to [14] the ion sheath width is a decreasing function of the plasma collisionality, which means that, for designing purposes, it is enough to take the limit of a collisionless plasma. In this case about 10 Debye lengths are enough to guarantee a drop of the potential by a factor of 20. In TCV the glow potential is equal to 400 V, while the energy threshold of He sputtering on a Mo target is estimated at 47.5 eV[15]. During the glow the Debye length is about $2.3 \cdot 10^{-7}$ m which means that 1 mm is largely sufficient for the electrical insulation purpose.

The clamps used in TCV are shown in Fig.3.31 and feature an additional protruding lip

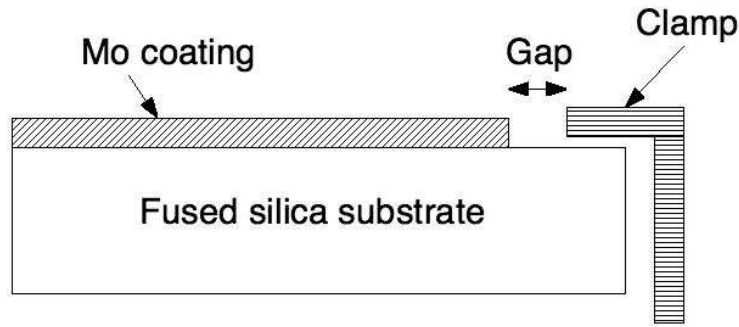


Figure 3.30: Horizontal view of first mirrors in TCV.

meant to protect the insulating gap from boron deposited during the boronization process which could short-circuit the Mo reflecting surface to the clamps.

Due to mechanical vibrations of the vessel and to their almost vertical orientation ($\simeq 23^\circ$), all the in-vessel mirrors are clamped on four points, instead of the usual three, to ensure a safer support. To avoid a deformation of the reflecting surface due to the fourth clamp, the mirror support was manufactured with a groove designed to accommodate a spring between the mirror support and the mirror rear surface, which provides an additional degree of freedom; in Fig.3.32 we show one of the in-vessel mirrors with its support. The spring should deliver enough force to keep the mirror in contact with the clamps, but should also be sufficiently compressible to actually supply the additional degree of freedom cited above. Several types of springs were tested on the bench mirrors of the same size and approximately the same weight as the ones actually used in TCV; the best performing spring was model *106-MBA-HST2*, manufactured by *Georg Rutz AG* (Germany), which delivers a force of 0.5 N/cm when compressed by 15% of its uncompressed height (4 mm). In accordance with the specifications of the spring, the grooves and the mirror mounts were designed to obtain a nominal compression of 15%, and a maximum allowed of 30%.

The out-vessel mirrors not positioned on the optical table were all manufactured by *Precision Glass & Optics* (California) as Pyrex substrates coated with protected aluminium; the surface figure was specified as $\lambda/4$ at 632 nm over 90% of the diameter. Only the largest mirror, a 40 cm diameter, circular mirror, positioned before the parabolic mirror in the optical path, has a BK7 substrate polished at $\lambda/10$ per 150 mm linear dimension over 90% of the reflecting surface, and is also coated with protected aluminium.

The off-axis parabolic mirror of the required size was not available off-the-shelf and had to be specifically manufactured. The cheapest solution was, by far, to buy a 76.2 cm wide, f/4.5 parent paraboloid, manufactured by *Optical Mechanics Inc.* (Iowa) as a Pyrex substrate polished to 0.07λ rms at 530 nm, with cosmetics 60-40 scratch and dig and exact focal length 3.454 m. The parabola was cut by *Rayotek Scientific Inc.* (California) into

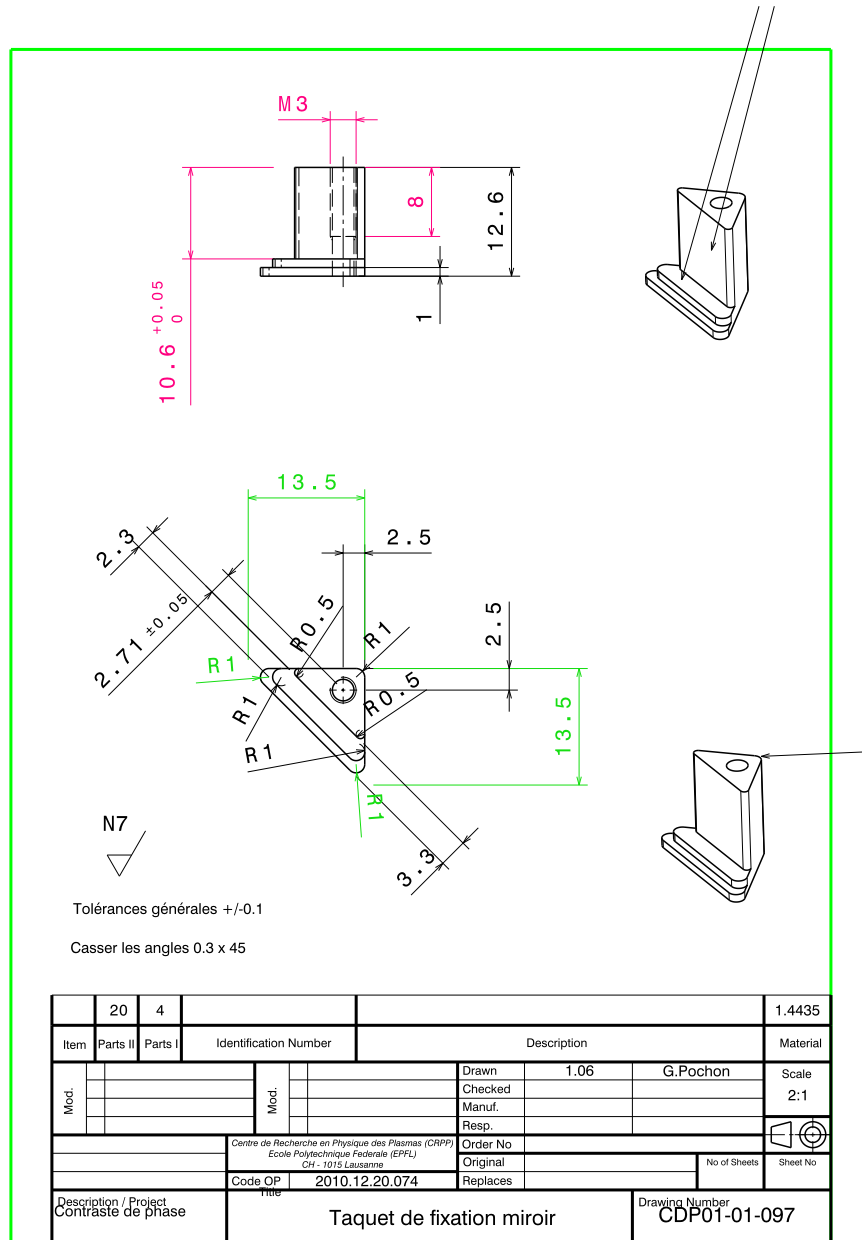


Figure 3.31: Clamps used in TCV for in-vessel mirrors; the additional lip is meant to prevent short-circuits between the clamps themselves and the Mo reflecting surface, possibly caused by boron deposition.

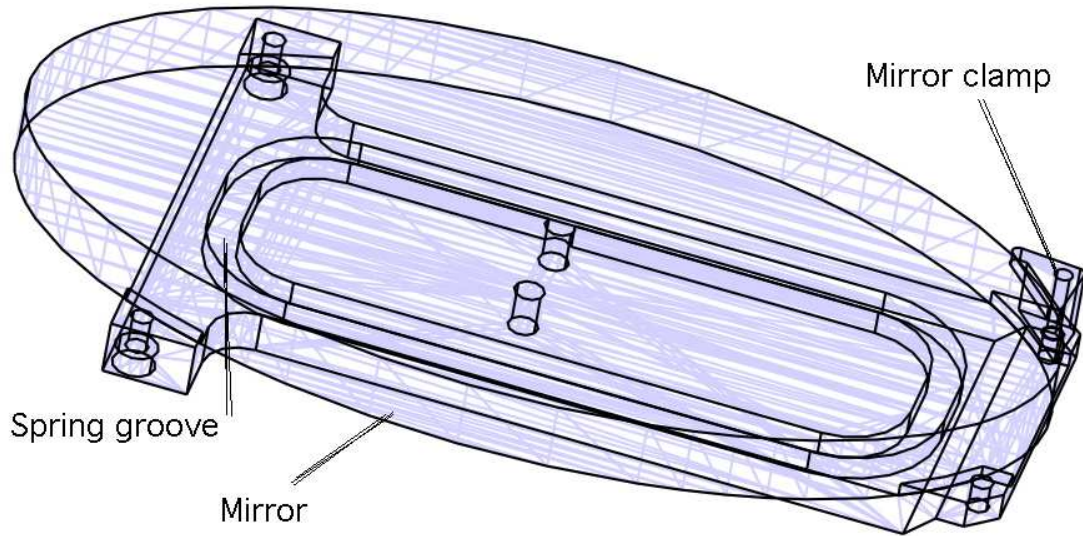


Figure 3.32: CATIA design of one in-vessel mirror with the groove dug in the support underneath the mirror to accommodate a backing spring.

4 pieces, two of them 36.83 cm wide and the remaining two 24.13 cm wide. The four resulting off-axis paraboloids were coated with protected Ag again by *Optical Mechanics Inc.*. Additional flat mirrors to be positioned on the optical table were bought from *ESCO Optics* (New Jersey) as Pyrex substrates coated with protected Al, 40-20 scratch and dig and $\lambda/10$ flatness.

3.6.7 Windows for vacuum interface

The windows for vacuum-interface were bought from *ULO Optics* (UK). They are both circular with a diameter of 100 mm, and thickness 10 mm. They are both made of ZnSe coated on both sides against reflection at $10.6 \mu\text{m}$. Flatness is $\lambda/50$ at $10.6 \mu\text{m}$ over 85% of the diameter. The in-vessel mirrors in the receiving port are 90 mm wide in the smaller direction, therefore the window has to be considered as the aperture stop of the system when the beam is centered on it. The transmission was stated to be larger than 99.4% for perpendicular incidence; and was indeed experimentally measured to be larger than 99%. Each window transmits about 60% of the visible laser power used for alignment; therefore, also in view of additional ZnSe optics, *viz.* lenses on the optical table, a possible double AR-coating at $10.6 \mu\text{m}$ and 632 nm was considered but, since the cost was much higher than the price of a new visible laser with enough power to compensate for losses induced by the windows, only the AR-coating at $10.6 \mu\text{m}$ was eventually chosen.

The window thickness has to be large enough to withstand the pressure load, i.e. 1 bar. In view of the significant cost of ZnSe optics with excellent optical quality, as well as the potential safety issues, it is vital that the windows be sufficiently thick to withstand this

load over long periods of times without breaking. Even though an increase in thickness reduces the optical transmission slightly, the losses are dominated by surface reflections, which can be eliminated by anti-reflective coatings. The required thickness depends on a number of factors, namely

- Mounting flange size
- Stress resulting from mounting or sealing
- Flange clamping stresses
- Mounting flange flatness
- Stress due to thermal expansion
- Vibration effects
- Pressure cycling or surges
- Thermal shock/cycling
- Mounting surface rigidity
- Mounting surface roughness
- Optic edge roughness
- Desired optical specifications

Given the impossibility to perform precise calculations taking into account all these factors, the following formula for the required thickness T is usually adopted for a circular unclamped window supported by a flat flange around its edge

$$T = \sqrt{\frac{1.1Pr^2S}{M}} \quad (3.117)$$

where P is the pressure load, r the radius of the window, S is a safety factor and M is the rupture modulus of the material. For ZnSe the required thickness is of the order of 5 mm. The differential equation governing the vertical displacement w of a membrane loaded with pressure $p(x, y)$ is the Germain-Lagrange equation

$$\nabla^4 w(x, y) = \frac{p(x, y)}{D} \quad (3.118)$$

where $D = ET^3/12(1 - \nu^2)$, T being the membrane thickness, E the Young modulus and ν the Poisson ratio. For ZnSe $E = 74.3$ GPa and $\nu = 0.31$. Normalizing every length

to the windows radius R_0 and transforming to cylindrical coordinates, Eq.3.118 can be solved with the following boundary conditions

$$w_n(1) = 0, \quad \frac{\partial w_n}{\partial r_n}(0) = 0, \quad \frac{\partial^2 w_n}{\partial r_n^2}(0) = 0 \quad (3.119)$$

which lead to the following solution (the third condition imposes two integration constants to be zero)

$$w_n \equiv \frac{w}{R_0} = \frac{3(1 - \nu^2)p}{16E(T/R_0)^3} \left[\left(\frac{r}{R_0} \right)^4 - 1 \right]; \quad (3.120)$$

this gives $1.4\mu\text{m}$ in the center of a 10 mm thick window, whereas a thickness of 5 mm would result in about $11.8\mu\text{m}$. The induced curvature is zero in the center and maximum at the edge, the use of the thick lens equation yields a focal length larger than 90 m over the clear aperture of the window. The window diameters were chosen to be identical to compensate this effect, even though the window in the launching port could have been slightly smaller since the effective beam, being undiffracted, is smaller than in the receiving port.

We shall now describe the window supports.

Windows need to be hermetically sealed against a pressure load of 1 bar, therefore windows cannot be clamped but are supported instead by two flat flanges around the edge; the seal is provided by O-rings between the window and each flange. An O-ring, also known as a packing, or a toric joint, is a mechanical gasket in the shape of a torus; it is a loop of elastomer with a disc-shaped cross section, designed to be seated in a groove and compressed during assembly between two or more parts, creating a seal at the interface. O-rings are manufactured in a number of different materials, each of which is specified to have specific physical and chemical properties in given environmental conditions. The O-ring has to maintain its elasticity at the baking temperature of TCV, which, as this thesis is written, is 250 celsius. There is not yet a mapping of the temperature in the TCV vessel during the baking, so, since the flanges are positioned in the interior of the vacuum vessel, the maximum temperature had to be assumed. Moreover an increase of the temperature baking is also foreseen as a possibility for the future. O-rings were therefore chosen to be compatible with the present baking temperature, i.e. 250 celsius, with an additional cooling system which is used now only to provide a safety margin but will be imperatively required if the baking temperature will be increased above the O-ring thermal limit.

The chosen material is *Kalrez*, a perfluoroelastomeric material designed to tolerate up to 327 celsius, produced by *DuPont* (France). The two sides of each window are not compressed against identical O-rings but, to optimize the resistance in vacuum, a more elastic quality of *Kalrez* was chosen for the vacuum side. The grooves in the flange were also specifically designed for each O-ring; in Table 3.1 we report the design specifications.

	Air side	Vacuum side
Installed compression [%]	13.2	12.2
Operating compression [%]	19.1	21.5
Free volume [%]	20.9	19.7
Groove width [mm]	10	8.03
Groove depth [mm]	2.965	2.2
O-ring ID [mm]	88.49	88.57
O-ring ED [mm]	92.02	91.19
Metal-to-Metal Clearance gap [mm]	0.1	0.1
Rupture module [MPa]	17.91	21.7
Max operating T [°C]	327	280

Table 3.1: Design parameters of the Kalrez O-rings used to seal the ZnSe windows.

It must be stressed that the O-rings and the grooves are designed to withstand about 280 degrees celsius even if the cooling system fails.

The flange is designed in such a way as to clamp the window on its outermost annulus of 7.5 mm width, therefore leaving the central circle of 85 mm in diameter, which is the area over which flatness is specified, as the clear aperture of the system. The aperture stop radius is therefore 42.5 mm.

3.6.8 Bellows

Bellows are to be designed based on a number of parameters: pressure drop, baking temperature, linear stroke, number of cycles, external and internal diameters. The launching port requires the maximum space available for mirror positioning, since one of the mirrors has to be positioned in the space enclosed by the bellows itself and the beam travels at finite angles with respect to the bellows sliding direction. The receiving port does not present this problem as the beam is designed to exit the port in the radial direction, that is parallel to the bellows sliding direction, and the space available allow to position the bellows beyond the last in-vessel mirror, therefore the internal bellows diameter is constrained only by the beam size. The pressure drop is obviously 1 bar.

The baking temperature, for the same considerations exposed in Sec.3.6.7, was required to be 350 °C; the linear strokes, and thus the number of convolutions, are derived by imposing that system be able to position the innermost point of the front-mirrors at least 2 cm beyond the wall, that is 4 cm beyond the tiles, for maximum protection when the system is not operated, or during baking and boronization operations.

If the system has to be operated on a daily basis, considering a maximum of 4 cycles a day, 250 days of operation a year, we designed the bellows to operate for 10 years, i.e. 10000 cycles.

Both sets of bellows were manufactured by *Comvat* (Switzerland) in stainless steel, grade 316L.

3.6.9 The optical table

PCI can be set to detect ion or electron spatial scales by changing the optical magnification of the imaging system. An optimal design is such that, to change the total magnification, only optics on the optical table and after the phase plate need to be changed. This translates, for the relay optic, into a precise focal length and a precise distance from the paraboloid. The focal lengths of the paraboloid and of the relay lens and their distance determine the effective focal length which, in turn, gives the minimum phase plate diameter, for a given scattering angle, as well as the diameter of the first lens after the phase plate, and the phase groove diameter. Moreover the distance between the paraboloid and the relay lens determines the diameter of the relay lens itself, again for a given maximum scattering angle.

A number of different optical designs were explored in the attempt to satisfy all the optical requirements in terms of total magnification, minimization of the size of lenses and mirrors, minimization of the total beam path on the optical table (to minimize the size of the optical table itself and the number of optics to be installed on it), minimization of aberrations and optimization of the blur on focal planes.

The optical table was manufactured by *Thorlabs* (Germany) and was chosen to be 2 m long and 1 m wide, to be installed horizontally.

In Figs.3.33 and 3.34 we show the layout of the optical table for the two best performing optical designs for each of the optical magnifications of 0.12 and 0.55, respectively. The physical parameters for these four configurations are described in Table 3.2. Given the dimensions of the linear detector array, the two optical magnifications correspond to $0.9 \text{ cm}^{-1} \leq k \leq 13.5 \text{ cm}^{-1}$ and $4.1 \text{ cm}^{-1} \leq k \leq 62 \text{ cm}^{-1}$, respectively. It has to be underlined that the two magnifications have been chosen so as to result in overlapping spectral regions, which can therefore be benchmarked against each other.

The lenses were manufactured by *ULO Optics* (UK) and *Lambert Optics Ltd.* (Nevada) and were split between the two firms according to the most advantageous quotes proposed. The substrate material is ZnSe coated on both sides against reflection at $10.6 \mu\text{m}$. *Lambert Optics* lenses are characterized by scratch and dig 40-20 and surface accuracy $\lambda/4$ at 632 nm. *ULO Optics* lenses are specified with rms roughness less than 2 nm and surface accuracy $\lambda/80$ at $10.6 \mu\text{m}$. Two 45° ZnSe beam combiners with surface figure of $\lambda/4$ at

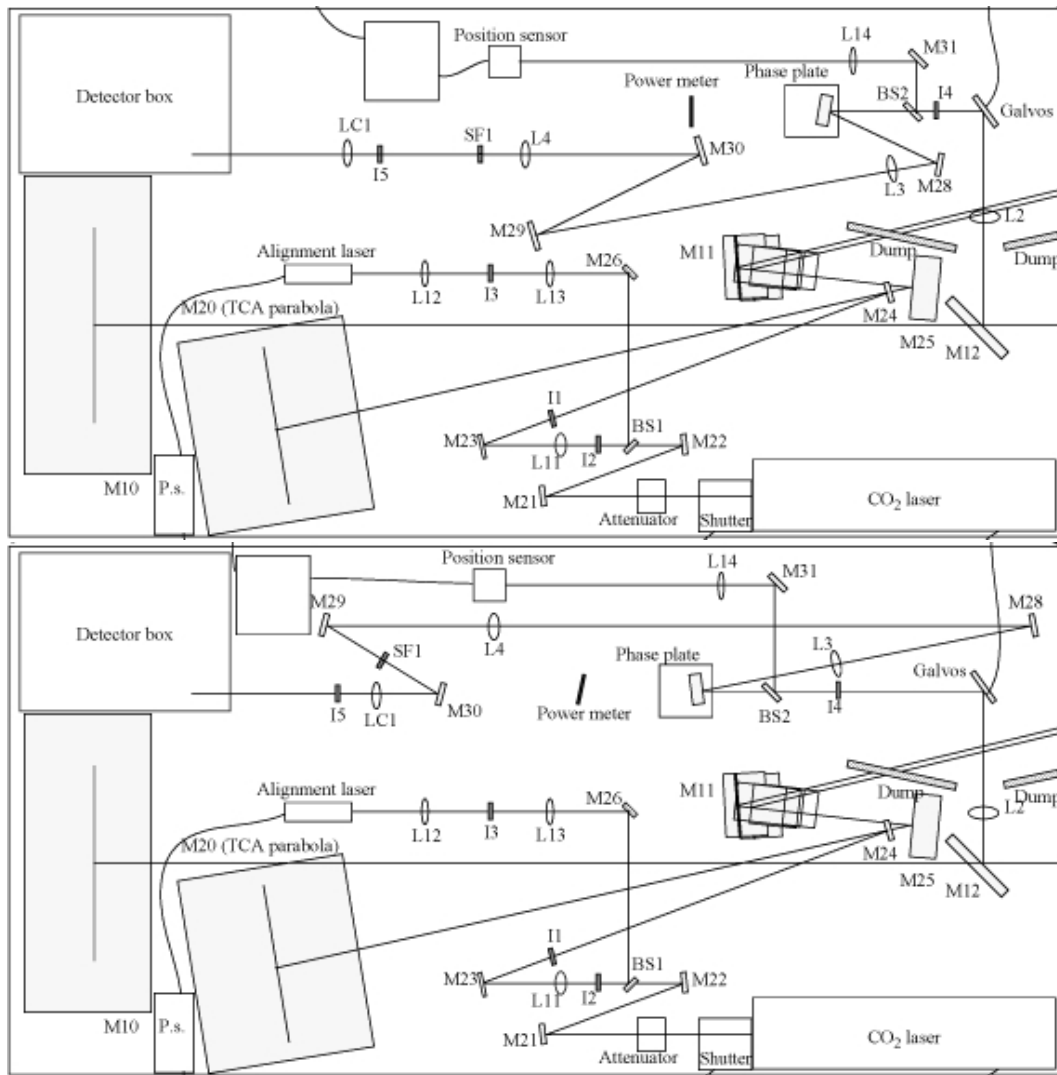


Figure 3.33: Schematic views of two feasible configurations on the optical table having a total magnification equal to 0.12. Mirrors are indicated as M, lenses as L, irises as I, the spatial filter as SF, M20 is the off-axis parabolic mirror used to expand the beam to the desired width, M10 is the focusing off-axis parabola.

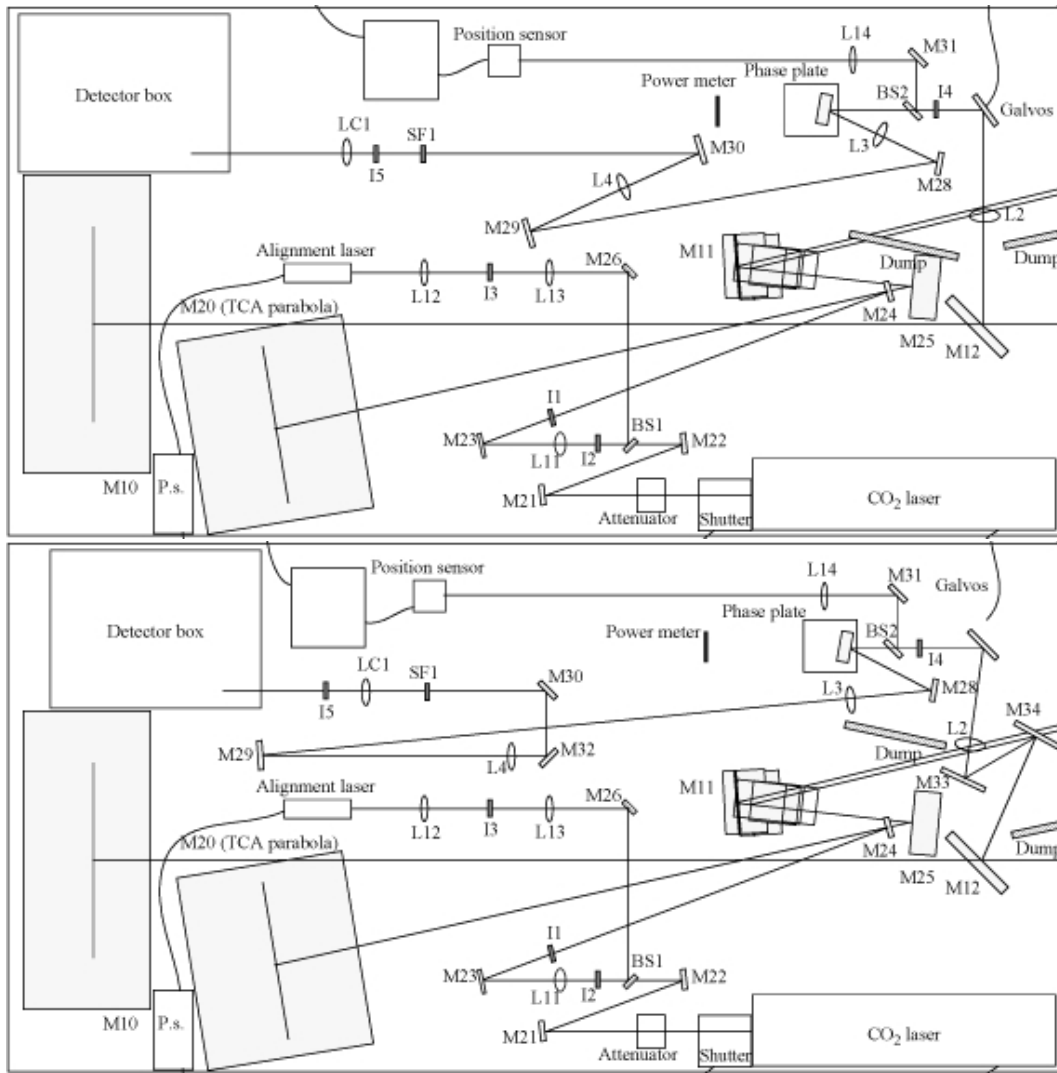


Figure 3.34: Schematic views of two feasible configurations on the optical table having a total magnification equal to 0.55. Mirrors are indicated as M, lenses as L, irises as I, the spatial filter as SF, M20 is the off-axis parabolic mirror used to expand the beam to the desired width, M10 is the focusing off-axis parabola.

	⌘ 1	⌘ 2	⌘ 3	⌘ 4
w_0 [m]	0.045	0.045	0.008	0.008
θ_0 [rad]	0.0023	0.0023	0.01	0.01
M	0.12	0.12	0.55	0.54
Blur [μm]	74.3	35.4	109	58
OPD [μm]	0.596	0.19	0.313	0.232
F_1 [m]	3.43	3.43	3.43	3.43
F_2 [m]	0.381	0.508	0.381	0.381
F_3 [m]	0.254	0.254	0.254	0.381
F_4 [m]	0.381	0.508	0.381	0.381
D_1 [m]	10	10	10	10
D_2 [m]	4.93	4.82	4.93	5.17
D_3 [m]	0.82	1.08	0.629	0.878
D_4 [m]	1.39	1.39	1.2	1.36
$\partial M/\partial D_1$ [m^{-1}]	-2.92e-3	-2.76e-3	-0.366	-0.296
$\partial M/\partial D_2$ [m^{-1}]	0.0563	5.7e-2	-1.04	-0.781
$\partial M/\partial D_3$ [m^{-1}]	-0.382	-0.241	-5.81	-2.68
$\partial M/\partial D_4$ [m^{-1}]	-0.203	-0.231	-2.16	-2.01
$\partial \text{Blur}/\partial D_1$	-2.03e-5	-3.42e-6	-3.72e-5	-7.17e-5
$\partial \text{Blur}/\partial D_2$	1.25e-4	-2.02e-5	-2.96e-4	-3.34e-4
$\partial \text{Blur}/\partial D_3$	4.09e-4	5.09e-5	7.11e-5	9.75e-5
$\partial \text{Blur}/\partial D_4$	-1.02e-4	-2e-5	-2.09e-4	-1.88e-4

Table 3.2: Physical parameters for the four adopted optical designs. M is the total magnification, F_x the focal length of lens x , D_x the distance between lens x and lens $x - 1$, $x = 0$ corresponds to the object plane.

10.6 μm were also bought from *ULO Optics*.

3.6.10 Detectors

The PCI diagnostic will make use of two detectors already used on the tokamak TCA and available at the CRPP: the first one is a single detector manufactured by *Société Anonyme de Telecommunication* (France), indicated as *SAT* in the following, and the second one is a linear array manufactured by *Infrared Associates Inc.* (Florida), indicated as *array* in the following. The physical properties are specified in Table 3.3. Considering Eq.3.104, for the

Kind	Single-element PV	Array PC
Area per element [mm^2]	0.196	0.06
D^* [$\text{cm}\sqrt{\text{Hz}/\text{W}}$] (declared)	$5 \cdot 10^{10}$	$3 \cdot 10^{10}$
D^* [$\text{cm}\sqrt{\text{Hz}/\text{W}}$] (measured)	$2.5 \cdot 10^{10}$	$1.5 \cdot 10^{10}$
Saturation power [mW]	14	0.12
Operating T [K]	77	77
Bandwidth [MHz]	10	1
Spacing [μm]	n.a.	50

Table 3.3: Physical properties of single-element and array detectors.

detector array we find a minimum measurable fluctuation phase of $1.2 \cdot 10^{-5} \text{rad MHz}^{-1/2}$ which corresponds, for an integration length of 10 cm, to $4 \cdot 10^{15} \text{ m}^{-3} \text{MHz}^{-1/2}$. For the SAT detector, considering the same integration length we obtain $8 \cdot 10^{14} \text{ m}^{-3} \text{MHz}^{-1/2}$ as minimum detectable fluctuating density. This quantities were considered in the choice of the acquisition system.

- The measured bandwidth has been tested only up to 500 kHz which was the maximum possible modulation frequency of the laser power.
- In the array detector only 24 elements are actually working, numbers 2-6-7-10-14-22 do not respond to the input signal.

In Fig.3.35 we show the calibration of the preamplifiers to be used with the linear array and the single-element detector. The linear array has two sets of amplifiers, the first operating between 50 kHz and 150 kHz, the second one between 10 kHz and 3 MHz. The single element detector has also two sets, from dc to 10 kHz and from dc to 200 kHz, respectively. A new linear array of detectors, with or without matched pre-amplifiers, cannot be purchased within current budget limitations.

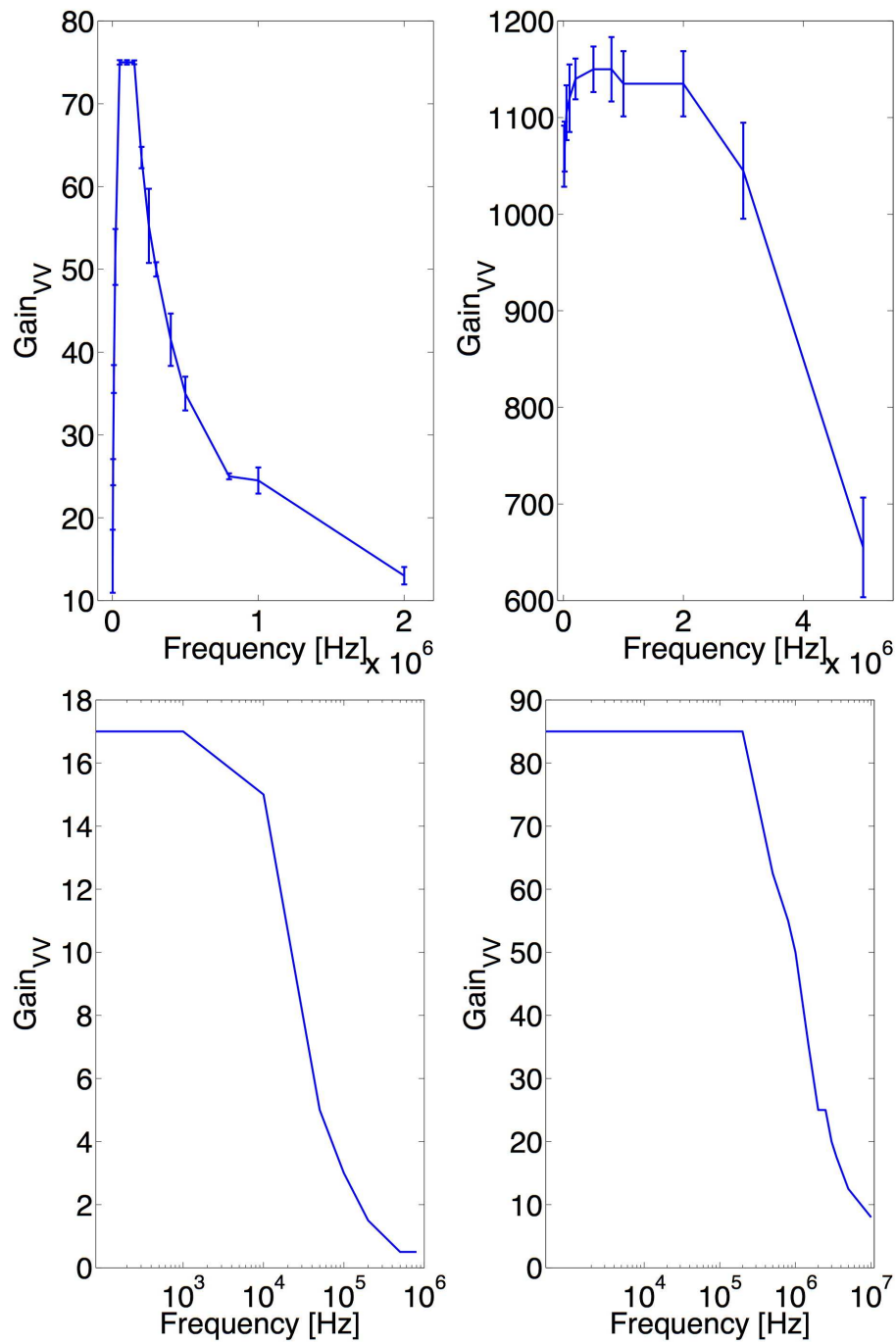


Figure 3.35: (Top) Voltage-to-Voltage gain of the thirty preamplifiers of the detector array in the low and the high frequency range. Mean values and errorbars are averaged over all pre-amplifiers. (Bottom) Voltage-to-Voltage gain of the single element pre-amplifier in the two frequency ranges.

3.6.11 Data acquisition

The acquisition system is one the most expensive parts of the diagnostics. Even though the detector array has only 24 working elements it was decided to buy a 32 channel digitizer manufactured by *D-TACQ Solutions Ltd.* (Scotland) in view of a possible future upgrade of the detector array. With the same spirit the acquisition system can sample at a much higher frequency than the bandwidth of the detector array; the choice of the highest sampling frequency was dictated by physics arguments: the highest frequency of fluctuations expected in the TCV tokamak.

The cost of the acquisition system depends mainly upon the number of modules needed. Since the number of channels that can fit into a module is a function of the sampling frequency, the cost estimate strongly depends on its value. In the following a number of possibilities are shown.

The standard digitizer, widely used on TCV, is *ACQ216CPCI-16-50-M5-RTMDDS* which can be configured for the following sampling rates:

- 16 channels at 16 mega samples per second (MSPS)
- 12 channels at 22 MSPS
- 8 channels at 25 MSPS
- 4 channels at 50 MSPS

Other properties are: 14 bit as resolution, simultaneous sampling, 1 GB memory (3 sec at full tilt), Gigabit Ethernet on Rear Transition Module (RTM), voltage ranges $\pm 3V$, Linux kernel 2.6 embedded. The output voltage was chosen after an evaluation of the bit noise compared to the detector noise.

A set of about one thousand linear, electrostatic, ETG simulations were performed with the GS2 code to estimate the maximum frequency to be expected in TCV. Simulations were performed with kinetic electrons and adiabatic ions, evolving five poloidal modes in the range $0.1 \leq k_{\theta} \rho_e \leq 0.8$. Results suggest that the less expensive option, i.e. two modules with 16 channels sampling at 16 MSPS each, is sufficient for TCV. Indeed, 5 MHz seems to be acceptable since the highest frequencies are lower than $3\text{MHz}\sqrt{T_e[\text{keV}]}$ for a reversed shear, which would result in frequencies around 4-5 MHz (the most unstable mode would be at about 1-3 MHz). Frequencies higher than 5 MHz are expected for $R/LT_e \geq 30$ and $R/Ln_e \geq 2$, which would be quite unusual for TCV. Positive shear cases show frequencies definitely lower than 4 MHz.

Each module is also equipped with a hardware filter at 5MHz to avoid aliasing of the signal and an External Clock Multiplier that multiplies an externally input signal by 12. The clock is therefore generated with the use of the standard 1MHz signal, fed into

the External Clock Multiplier to generate a 12 MHz signal which, with the use of a Digital Direct Synthesis clock, originates any arbitrary lower frequency signal. The jitter produced is ± 6 ns, which is then negligible compared to the sampling frequency.

The standard acquisition frequency is set to 12 MSPS; signals are additionally filtered at 3 MHz, decimated by a factor of 2, and stored also at 6 MSPS.

If higher fluctuation frequencies are to be acquired, two possibilities are open: frequencies a few times higher than the standard ones or frequencies a few tens of times higher. The first case is typical of fluctuations at the electron scale driven by high unstable wave-vectors ($k_{\theta}\rho_e \geq 2$); we will not be concerned here with S/N considerations concerning the amount of phase shift at these wavelengths but we will make only considerations concerning the acquisition frequency. In this case the acquisition system is capable of sampling 8 channels at 50 MSPS, thus possibly reducing the spatial resolution of the measurements, provided a new array detector with sufficient bandwidth becomes available. The change in the spatial resolution depends on the length of the new linear detector and on the magnification of the imaging system.

The second case is typical of externally launched RF waves at a multiple of the ion cyclotron frequency which, for TCV, is about 21 MHz for hydrogen. There is at present no ion cyclotron heating on TCV, but this could conceivably be added in the future. Whether the hydrogen first harmonic or Mode Converted scenarios at the cyclotron frequency of an impurity are employed in TCV, frequencies of interest will be close to the Nyquist limit of this acquisition system and therefore their detection will probably require an optically heterodyne configuration[3].

An optically heterodyne configuration requires the use of a modulator; on the market available options are Acousto-Optic (AOM) and Electro-Optic (EOM) Modulators. The ACM makes use of a radio-frequency wave which, traveling in an acousto-optic cell, splits the probing laser beam into an un-diffracted component and a diffracted one which is up-shifted in frequency by the frequency of the RF wave. The diffracted beam can then be recombined with the un-diffracted one originating a power modulation at the RF frequency

$$E = \alpha E_0 \cos(\Omega t) + \beta E_0 \cos[(\Omega + \Delta\Omega)t] \implies I = I_0(\alpha^2 + \beta^2) + \alpha\beta I_0 \cos(\Delta\Omega t) \quad (3.121)$$

where Ω is the laser frequency, $\Delta\Omega$ the modulation frequency and α and β real positive numbers such that the sum of their squared values is smaller than unity; these model the depletion of the original power, I_0 , and the fraction converted to the frequency shifted beam, respectively.

Fluctuating components will now appear at the original frequency ω and at two sidebands $\Delta\Omega \pm \omega$; the signal is then mixed with the reference signal and downshifted by $\Delta\Omega$. If the acquisition electronics were able to process both sidebands, the signal to noise ratio,

normalized to its homodyne counterpart, would read

$$(SNR)_{rel} = \alpha^2 \beta^2 \quad (3.122)$$

and half of it if the acquisition system was not able to. The shot-noise is almost entirely determined by the Local Oscillator (LO), whose relative power fraction is equal to $\alpha^2 + \beta^2$. The total relative signal to noise ratio can be written as

$$(SNR)_{rel} = \begin{cases} \alpha^2 \beta^2 / 4 & \text{if intrinsic noise is dominant} \\ 0.25 \alpha^2 \beta^2 / (\alpha^2 + \beta^2) & \text{if shot-noise is dominant} \end{cases} \quad (3.123)$$

if only one side-bands is processed, and the double if both of them are.

AOMs offered by *Isomet* (Virginia), *Brimrose* (Maryland) and *AA-Optoelectronic* (France), generate a minimum modulation frequency of 40 MHz which, considering the sampling rate of the acquisition system, translates into measurements in the 32-48 MHz region. This scheme results in a factor of 8 signal-to-noise loss. Alternatively only one of the two beams exiting the AOM can be used, with amplitude modulation applied directly to the AOM, at any frequency from 0 to 20 MHz with a factor of 10 S/N loss.

To increase the overall efficiency, Weisen proposed [8] a configuration in which the direct and the frequency up-shifted beams cross in the plasma at a small angle, larger than the maximum scattering angle to be resolved. A spatial filter then blocks the unscattered components of the unshifted beam. The PCI signal is then the interference of the scattered components of the unshifted beam and the unscattered components of the shifted one. In our design, this configuration cannot be achieved because the shifted beam would be clipped by the numerous optics.

Alternatively to AOMs, EOMs employ birefringent crystals which undergo modifications of their refractive index in response to an applied electric-field. Coupled to appropriate polarizers, they produce amplitude modulations at the frequency of the electric field applied to the crystal. Polarizers transmit about 50% of the input power. An EOM permits a continuous modulation from DC up to 100MHz, with the exceptions of certain frequencies, at which mechanical resonances within the crystal affect the response. The cost for the Pockels cells was estimated by *Cleveland Crystals* (Ohio) as high as 20000 CHF, without guarantees on the performance at 10.6 microns. The expected reduction of the S/N ratio, with respect to the homodyne case is about 97%. Because of the large losses in S/N in these heterodyne schemes, they are more suitable for measurements of coherent modes, such as externally launched rf waves. In the first implementation of the diagnostic on TCV we do not foresee to employ this technique.

3.7 Data analysis techniques

Since the Phase Contrast method provides an image of density fluctuations, the spatial scale properties of the instabilities have to be deduced directly from the image. In this respect one can choose from various approaches, among which the most popular are: spatial correlation lengths, Fourier series and wavelets analysis.

The spatial correlation is probably the most useful and straightforward information if one wants to compare experimental results to global gyrokinetic codes which calculate the spatial envelope of the instability, i.e. a correlation length, which is formally defined as the spatial distance above which the zero time lag cross-correlation coefficient between two samples falls below the value $1/e$.

$$C_{1,2}(|\vec{l}|, 0) = \frac{E[c_1(\vec{r}, t)c_2(\vec{r} + \vec{l}, t)]}{\sqrt{E[c_1(\vec{r}, t)^2]E[c_2(\vec{r} + \vec{l}, t)^2]}} \quad (3.124)$$

where E stands for *expectation* while c_1 and c_2 are two generic signals around their expected values.

It is also common, and more dense in information, to express the spatial scale as a Fourier series which gives an immediate interpretation of the instabilities as a sum of wavelengths. However, to accurately estimate a Fourier series one needs a sufficiently high number of samples to obtain a good estimate. When analyzing time series, the number of samples is directly proportional to the sampling rate, while when performing spatial analysis, the number of points is the number of detectors. If the detector bandwidth is sufficiently large, it is not, in general, problematic to increase by one order of magnitude the temporal digitizing frequency, while it is much more expensive to increase, by the same ratio, the number of detectors; this leads to estimates of spatial scales based on a relatively low number of samples.

As described in Sec.3.6.10, our linear detector has twenty-four working elements not uniformly spaced due to the presence of six defective elements. The low number of spatial points and their non uniform spatial distribution suggests the use of alternative approaches to standard Fourier analysis to validate the results obtained. Among those we describe the Maximum Entropy Method (MEM) [17] and, particularly concerning the non-uniformity of the samples, alternative Fourier spectrum estimates [21, 22].

Other methods based on the recovery of missed samples in the case of oversampling with respect to the signal bandwidth exist, such as the Papoulis-Gerchberg Iteration, the Minimum Dimension Formulation and related improved or modified versions[24]. The former is based on oversampling, with respect to the signal bandwidth, such that, starting from an initial guess of the missing samples, by filtering the signal up to the expected signal bandwidth and substituting the actual samples in the filtered signal, after a few iterations,

the missing samples are recovered. The latter is based on the sampling theorem which we report

The Sampling theorem *If $f(t)$ is continuous and bandlimited to ω_m , then $f(t)$ is uniquely defined by its samples taken at twice ω_m . The minimum sampling frequency is $\omega_s = 2\omega_m$ and $T = \pi/\omega_m$ is the maximum sampling period. Then $f(t)$ can be recovered by the interpolation formula*

$$f(t) = \sum_{n=-\infty}^{\infty} f(nT) \text{sinc}(t - nT) \quad (3.125)$$

If we have k unknown samples $f(t_k)$, we can write them as

$$f(t_k) = \sum_{n=-\infty}^{\infty} f(t_k) \text{sinc}(t_k - nT) = \sum_{h=1}^k f(t_h) \text{sinc}(t_k - t_h) + h_k \quad (3.126)$$

where h_k are sums of known samples. Therefore Eq.3.126 can be re-written as

$$u = Su + g \quad (3.127)$$

by inverting the matrix S the unknown vector u can be found.

3.7.1 Maximum Entropy Method

The Maximum Entropy Method (MEM) consists of performing a linear prediction of the data by means of an Auto Regressive (AR) model whose coefficients are then used in the power spectrum estimates. Let us give an overview of the whole algorithm. An Auto Regressive Moving Average (ARMA) model of orders p and q is a method historically used to find a best fit of a time series to its past values, and use the results to predict the future behavior. It can be formally written as

$$\sum_{k=0}^p \alpha_k y^{(k)}(t) = \sum_{k=0}^q \beta_k x^{(k)}(t) + \epsilon(t) \quad (3.128)$$

where x^i are the input data, y^i the output data, the subscript (k) indicates the k^{th} derivative, α and β are the parameters of the model and ϵ is white noise. It is formed by an autoregressive part of order p and a moving average part of order q . Its discretized version reads

$$\sum_{k=0}^p \alpha_k y(t - k\Delta t) = \sum_{k=0}^q \beta_k x(t - k\Delta t) + \epsilon(t) \quad (3.129)$$

Considering only the AR part and dividing everything by α_0 we obtain a frequency transfer function of the form

$$H(f) = \frac{1}{\alpha_0} \frac{1}{1 + \sum_{k=1}^p \frac{\alpha_k}{\alpha_0} e^{-2\pi i k f \Delta t}} \quad (3.130)$$

We thus obtain a model which is an all-pole infinite impulse response filter. There are a few constraints on the parameters in order to assure that the process X is wide sense

stationary[27]. The model can also be made nonlinear by adding quadratic and even higher order terms of the forms

$$X_n X_{n+1} \quad X_n X_{n+1} X_{n+2} \quad X_n X_{n+1} \dots X_{n+p} \quad (3.131)$$

where $p+1$ is the order of the nonlinearity; these models will not be considered here.

Let us now address the estimate of the Fourier spectrum. If we do not restrict ourselves to real frequencies in the Nyquist interval but consider the whole complex plane, we obtain the following z -plane which is one-to-one mapped onto the Nyquist interval on the real axis

$$z = e^{2\pi i f \Delta t} \quad (3.132)$$

where Δt is the sampling interval. The Fourier discretized power spectrum can be written as

$$P(f) = |\sum_{j=-N/2}^{j=N/2} c_j z^j|^2. \quad (3.133)$$

The complex plane formulation allows us to interpret the meaning of the power spectrum estimate as a truncated Laurent series, which is only an approximation of an analytical function as the latter is fully described only by the full infinite series, which is equivalent to the usual infinite time or spatial domain description.

The trick of the method lies in approximating Eq.3.133 by a rational function in the denominator

$$P(f) = \frac{a_0}{|1 + \sum_{j=1}^N a_j z^j|^2} \quad (3.134)$$

with the constraint that the N a_j must agree with the first N terms of the Laurent expansion of the real power spectrum. The justification of the trick is the capability to fit a potentially spikey spectrum with a function which possesses poles instead of zeros on the unit circle, which corresponds to the Nyquist frequency. The approximation stated by Eq.3.134 is known as *all-poles model*, *Maximum Entropy Method*, or *Auto Regressive model*. Now, the new formula for the power spectrum looks like the linear filter response function in the special case of an AR model (Eq.3.130), thus allowing us to approximate the power spectrum of a signal by evaluating an AR linear model. The advantage of this model is its capability to fit spikey spectral features of the real power spectrum.

Let us finally evaluate the coefficients of the AR model. Let y_i be the realizations of the wide sense stationary process Y , z_i its sampled values and ϵ_i the error associated with the measurement

$$z_i = y_i + \epsilon_i \quad (3.135)$$

at each time. The AR model gives

$$\hat{y} = \sum_{k=1}^p \alpha_k z_k + \delta \quad (3.136)$$

where δ is the deviation of the model from the measurements. The most obvious *modus operandi* is to minimize δ in a least squares sense, thus, by denoting ensemble averages by angular brackets, we obtain

$$\begin{aligned} \langle \delta^2 \rangle &= \langle [\sum_{k=1}^p \alpha_k (y_k + \epsilon_k) - \hat{y}_k]^2 \rangle \\ &= \sum_{h,k=1}^p (\langle y_k y_h \rangle + \langle \epsilon_k \epsilon_h \rangle) \alpha_h \alpha_k - 2 \sum_{k=1}^p \langle \hat{y}_k \rangle \alpha_k + \langle \hat{y}^2 \rangle \end{aligned} \quad (3.137)$$

minimizing with respect to the model coefficients leads to a system of linear equations which can be resolved with standard techniques.

The accuracy of the model depends on the number of coefficients, i.e. the number of poles, with respect to the number of data points. In Fig.3.36 we show the power spectra, as a function of the relative number of poles and samples, in the cases of a large number ($\simeq 1000$) and a low number ($\simeq 30$) of evenly spaced data. The result suggests the use of a moderate number of poles which needs to be larger than a few and less than about one hundred.

3.7.2 Unevenly spaced data

Usually most of the algorithms are based on the assumption that the sampling rate is constant in time or space, thus allowing the use of algorithms for the Fast evaluation of the Fourier Transform (FFT) of the signal. These algorithms are based on the original idea of Cooley-Tuckey [23] which permits to evaluate $\sim \log_2 N$ operations instead of N^2 , N being the length of the signal. In the case of unevenly spaced samples the FFT algorithm is not directly applicable anymore and possible solutions are to interpolate the data on an evenly spaced grid or, in the case of missing points, to replace missing data with zeros and then apply standard FFT algorithms. However, these techniques, in the case of a small data-set, will perform poorly as, in a sense, they invent the signal to analyze; especially in the case of adjacent missing points, which give rise to spurious peaks at frequencies comparable to gaps. An alternative approach is the Lomb-Scargle (LS) periodogram. This method was first proposed by Lomb [21] and later re-elaborated by Scargle [22], and consists of evaluating sines and cosines at the actual sampled locations, in time or space, to compute the normalized Lomb periodogram

$$P(f) = \frac{1}{2\sigma^2} \left\{ \frac{[\sum_{j=1}^N (y_j - \bar{y}) \cos(2\pi f(t_j - \tau))]^2}{\sum_{j=1}^N \cos^2(2\pi f(t_j - \tau))} + \frac{[\sum_{j=1}^N (y_j - \bar{y}) \sin(2\pi f(t_j - \tau))]^2}{\sum_{j=1}^N \sin^2(2\pi f(t_j - \tau))} \right\} \quad (3.138)$$

where y_i are sampled data at points t_i , \bar{y} denotes the average, σ its standard deviation and τ , defined as

$$\tan(2\pi f\tau) = \frac{\sum_{i=1}^N \sin(2\pi f t_i)}{\sum_{i=1}^N \cos(2\pi f t_i)}, \quad (3.139)$$

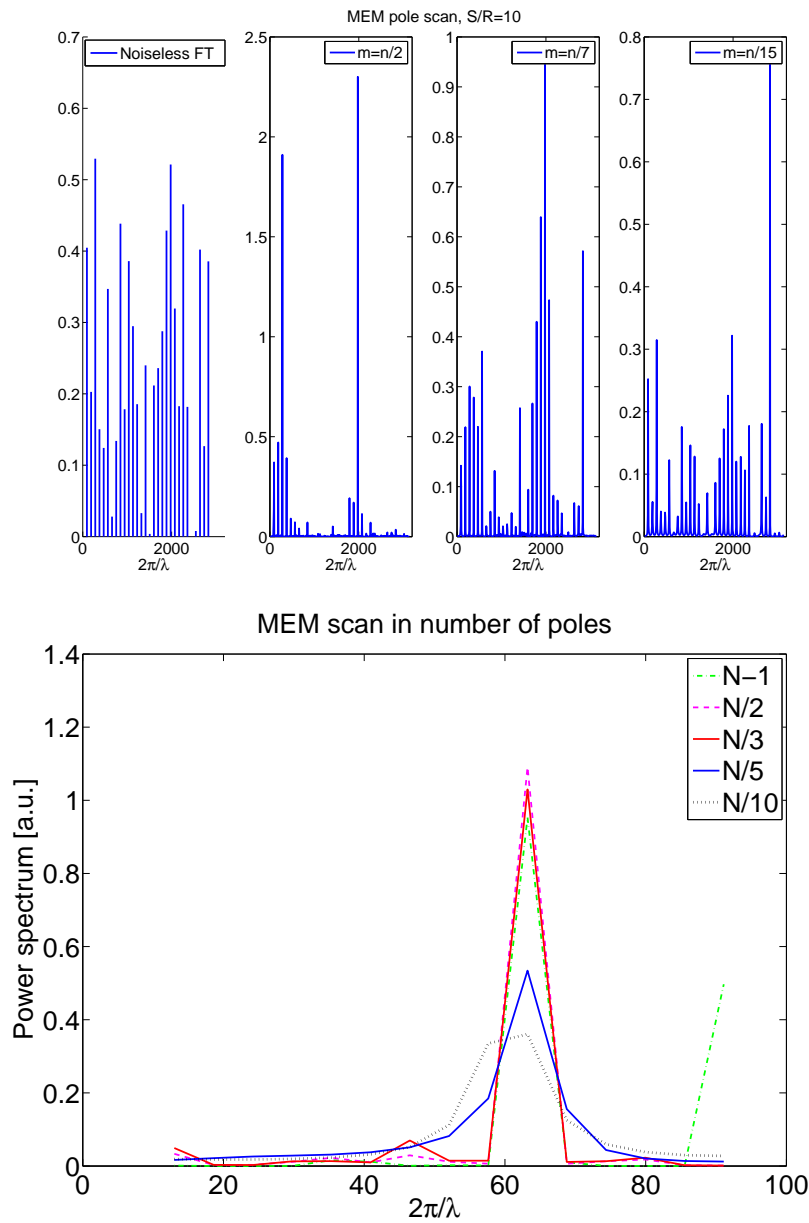


Figure 3.36: (Top) Power spectral estimate of a random set of Fourier components, polluted with white gaussian noise at SNR=10, as a function of the relative number of data, n , and poles, m . (Bottom) Same as left but with one single Fourier mode at $\lambda = 0.1$

is a constant which makes the data invariant to any shift and, more important, is such that Eq.3.138 would be the result if one estimated, at a given frequency f , the least squares fit of the signal to the model equation

$$y(t) = A \cos(2\pi ft) + B \sin(2\pi ft). \quad (3.140)$$

This method permits also the evaluation of frequencies above the Nyquist frequency corresponding to the average sampling rate, without any ambiguity due to aliasing; in particular it is extremely efficient in case of clustered data.

Let us now compare standard FFT techniques, MEM and LS on a large (≈ 1000), evenly spaced, data-set. In Fig.3.37 we compare standard FFT, MEM and LS on a set of random Fourier components added with white gaussian noise at SNR=10. It is evident that standard FFT and LS behave better than MEM.

If we now turn our attention to a low, unevenly spaced, data-set (corresponding to the

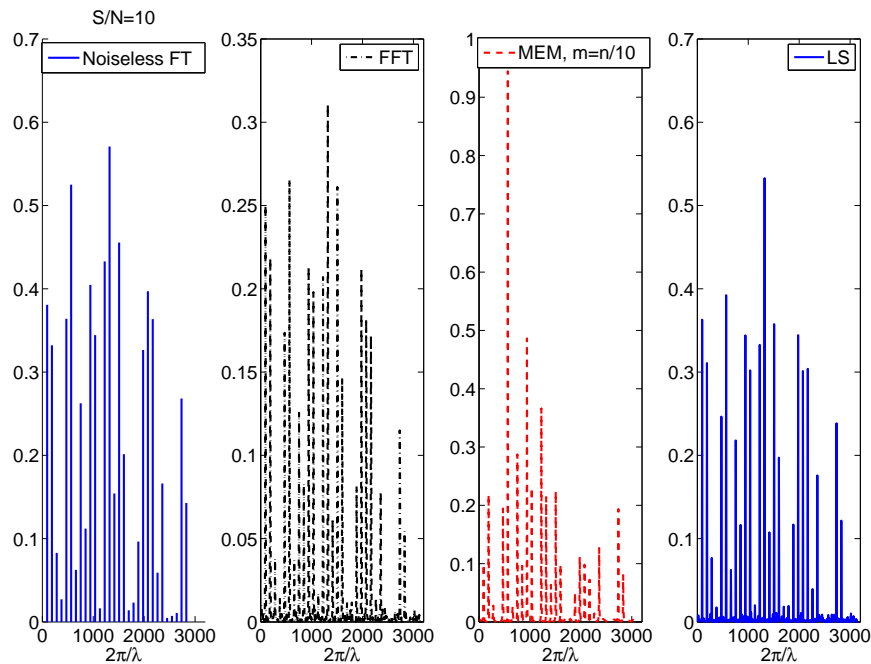


Figure 3.37: Comparison of MEM, FFT and LS algorithms applied to a number of random Fourier modes added with white gaussian noise at SNR=10.

PCI detector array), the relative performances of MEM, FFT and LS become much closer and are almost equivalent, as shown in Fig.3.38.

A dedicated graphical MATLAB routine was written to analyze the data of PCI and Doppler reflectometry. The routine includes modules to estimate the geometrical information needed by both systems. Analysis functions include standard routines as FFT as well as wavelet de-noising functions, non-linear analysis methods such as bi-spectra, and

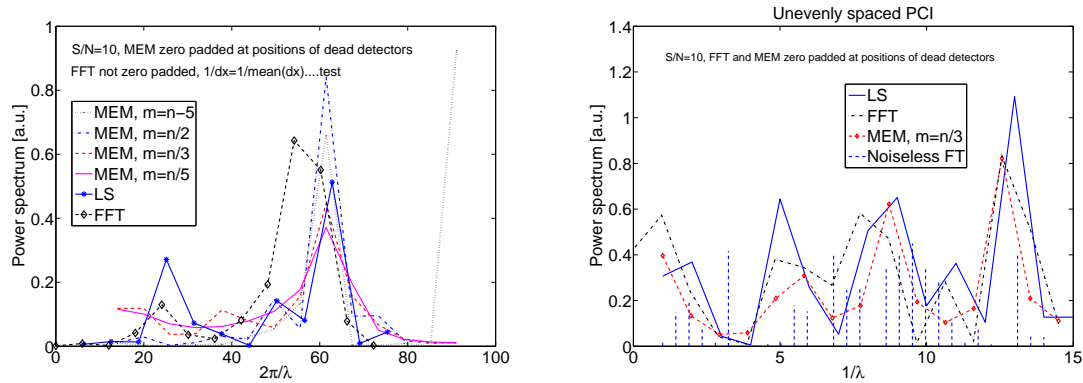


Figure 3.38: Comparison of zero-padded MEM mode, for a number of modes, FT and LS algorithm applied to (left) one single Fourier mode at $\lambda = 0.1$ and (right) a number of random Fourier modes. In both cases a white gaussian noise, with SNR=10, was added.

the numerical methods described above.

The following section describes the hardware and the analysis of preliminary data produced by the prototype Doppler Reflectometer (PREF) installed on the TCV tokamak at the very end of 2006. The present status of the PCI and PREF diagnostics is offered in Sec.3.9.

3.8 Doppler reflectometer

In Sec. 2.3 we showed that, among all the possible reflectometry configurations, the so-called Doppler configuration is the most interesting one as it can provide information concerning the plasma fluid velocity. In particular, since TCV has an excellent flexibility in terms of plasma positioning in the vacuum vessel, it is naturally a well suited tokamak for this kind of diagnostic.

We recall that Doppler reflectometry is also very attractive because, if used in a configuration with two or multiple nearby frequencies, it allows one to estimate the radial derivative of the fluid velocity, which is expected, on theoretical grounds[26], to suppress anomalous transport. However, considering the high investments and port allocation required on an already busy tokamak such as TCV, before installing a complete system featuring multiple frequencies, possibly sweepable as in radial correlation reflectometry, it appears imperative to evaluate the future performance of the system. At the end of 2006 it was decided to install a prototype Doppler reflectometer on loan from *Stuttgart University*, Germany.

Two systems are available: 70 GHz and 78 GHz; both are homodyne and can be used in O or X mode. One source at a time can be installed in the midplane port of sector 7,

which is shared with an oblique ECE diagnostic. The launching system, which is a replica of the launchers used for high-power electron cyclotron heating, consists of four mirrors injecting the microwave beam in the vacuum vessel with a poloidal angle between 10 and 55 degrees. The rotatable mirror can be moved at a maximum speed of 160 degrees/sec and can be swept even during a TCV pulse.

The acquisition system is a *CAMAC ADC* sampling at 10 MHz. The sampling frequency was chosen after an evaluation of the expected Doppler shift in various plasma configurations. With the 70 and 78 GHz probing frequencies, cut-off densities are equal to 6.3 and $7.8 \cdot 10^{19} \text{ m}^{-3}$ in O-mode, and typically 2.7 and $3.8 \cdot 10^{19} \text{ m}^{-3}$ in X-mode. The frequency shift $\Delta\omega$ is given by

$$\Delta\omega = \mathbf{k}_0 \cdot \mathbf{v}_e \quad (3.141)$$

where \mathbf{k}_0 is the probing wave vector and \mathbf{v}_e is the electron velocity in the laboratory frame, equal to the fluid velocity, of which the dominant component is generally assumed to be the $\mathbf{E} \wedge \mathbf{B}$, plus the turbulence phase velocity. The Bragg condition selects "only" one scattering vector and is therefore sensitive only to the phase velocity corresponding to that scattering vector. In TCV the resulting Doppler shift is to be expected in the range 0.1-2 MHz, depending on the incident angle. In view of this expectation, the passband filter of the electronics was modified to set the lower cut-off to 37 kHz, instead of the original 370 kHz.

In late 2006 a set of parasitic measurements were carried out to assess the performance of the prototype reflectometer. The reflectometer proved to be feasible as it is characterized by a very high SNR, more than two orders of magnitude, as shown in Fig.3.39.

The very high SNR allows one to distinguish clear signatures of physical events such as, core MHD phenomena, ELMs, L-H transitions and H-L back-transitions: we show an overview of all these events in an ohmic shot in Fig.3.40.

It should be noted, however, that the reflectometer is highly sensitive to electro-magnetic pick-up.

We finally prove the existence of a Doppler shift. In shot 33525, an ohmic diverted L-mode, the cut-off position is expected to be near the edge, $\rho \simeq 0.9$, and the reflectometer reveals, as shown in Fig.3.41 a clean spectrum centered at about $250 \pm 25\text{kHz}$. The poloidal injection angle was fixed at 20° resulting in a scattering wave number equal to $6.7 \pm 0.2 \text{ cm}^{-1}$, or a total velocity equal to about $2300 \pm 300 \text{ m/s}$, which is comparable to the electron diamagnetic velocity which, at the cut-off location, is about 2500 m/s .

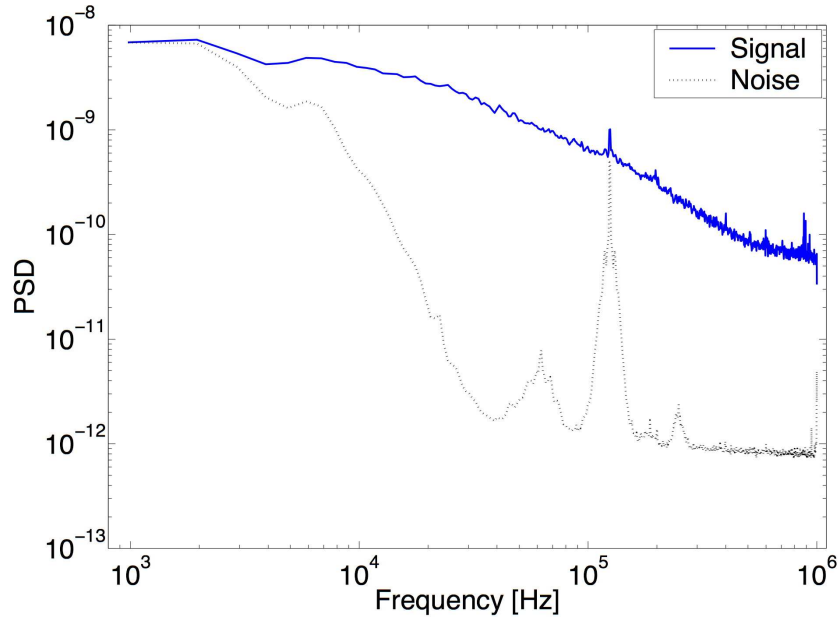


Figure 3.39: Power spectral density of the third-harmonic ECRH heated TCV shot 33576 showing an estimate of the SNR of the prototype reflectometer. The noise signal was acquired during shot 33571 after a major disruption. Noise is dominated by a highly monochromatic pick-up at 125 kHz; it is interesting to notice that, at that frequency, the noise level quantitatively accounts for the spike in the signal.

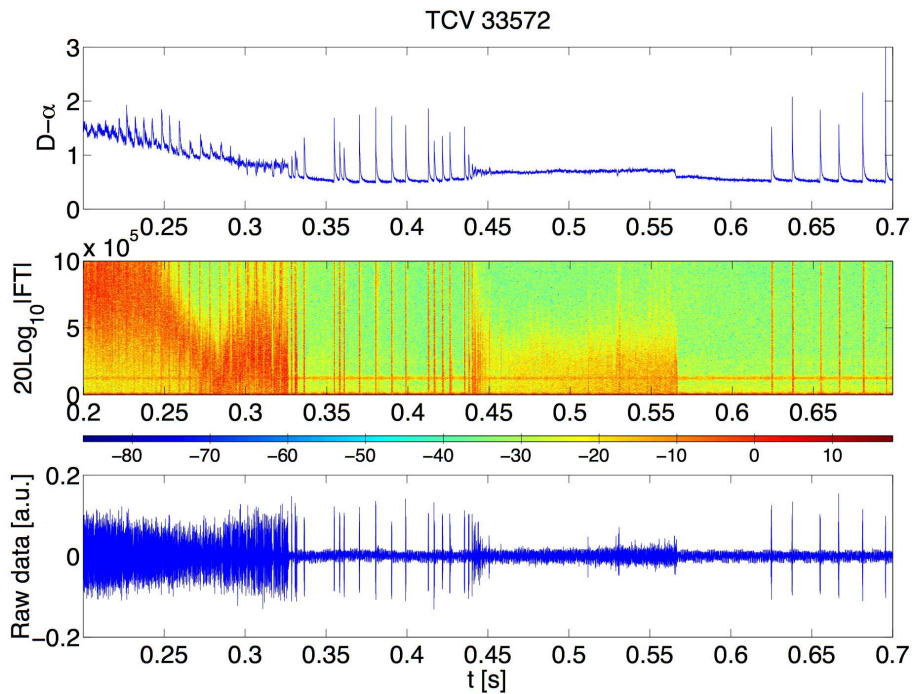


Figure 3.40: (Top) $D-\alpha$ signal of TCV shot 33572 as a function of time. (Centre) Time frequency spectrogram of the reflectometer signal. We notice clear signatures of core MHD events in the L-mode phase, L-H and H-L transitions, ELMs and a 125 kHz noise pick-up. (Bottom) Raw reflectometer data showing ELMs and the L-H and H-L transitions.

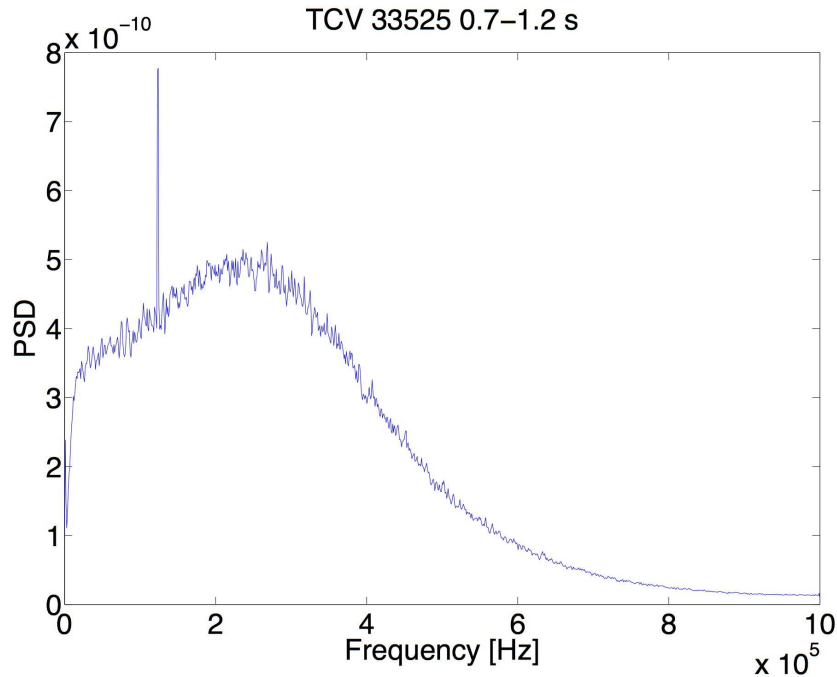


Figure 3.41: Power spectral density of the Doppler reflectometer for TCV shot 33525 between 0.7 and 1.2 seconds.

3.9 Present status

In this chapter we described the theoretical basis and the practical realization of the PCI diagnostic, in the tangential configuration, and of the Doppler Reflectometer; in this section we briefly discuss the present status of both diagnostics and how these will be employed in the near future.

All the components of the PCI diagnostics have been procured, the in-vessel and out-vessel optics have been installed and aligned up to the optical table. The final alignment is expected to take a few full working days and the diagnostic is foreseen to be operational by the end of 2009.

Initially the diagnostic will be probably used parasitically to assess its performance and exact response properties, this also in view of its completely new set-up. Later on it is reasonable to foresee its utilization on a large number of TCV pulses, with particular emphasis on key arguments in the research on magnetically confined plasmas. Indeed, dedicated sessions have already been allocated to investigate turbulence characteristics in Internal Transport Barriers (ITB), especially concerning their spatial variation across the foot and the head of the barrier, which are expected to be zones of micro-stability discontinuities; the impact of negative triangularity on turbulence in L-mode plasmas, especially regarding the radial behavior; effect of negative triangularity in ITBs, especially concerning a possible enhanced stabilization due to an increased Shafranov shift radial gradient induced by negative triangularity; impact of plasma shape on H-mode plasmas,

in particular on the stability of the Edge Transport Barrier.

The Doppler reflectometer is already operational and will be used in parallel to the PCI diagnostic to estimate $E \wedge B$ shear and its impact on transport.

3.10 Appendix: Evaluation of diffracting apertures

We want to evaluate here the effect of multiple diffractions induced by N apertures of radii a_i positioned at distances z_i between each other starting from the waist along the beam propagation direction, i.e. the waist is assumed to be at $z = 0$, the first aperture at $z = z_1$, the second at $z = z_1 + z_2$ and the last at $z = \sum_{i=1}^N z_i$.

We will limit ourselves to a case where the paraxial approximation holds, i.e. we will make use of multiple applications of the Fresnel-Kirchhoff integral (Eq.3.47) on an unperturbed gaussian beam (Eq.3.48).

Let us adopt the following cylindrical coordinates $(\rho_i, \phi_i, \xi_i) = (r_i/w_0, \phi_i, z_i/z_R)$ denoting variable in the planes z_i s, the first application gives at $z = z_2$

$$E(\mathbf{x}_\perp, z_2, a_1) = \sqrt{\frac{1}{\pi}} \frac{i e^{ik_0(z_1+z_2) - i \arctan(\xi_1)}}{\pi w_0 \xi_2 \sqrt{1 + \xi_1^2}} e^{i \rho_2^2 / \xi_2} \int_0^{2\pi} d\phi_1 \int_0^{a_1/w_0} \rho_1 d\rho_1 e^{i \rho_1^2 \left(\frac{1}{\xi_2} + \frac{i - \xi_1}{1 + \xi_1^2} \right)} e^{-2i \frac{\rho_1 \rho_2 \cos(\phi_1 - \phi_2)}{\xi_2}} \quad (3.142)$$

The symmetry of the problem imposes the equation to be independent of ϕ_2 thus allowing the integral over ϕ_1 to be equal to $2\pi J_0(2\rho_1\rho_2/\xi_2)$. The argument of the Bessel function is of order $z_R/z_2 \gg 1$ making a Taylor series expansion impossible; taking the limit $\lim_{x \rightarrow \infty} J_0(x) = \sqrt{2/(\pi x)} \cos(x - \pi/4)$ does not lead to analytical expressions either. Inverting the order of integrations we would obtain even more complicated functions which do not admit a primitive expressed as a combination of elementary functions. Let us therefore apply again the Fresnel-Kirchhoff integral to Eq.3.142 to obtain, at $z = z_3$

$$E(\mathbf{x}_\perp, z_3, a_{1,2}) = \sqrt{\frac{1}{\pi}} \frac{(2i)^2 e^{ik_0(z_1+z_2+z_3) - i \arctan(\xi_1)}}{w_0 \xi_2 \xi_3 \sqrt{1 + \xi_1^2}} \int_0^{a_2/w_0} \rho_2 d\rho_2 e^{i \left[\frac{\rho_2^2}{\xi_3} + \rho_2^2 \left(\frac{1}{\xi_2} + \frac{1}{\xi_3} \right) \right]} J_0 \left(\frac{2\rho_2\rho_3}{\xi_3} \right) \int_0^{a_1/w_0} \rho_1 d\rho_1 e^{i \rho_1^2 \left(\frac{1}{\xi_2} + \frac{i - \xi_1}{1 + \xi_1^2} \right)} J_0 \left(\frac{2\rho_1\rho_2}{\xi_2} \right) \quad (3.143)$$

after all the diffracting apertures we obtain

$$E(\mathbf{x}_\perp, z_n, a_{1,\dots,n}) = \sqrt{\frac{1}{\pi}} \frac{(2i)^n e^{ik_0 \sum_i z_i - i \arctan(\xi_1)}}{w_0 \prod_{i=2}^N \xi_i \sqrt{1 + \xi_1^2}} e^{i \frac{\rho_1^2}{\xi_4}} \sum_{i=2}^{N-1} \int_0^{a_i/w_0} \rho_i d\rho_i e^{i \rho_i^2 \left(\frac{1}{\xi_i} + \frac{1}{\xi_{i+1}} \right)} \int_0^{a_1/w_0} \rho_1 d\rho_1 e^{i \rho_1^2 \left(\frac{1}{\xi_2} + \frac{\xi_1 + i}{1 + \xi_1^2} \right)} \prod_{i=1}^{n-1} J_0 \left(2 \frac{\rho_i \rho_{i+1}}{\xi_{i+1}} \right) \quad (3.144)$$

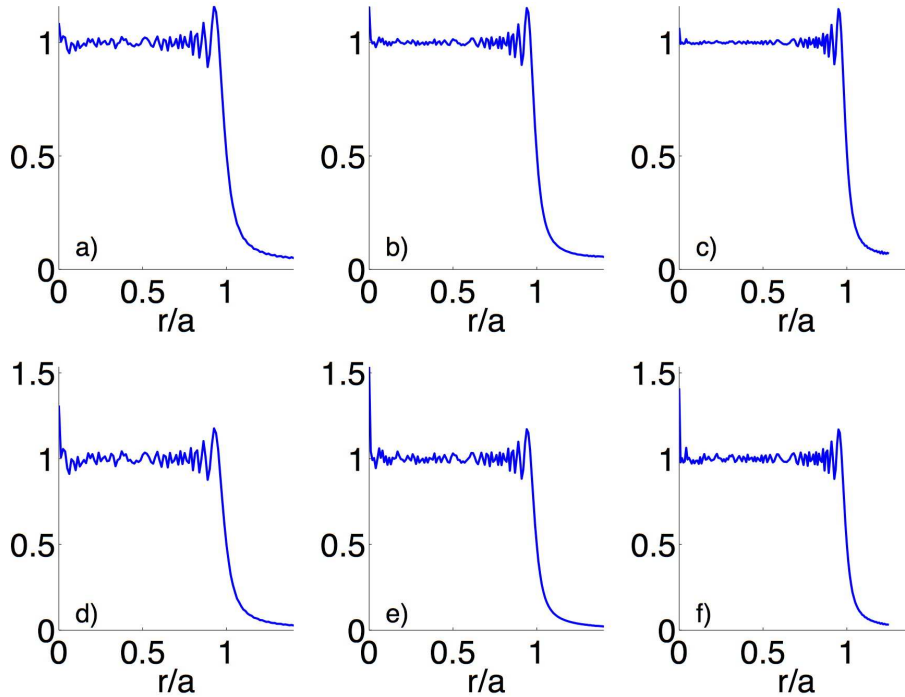


Figure 3.42: Absolute value of the transfer function of the first diffracting aperture (top) and of the additional ones (bottom) for $\alpha = 0.8$ (a), $\alpha = 1$ (b), $\alpha = 1.2$ (c), for $\xi_1 = 0.0028$, $\xi_2 = 0.0014$.

To have an idea of the propagation, let us now numerically evaluate first the recurrence integral

$$\frac{2l}{\xi_{i+1}} e^{ik_0 z_{i+1}} \int_0^{a_i/w_0} \rho_i d\rho_i e^{i \frac{\rho_i^2 + \rho_{i+1}^2}{\xi_{i+1}}} J_0 \left(2 \frac{\rho_i \rho_{i+1}}{\xi_{i+1}} \right) \quad (3.145)$$

for a number of values ξ_i and $\alpha_i = a_i/w_0$. In Fig.3.42 one can appreciate how diffraction effects are a decreasing function of α , which would point to the maximum allowable value. However, as already mentioned in Sec.3.3 it is important to keep a beam waist as large as possible for turbulence studies. If we calculate the standard deviation from unity for $r/a \leq 1$, which models the absence of diffraction effects, we obtain, for the three cases in Fig.3.42 0.1 – 0.09 – 0.08 for the top graphs and 0.12 – 0.11 – 0.1 for the bottom ones. We did not consider the reference function to be $1 - H(r/a - 1)$ as the standard deviation is then dominated by values outside $r/a = 1$, thus biasing the analysis. Other conditions might be considered, such as the values in particular points, however we consider $\alpha = 1.2$ satisfactory for our purposes.

Let us now analyze the behavior of a change in either ξ_1 or ξ_2 which we report in Figs.3.43 and 3.44. It is evident how ξ_1 barely affects the overall behavior of both curves as, being small, it is effective only in the numerator of Eq.3.142 and does not appear at all in Eq.3.145; while ξ_2 affects both the response in the center of the beam and at the edge. Since the recursive integral has to be evaluated for each optics, including mirrors

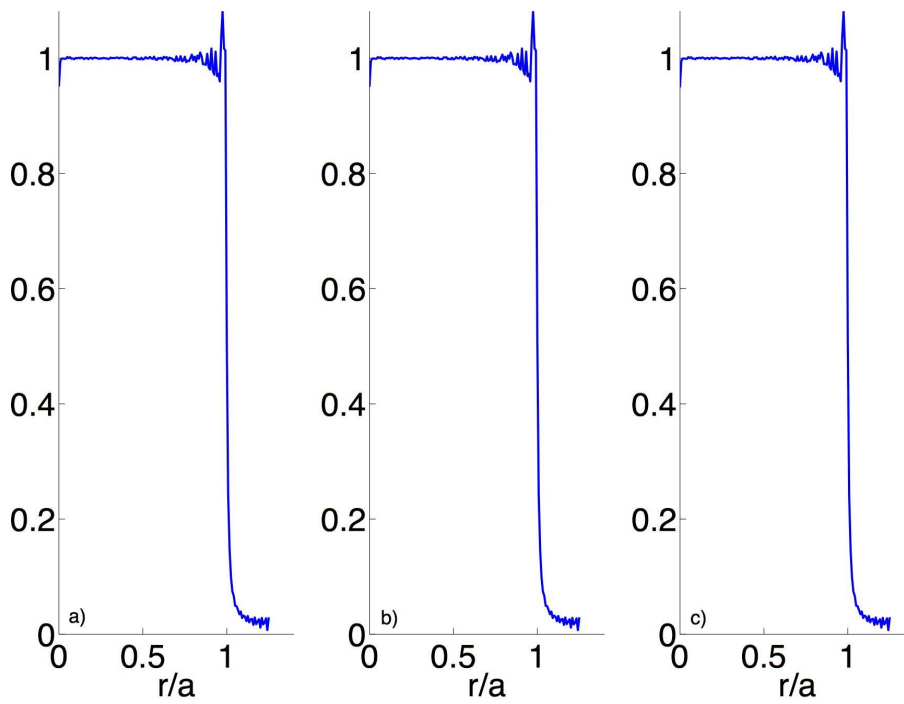


Figure 3.43: Absolute value of the transfer function of the first diffracting aperture for $\xi_1 = 0$ (a), $\xi_1 = 0.002$ (b), $\xi_1 = 0.01$ (c), for $\alpha = 1.2$ and $\xi_2 = 0.0001$.

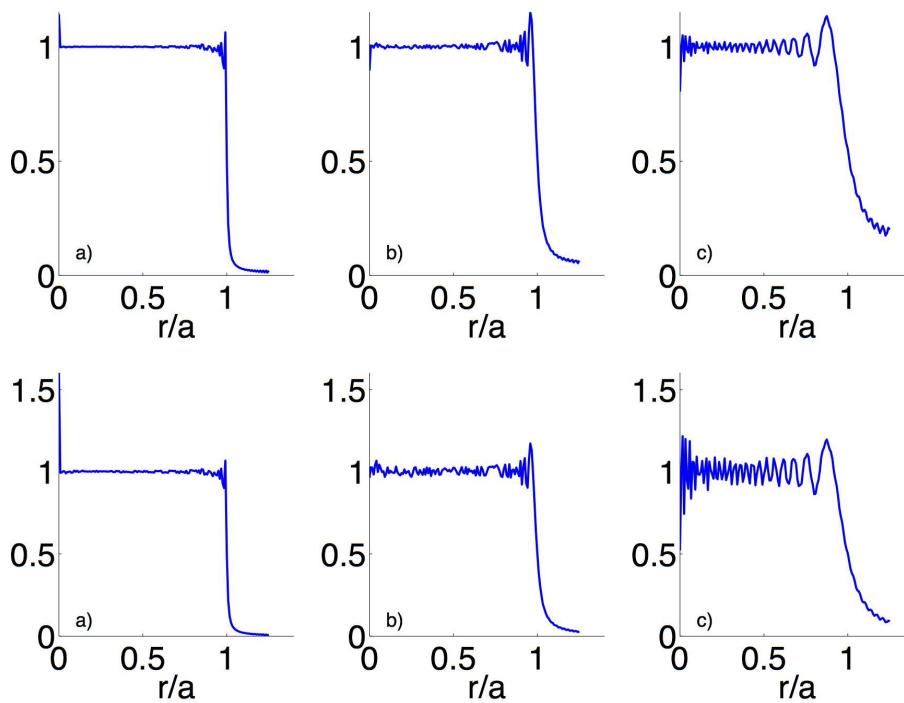


Figure 3.44: Absolute value of the transfer function of the first diffracting aperture (top) and of the additional ones (bottom) for $\xi_2 = 8 \cdot 10^{-5}$ (a), $\xi_2 = 0.001$ (b), $\xi_2 = 0.01$ (c), for $\alpha = 1.2$ and $\xi_1 = 0.0003$.

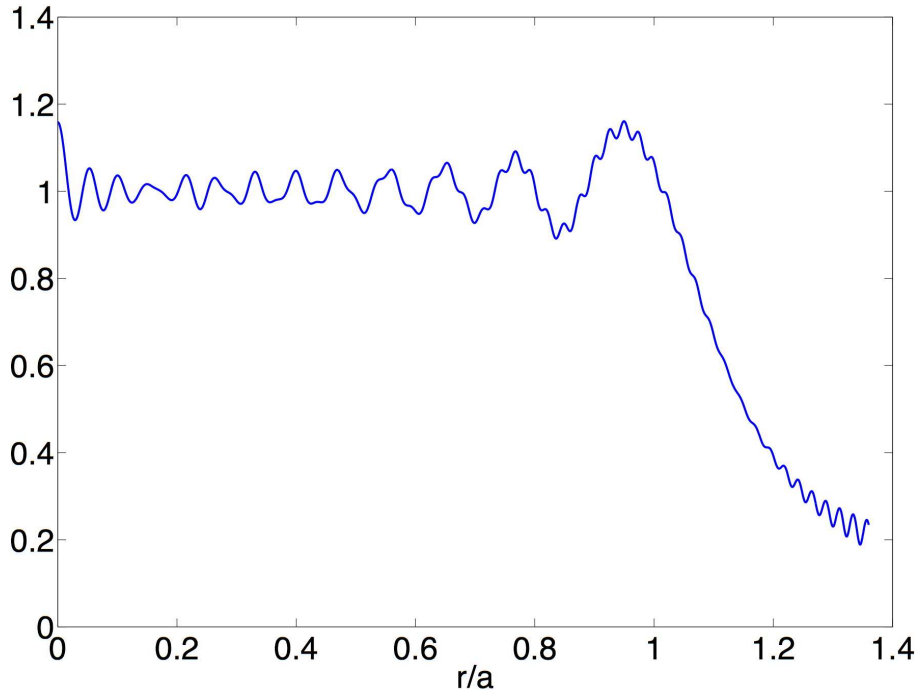


Figure 3.45: Absolute value of the transfer function of the PCI system for configuration 1.

or transmitting windows, it is important that it assumes different values on each optics in order not to enhance any deviation from unity but rather to average them out.

Let us now consider the effect of a focusing optical elements, such as a lens or a parabolic mirror, of focal length f . During the passage across the focusing optic, the gaussian beam undergoes a phase change equal to $k_0 r^2 / (2f)$. To convince ourselves of this result we can consider the propagation of a gaussian beam of complex parameter q (see Sec.3.2) across an optical medium of matrix ABCD. The gaussian beam complex parameter q_f , at the end of the optical element, can be reconstructed from the value before the optical element q_i by

$$\frac{1}{q_f} = \frac{C + D/q_i}{A + B/q_i} \quad (3.146)$$

which, in the case of a thin lens gives

$$\frac{1}{q_f} = -\frac{1}{f} + \frac{1}{q_i} \quad (3.147)$$

since the gaussian beam contains the factor $\exp[-ik_0 r^2 / (2q)]$, by passing through a focusing optics, a gaussian beam collects a phase shift equal to $k_0 r^2 / (2f)$.

Let us now apply the Fresnel-Kirchhoff integral from the waist to the detector plane to estimate diffraction effects in configuration 1; the result is plotted in Fig.3.45.

Bibliography

- [1] F. Zernicke, *Physica* **1** (1934) 689
- [2] M. Born and E. Wolf, *Principles of optics*, Pergamon press 1970
- [3] S. Coda, *Ph.D. thesis, Massachusetts Institute of Technology*, 1997
- [4] O. Svelto and D. Hanna, *Principles of lasers*, Springer, 1998
- [5] E.L. Dereniak and G.D. Boreman, *Infrared detectors and systems*, John Wiley and Sons Inc., 1996
- [6] F.M. Poli *et al.*, *Phys. Plasmas* **14** (2007) 052311
- [7] A. Truc *et al.*, *Rev. Sci. Instr.* **63** (1992) 3716
- [8] H. Weisen *et al.*, *Ph.D. thesis, Ecole Polytechnique Fédérale de Lausanne*, 1987
- [9] A. Mazurenko, *Ph.D. thesis, Massachusetts Institute of Technology*, 2001
- [10] M. Wischmeier, *Ph.D., Ecole Polytechnique Fédérale de Lausanne*, 2004
- [11] TRIDYN_{FZD}, Forschungszentrum Dresden-Rossendorf
- [12] E.D. Palik, *Handbook of optical constants, vol.I-II, Academic Press, Inc.* 1991
- [13] J.H. Weaver *et al.*, *Phys. Rev. Sect.* **B10** (1973) 501
- [14] T.E. Sheridan, J.Goree, *Phys. of Fluids* **B 3**(10) (1991) 2796
- [15] "Sputtering Data", *IPP Report 9/82* 1993
- [16] R. von Mises, *On Saint-Venant's Principle*, *Bull. AMS*, **51** (1945) 555
- [17] W.H. Press, S.A. Teukolsky, W.T. Vetterling, B.P. Flannery, *Numerical Recipes in fortran, 2nd edition*, Cambridge, (1992)
- [18] Landau H., *Acta Mathematica* **117** (1967) 37
- [19] Carleson L., *A. Beurling. Collected works. Vol.II* Birkhäuser, Boston, 341-365

- [20] Aldroubi A. and Grochenig K., *Journal of Fourier Analysis and Applications* **6** (2000) 93
- [21] Lomb N.R., *Astrophysics and Space Science* **47** (1976) 447
- [22] Scargle J.D., *The Astrophysical Journal* **263** (1982) 835
- [23] J.W. Cooley and J.W. Tuckey, *Mathematics of computation* **19** (1965) 297
- [24] F. Marvasti, *Non-uniform sampling: theory and practice, Kindle edition*, 2001
- [25] A. Siegman, *Lasers, University Science Book*, 1986
- [26] P.W. Terry, *Rev. Modern Phys.* **72** (2000) 109
- [27] G. Box, G.M. Jenkins and G.C. Reinsel. *Time Series Analysis: Forecasting and Control*, Prentice-Hall, 1994
- [28] W. Ekstein *et al.*, *Sputtering data*, IPP report 9/82, 1993

Chapter 4

Modeling of shaping effects on turbulent transport

4.1 Introduction

In this chapter we will focus on the influence of plasma shaping on micro-instabilities, in particular on modes interacting with trapped electrons. The results of this chapter are meant to theoretically explain a number of experimental results obtained in the TCV tokamak concerning the influence of plasma shaping on electron heat transport.

As the reader can guess from the title, the work described in this chapter is intimately tied to the plasma equilibrium reconstruction; therefore we start with a description of a general equilibrium and a description of the numerical tools used to reconstruct the equilibrium of the TCV shots we analyzed. We will then describe the numerical tools used to calculate plasma micro-instabilities, i.e. the GS2 code, and we will finally present our results.

4.2 Plasma equilibrium and shape

A general plasma equilibrium is described by the MHD equations

$$\mathbf{J} \wedge \mathbf{B} = \nabla \cdot \bar{\mathbf{P}} \quad \mu_0 \mathbf{J} = \nabla \wedge \mathbf{B} \quad \nabla \cdot \mathbf{B} = 0 \quad (4.1)$$

where \mathbf{J} is the plasma current density, \mathbf{B} the magnetic field and $\bar{\mathbf{P}}$ the pressure tensor. The general solution of $\nabla \cdot \mathbf{B} = 0$ in an axysymmetric system, such as a tokamak, is given, in cylindrical coordinates (R, φ, Z) , by

$$\mathbf{B} = \nabla \psi \wedge \nabla \varphi + F(\psi) \nabla \varphi \quad (4.2)$$

where φ is the toroidal angle, the variable of symmetry, $F(\psi) = RB_\varphi$ and $\psi(R, Z)$ the poloidal flux defined by

$$\psi = \frac{1}{2\pi} \int_{\Sigma} \mathbf{B} \cdot d\hat{\sigma} \quad (4.3)$$

and Σ is the surface enclosed by a given field line. Eqs.4.1a,b imply that if the plasma pressure is isotropic, it has to be constant on magnetic field lines and also on current lines; Eq.4.2 implies $\mathbf{B}_{\text{pol}} \cdot \nabla\psi = 0$, which means that the poloidal flux is constant on constant pressure regions. Therefore the poloidal flux is called flux label because it can be used to label nested magnetic flux surfaces. There are a number of possible alternative flux labels, e.g. the toroidal flux, its square root, the minor radius in a perfectly circular plasma etc. We will use in the following, unless specifically stated otherwise, the square root of the normalized volume, ρ_V , which, to zeroth order in the expansion parameter given by the Shafranov shift divided by the major radius, can be written as the ratio of two surfaces and is therefore a sort of linear dimension

$$\rho_V \equiv \sqrt{\frac{\int_V d^3r}{\int_{V_{LCFS}} d^3r}} \simeq \sqrt{\frac{2\pi(R_{0,LCFS} + \Delta) \int_{\Sigma} d^2r}{2\pi R_{0,LCFS} \int_{\Sigma_{LCFS}} d^2r}} \simeq \sqrt{\frac{\int_{\Sigma} d^2r}{\int_{\Sigma_{LCFS}} d^2r}} \quad (4.4)$$

where LCFS means the Last Closed Flux Surface, Δ is the Shafranov shift of the radial position of the geometric center of the flux surface under consideration with respect to the geometric center of the LCFS, $R_{0,LCFS}$. In the case of a circular, concentric plasma it reduces to the normalized minor radius.

In case of an axisymmetrical system such as a tokamak, Eqs.4.1 lead to the Grad-Shafranov equation [1, 2]

$$R \frac{\partial}{\partial R} \frac{\partial \psi}{R \partial R} + \frac{\partial^2 \psi}{\partial z^2} = -\mu_0 R^2 \frac{dP(\psi)}{d\psi} - F(\psi) \frac{dF(\psi)}{d\psi} \quad (4.5)$$

where F is defined as RB_ϕ . The Grad-Shafranov equation is thus a two-dimensional, non linear, elliptic partial differential equation where the poloidal flux, ψ , is both an independent and a dependent variable. By solving this equation one obtains the spatial mapping of current density, pressure and magnetic field.

Since the poloidal flux is a flux function, it is useful to plot its contour lines to have an overview of the equilibrium because, to first order, kinetic quantities are only a function of ψ .

The (R,Z) mapping of any flux surface is also commonly described in terms of so-called moments of plasma shape which are meant to be compact representations of flux surfaces. Historically the first plasma moment considered was the inverse aspect ratio, i.e. the ratio of the minor radius, r , to the major radius, R_0 , because a circular flux surface cross-section is completely described by the major radius and the aspect ratio according to the system of equations

$$R = R_0 + r \cos(\theta) \quad (a), \quad Z = Z_0 + r \sin(\theta) \quad (b) \quad (4.6)$$

where θ is the geometric poloidal angle and the aspect ratio is defined as R_0/r .

Subsequently, elongated plasmas were generated, i.e. plasmas with an elliptical cross

section, described by a parameter, κ , called elongation

$$R = R_0 + r \cos(\theta) \qquad Z = Z_0 + \kappa r \sin(\theta) \qquad (4.7)$$

More peculiar plasma shapes were then generated with a so-called D shape, modeled by a higher shape moment called triangularity, δ ; additional corrections can be modelled by a higher moment called squareness, λ .

$$R = R_0 + r \cos[\theta + \delta \sin(\theta) + \lambda \sin(2\theta)] \qquad Z = Z_0 + \kappa r \sin(\theta) \qquad (4.8)$$

As is evident from Eq.4.8b elongation is also defined as

$$\kappa = \frac{Z_{max} - Z_{min}}{R_{max} - R_{min}} \qquad (4.9)$$

while, if we now choose the poloidal angle corresponding to Z_{max} , i.e. $\theta = \pi/2$, Eq.4.8a reduces to

$$R(Z_{max}) = R_0 - r \sin(\delta) \Rightarrow \delta = \arcsin\left(\frac{R_0 - R(Z_{max})}{r}\right) \qquad (4.10)$$

in the limit of small triangularities Eq.4.10 reduces to

$$\delta = \frac{R_0 - R(Z_{max})}{r} \qquad (4.11)$$

which is an alternative definition of triangularity often found in literature. This ambiguity in the definition of triangularity might lead to slight differences in numerical values. The first correction in the Taylor development of the $\sin(\delta)$ function is $\delta^3/6$ which is equal to $\delta/10$, i.e. a difference of 10% between the two definitions, for $\delta = 0.78$. We will see in the following, however, that this value is at the high end of the achievable range; for more typical values of the triangularity the two definitions above are effectively equivalent.

As of this writing, there is considerable interest in up-down asymmetric plasmas, i.e. plasmas characterized by different lower and upper triangularities, because such asymmetries break the symmetry of the distribution function along the field line in a manner which can lead to non-zero k_{\parallel} of micro-instabilities and thus to turbulent momentum fluxes which are suspected to regulate the bulk plasma rotation [3].

As a postscript, the first equality in Eq.4.4 holds exactly even if the plasma is elongated or squared but not triangular; in this case the correction to be added to each integral approximately scales as $-\delta\epsilon$, ϵ being the inverse aspect ratio.

In Fig.4.1 we depict equilibria corresponding to different values of the shape moments.

4.3 Particle drifts in magnetized plasmas

In this section we will quickly review the primary particle drifts in magnetized plasmas as, for the reader unfamiliar to plasma physics in toroidal devices, they are key points

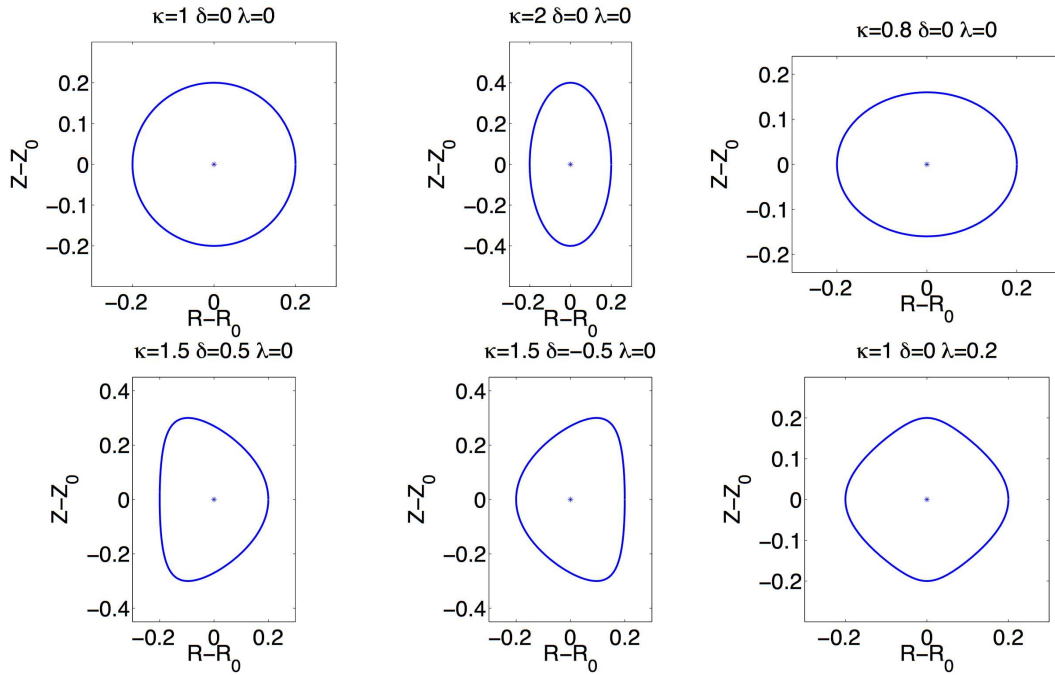


Figure 4.1: An illustrative set of equilibria obtained by varying the shape moments. Shown in the figure is the flux surface corresponding to a minor radius of 0.2 m. The case $\{\kappa = 0.8, \delta = 0, \lambda = 0\}$ cannot be realized in practice, it merely illustrates how a plasma with $\kappa < 1$ would look like.

for understanding the results of this chapter. In particular, considering how numerical simulations were performed, we will only consider drifts arising from non-uniform and static fields.

Charged particles diamagnetically gyrate around magnetic field lines and, in the case of a homogeneous magnetic field, it can be easily shown that their orbit is circular. In the case of an inhomogeneous magnetic field the orbit is not exactly circular and, to find the deviation, we will use the Larmor radius corresponding to a homogeneous field, divided by the magnetic field scale length, as the Taylor expansion parameter. We start by writing the second law of dynamics

$$m \frac{d\mathbf{v}}{dt} = q(\mathbf{E} + \mathbf{v} \wedge \mathbf{B}) \quad (4.12)$$

where m and q are, respectively, the particle mass and charge. The magnetic field can be developed to first order as

$$\mathbf{B} = \mathbf{B}_{gc} - \frac{m}{q|\mathbf{B}_{gc}|} [(\mathbf{v}_{\perp} \wedge \hat{\mathbf{b}}) \cdot \nabla] \mathbf{B} \quad (4.13)$$

where the subscript gc stands for guiding centre.

Let us now write the total particle velocity as the sum of the parallel velocity of the guiding centre plus the perpendicular velocity around its trajectory, plus a possible drift which, being due to the spatial inhomogeneity of the magnetic field, is assumed to be of

the order of the Larmor radius divided by the spatial scale of the magnetic field variation

$$\mathbf{v} = v_{\parallel} \hat{\mathbf{b}} + v_{\perp} [\cos(\Omega_c t) \hat{n} + \sin(\Omega_c t) \hat{b}_n] + \mathbf{v}_d \quad (4.14)$$

where $\Omega_c = qB_{gc}/m$ is the cyclotron frequency, \hat{n} and \hat{b}_n stand for normal and bi-normal to the field line, respectively.

By averaging over many cyclotron periods, Eq.4.12 reads

$$\frac{dv_{\parallel} \hat{\mathbf{b}}}{dt} + \frac{d\mathbf{v}_d}{dt} = \frac{q}{m} \left(\mathbf{E} + \mathbf{v} \wedge \left[B_{gc} \hat{\mathbf{b}} - \left\langle \frac{m}{q|\mathbf{B}_{gc}|} [(\mathbf{v}_{\perp} \wedge \hat{\mathbf{b}}) \cdot \nabla] \mathbf{B} \right\rangle \right] \right) \quad (4.15)$$

where the angular bracket stands for averaging over cyclotron periods.

If the plasma is in a stationary state, i.e. the guiding center velocity is constant, and we consider only first order corrections, then by taking the cross product with $\hat{\mathbf{b}}$ we obtain

$$\begin{aligned} v_{\parallel} \frac{d\hat{\mathbf{b}}}{dt} \wedge \hat{\mathbf{b}} &= v_{\parallel} (v_{\parallel} \hat{\mathbf{b}} \cdot \nabla \hat{\mathbf{b}}) \wedge \hat{\mathbf{b}} \\ &= \frac{q}{m} \left(\mathbf{E} \wedge \hat{\mathbf{b}} + (\mathbf{v}_d \wedge B_{gc} \hat{\mathbf{b}}) \wedge \hat{\mathbf{b}} - \frac{m}{q|\mathbf{B}_{gc}|} \langle \mathbf{v}_{\perp} \wedge [(\mathbf{v}_{\perp} \wedge \hat{\mathbf{b}}) \cdot \nabla] \mathbf{B} \rangle \wedge \hat{\mathbf{b}} \right) \end{aligned} \quad (4.16)$$

By vector identity

$$(\mathbf{v}_d \wedge B_{gc} \hat{\mathbf{b}}) \wedge \hat{\mathbf{b}} = B_{gc} \hat{\mathbf{b}} (\mathbf{v}_d \cdot \hat{\mathbf{b}}) - \mathbf{v}_d (B_{gc} \hat{\mathbf{b}} \cdot \hat{\mathbf{b}}) \quad (4.17)$$

since we are considering drifts perpendicular to the magnetic field direction the first term on the r.h.s. is equal to zero, and Eqs.4.16 and 4.17 are combined to yield

$$\mathbf{v}_d = \mathbf{v}_{\mathbf{E} \wedge \mathbf{B}} - \frac{m}{qB_{gc}} v_{\parallel} (v_{\parallel} \hat{\mathbf{b}} \cdot \nabla \hat{\mathbf{b}}) \wedge \hat{\mathbf{b}} - \frac{m}{qB_{gc}^2} \langle \mathbf{v}_{\perp} \wedge [(\mathbf{v}_{\perp} \wedge \hat{\mathbf{b}}) \cdot \nabla] \mathbf{B} \rangle \wedge \hat{\mathbf{b}} \quad (4.18)$$

where we have defined

$$\mathbf{v}_{\mathbf{E} \wedge \mathbf{B}} = \frac{\mathbf{E} \wedge \hat{\mathbf{b}}}{B_{gc}} \quad (4.19)$$

In Eq.4.18 the first term on the right hand side is the ambipolar $\mathbf{E} \wedge \mathbf{B}$ drift, the second is the curvature drift and the third is the ∇B drift. If the particle's parallel and perpendicular velocities vary over a larger spatial scale than the Larmor radius then we can write

$$\mathbf{v}_d = \mathbf{v}_{\mathbf{E} \wedge \mathbf{B}} - \frac{m}{qB_{gc}} v_{\parallel}^2 (\hat{\mathbf{b}} \cdot \nabla \hat{\mathbf{b}}) \wedge \hat{\mathbf{b}} - \frac{mv_{\perp}^2}{2qB_{gc}^2} \nabla |\mathbf{B}| \wedge \hat{\mathbf{b}} \quad (4.20)$$

In the case of time-independent e-m fields $\nabla \wedge \mathbf{B} = \mu_0 \mathbf{J}$ and so, by employing the vector identity

$$\frac{1}{2} \nabla (\mathbf{B} \cdot \mathbf{B}) = \mathbf{B} \wedge (\nabla \wedge \mathbf{B}) + (\mathbf{B} \cdot \nabla) \mathbf{B} \quad (4.21)$$

and the equilibrium equation $\mathbf{J} \wedge \mathbf{B} = \nabla \mathbf{P}$, we can re-write the drift as

$$\mathbf{v}_d = \mathbf{v}_{\mathbf{E} \wedge \mathbf{B}} - \frac{m}{qB_{gc}^2} v_{\parallel}^2 \left(\nabla |\mathbf{B}| \wedge \hat{\mathbf{b}} + \frac{B_{gc}}{2} \nabla \beta \wedge \hat{\mathbf{b}} \right) - \frac{mv_{\perp}^2}{2qB_{gc}^2} \nabla |\mathbf{B}| \wedge \hat{\mathbf{b}} \quad (4.22)$$

where $\beta = 2\mu_0 P/B_{gc}^2$. Eq.4.22 shows how, apart from the difference in the perpendicular and parallel energies, the curvature drift differs from the ∇B drift by the gradient in the toroidal beta.

Let us now evaluate these drifts for trapped particles, i.e. particles forced to bounce back and forth due to a mirroring effect induced by the inhomogeneity of the magnetic field. The periodic motion of a trapped particle guiding center defines the so-called banana orbit which can be averaged again over its trajectory to calculate its average drift. It turns out that in the case of an unperturbed tokamak, i.e. neglecting the toroidal field ripple and any deviation from the ideal magnetic configuration, the average banana orbit undergoes a net drift in the toroidal direction which is due to the combined effect of parallel motion and vertical drifts described above. This is called the toroidal precession drift.

An adiabatic invariant is the lowest order approximation to a Poincaré invariant

$$\mathfrak{S} = \oint_C \mathbf{p} \cdot d\mathbf{q} \quad (4.23)$$

(\mathbf{p}, \mathbf{q}) being the usual phase space variables.

Let us consider, as C , the periodic motion of the guiding center of a trapped particle, which approximates the real particle orbit to zeroth order in the Larmor radius expansion; the Poincaré invariant is approximated by the so-called longitudinal adiabatic invariant[4]

$$\mathfrak{S} \simeq J = \oint_C p_{\parallel} ds \quad (4.24)$$

where ds is an element of arc along a given field-line and $p_{\parallel} = \mathbf{p} \cdot \hat{\mathbf{b}}$. Averaging magnetic curvature and field gradients over the bouncing period results in an average drift of particles in the toroidal direction which, in the case of low trapped particle energy is given by [5]

$$\langle \dot{\varphi} \rangle(\psi, E, \mu) = -\frac{1}{q} \frac{\partial J / \partial \psi}{\partial J / \partial E} \quad (4.25)$$

where E is the particle energy, q its charge, μ its magnetic moment and ψ is the poloidal flux of a given flux surface.

Let us now quote, with the same notations as in [6], the toroidal precession drift in the particular case of large aspect ratio, circular and concentric flux surfaces which, having zero Shafranov shift, are therefore modeled as having zero pressure gradient.

$$\langle \dot{\varphi} \rangle \propto G(X, r/R, s) E \propto \lambda \left\{ s \left[X - 1 + \frac{\mathbf{E}(X)}{\mathbf{K}(X)} \right] + \frac{1}{2} \left[\frac{\mathbf{E}(X)}{\mathbf{K}(X)} - \frac{1}{2} \right] \right\} E \quad (4.26)$$

where \mathbf{E} and \mathbf{K} are the complete elliptic integrals of first and second kind, respectively, s is the magnetic shear and

$$X = \frac{1 - \lambda + \lambda r/R}{2\lambda r/R} \quad \lambda = \frac{\mu B_0}{E} \quad (4.27)$$

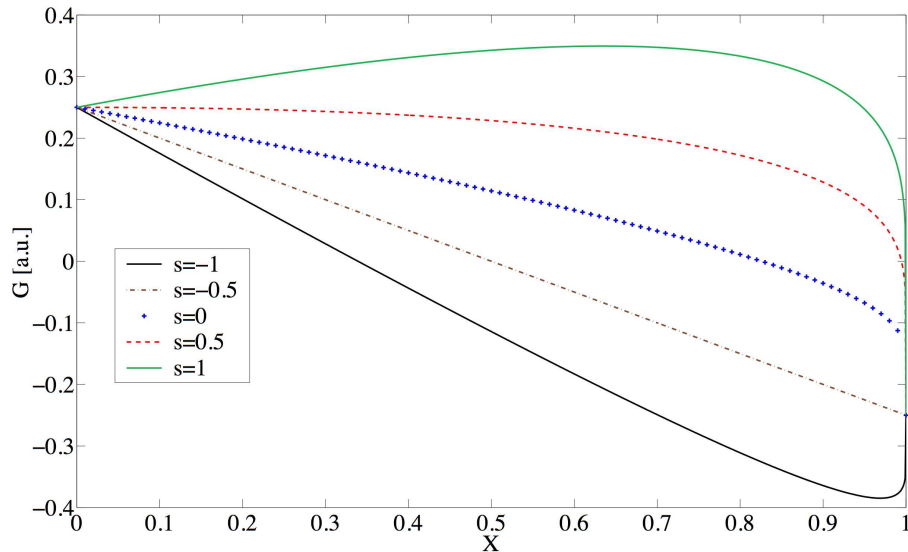


Figure 4.2: Values, in arbitrary units, of the geometrical factor determining the toroidal precession drift, for a number of magnetic shear values.

r and R being the minor and major radii of a given flux surface, respectively, and B_0 the magnetic field on the geometric center of the flux surface. In the limits $X \rightarrow 0$, corresponding to the deeply trapped limit, and $X \rightarrow 1$, corresponding to the barely trapped limit, the G factor is equal to

$$\lim_{X \rightarrow 0} G = \frac{B_0}{B_{min}} \qquad \lim_{X \rightarrow 1} G = -\frac{B_0}{B_{max}} \qquad (4.28)$$

meaning that deeply trapped and barely trapped particles drift in opposite directions independently of magnetic shear. Let us now look at the whole pitch angle space dependence of the G factor in Fig.4.2: it is evident how, depending on the magnetic shear, trapped particles can drift in different directions thus resonating or not with a given perturbation (see Sec.4.4).

4.4 Trapped particles instability

Let us immediately see what is probably the most important effect of the toroidal precession drift in magnetically confined plasmas by reviewing, as an introduction to the results of this chapter, the basic mechanism of the Trapped Electron Mode first described by Kadomtsev and Pogutse in[45].

Let us divide particles into passing and trapped, i.e., into particles free to move along a magnetic field line and particles forced to bounce back and forth due to a mirroring effect induced by the inhomogeneity of the magnetic field. There exist two types of trapped particles: the ones trapped into the magnetic mirror generated by the toroidicity of the

problem, and the ones trapped in the helical windings of magnetic fields which do not possess axial symmetry, such as stellarators. In reality, tokamaks also have the second type of trapped particles due to the toroidal field ripple; however, since this is very small in TCV (see Chapter 1), their presence will be neglected.

The basic mechanism of the instability is the following: any given inhomogeneity along the magnetic field causes a different effect on passing and trapped particles trajectories. In particular, in the case of slow waves, i.e., waves with low parallel velocity compared to the thermal speed ($\omega \ll k_{\parallel} v_{th}$), passing particles are adiabatic, i.e., achieve a Boltzmann distribution by virtue of their fast parallel motion, while trapped particles with a small parallel velocity do not average the perturbation and can resonate with it: this gives rise to the instability.

Kadomtsev and Pogutse consider the case of a circular, collisionless plasma, with electrostatic fluctuations of low frequency compared to the cyclotron frequency; this case is modeled by the linearized collisionless Vlasov equation

$$\left. \frac{d\tilde{f}}{dt} \right|_{u.p.t.} = \frac{\partial \tilde{f}}{\partial t} + \mathbf{v} \cdot \nabla \tilde{f} + \frac{e}{M} (-\nabla \phi_0 + \mathbf{v} \wedge \mathbf{B}) \cdot \frac{\partial \tilde{f}}{\partial \mathbf{v}} = \frac{e}{M} \nabla \tilde{\phi} \frac{\partial f_0}{\partial \mathbf{v}} \quad (4.29)$$

where e is the particle's charge, M its mass, while the perturbed distribution function and the electrostatic field are expressed as

$$f = f_0 + \tilde{f} \quad \phi = \phi_0 + \tilde{\phi} \quad (4.30)$$

f_0 being the equilibrium distribution satisfying the equation

$$\mathbf{v} \nabla f_0 + \frac{e}{M} (\nabla \phi_0 + \mathbf{v} \wedge \mathbf{B}) \frac{\partial f_0}{\partial \mathbf{v}} = 0 \quad (4.31)$$

and *u.p.t.* stands for unperturbed particle trajectory.

The $\nabla \phi_0$ term is neglected in this localized treatment and the perturbation is assumed to be periodic in the toroidal and poloidal angles, φ and θ , respectively

$$\tilde{\phi} = e^{ikr - \omega t + im\theta - il\varphi} \hat{\phi}(\theta) \quad (4.32)$$

where the hat function is assumed to be periodic in the poloidal angle θ . The perturbed distribution function of specie j is split into its adiabatic, i.e. Boltzmann, and non-adiabatic, \tilde{g} , contributions

$$\tilde{f}_j = f_{0,j} e^{-e_j \tilde{\phi} / T_j} - f_{0,j} + \tilde{g} \quad (4.33)$$

which, after a linearization of the adiabatic term, gives

$$\tilde{f}_j = -f_{0,j} \frac{e_j \tilde{\phi}}{T_j} + \tilde{g} \quad (4.34)$$

Substituting Eq.4.34 into Eq.4.29 gives

$$\left. \frac{d\tilde{g}}{dt} \right|_{u.p.t.} = \frac{e_j}{T_j} \frac{\partial \tilde{\phi}}{\partial t} f_{0,j} + \frac{1}{B} \nabla \tilde{\phi} \nabla f_{0,j} \quad (4.35)$$

Passing from particle coordinates to guiding center coordinates and performing the gyro-averaging, one finds [7] (or in a more recent document [6])

$$\left. \frac{d\tilde{g}}{dt} \right|_{u.g.c.t.} = \left(\frac{e_j}{T_j} f_{0,j} \frac{\partial}{\partial t} + \frac{1}{B} \nabla f_{0,j} \nabla \right) \int dk J_0 \left(\frac{k_{\perp} v_{\perp}}{\Omega} \right) e^{i(kr_j + m\theta_j - l\varphi_j)} \hat{\phi} \quad (4.36)$$

where J_0 is the Bessel function, Ω is the cyclotron frequency and *u.g.c.t.* stands for unperturbed guiding center trajectory. Upon integration over time gives

$$\begin{aligned} \tilde{g} = -i \frac{e_j}{T_j} f_{0,j} \int dk J_0 \left(\frac{k_{\perp} v_{\perp}}{\Omega} \right) e^{-ik(\omega - \omega^*)} \hat{\phi} \times \\ \int_{-\infty}^0 dt e^{ik[r'_j(t)-r] + im(\theta'_j(t)-\theta) - il(\varphi'_j(t)-\varphi) - i\omega t} \end{aligned} \quad (4.37)$$

where the coordinates $\{r', \theta', \varphi'\}_{t=0} = \{r, \theta, \varphi\}$. The perturbed density is obtained by integrating over velocity space to obtain

$$\begin{aligned} \tilde{n}_j = -n_{0,j} \frac{e_j \tilde{\phi}}{T_j} - i \int_{-\infty}^0 dt \int d\mathbf{v} dk e^{-i\omega t + ik[r'_j(t)-r] + im(\theta'_j(t)-\theta) - il(\varphi'_j(t)-\varphi)} \times \\ J_0^2 \left(\frac{k_{\perp} v_{\perp}}{\Omega} \right) \frac{1}{T_j} f_{M,j}(\omega - \omega_j^*) \hat{\phi}. \end{aligned} \quad (4.38)$$

where

$$\omega_j^* = \frac{T_j m}{e_j B r} \frac{1}{f_{M,j}} \frac{df_{M,j}}{dr} \sim \frac{m \rho_j v_j}{a^2} \quad (4.39)$$

is the diamagnetic drift frequency. The appearance of the additional Bessel function is due to gyro-averaging after transforming from guiding center to particle coordinates.

Imposing quasi-neutrality Kadomtsev and Pogutse obtain the following dispersion relation

$$\begin{aligned} \left(\frac{1}{T_e} + \frac{1}{T_i} \right) n_0 \hat{\phi} = -i \sum_{j=e,i} \int_{-\infty}^0 dt \int d\mathbf{v} dk e^{-i\omega t + ik[r'_j(t)-r] + im(\theta'_j(t)-\theta) - il(\varphi'_j(t)-\varphi)} \times \\ J_0^2 \left(\frac{k_{\perp} v_{\perp}}{\Omega} \right) \frac{1}{T_j} f_{0,j}(\omega - \omega_j^*) \hat{\phi} \end{aligned} \quad (4.40)$$

where $e_j = -e$ for electrons and the opposite for ions. Eq.4.40 is valid in the limit $m \gg 1$, so that $m\tilde{\phi} \gg \partial\hat{\phi}/\partial\theta$, and $\omega \ll \Omega$ and has to be integrated over the guiding center trajectory.

Considering only large scale perturbations, which are the most deleterious to plasma confinement, the characteristic spatial scale of the electrostatic perturbation is assumed to be much larger than the radial excursion of particles out of the flux surface due to perpendicular unperturbed magnetic drifts, therefore the Bessel function is approximated by 1.

The width of the electrostatic potential is furthermore assumed to be small compared to the plasma minor radius, thus implying the existence of local values of the eigenfrequency $\omega = \omega(\mathbf{r})$.

In the integral over passing particles we can write

$$\theta' - \theta \simeq \frac{v_{\parallel} t'}{Rq} \quad \varphi' - \varphi \simeq q(\theta' - \theta) \quad (4.41)$$

therefore the integral over dt' generates the factor $i[\omega - (m - lq)v_{\parallel}/(qR)]^{-1}$ which can be neglected compared to ω^{-1} provided that

$$(m - lq)v_{\parallel} \frac{1}{qR} \simeq (m - lq) \frac{v_j \rho_j m}{a^2} \frac{a}{\rho_j m q} \frac{\epsilon}{q} \sim (m - lq) \omega^* \frac{a}{\rho_j m q} \frac{\epsilon}{q} \gg \omega \quad (4.42)$$

which in turn implies

$$(m - lq) \gg \frac{\rho_j m}{a} \quad (4.43)$$

provided that

$$\omega^* \frac{\epsilon}{q} \gtrsim \omega \quad (4.44)$$

therefore the contribution of passing particles is unimportant.

In the case of trapped particles, the equivalent of Eq.4.41 is

$$\varphi' - \varphi \simeq q(\theta' - \theta) + \xi' \quad (4.45)$$

ξ' being the deviation from a given magnetic field line on the flux surface considered.

Considering the case $m - lq \ll 1$, which is equivalent to assuming the hat functions above to have a minimum number of nodes along θ , the integral of $(m - lq)(\theta' - \theta)$ is a periodic function of order $m - lq$ which can then be neglected. Averaging over the bouncing period τ_j , we can write $\xi' \simeq \langle \xi' \rangle = \langle \dot{\phi} \rangle t$ therefore Eq.4.40 yields

$$\left(\frac{1}{T_e} + \frac{1}{T_i} \right) n_0 \tilde{\phi} = \sum_{j=e,i} \frac{1}{T_j} \int d\mathbf{v} f_{0,j} \frac{\omega - \omega_j^*}{\omega + l \langle \dot{\phi} \rangle} \int_{-\tau_j}^0 dt' \frac{\hat{\phi}}{\tau_j} \quad (4.46)$$

Eq.4.46 implies that the toroidal precession drift is responsible for the Trapped Electron instability, since the drift velocity appears in the denominator of the dispersion equation and, therefore, can resonate with the frequency of the perturbation. It should be noted, however, that the resonance takes place if and only if banana orbits drift in the direction of the perturbation.

In general, TEM fall in the same frequency range as the toroidal-ITG instability, therefore they can interact with each other and the resulting instability is dominated by the former, the latter or is a mixed regime, depending on ion and electron drives (see [6] and references therein) and on plasma collisionality [8].

4.5 Gyro-kinetics and the GS2 code

Gyrokinetics (GK) is a branch of plasma physics derived from kinetics and electromagnetism used in magnetically confined plasmas to describe phenomena that are slow compared to the particle gyro-motion, i.e. micro-instabilities. The trajectory of a charged particle in a magnetic field is a helix that winds around the field line. This trajectory can be decomposed into a relatively slow motion of the guiding center along the field line and a fast circular motion called cyclotron motion. For most plasma physics problems other than high-frequency wave absorption or emission, the latter motion is irrelevant. Gyrokinetics provides a way to describe the evolution of particles without taking into account the circular motion, except for finite Larmor radius effects, discarding the irrelevant information on the gyration angle by averaging over it, that is

$$\langle X(*) \rangle = \frac{\int_0^{2\pi} d\alpha X(\alpha, *)}{2\pi} \quad (4.47)$$

where * stands for all quantities the X variable depends on except the gyro-angle.

The Vlasov equation is a seven dimensional (space, velocity and time) equation describing the distribution function, f , of an *ensemble* of particles of any kind.

$$\frac{\partial f}{\partial t} - [H, f] = 0 \quad (4.48)$$

where H is the Hamiltonian of a single particle and $[,]$ is the Poisson bracket.

Let us first change variables from a canonical phase-space $\mathbf{z} \equiv (\mathbf{q}, \mathbf{p})$ to guiding center coordinates $\mathbf{Z} \equiv (\mathbf{r}_g, v_{\parallel}, v_{\perp}, \alpha)$, by using Catto's transformations[9] to tie the guiding center position \mathbf{r}_g and the particle position \mathbf{r}

$$\mathbf{r}_g = \mathbf{r} + \frac{m\mathbf{v} \wedge \hat{\mathbf{b}}}{qB_0} \quad (4.49)$$

where B_0 is the magnetic field at the guiding center position, q the particle charge and m its mass. By perturbing the distribution function $f = F_0 + \delta f$, the GK equation is obtained by gyro-averaging

$$\frac{\partial \langle f \rangle}{\partial t} - \langle [H, f]_{\mathbf{z}} \rangle = 0. \quad (4.50)$$

We briefly mention the existence of a modern method of deriving the GK equation by using the Lie transformation theory to change the coordinates to a system $\bar{\mathbf{Z}}$ where the new magnetic momentum remains an exact invariant in the presence of fluctuations, and the Vlasov equation takes a simple form,

$$\frac{\partial \bar{F}}{\partial t} - [\bar{H}, \bar{F}]_{\bar{\mathbf{Z}}} = 0, \quad (4.51)$$

where $\overline{F}(\overline{\mathbf{Z}}, t) = f(\mathbf{z}, t)$, and \overline{H} is the gyrokinetic Hamiltonian[10].

The conventional gyrokinetic formulation is a consistent expansion of the full kinetic equation in the small parameter ρ^* , defined as the ratio of the ion Larmor radius to the plasma minor radius, ordering

$$\omega/\Omega_i \sim k_{\parallel}/k_{\perp} \sim e\delta\phi/T_e \sim \rho_s/L_{n,T} \sim \delta f/F_0 \sim O(\rho^*) \quad (4.52)$$

and $k_{\perp}\rho_s \sim O(1)$. It is known that $\delta n/n_0$ may become large in the tokamak edge where steep gradients are observed, and there is a worry that conventional gyrokinetics may break down. Numerical codes solving the Vlasov equation can solve it either in a thin annulus around a given flux surface or in a larger spatial domain, and are accordingly called flux-tube or global codes, respectively. Flux-tube codes have no radial variation of the equilibrium and exhibit no ρ^* dependence (ρ^* scales out of the equations). Thus, the flux-tube limit is commonly referred to as the $O(1)$ theory. More details on flux-tube code geometry can be found in Sec.4.6.3; for a full description of field-aligned coordinate systems and flux-tube codes we address the reader to[11].

GS2 is a widely benchmarked code which solves the gyrokinetic Vlasov-Maxwell system of equations as an initial value problem. The code employs a splitting operator which allows a ballooning representation for the linear terms, solved implicitly, and a flux tube domain treatment for the non-linear terms explicitly advanced in time with a second-order Adams-Bashforth[14] scheme; GS2 allows the user to choose the amount of implicitness for each kinetic species. The code can handle different ion species and collisions (a diffusion pitch-angle or the Krook operator are available) and is fully electromagnetic. The magnetic geometry can be given in input as an analytical model (s- α or Miller) or as a numerical equilibrium obtained from an equilibrium solving code, such as EFIT or CHEASE[38].

In the field-line following coordinates, the non-linear gyrokinetic equation for the non-adiabatic part of the perturbed distribution function $\tilde{g} = \delta f - F_0 q \delta\phi/T$ may be written as [12, 13]

$$\frac{\partial \tilde{g}}{\partial t} + [\tilde{\chi}, \tilde{g}]/B + v_{\parallel} \mathbf{b} \cdot \nabla \tilde{g} + i\omega_d \tilde{g} = i\omega^* \tilde{\chi} - q \frac{\partial F_0}{\partial E} \frac{\partial \tilde{\chi}}{\partial t} \quad (4.53)$$

where ω^* is the diamagnetic drift. The distribution function F_0 depends only on the flux surface label Ψ and on the particle energy $E = mv^2/2$. The perpendicular curvature and ∇B drifts are given by

$$\omega_d = \mathbf{k}_{\perp} \cdot \mathbf{B} \wedge (mv_{\parallel}^2 \mathbf{b} \cdot \nabla \mathbf{b} + \mu \nabla B)/(Bm\Omega) \quad (4.54)$$

where $\mu = mv_{\perp}^2/(2B)$, $[*,*]$ is the Poisson bracket, and the e-m fields are represented by

$$\tilde{\chi} = J_0(k_{\perp}\rho) \left(\tilde{\phi} - v_{\parallel} \tilde{A}_{\parallel} \right) + \frac{J_1(k_{\perp}\rho)}{k_{\perp}\rho} \frac{mv_{\perp}^2}{q} \frac{\tilde{B}_{\parallel}}{B} \quad (4.55)$$

and are self-consistently solved through the GK Poisson-Ampere equations

$$\nabla_{\perp}^2 \tilde{\phi} = \Sigma_s \frac{q}{\epsilon_0} \int d\mathbf{v} \left[q \tilde{\phi} \frac{\partial F_0}{\partial E} + J_0(k_{\perp} \rho) \tilde{g} \right] \quad (4.56)$$

$$\nabla_{\perp}^2 \tilde{A}_{\parallel} = -\mu_0 \Sigma_s \int d\mathbf{v} q v_{\parallel} J_0(k_{\perp} \rho) \tilde{g} \quad (4.57)$$

$$\frac{\tilde{B}_{\parallel}}{B} = -\frac{\mu_0}{B^2} \Sigma_s \int d\mathbf{v} m v_{\perp}^2 \frac{J_1(k_{\perp} \rho)}{k_{\perp} \rho} \tilde{g} \quad (4.58)$$

where J_0 and J_1 are the Bessel functions.

The coordinates used in the code are the energy E , the quantity $\lambda = \mu/E$ related to the particle's pitch angle range, and the field-line coordinate θ , which is the poloidal angle. For each E and λ there are 2 possible parallel velocities, which makes the number of parallel passing region points twice the value actually set in the code. The velocity integrals are the following:

$$\int d\mathbf{v} = \frac{\sqrt{2\pi} B(\theta)}{m^{3/2}} \int dE \frac{\sqrt{E} d\lambda}{\sqrt{1 - \lambda B(\theta)}} \quad (4.59)$$

A gaussian integration rule is adopted in the evaluation of these integrals to maximize the accuracy over the computational effort, especially at the trapped/passing boundary. Since the distribution function generally behaves differently in the trapped and passing regions, the grid is different in these two regions. In the trapped region the λ grid is chosen so that the points where $v_{\parallel} = 0$ correspond to grid points in θ , i.e., $1 - \lambda_i B(\theta_i) = 0$. The grid is equally spaced in the field-line direction and integrals over E are evaluated with gaussian integration rule. The distribution function must vanish as $\theta \rightarrow \pm\infty$ thus the boundary conditions applied in the code are the following

- $\delta f = 0$ at the rightmost grid point in θ for $v_{\parallel} < 0$, i.e., at the end of the flux tube
- $\delta f = 0$ at the leftmost grid point in θ for $v_{\parallel} > 0$, i.e., at the beginning of the flux tube

so that no particle is convected into the simulation domain from infinity.

For trapped particles, at given E and λ , which means for a given spatial extent in θ , the distribution function for $v_{\parallel} > 0$ must be equal to the distribution function for $v_{\parallel} < 0$ at the mirror point.

The code allows to option to simulate only half domain if symmetric eigenfunctions exist, which is the case for an up-down symmetric equilibrium.

4.6 The effect of plasma shape on performance

4.6.1 Historical results

Plasma shape has been theoretically and experimentally recognized as a major player in plasma performance through its effect on both MHD and microturbulence. A fusion relevant tokamak needs to operate at high pressure to maximize the reactor efficiency by means of a high fusion rate and, in the case of advanced-tokamak scenarios, a high bootstrap current and a low externally driven current. However there are limits to the density, pressure and current which a plasma can withstand and above which MHD instabilities occur, destroying the desired configuration. The influence of plasma shape on MHD stability was theoretically studied in [16, 17] and has been experimentally observed in the TCV, DIII-D and JET tokamaks in various scenarios[17, 18, 19, 20].

The improvement in performance with shaping in an elongated plasma is due to the increased maximum MHD-stable current (at fixed safety factor) carried by an elongated plasma, which in turn increases the maximum achievable beta according to the Troyon scaling[21].

Concerning the effect of shaping on microturbulence, a few linear gyrokinetic (GK) studies have been performed, showing in general a stabilizing effect of elongation on Ion Temperature Gradient (ITG) modes[22, 23] and Trapped Electron Modes (TEM)[24]. More recently the first non-linear gyrokinetic attempts to characterize the influence of plasma shape on ITG turbulence, with the local GS2 code[25], have confirmed the stabilizing effect of elongation[26]. When performing elongation studies, it is important to remove any effects due to the total current because, as non linear results obtained with the ORB5 code[27] have revealed, at fixed shape and at fixed pressure and current profiles a larger total current reduces the ITG driven non-linear transport according to the scaling $\chi_i \propto 1/I_{\text{tot}}$ [28]. This results from the consequent rescaling of the safety factor which geodesic acoustic modes (GAMs) and zonal flows depend on. Latest results from the GYRO code[29] indicate that elongation is beneficial in regard to a mixed ITG/TEM turbulence.

All the analysis performed so far either focused on elongation alone or found that the effect of triangularity is negligible in comparison. By contrast, in this section we will focus almost exclusively, both linearly and non-linearly, on modeling the effect of triangularity on confinement as observed in TCV[15].

The TCV tokamak, *Tokamak à Configuration Variable*[30], was specifically designed and built to explore the influence of shape on the plasma properties. Indeed, as mentioned in Chapter 1, it can operate with edge elongation between 1 and 2.8 and with edge triangularity between 1 and -0.7. Dedicated experimental campaigns were devoted to studying the influence of plasma shape on energy confinement in L-mode; this choice was dictated

primarily by the need to minimize the influence of the magnetic topology on plasma edge stability and focus on core transport studies. Initially, ohmic plasmas were considered with line averaged densities ranging from 5 to $9 \cdot 10^{19} \text{m}^{-3}$, plasma elongation, κ , between 1 and 2.7 and triangularity, δ , between -0.3 and 0.55. The energy confinement time, τ_E , increased considerably with elongation but was independent of triangularity[31, 32, 33]. This behavior was explained by a steepening of the average temperature gradient due to flux surface compression, whereas no dependence of the underlying electron diffusivity on plasma shape was observed. At a later stage, L-mode, centrally EC-heated plasmas were studied at a lower line averaged density $1.8 \cdot 10^{19} \text{m}^{-3}$, intermediate elongation $\kappa=1.5$ and triangularity between -0.65 and 0.55, revealing a strong dependence of the electron energy confinement time on triangularity, which could be cast in the form $(1 + \delta)^{-0.35}$ [34], and could not be explained by the flux surface compression effect mentioned before.

These results motivated a later, more detailed study of plasma confinement in a triangularity scan of EC-heated plasmas. Elongation was kept fixed, at $\kappa = 1.6$, because any change in it introduces major changes in plasma parameters such as current and volume which seriously complicate the analysis. Plasmas were limited on the central column and were characterized by a major radius 0.88 m, a horizontal midplane minor radius $a = (R_{max} - R_{min})/2 = 0.25$ m, a toroidal magnetic field $B_T = 1.44$ T, a line averaged density in the range $1 \div 2.2 \cdot 10^{19} \text{m}^{-3}$ and a flat-top current $260 \div 280$ kA. The electron temperature and density profiles were measured with a Thomson scattering system, characterized by an acquisition rate of 20 Hz and a radial resolution of roughly 0.02 m. The C^{6+} ion temperature profile was measured by a Charge Exchange Recombination Spectroscopy (CXRS) diagnostic. The ECH injected power was between 0.45 and 1.8 MW, deposited just outside the $q=1$ surface at $\rho = 0.4$ to mitigate sawteeth. The absorbed ECH power fraction was calculated by the linear ray tracing code TORAY-GA[35] and, for the densities used in this study, was 100% during the first path through the resonance, so no power was reflected by the vacuum chamber wall. Additionally, the launching direction was adjusted in each condition to ensure that the wave vector was always perpendicular to the total magnetic field at the resonant layer, so no current drive was provided by the RF power. The electron heat transport is calculated via power balance analysis, taking into account EC power deposition, ohmic power and electron-ion equipartition. Interested readers are referred to[15, 36] for further details. The main result of the experiments was the stabilizing role of negative triangularity: in particular, the same electron temperature and density profiles were achieved for plasmas with triangularity of the Last Closed Flux Surface (LCFS) equal to 0.4 and -0.4, respectively, injecting in the latter case half as much power as in the former. This implies that flipping the edge triangularity from 0.4 to -0.4 essentially halves the electron heat transport. Conversely, injecting the same amount of EC power resulted in considerably higher temperature in the $\delta < 0$ case with respect to

the $\delta > 0$ one. In the remainder of this paper we will focus on two TCV shots (shots 28014 and 28008) having the same electron density and temperature profiles but two different edge triangularity values, being equal to 0.4 and -0.4, respectively. These two shots were analyzed in [15] and an overview is shown in Figs.4.3 and 4.4. They are characterized by the same kinetic profiles within the errorbars except for the ion temperatures, which were about 15% higher in the center for the negative δ case, although approximately the same at $\rho = 0.7$; however in the simulations we will neglect this effect which, on the basis of linear simulations, is expected to be small. Note in particular that T_e/T_i is larger than 2 in these discharges.

It is worth commenting briefly on the radial behavior of elongation and triangularity. As is evident from Fig.4.3, the plasma shape moments have finite penetration lengths, i.e. they are not constant along the radius. Their penetration length is governed by magnetic shear which is slightly different in these two shots. In particular if the safety factor profile were flat, the elongation would freely propagate up to the magnetic axis. Instead, since the magnetic shear reaches its maximum values at the edge, it is there that the shape moments are mostly damped. Additionally, due to the difference in the edge triangularity values, the safety factors, and thus the magnetic shears, differ mostly at the edge giving rise to different elongation penetration lengths for these two shots. In the following sections we will address this point further.

These TCV discharges motivated an investigation concerning their microstability, in order to assess the direct influence of plasma shape on electron transport coefficients.

4.6.2 Methodology of numerical simulations

The simulations have been performed with the flux-tube code GS2[25]. A pitch-angle diffusion operator was chosen for treating collisions. Although the code is fully electromagnetic, the simulations performed here are in the electrostatic limit owing to the low beta values in the experiments considered ($2\mu_0\langle p\rangle/B_0^2 \simeq 10^{-3}$). The simulations were performed with three kinetic species (electrons, deuterium and carbon as impurity), 16 to 32 energy grid points, 20 to 40 circulating-particle pitch angles, 16 to 32 trapped-particle pitch angles. Carbon was retained as impurity due to the high Z_{eff} which, being no less than 3.5, leads to a C concentration equal to 20% of that of deuterium. We performed separate convergence studies for positive and negative triangularities, of which the former case is slightly more demanding, and they indicate that at least 11 poloidal modes and 70 radial modes are necessary to attain an accuracy of about 8% on the saturated heat flux; this value will be used in the following as an upper-limit estimation of the error bar associated with every non-linear simulation. All the non-linear simulations discussed in this

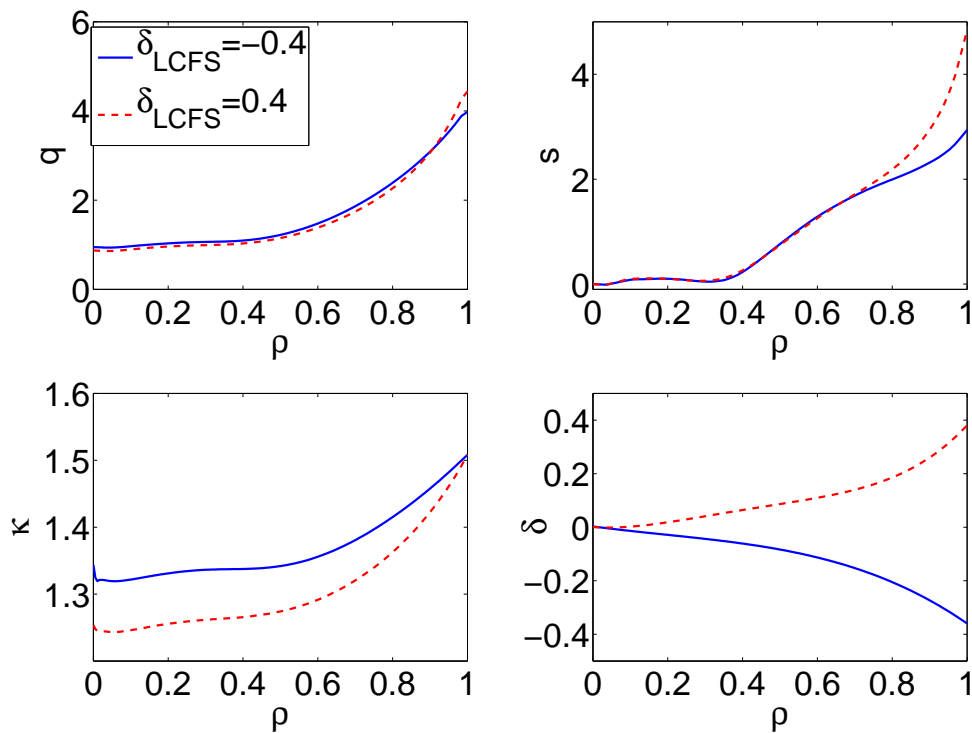


Figure 4.3: Overview of the equilibrium parameters of TCV shots 28008 and 28014. Radial profiles of safety factor (a), magnetic shear (b), elongation (c) and triangularity (d). The q profiles in (a) have been more accurately calculated than in [15]

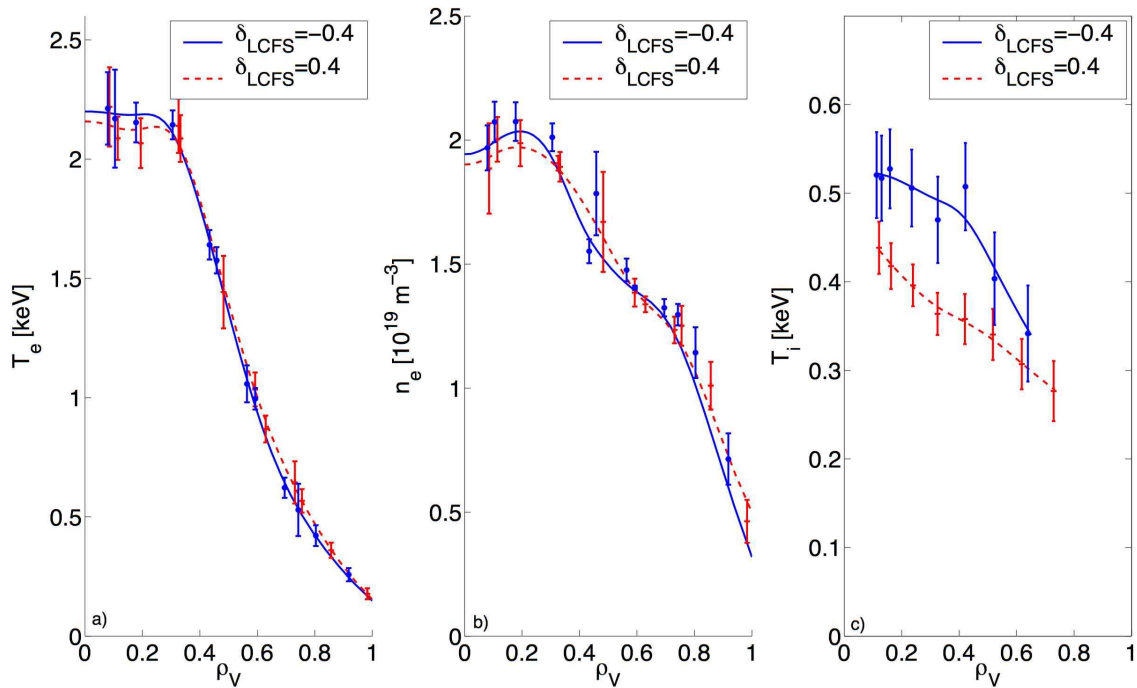


Figure 4.4: Overview of the kinetic profiles of TCv shots 28008 and 28014. Radial profiles of electron temperature (a) and density (b) from Thomson scattering diagnostic, and the ion temperature (c) from CXRS. All the figures show raw data as well as spline-fitted values. This picture was reformatted from [15].

paper have been performed with 15 poloidal modes and 85 radial modes in a simulation domain which, at $\theta=0$, is $132.9 \rho_i$ wide in the θ direction and $207.3 \rho_i$ wide in the radial direction, resulting in turbulent modes evolved in the following ranges: $0 \leq k_\theta \rho_i \leq 0.67$, $|k_x \rho_i| \leq 1.27$ and $\Delta k_x \rho_i = 0.03$, $\Delta k_\theta \rho_i = 0.05$; here ρ_i is the ion Larmor radius and θ is the poloidal angle along the field line. The grid limits have been chosen after exploratory nonlinear runs were performed over a broader range. In particular the upper limit $k_\theta \rho_i < 0.67$, which is close to the most unstable mode as seen in Fig.4.5a, is in fact well above the wave number generating the maximum heat flux, which is $k_\theta \rho_i \simeq 0.15$; at $k_\theta \rho_i = 0.67$ the heat flux drops to 7% of the maximum (see also Fig.4.6b). More details concerning convergence studies are illustrated in Sec. 4.11. A typical run requires about $3 \cdot 10^4$ dynamically adjusted time steps. An initial equilibrium reconstruction, performed with the LIUQE code [40], to determine the plasma boundary was followed by a simulation with the PRETOR[37] transport code to derive the steady-state current profile, which was then provided in input to the CHEASE[38] equilibrium code to calculate the complete equilibria directly read by GS2. This method ensures a correct evaluation of the magnetic topology. Alternatively, an analytical description, such as the Miller parametrization[39], could be used. However, in this case it would be imperative to choose the parameters such that they are all consistent with the equilibrium they refer to. Let us illustrate this

point in the case of a triangularity scan: by solely changing the value of the triangularity on a given flux surface one does not obtain the actual experimental equilibrium relative to the desired triangularity because, in reality, triangularity is correlated with its radial derivative and with the surface's Shafranov shift, which have to be changed as well. To correctly evaluate the additional geometrical terms needed in the analytical parametrization, an actual equilibrium reconstruction is therefore required. The method employed reads the output of an MHD equilibrium code (CHEASE) directly, thus automatically providing the correct geometrical information to GS2.

To isolate just the effect of plasma shape, the GS2 simulations have been performed by keeping fixed temperature, density and effective charge profiles when comparing different triangularities; the actual experimental profiles are indeed identical within the error bars.

4.6.3 Geometrical background

In this section we will briefly elucidate some geometrical concepts useful to the reader not familiar with the GS2 code and, in general, with ballooning coordinates. An axisymmetric equilibrium magnetic field made of closed surfaces may be represented in terms of scalar potentials[41]

$$\mathbf{B} = \nabla\alpha \wedge \nabla\psi, \quad \alpha = \varphi - q(\psi)\theta - \nu(\psi, \theta), \quad (4.60)$$

where q is the safety factor and the scalar potentials are ψ , the poloidal flux, θ , the poloidal angle, and $\varphi - \nu$, the toroidal angle minus ν , which is a periodic function in φ and θ . The field lines are straight and lie in the $(\varphi - \nu, \theta)$ plane. A convenient coordinate system is (ψ, α, θ) where ψ defines the flux surface of interest, α identifies each field line on a flux surface and θ labels the position along the field line α on the flux surface ψ .

In ballooning coordinates, the quasi-orthogonality between the equilibrium magnetic field, \mathbf{B}_0 , and the dominant instability is modeled by assuming that any perturbation of a given quantity X may be expressed as[12]

$$X = \hat{X}(\theta)e^{iS}, \quad (4.61)$$

where \hat{X} is the complex amplitude of the perturbation and S is the ballooning eikonal, such that

$$\mathbf{B}_0 \cdot \nabla S = \nabla\alpha \wedge \nabla\psi \cdot \nabla S = 0. \quad (4.62)$$

This condition models the alignment of perturbations along the field line. In turn this implies that S must be a function of ψ and α , and could thus be expressed as $S = n_0[\alpha + q(\psi)\theta_0]$. Here n_0 is an integer labeling the mode instability and θ_0 is the ballooning angle which ties radial and poloidal mode numbers through the relation $k_x = -k_\theta s\theta_0$,

where s is the magnetic shear[12].

The non-linear gyrokinetic equation, in ballooning coordinates, is given by

$$\left(\frac{\partial}{\partial t} + v_{\parallel} \hat{\mathbf{b}} \cdot \nabla + [\tilde{\chi}, \cdot]/B + i\omega_D \right) \tilde{g} = i\omega_*^T \tilde{\chi} - e \frac{\partial F_0}{\partial E} \frac{\partial \tilde{\chi}}{\partial t}, \quad (4.63)$$

where \tilde{g} is the non adiabatic part of the distribution function, F_0 is the Maxwellian equilibrium distribution function, E the energy coordinate, $[\cdot, \cdot]$ is the Poisson bracket of the spatial derivatives which models the non linear ExB drift, $\omega_D = \nabla S \cdot \mathbf{B}_0 \wedge (mv_{\parallel}^2 \hat{\mathbf{b}} \cdot \nabla \hat{\mathbf{b}} + \mu \nabla B_0 + Z_e \nabla \Phi_0)/(mB_0\Omega)$ is the curvature and ∇B drift, $\tilde{\chi} = J_0(k_{\perp} \rho_i) \tilde{\phi}$ is the gyro-averaged electrostatic potential and ω_*^T is the diamagnetic frequency. The latter, according to [12], can be written as

$$\omega_*^T = \frac{\hat{\mathbf{b}} \wedge \nabla S \cdot \nabla F_0}{B_0} = n_0 \frac{\hat{\mathbf{b}} \wedge \nabla [\alpha + q(\psi)\theta_0] \cdot \nabla F_0}{B_0} = n_0 \frac{\hat{\mathbf{b}} \wedge \nabla [\alpha + q(\psi)\theta_0] \cdot \nabla \psi}{B_0} \frac{\partial F_0}{\partial \psi}. \quad (4.64)$$

Using Eq.4.60a, the rotation property of the triple product and the fact that the safety factor, being a flux function, depends only on ψ we obtain

$$\omega_*^T = n_0 \frac{\partial F_0}{\partial \psi} \quad (4.65)$$

which is then only a function of the toroidal mode number of the instability, n_0 . Therefore in Eq.4.63 only the parallel advection $\hat{\mathbf{b}} \cdot \nabla$, the ∇S term, the curvature and ∇B drift operators and the magnetic field itself depend on the coordinate θ along the field line[12], and so may change according to the equilibrium reconstruction. Also an additional term, $\nabla \rho$, depends on θ and enters in the evaluation of volume integrals and flux surface averages.

Once the toroidal mode number n_0 of the perturbation and the radial derivative of the equilibrium distribution function are fixed, any change in the equilibrium reconstruction is reflected into changes in the the aforementioned quantities.

Let us now develop one of these terms, $|k_{\perp}|^2$, which will be used in the following

$$|k_{\perp}|^2 = |\nabla S|^2 = n_0^2 |\nabla(\alpha + q\theta_0)|^2 \propto k_{\theta}^2 |\nabla \alpha \cdot \nabla \alpha + 2\theta_0 \nabla \alpha \cdot \nabla q + \theta_0^2 \nabla q \cdot \nabla q|. \quad (4.66)$$

In the circular, high aspect ratio, zero β , limit this can be written as

$$|\nabla S|^2 \propto k_{\theta}^2 |1 + s^2 \theta^2 - 2s^2 \theta_0 \theta + \theta_0^2 s^2|. \quad (4.67)$$

4.6.4 Linear simulations

Before performing a non-linear analysis, linear simulations are useful to understand the basic properties of the instabilities under consideration and to explore all underlying

features of the experimental regime, in particular to uncover possible hidden variables that may affect turbulence independently of triangularity. All the runs described in this section have been performed with three kinetic species: electrons, deuterium, and carbon as impurity; the radial wave number has been chosen to be equal to zero and with the actual reconstructed equilibrium located at $\rho = 0.7$, where ρ is defined as the square root of the normalized volume, Eq.4.4. The choice of this radial location corresponds to a compromise between the interest of simulating core turbulence and the fact that shape effects are more visible at the plasma edge. Indeed shape and toroidicity decrease when going from the edge to the magnetic axis.

Since the real frequencies of all unstable modes evolved are in the electron diamagnetic direction (negative sign in our convention) and since the majority of the heat flux is carried by the trapped electrons, we can conclude that the core of these TCV plasmas is dominated by TEM turbulence. To strengthen our confidence in this claim and to assess the impact of experimental uncertainties, we performed additional simulations varying the electron and ion temperature profiles as well as the density profiles over their experimental error bars to see how far from a possible regime transition these data are; the results are summarized in Table 4.1 and do not show any change of behavior. The T_e/T_i ratio has been changed by 25% even though its experimental uncertainty is lower.

case	variation	max $\Delta\omega$	max $\Delta\gamma$
R/L_{T_e}	-10%	-4%	-5%
R/L_{n_x}	-25%	-10%	-15%
T_e/T_i	-25%	-16%	-10%
T_e/T_i	+25%	+22%	-13%
R/LT_i	+10%	+3%	+2.4%

Table 4.1: Linear scan in experimental profiles showing the maximum variation in ω and γ , calculated over the linear spectrum of Fig.4.5, obtained by varying the equilibrium profile values within the experimental error bars.

The calculated spectra for TCV shots 28014 and 28008 are depicted in Figs.4.5 and 4.6 and show two important features. First, the growth rate of the most unstable mode for each poloidal wave vector is lower in the negative δ case compared to the positive one. Second, the values of the reconstructed field line averaged k_\perp are, for low toroidal mode number, higher in the negative δ case with respect to the positive one, while the opposite holds for high mode numbers. The average k_\perp has been calculated as follows[42]

$$\langle k_\perp^2 \rangle = \frac{\int_{\theta_{min}}^{\theta_{max}} d\theta k_\perp^2(\theta) |\tilde{\phi}(\theta)|^2}{\int_{\theta_{min}}^{\theta_{max}} d\theta |\tilde{\phi}(\theta)|^2}, \quad (4.68)$$

where $\tilde{\phi}$ is the fluctuating electrostatic potential, k_\perp is defined as in Eq.4.66 and $\theta_{min,max}$ specify the flux tube length used in the simulation. This formula weights the perpendicular

wave vector with the energy of the fluctuations, therefore in case of strongly ballooning modes it enhances the contribution from the low field side of the plasma. When only the modes at $\theta_0 = 0$ are considered, which are usually the most unstable, it can be seen that in the high aspect ratio, zero β , circular limit equation Eq.4.68 reduces to

$$\langle k_{\perp}^2 \rangle = k_{\theta}^2 \left[1 + s^2 \frac{\int_{\theta_{min}}^{\theta_{max}} d\theta \theta^2 |\tilde{\phi}(\theta)|^2}{\int_{\theta_{min}}^{\theta_{max}} d\theta |\tilde{\phi}(\theta)|^2} \right] = k_{\theta}^2 (1 + s^2 \langle \theta^2 \rangle), \quad (4.69)$$

in agreement with [42]. The consequence of these two effects is, in a mixing-length picture, a double stabilization at low mode numbers, where most of the transport occurs, due to the reduced growth rates and to a shorter perpendicular wavelength; this result is plotted in Fig.4.6b which also makes it apparent that the first stabilizing mechanism (on γ) dominates at high poloidal wave vectors. This conclusion is consistent with results previously obtained with the linear global code LORB [43, 44].

As a first qualitative survey of the effect of plasma shape on plasma confinement, one can perform a two dimensional scan in edge triangularity and edge elongation with a given pressure and current profile. The scan is performed by taking density and temperature profiles of a given pulse (28014 in our case) and then by changing the equilibrium reconstruction: i.e. recalculating the equilibrium starting with the same pressure and current profile and imposing a different shape to the Last Closed Flux Surface (LCFS). The recalculated q profiles change up to about 10% along the maximum δ scan at each value of elongation. The maximum change in elongation at fixed triangularity is about 20%, almost irrespective of triangularity. The absolute elongation difference also stays almost constant up to the magnetic axis.

The resulting mixing-length heat diffusivity, calculated as the maximum of $\gamma / \langle k_{\perp}^2 \rangle$ [42], as a function of the shape parameters is shown in Fig.4.7. It is apparent that turbulence is quenched by lowering triangularity, especially to negative values, or by increasing elongation, as the contour levels over most of the $\kappa - \delta$ space can be approximately described by $\kappa \simeq \delta + \text{const}$ lines. A more detailed examination, however, reveals a more complex dependence on elongation at different values of triangularity. In fact an increase in κ is always stabilizing at negative δ , whereas for positive triangularities it is initially destabilizing and then stabilizing again. This behavior is not due to the growth rate but to the average $\langle k_{\perp}^2 \rangle$, and in turn to the shape of the electrostatic potential along the field line, as can be seen in Fig.4.8 which plots growth rate and equivalent perpendicular scale of the fluctuation corresponding to the maximum of $\gamma / \langle k_{\perp}^2 \rangle$.

Next, we proceed to explore whether the variations induced by a change in triangularity in other discharge quantities could themselves have an influence on microturbulence. Since the TCV shots under analysis are dominated by TEM turbulence, one might speculate that the negative δ stabilization could be due to a difference in aspect ratio resulting in a

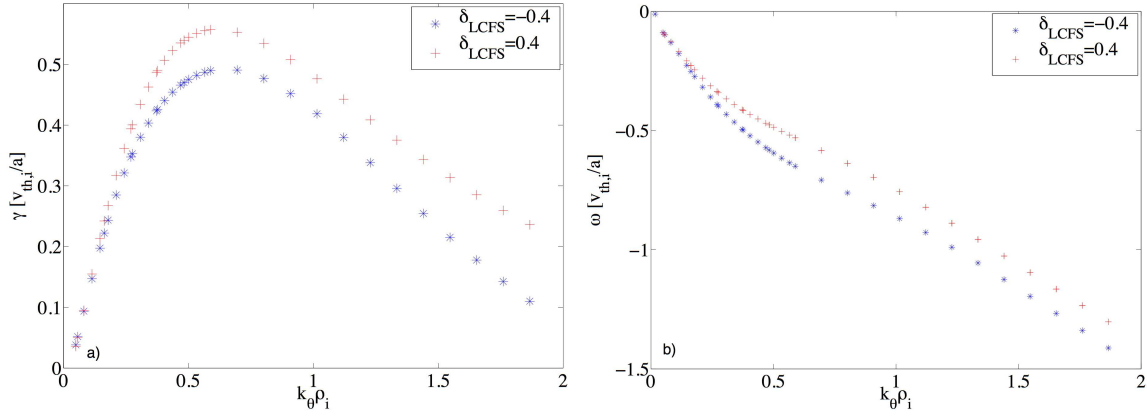


Figure 4.5: TEM dispersion relations from linear GS2 simulations for TCV shots 28014 and 28008 (growth rate on the left, real frequency on the right). The negative δ case is characterized by lower growth rates than the positive one.

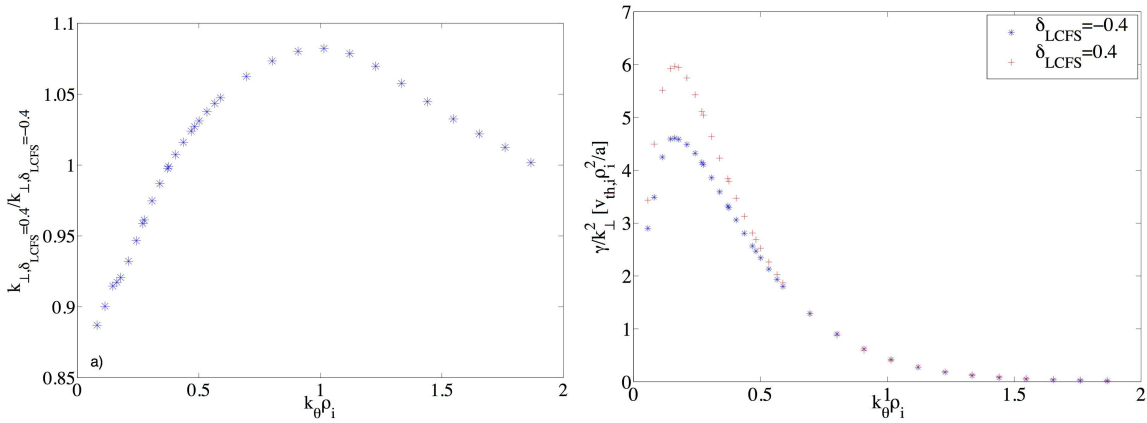


Figure 4.6: a) Ratio of k_\perp for TCV shots 28008 and 28014, estimated from Eq.4.68, as a function of k_θ . b) Mixing length estimate via Eq.4.66 of the electron heat flux calculated by GS2 at $\rho=0.7$ for TCV shots 28008 and 28014.

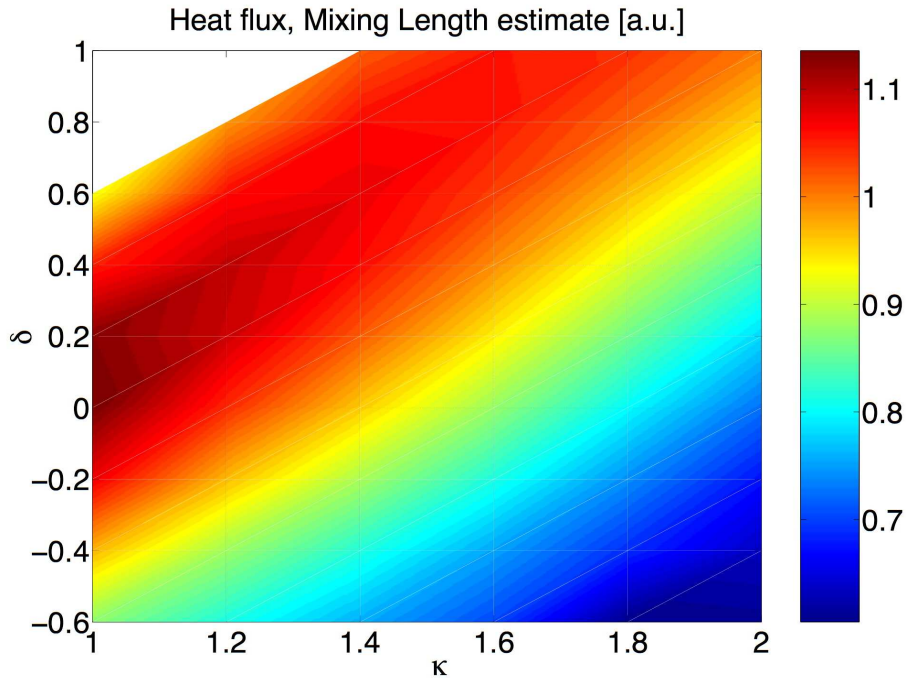


Figure 4.7: Mixing length estimate, calculated as the maximum of $\gamma/\langle k_{\perp}^2 \rangle$, of the electron heat flux obtained with GS2 at $\rho = 0.7$, as functions of edge triangularity and elongation. The top-left corner of the figure is empty because it corresponds to unrealisable equilibria.

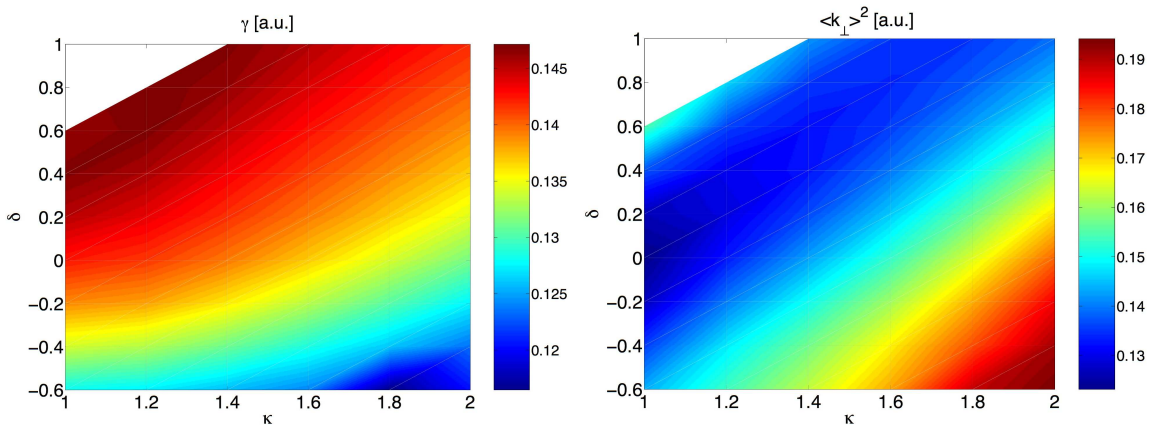


Figure 4.8: Growth rate (left) and averaged $\langle k_{\perp}^2 \rangle$ of the mode corresponding to the maximum of $\gamma/\langle k_{\perp}^2 \rangle$ obtained with GS2 at $\rho = 0.7$ as functions of edge triangularity and elongation.

different trapped particle fraction. In Fig.4.9a we plot the inverse aspect ratio, calculated as

$$(R_{max} - R_{min}) / (R_{max} + R_{min}) \quad (4.70)$$

and, alternatively, in Fig.4.9b through the expression

$$\langle a/R_0 \rangle = \frac{1}{R_0} \sqrt{\frac{\int_{\theta_{min}}^{\theta_{max}} d\theta r^2 |\tilde{\phi}(\theta)|^2}{\int_{\theta_{min}}^{\theta_{max}} d\theta |\tilde{\phi}(\theta)|^2}}, \quad (4.71)$$

which, in analogy to Eq.4.68, represents, by means of an average over the energy of the underlying instability, an effective aspect ratio seen by the particles (Fig.4.9b). Neither function follows the trend of Fig.4.7, and the relative variation of the trapped particle fraction, which is proportional to the square root of the inverse aspect ratio, is over a factor of 10 smaller than the heat-flux variation shown in Fig.4.7.

Another effect that has to be taken into account is the dependence of local elongation on

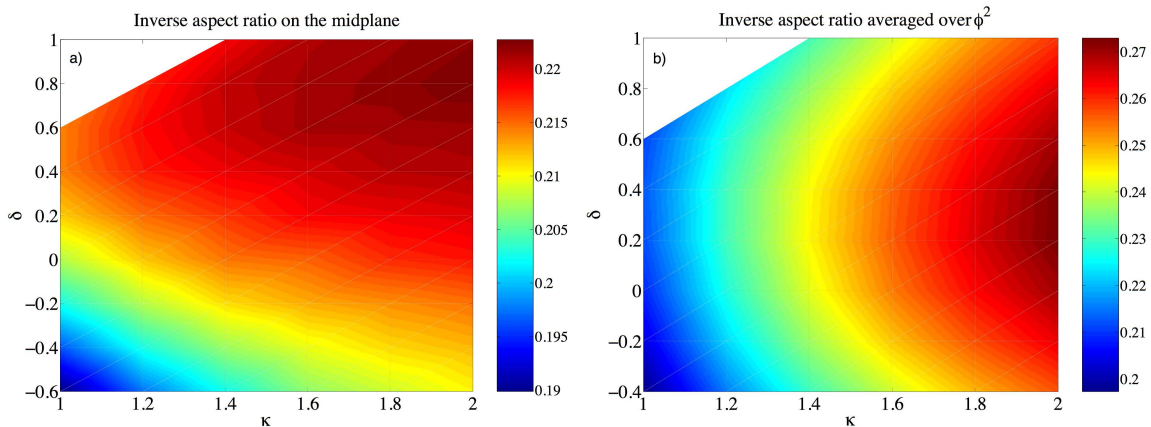


Figure 4.9: Inverse aspect ratio, defined by a) Eq.4.70 and b) Eq.4.71, as a function of triangularity and elongation of the LCFS.

triangularity. Even with the same elongation on the LCFS, the difference in Shafranov shift for two different values of triangularity may result in a different degree of penetration of the elongation into the plasma core. This in turn could cause a variation in TEM turbulence in addition to the direct influence of triangularity. However, for TCV shots 28008 and 28014 the difference in elongation is less than 4% over the whole minor radius; this, considering Fig.4.7, can only have a negligible effect compared to the observed 30% reduction in the maximum of $\gamma / \langle k_{\perp}^2 \rangle$.

Finally we consider the effect on the gradients induced by a change in triangularity. Indeed, even though the profiles as functions of the flux surface coordinate are identical, the local values of the spatial gradients generally differ due to flux surface compression. In particular the enhanced Shafranov shift induced by negative triangularities compared to positive ones, leads to a more peaked pressure profile on the low field side, whereas the

opposite happens on the high field side. To investigate this effect we performed a pressure gradient scan on linear simulations and compared the results expressed as functions of $(1/T)dT/d\rho$ or $\langle\nabla\rho\rangle(1/T)dT/d\rho$; if this effect was responsible for the difference under consideration the growth rates should be equal when plotted as a function of the latter quantity. Even though the difference in the growth rates almost halves, Fig.4.10, this effect cannot be wholly responsible for the observed disparity. Looking at Fig.4.10b one might be surprised by the fact that, even though the negative triangularity case has an enhanced Shafranov shift with respect to the positive triangularity one, and thus the flux surfaces are compressed in the unstable low-field side region, the gradient expressed in real space is lower. This is due to the fact that we calculated the temperature gradient using the $\nabla\rho$ averaged over the whole flux surface without $\tilde{\phi}$ weighting; therefore the result is due to the flux surface expansion on the high field side of the plasma which, outside mid-radius (see Fig.4.11), dominates over the compression on the low field side. If we had weighted the $\nabla\rho$ term with, for example, the electrostatic potential, to account *a posteriori* for the ballooning character of the instability, we would have ended up with a larger difference of the growth rates for these two shots, thus supporting even further a genuine effect of triangularity on plasma micro-stability.

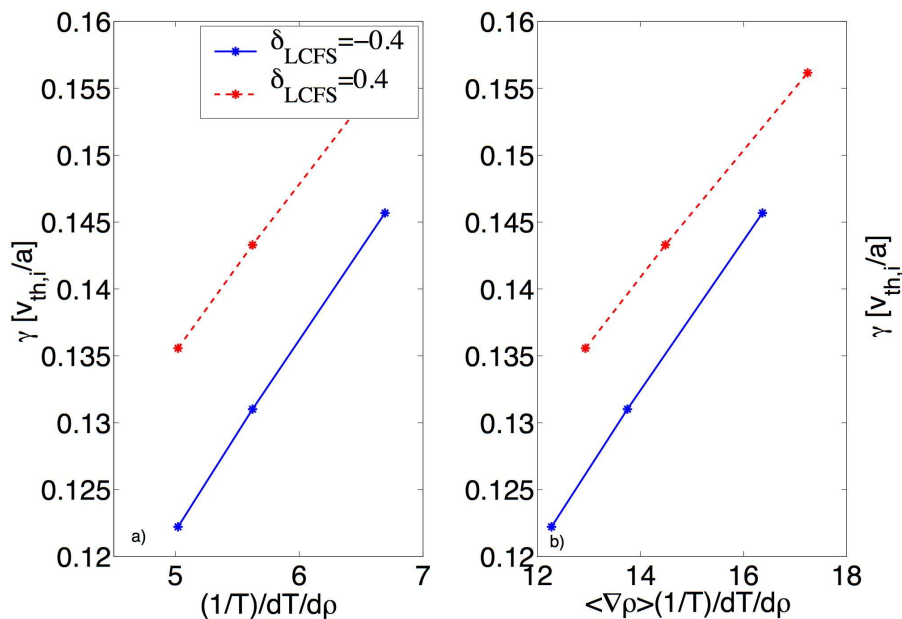


Figure 4.10: Linear growth rates of experimental cases 28014 and 28008 as functions of $(1/T)dT/d\rho$ (a) and $\langle\nabla\rho\rangle(1/T)dT/d\rho$ (b). The compression effect is not responsible for the observed difference.

The TEM was first theoretically investigated in [45] (see Sec.4.4), leading to the identification of the toroidal precession drift of trapped particles as the cause of the instability. Indeed, other parameters such as T_e/T_i and density and temperature scale lengths be-

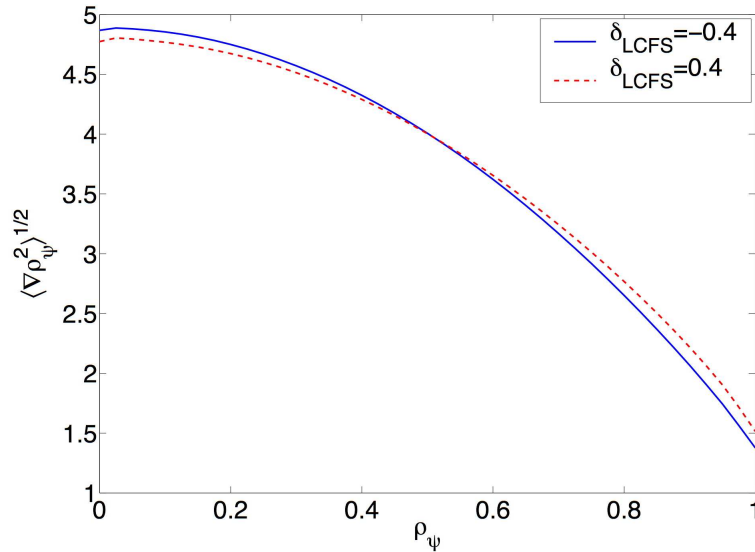


Figure 4.11: Square root of $\langle \nabla \rho^2 \rangle$ as a function of ρ for the two TCV shots under consideration. Outside mid-radius the negative triangularity case is characterized by a larger pressure gradient in real space, for the same pressure gradient in ψ space. Inside mid-radius the trend is the opposite but plasma shaping effects there are too small to be detected.

ing equal, which is the case in the present experiments, it is natural to search for the cause of the observed dependence in the drifts induced by the magnetic topology. Even though the only operational difference between these TCV shots is the edge triangularity, this translates into differences in several quantities, both macroscopic, such as the Shafranov shift, and microscopic, such as the magnetic drifts. To understand how the different microscopic drifts interact, the positive triangularity case has been changed artificially by replacing one or more drives in the gyrokinetic equation, one at a time, with their corresponding values taken from the negative triangularity case. In particular, in

Equil.	$\delta = 0.4$	$\delta = -0.4$	ω_D	$\omega_D + \nabla_\perp$	$\omega_D + \nabla_{//}$	∇_\perp	$\nabla_\perp + \nabla_{//}$	$\nabla_{//}$
χ_{ML}	1	0.77	0.90	0.74	0.92	0.82	0.84	0.98

Table 4.2: Normalized heat diffusivity through mixing length estimate of real cases ($\delta = \pm 0.4$ at $\rho = 0.7$) and of the artificially changed equilibria explained in the text (all the others).

the toroidal gyrokinetic equation one could isolate the effects of curvature and ∇B drifts (which have been simultaneously changed because, as can be seen in Eq.4.22, they differ only in the negligible $\nabla\beta$ and are indicated as ω_D in Table 4.2), the parallel advection (indicated as $\nabla_{//}$ in Table 4.2) and the gradient of the ballooning eikonal, which reflects the effect of magnetic shear and can be interpreted as k_\perp (this parameter is indicated as ∇_\perp in Table 4.2 and has been changed independently of the perpendicular drifts for the sake of numerical investigation). The result of this linear test is depicted in Table 4.2,

which reports the heat diffusivities, normalized to the positive triangularity case value, calculated as the maximum of $\gamma/\langle k_{\perp}^2 \rangle$ [42]. In Table 4.2 it is evident that parallel and perpendicular dynamics behave differently: the curvature and ∇B drifts together with k_{\perp} act to reduce the linear χ_{ML} of the perturbation in the negative δ case, whereas the parallel advection does not appreciably influence it. In particular the ∇_{\perp} of a negative δ configuration narrows the electrostatic potential which, in turn, reduces the equivalent perpendicular wavelength of the fluctuation. Additional tests mixing the electrostatic potential, the growth rate and the k_{\perp} geometrical factor were performed; they result in mixed regimes but are not reported here as considered not significant.

4.6.5 Non-linear simulations

The linear simulations discussed in the previous section show a qualitative trend matching that observed in the experimental TCV shots. Nevertheless it should be noted that linear mixing-length estimates only give a 30% difference in diffusivity between the two equilibria, whereas the experimental value is about 100%: nonlinear effects might therefore be paramount in accounting for the larger variation observed in the experiment. Using the numerical grids described in Sec.4.6.2, non-linear runs have been performed to check whether the $E \wedge B$ non-linearity plays any role in the microstability analysis of these shots. As will be discussed in the following, it is indeed observed that non-linearity plays a further stabilizing role, increasing the difference between the positive and the negative triangularity cases, thus showing how the mixing length approximation is not adequate for describing all the physical details even if it succeeds in capturing the relevant trends. This can be appreciated in Fig.4.12, which compares the ratio between the experimental thermal diffusivities, reconstructed from a power balance analysis, of the two TCV pulses under analysis and the corresponding simulated ratios at three radial points. The non-linear simulations are performed in the collisionless limit. It can be seen that the reduction in transport with negative triangularity is qualitatively reproduced, but a satisfactory quantitative match is only obtained near the plasma edge. The smaller ratios seen in the simulation towards the inside of the plasma can be explained by the finite penetration depth of triangularity. In particular, if at $\rho = 1$ the triangularities are ± 0.4 , at $\rho = 0.7$ they are equal to ± 0.17 and at $\rho = 0.4$ they are lower by a further factor of 3, being equal to about ± 0.07 (see Fig.4.3). So since, going towards the magnetic axis, the fraction of trapped particles tends to zero and the difference in triangularity vanishes, the resulting difference in the trapped particle contribution to the total transport is annulled. Even though passing particles are also stabilized by negative triangularity, they contribute less to the total transport and with a smaller absolute difference with respect to trapped particles. All this results in the two simulations giving approximately the same

result at $\rho \simeq 0.4$. This claim is supported by Fig.4.13, which shows the decrease of the trapped particle contribution to the total transport for the two extreme radial locations in Fig.4.12.

Since the density and temperature profiles are everywhere equal in the two shots, the anomalous transport reduction has to occur over the whole minor radius; the doubling of the experimental confinement time cannot therefore be explained by a stiffness argument which would imply an increased stored energy due to a mode stabilization that is approximately localized close to the plasma edge. In particular, the experimental diffusivity ratio is still approximately 2 even at the innermost location studied. Since a local analysis is patently unable to reproduce this result, as discussed above, global effects may be at play which cannot be reproduced by the present modelling. In the following all the numerical analysis will be performed at $\rho = 0.7$.

Experimentally, the electron diffusivity is found to depend on a combination of various

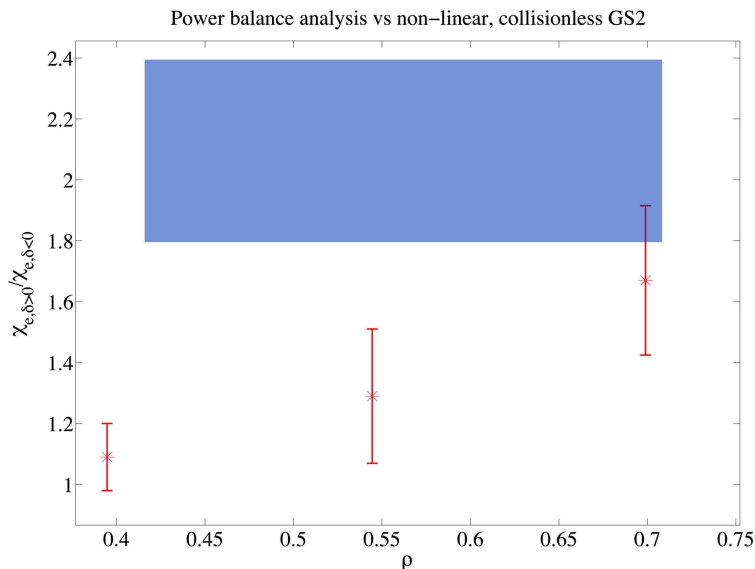


Figure 4.12: Blue rectangle: range in which lies the ratio of experimental electron thermal conductivities, as a function of the square root of the normalized volume, between discharges with edge triangularities equal to ± 0.4 . The area excludes the regions where the EC power was deposited ($\rho < 0.4$) and where the impurity line emission is too large, making the measurement uncertain ($\rho > 0.7$). Red points: same ratio simulated by non-linear, collisionless, GS2 runs; the mean values are calculated in the saturated phase of the simulation.

physical quantities such as T_e , n_e and Z_{eff} . In particular, an inverse linear scaling was found with respect to a particular combination corresponding to the effective collisionality, i.e. the electron collisionality normalized to the electron drift frequency, with the proportionality factor depending in turn on triangularity[15]. As can be seen in Fig.4.14, non-linear collisional simulations reproduce similar behavior with numerical values of the same order of magnitude as the experimental ones. In these non-linear simulations the

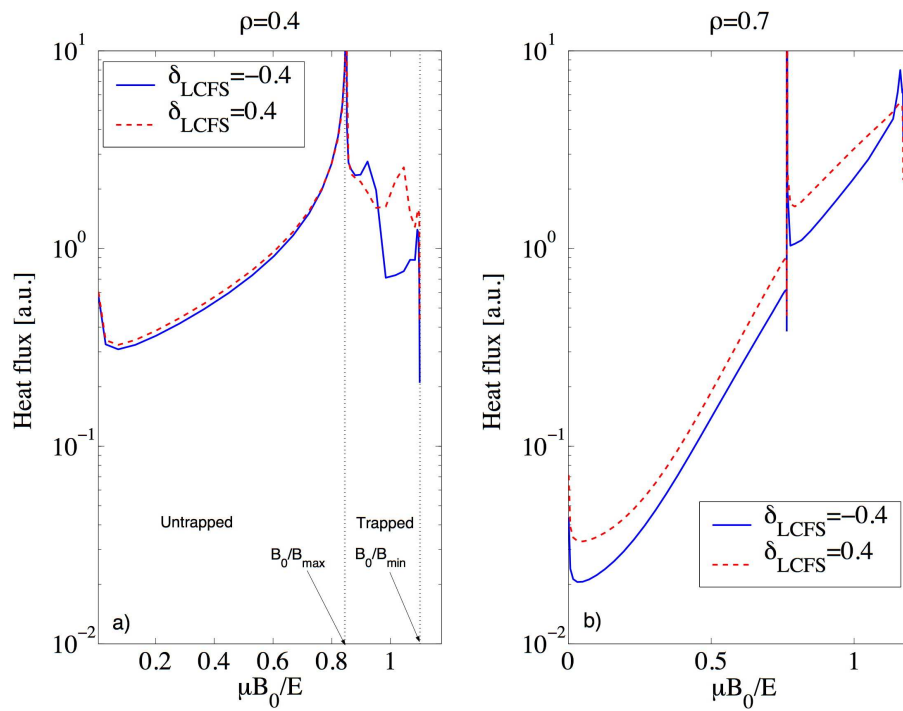


Figure 4.13: Comparison of the non-linear simulated heat transport as a function of pitch angle for positive and negative triangularities calculated at $\rho=0.4$ (a) and 0.7 (b).

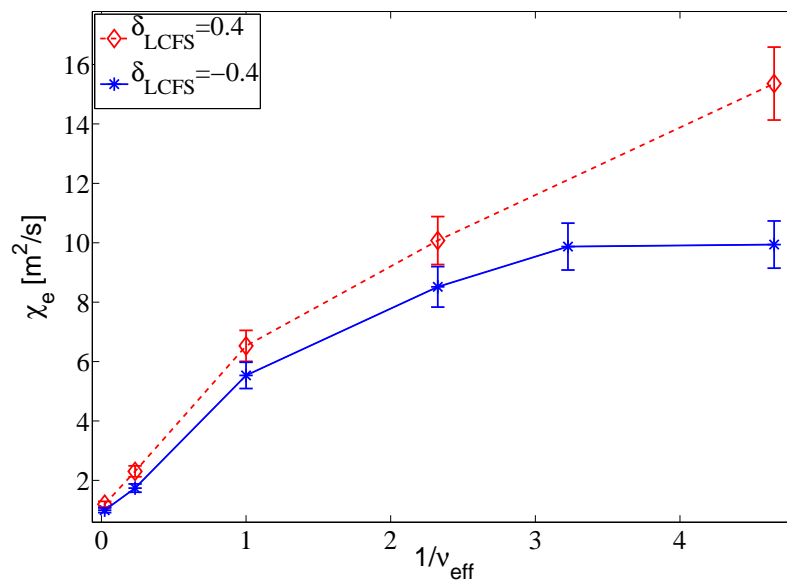


Figure 4.14: Effect of collisionality on the non-linearly simulated electron heat diffusivity.

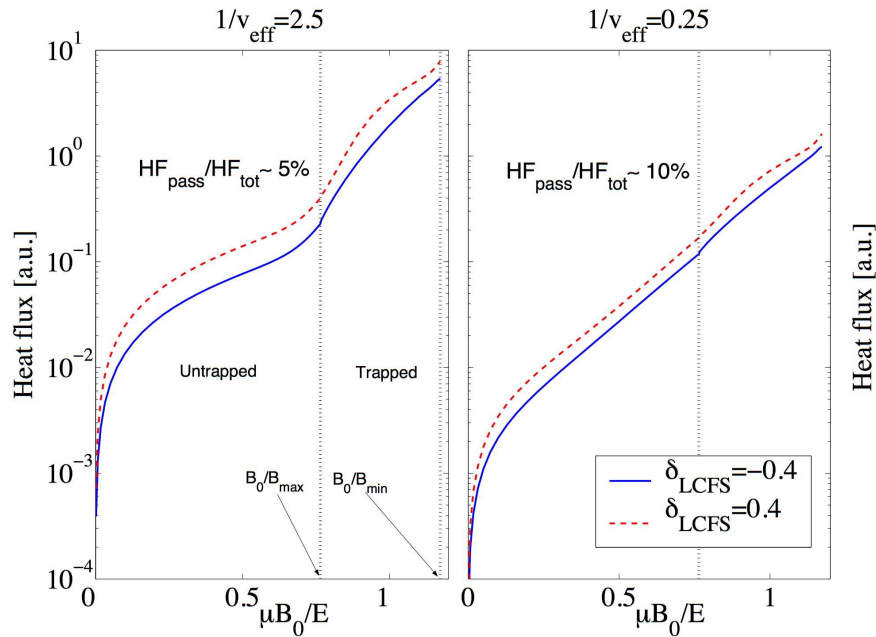


Figure 4.15: Heat Flux integrated over pitch angle (cumulative integral) vs pitch angle for two values of collisionality. At higher ν_{eff} the relative contribution from passing electrons to the total flux increases. Even though their contribution to the total flux is small, note how negative δ stabilizes also passing electrons.

estimated saturated heat flux is carried primarily by the electron species and, additionally, the electron heat flux is mainly due to trapped particles (see Fig.4.15), which confirms the TEM nature of the turbulence under investigation. This insight works in favour of an intuitive explanation of the collisionality dependence observed in both simulations and experiments. Indeed, collisional detrapping and dephasing processes alter the phase space configuration of the instability, leading to more and more particles being taken out of the highly unstable trapped region and transferred into the less unstable passing region, or dephased with the instability, and therefore contributing less to the overall transport. This is also reflected in a higher relative contribution of the passing electrons to the total (and decreased) calculated heat flux increasing, for the cases plotted in Fig.4.15, from 5 to 10%. Thus, in terms of the effect on heat transport, reversing the triangularity from positive to negative is equivalent to increasing the collisionality by a given factor. In other words, TEM in a negative triangularity plasma are stabilized as if the plasma were much more collisional; thus allowing the same amount of transport with, for example, a much lower density and/or a much cleaner plasma. In Fig.4.15 the particle contribution to the total transport as a function of pitch angle is given by the slope of the curves, so it is possible to appreciate how the roles of barely trapped and barely passing electrons become increasingly similar as collisionality is increased.

4.7 Investigation of instability drives

Artificial changes in the equilibrium can be applied to nonlinear simulations in a similar manner as was discussed in Section 4.6.4 for the linear case. The conclusions of that section concerning the roles of the individual drives can thus be put to the test in the nonlinear case. In Table 4.3 it can be seen how a change in either the ∇B and curvature drift or in the equivalent k_{\perp} entering in the quasi-neutrality calculations and gyroaveraging, lead to an approximately equal degree of turbulence suppression. Thus the slight difference found between these two terms in the linear approximation essentially disappears in the non-linear phase. However it is important to note that when these terms are changed simultaneously, which has to be the case in order for the simulations to be physically meaningful since the terms are connected by the relation $\omega_D = \nabla S \cdot \mathbf{B}_0 \wedge (mv_{\parallel}^2 \hat{\mathbf{b}} \cdot \nabla \hat{\mathbf{b}} + \mu \nabla B_0 + Z_e \nabla \Phi_0) / (mB_0\Omega)$ [12], the heat flux variation is reproduced almost exactly, thus confirming that the observed stabilization is induced by a combined effect of different perpendicular drifts and consistent perpendicular scales of the fluctuations. In the table it is also evident how the $\nabla \rho$ term, which enters in the calculations of volume integrals and surface averages, is not alone responsible for the difference, which is then due to the linear terms, although the full non-linear equation increases the difference between the two triangularities compared to the results of Table 4.2.

Equil.	$\delta > 0$	$\delta < 0$	ω_D	∇_{\perp}	$\nabla \rho$	$\nabla_{\perp} + \omega_D$
Saturated heat flux	1	0.59	0.55	0.53	0.78	0.58

Table 4.3: Same as Table 4.2 for corresponding non-linear simulations.

Since, as already mentioned in section 4.6.4, TEM are destabilized by the resonance between the real frequency of the perturbation and the toroidal precessional drift frequency of trapped electrons, it is interesting to evaluate the dependence of the toroidal precessional drift on triangularity. When the banana width can be neglected with respect to the equilibrium scale lengths, which is one of the assumptions of a local code, the toroidal precessional drift reads [5]

$$\langle \dot{\varphi} \rangle = \frac{1}{q} \frac{\partial I_{\parallel} / \partial \psi}{\partial I_{\parallel} / \partial E}, \quad (4.72)$$

where E is the energy of the particle, q its charge and I_{\parallel} is the second (or longitudinal) adiabatic invariant, defined as

$$I_{\parallel}(\psi, E, \mu) = \oint dl_{\parallel} v_{\parallel} = 2 \int_{-\theta_b}^{\theta_b} d\theta J B |v_{\parallel}|. \quad (4.73)$$

Here $\pm \theta_b$ are the bouncing points of the electron with energy E and pitch angle $\mu(B(\psi, \theta_b) = E/\mu)$, J is the Jacobian of the transformation to the field-aligned coordinate system and

B is the amplitude of the magnetic field. Equation 4.72 can then be rewritten as

$$\begin{aligned} \langle \dot{\varphi} \rangle(\psi, E, \mu) &= \frac{1}{q} \frac{\partial I_{\parallel} / \partial \psi}{\partial I_{\parallel} / \partial E} = \\ &= \frac{2E}{q} \frac{\partial}{\partial \psi} \left(\int_{-\theta_b}^{\theta_b} d\theta J(\theta) B(\theta) \sqrt{1 - B(\theta)/B(\theta_b)} \right) / \int_{-\theta_b}^{\theta_b} d\theta J(\theta) B(\theta) / \sqrt{1 - B(\theta)/B(\theta_b)}, \end{aligned} \quad (4.74)$$

which is then a linear function of the particle energy.

Figure 4.16 shows that this quantity behaves very differently for deeply trapped and barely trapped particles; in particular the toroidal precessional drift tends to be higher for positive δ in the deeply trapped region while the opposite happens for negative δ ; this behavior is in agreement with an analytical expression of the toroidal precessional drift and with the Venus code[47], see Sec. 4.12 for more details. For a geometrical interpretation

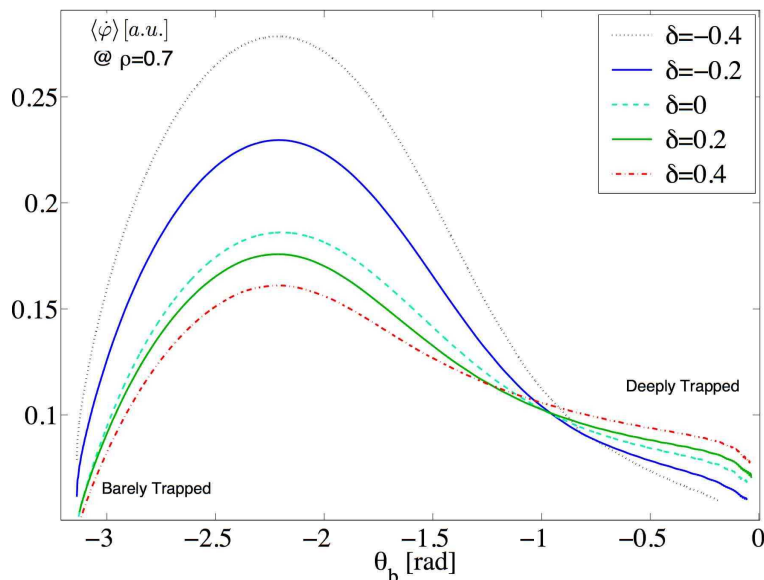


Figure 4.16: Toroidal precessional drift of a trapped electron of energy equal to the electron temperature, in arbitrary units, as a function of the trapped particle's bouncing points, for five different equilibria which have been generated from a single TCV shot, by changing the shape of the LCFS.

we show, in Fig.4.17, the shape of three equilibria and the bouncing angle represented in Fig.4.16. In order to investigate the resonance condition between the perturbation and the toroidal precessional drift frequency, we normalize the latter to the real frequency of the most linearly unstable mode, in agreement with the mixing-length estimate used in Section 4.6.4. Figure 4.18 shows the ratio $n_0 \langle \dot{\varphi} \rangle / \omega(n_0)$ for TCV shots 28008 and 28014, calculated for a particle energy equal to the thermal electron temperature.

A resonant condition in this plot would occur when the ordinate is close to 1. In the case shown it would appear that the negative triangularity case is closer to the resonance. However, as a rule of thumb, the resonance condition ought to be evaluated not for a

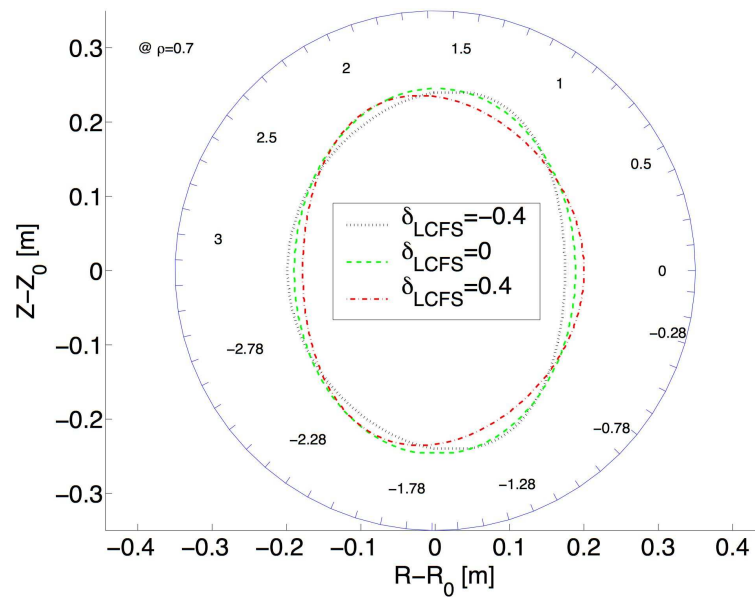


Figure 4.17: Shape of three equilibria of Fig.4.16 superimposed to the bouncing angle, indicating where the toroidal precessional drift of the equilibria cross.

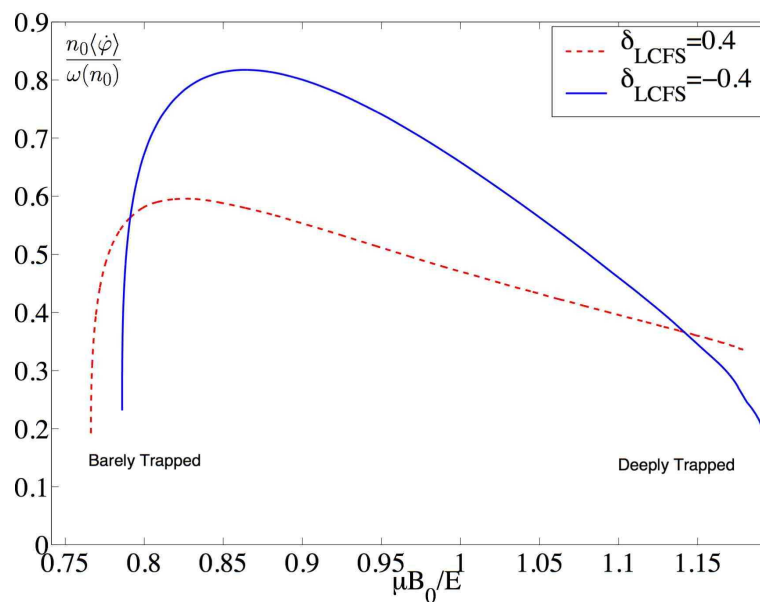


Figure 4.18: Toroidal precessional drift of a trapped electron of energy equal to the electron temperature, normalized to the real frequency of the mode which contributes most to the total transport, as a function of the pitch angle.

thermal particle, but rather at the energy where most of the transport occurs. Our GS2 simulations indicate that this happens for $2.5 \lesssim E/T_e \lesssim 3$; since the ratio shown in Fig. 17 is a linear function of the electron energy divided by the electron temperature, for E/T_e larger than 2 it is the positive delta case that is closer to the resonance, except in the deeply trapped region. In order to verify this rough estimate we can calculate the particle and heat fluxes by performing the energy integral, which is the only right approach to quantitatively calculate any difference in the resonance for the two cases. Earlier in this chapter we showed how these shots are largely dominated by TEM turbulence and, further, that there is no appreciable shape effect on the parallel advection term in the GK equation; this now justifies the use of the bounce-averaged GK linear equation. Considering a generic physical quantity X , its flux across a given flux surface is given by

$$\langle \Gamma_X \rangle = \frac{\int d^3r dE d\mu X \tilde{g} \mathbf{v}_{\mathbf{E} \wedge \mathbf{B}} \cdot \nabla \rho}{\int d^3r \nabla \rho} = - \frac{\int d^3r dE d\mu X \tilde{g} \nabla \phi \wedge \hat{\mathbf{b}}/B \cdot \nabla \rho}{\int d^3r \nabla \rho}, \quad (4.75)$$

where \tilde{g} is the non-adiabatic part of the distribution function, B the amplitude of the magnetic field and $\tilde{\phi}$ the electrostatic potential, and the integral is carried out over the whole flux tube. By expressing \tilde{g} and $\tilde{\phi}$ as Fourier sums, Eq.4.75 becomes

$$\langle \Gamma_X \rangle = \frac{\int d^3r dE d\mu X \sum_k \hat{g}_k \hat{\phi}_k^* i \mathbf{k} \wedge \hat{\mathbf{b}}/B \cdot \nabla \rho}{\int d^3r \nabla \rho}. \quad (4.76)$$

where the reality constraint on the electrostatic potential, $\hat{\phi}_{-k} = \hat{\phi}_k^*$, has been imposed. Since in the linear theory there is no saturation mechanism, let us normalize the X flux to the squared modulus of the electrostatic potential. Considering only the most unstable mode we may then write

$$\langle \Gamma_X^{nor} \rangle = \Re \frac{\int d^3r dE d\mu X \hat{g}_k \hat{\phi}_k^* i \mathbf{k} \wedge \hat{\mathbf{b}}/B \cdot \nabla \rho}{\frac{e^2}{T_e^2} \int d^3r \hat{\phi}_k \hat{\phi}_k^* \int d^3r \nabla \rho}. \quad (4.77)$$

the bounce-averaged kinetic equation in Fourier space reads[46]

$$\tilde{g} = \frac{\omega - \omega^* \left[1 - \eta_e \left(\frac{3}{2} - \frac{E}{T_e} \right) \right]}{\omega - n_0 \langle \dot{\varphi} \rangle} \frac{e \langle \phi \rangle}{T_e} e^{-E/T_e}, \quad (4.78)$$

where $\eta_e = d \log(T_e) / d \log(n_e)$, $\langle \phi \rangle$ is the bounce-averaged electrostatic potential, $\langle \dot{\varphi} \rangle$ is the bounce-averaged toroidal precessional drift frequency, ω is the mode's complex frequency and the diamagnetic frequency is expressed by $\omega^* = k_\theta T_e \nabla n_e / (q B n_e)$. Adopting the approximation $\phi \simeq \langle \phi \rangle$ and substituting Eq.4.78 into Eq.4.77 we obtain the following quasi-linear estimate for the X flux

$$\langle \Gamma_X^{nor} \rangle = \Re \int d^3r dE d\mu X \frac{\omega - \omega^* \left[1 - \eta_e \left(\frac{3}{2} - \frac{E}{T_e} \right) \right] i \mathbf{k} \wedge \hat{\mathbf{b}} / B \cdot \nabla \rho}{\omega - n_0 \langle \dot{\varphi} \rangle} e^{-E/T_e} \frac{e}{T_e} \int d^3r \nabla \rho. \quad (4.79)$$

Taking now as X the particle energy, Eq.4.79 gives the heat flux, while taking $X = 1$ we obtain the particle flux.

Figure 4.19 shows the μ integrand (i.e. energy and surface integral) of Eq.4.79 for TCV shots 28008 and 28014, indicating how negative triangularity acts, compared to positive triangularity, favorably everywhere in the pitch angle space except for the deeply trapped particles, which are less unstable in a positive triangularity configuration. Figure 4.17 indicates that this region is a subset of the bad curvature region. By performing the pitch angle integral we obtain that the heat and particle fluxes for the negative triangularity configuration are lower by about 15% than the ones corresponding to the opposite triangularity. Roughly the same result is reproduced qualitatively also by linear and non-linear GS2 simulations (Fig.4.20) which solve the whole GK equation coupled to the Poisson equation. The only differences in the non-linear run are the precise values of the ratio of the two heat fluxes and of the pitch angle value at which they cross over each other.

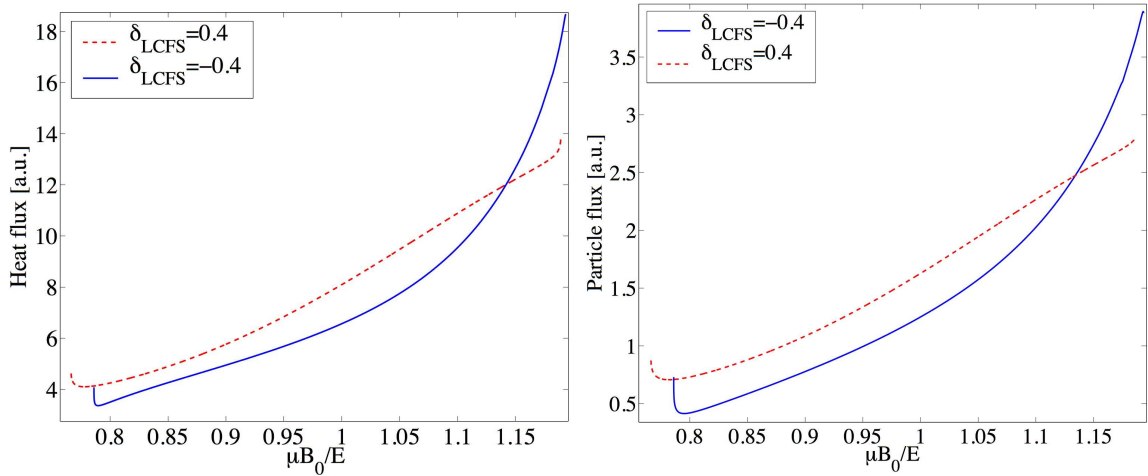


Figure 4.19: Quasi-linear estimates of the energy and particle fluxes as functions of the pitch angle, for TCV shots 28008 and 28014.

As the toroidal precessional drift seems to be playing such an important role in the microinstability of these TCV shots, it could be expected that its radial dependence would be a good diagnostic for interpreting the results of GS2. In Fig.4.21 we plot, as a function of the trapped particle bounce-angle, the value of $\langle \dot{\varphi} \rangle$ for TCV shots 28008 and 28014 at the three radial positions of Fig.4.12. The difference between the two cases gets smaller and smaller as one approaches the magnetic axis, due to the finite penetration depth of triangularity.

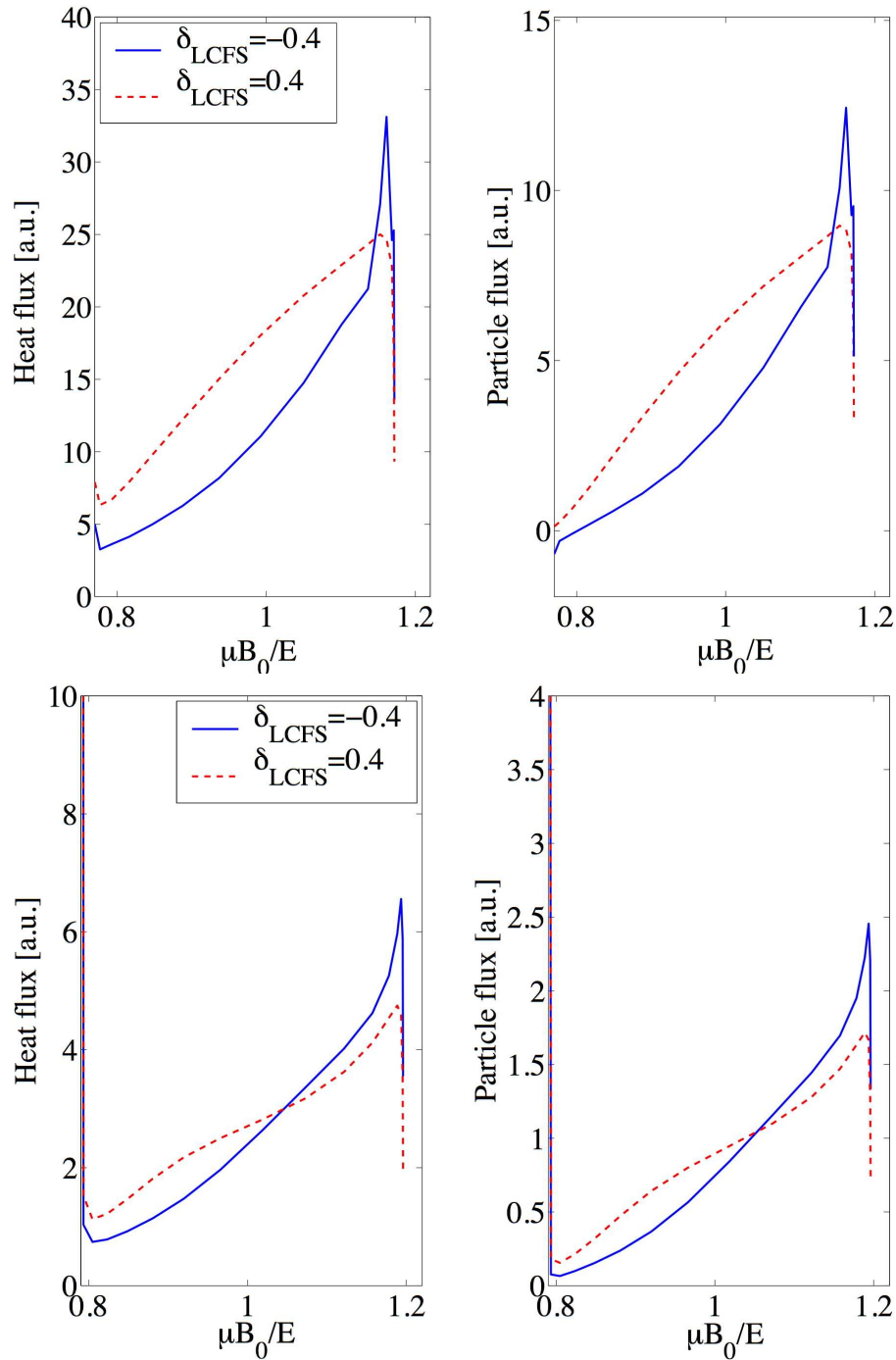


Figure 4.20: Non linear (top) and linear (bottom) GS2 estimates of the heat flux (left) and of the particle flux (right) as functions of the pitch angle, for TCV shots 28008 and 28014.

As briefly mentioned in Sec.4.6.4, since the toroidal precessional drift is a combined effect of parallel and perpendicular dynamics, the $\langle \dot{\varphi} \rangle$ diagnostic is not only consistent with the numerical exercises of Tables 4.2 and 4.3, but is actually a direct and powerful tool to interpret in detail the transport properties of plasmas dominated by TEM turbulence. It can be understood that the actual ratio of the toroidal precessional drift to the dominant mode frequency is of fundamental importance in the evaluation of the generated flux. To validate this picture we artificially changed the phase velocity of the dominant mode to assess its impact on the velocity integral; the result is plotted in Fig.4.22 which represents the particle flux in pitch angle space for the negative triangularity case. As can be noticed, the contribution of barely or deeply trapped particles can be enhanced or reduced by simply changing the phase velocity of the resonating mode without changing its growth rate.

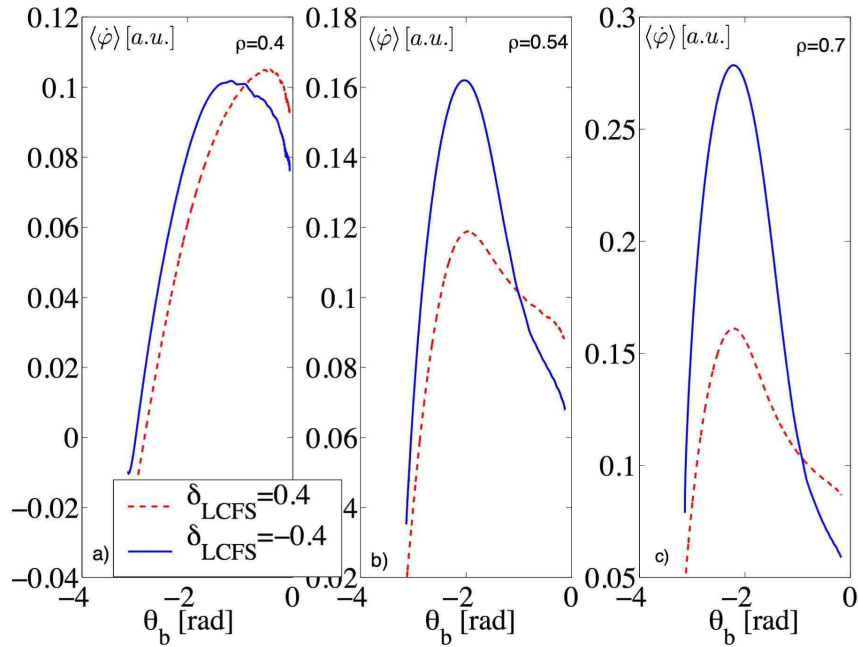


Figure 4.21: Toroidal precessional drift frequency, in arbitrary units, as a function of the bouncing angles [rad] of a trapped particle with energy equal to the plasma electron temperature, calculated at three radial positions.

4.8 Impurities and additional effects

In this section we will estimate the effects exerted by impurities on the confinement of the TCV shots analyzed. As already mentioned in Sec.4.6.1, shots at different edge triangularities are almost identical, in the sense that they do have the same kinetic profiles within the error-bars, except for a slight difference in the ion temperature. In particular

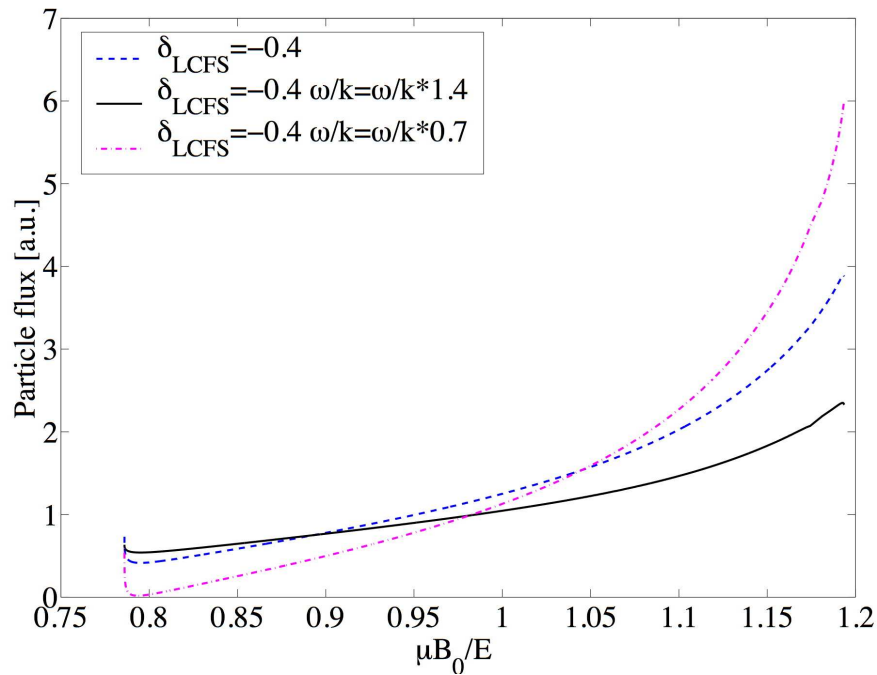


Figure 4.22: Quasi-linear particle flux for the negative triangularity equilibrium, at $\rho = 0.7$, with artificial changes of the dominant mode phase velocity.

the total current, the applied loop-voltage and the electron density and temperature are equal, therefore suggesting the same, or almost the same, current density distribution. Nevertheless, no information is available on the effective charge radial profile. Indeed, if there were no impurities, quasi-neutrality would impose the ion densities of the two shots to be equal but, since the ionic population is heterogeneous, an additional degree of freedom is present in the system, allowing the quasi-neutrality condition to be satisfied with different radial profiles of ion density. The quasi-neutrality equation and the definition of the effective charge (Z_{eff}) read

$$\sum_i Z_i n_i = n_e \qquad \sum_i Z_i^2 n_i = n_e Z_{\text{eff}}. \quad (4.80)$$

In the case of two ion species, namely, deuterium and carbon, which are the dominant species in the TCV shots under consideration, Eqs.4.80 reduce to

$$Z_D n_D + Z_C n_C = n_e \qquad Z_D^2 n_D + Z_C^2 n_C = n_e Z_{\text{eff}} \quad (4.81)$$

where subscripts C and D stand for carbon and deuterium, respectively. Therefore, for a given experimental electron density profile, a free choice in the, e.g., deuterium density profile determines the carbon density profile and, thus, the Z_{eff} profile.

In the absence of external particle sources such as NBI and pellets, the particle balance is determined by neoclassical particle fluxes, the so-called Ware pinch and penetration of

neutrals from the wall, and turbulent fluxes:

$$\frac{\partial n}{\partial t} + \nabla \cdot (\mathbf{\Gamma}_{\text{NC}} + \mathbf{\Gamma}_{\text{turb}}) = 0 \quad (4.82)$$

in steady-state the two fluxes need to be equal and opposite in sign.

It is in general difficult to precisely calculate the neutral penetration into the plasma core since it depends on actual temperature and density profiles as well as on the number of atomic species in the plasma. However, in our case it is reasonable to estimate the neutral penetrations for the two geometries to be equal since, up to $\rho \simeq 0.7$, all the measured kinetic profiles are indeed equal, including ion temperature. Nevertheless, non-linear simulations show a larger particle flux in the positive triangularity case. The neo-classical Ware pinch is estimated to be smaller than the particle flux simulated by GS2 by a factor 10 to 20, thus making its actual value, which depends on the bootstrap current (see Chap.1, Sec.4) and thus on the kinetic profiles, unimportant. If we assume the neo-classical fluxes to be equal in the two triangularity cases, It is imperative to find under which conditions also the turbulent particle fluxes can be equal.

In Sec.4.6.2 it is explained how the numerical equilibrium is calculated; it should be added here that the Z_{eff} profile was assumed to be flat and its value, equal to 3.5, was chosen to match the plasma resistivity calculated from the loop voltage and total current. Even though measurements performed with the charge exchange recombination spectroscopy suggest slightly larger values of the effective charge in the negative triangularity shot, the associated error-bars are too large to reach any definitive conclusion. Here we therefore relax the assumptions on Z_{eff} and will try to make a rough estimate of the effective charge profile by matching the quasi-linear electron particle fluxes of the two shots with different density profiles of the two ion species; the electron density profiles being the experimental values, and therefore equal for the two triangularities.

Let us solve Eqs.4.81 for n_D and n_C and then calculate their gradients:

$$\begin{bmatrix} \frac{\nabla n_D}{n_D} \\ \frac{\nabla n_C}{n_C} \end{bmatrix} = \begin{bmatrix} \frac{\nabla n_e}{n_e} - \frac{\nabla Z_{\text{eff}}}{Z_{\text{eff}}} \frac{Z_{\text{eff}}}{Z_C - Z_{\text{eff}}} \\ \frac{\nabla n_e}{n_e} + \frac{\nabla Z_{\text{eff}}}{Z_{\text{eff}}} \frac{Z_{\text{eff}}}{Z_{\text{eff}} - Z_D} \end{bmatrix} \quad (4.83)$$

By fixing the experimental electron density gradient and the value of Z_{eff} at one particular radius, the Z_{eff} scale length can be calculated on the basis of a given deuterium density profile shape; the carbon density profile follows then by quasi-neutrality. The procedure will be the following

1. Choice of a radial location near the edge, keeping in mind considerations on shape penetration expressed in Secs.4.6.4 and 4.6.5
2. Choice of Z_{eff} values at that location for positive and negative δ cases, which is the boundary condition for the differential equation in Z_{eff}

3. Scan the deuterium density scale length from 0.5 to 10 times the electron density scale length for both triangularities. In this range, which is assumed to be large enough to capture physically reasonable changes of the deuterium density scale length with respect to the electron one, we will look for possible solutions of the deuterium density scale length
4. Match the electron quasi-linear particle flux for the two geometries; this permits the derivation of the ion density scale length in one geometry as a function of its value in the other.
5. Calculate the corresponding relation between the Z_{eff} scale lengths for the two geometries, for a range of physically acceptable values. The result is shown in Fig.4.23.
6. Propagate the Z_{eff} to an inner radial location by means of the gradient found above
7. Iterate to find the whole Z_{eff} profile for each case (see Fig. 4.24)

The procedure outlined above can only identify a range of profiles, since the Z_{eff} scale lengths cannot be determined independently for the two geometries. However, the key issue is in fact the relation between the two profiles. Indeed, the whole purpose of the exercise is to check whether the negative δ case could be characterized by a larger Z_{eff} in the core, which could be responsible of an additional stabilization though collisionality. As can be seen in Fig.4.24 the quasi-linear model indicates indeed that the negative δ case

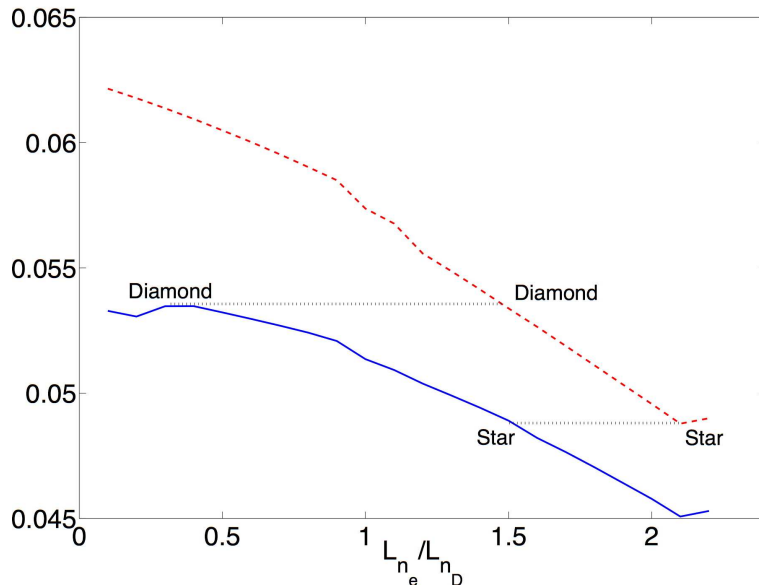


Figure 4.23: Quasi-linear particle flux, in arbitrary units, as a function of deuterium density scale length (the electron density scale length being fixed) for positive (red-dashed) and negative (blue-full) δ , indicating the lower and upper limits corresponding to stars and diamonds in Fig.4.24.

is characterized by larger Z_{eff} in the core independently of the boundary condition. Since the integral of the plasma current times the plasma resistance has to be equal for the two cases, as they were applied with the same loop-voltage within 5%, the central boundary condition in Fig.4.24 has to be preferred with respect to the other two as it results in similar average effective charge profiles for the two opposite triangularity cases. However, considering Fig.4.14, to obtain a collisional stabilization able to push the ratio of heat diffusivities to about two even at mid-radius, the required ratio in the effective charge values should be about two to three, instead of 1.2-1.5 as obtained in Fig.4.24. Therefore, while the difference in the impurity concentration does work in favor of reducing the discrepancy between experiments and theoretical modeling, it is largely insufficient at least in this linear model.

An additional comment on Fig.4.24 is required. The difference in the slopes of the effective charge profiles of the two cases goes to zero because the effect of plasma triangularity gradually vanishes towards the magnetic axis; this is another effect of the finite penetration length of triangularity.

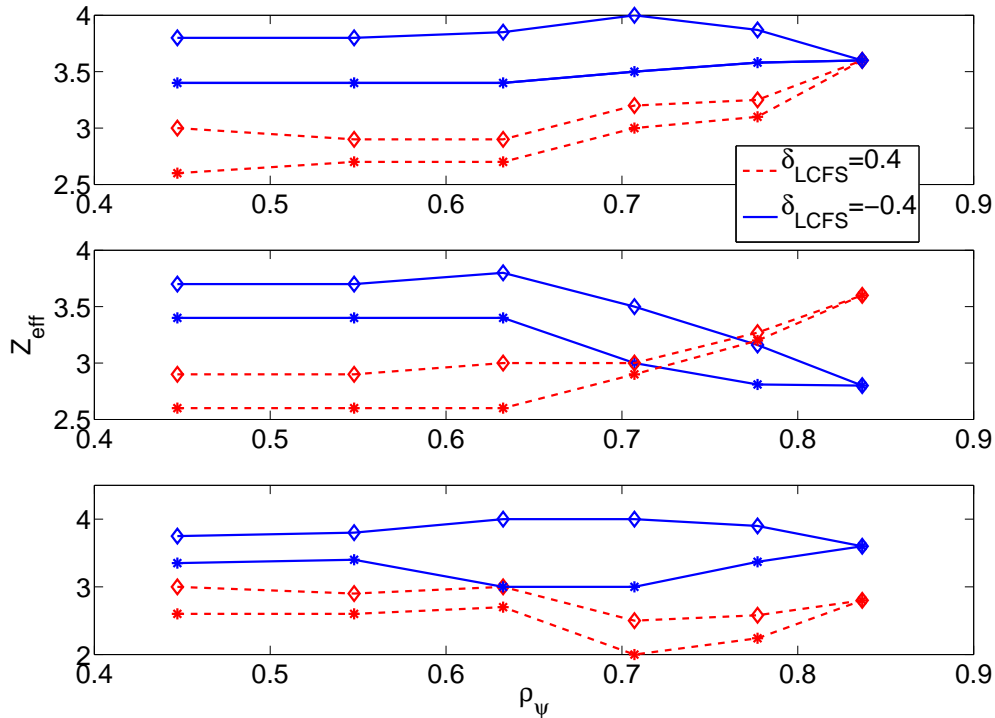


Figure 4.24: Radial profiles of the effective charge estimated by matching quasi-linear electron fluxes for positive and negative δ shots for three different boundary conditions. Stars and diamonds roughly indicate the upper and lower limits, providing an indication of the errorbars in the calculations.

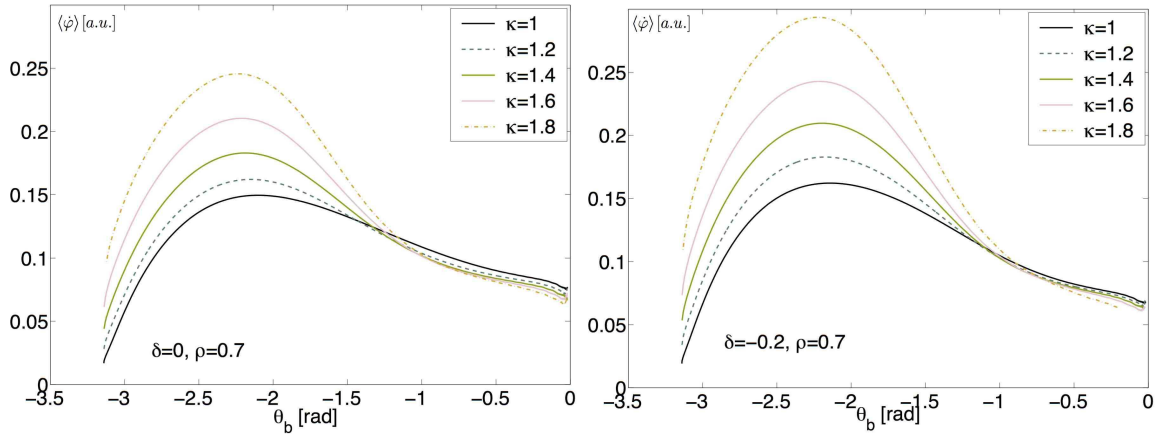


Figure 4.25: Toroidal precessional drift, in arbitrary units, plotted against trapped particle bouncing angle for a number of geometrical configurations for an electron of energy equal to the electron temperature.

Finally more accurate measurements of plasma rotation should be performed to assess a possible difference in the $E \wedge B$ shear between the two equilibria which could lead to additional differences in the micro-stability of these two shots.

4.9 General dependence of the toroidal precessional drift on plasma shape

After the results exposed in the previous sections, it is legitimate to ask whether there is a direct relationship between the dependence of the toroidal precessional drift on plasma shape and the mixing-length estimate plotted in Fig.4.7. We recall that all the equilibria used in Fig.4.7 were generated keeping the same current density and pressure profiles, therefore all the GK simulations are characterized by approximately the same turbulent regime which, as we have already said in Secs.4.6.4 and 4.6.5, is the TEM regime.

Let us calculate the toroidal precessional drift using Eq.4.74 for different values of elongation and triangularity. In Fig.4.25 we plot κ scans for two values of triangularity and a fair similarity can be found with Fig.4.16.

Indeed an increase in elongation gives rise to a larger toroidal drift frequency for trapped particles reaching the high field side region; as we have already seen in the case of triangularity at mid elongation, this is stabilizing because it shifts the resonance down in energy for that distribution function. Slightly different is the behavior of deeply trapped particles whose toroidal drift is almost independent of elongation, especially at low values

of triangularity. This is to be expected purely on the basis of the geometrical shape of the low field side of the flux surface whose sensitivity the elongation increases with triangularity; indeed, considering Eq.4.8 we can write to second order in the poloidal angle, i.e. considering the deeply trapped particle limit

$$R \simeq R_0 + r \left[1 - \frac{\theta^2(1 + \delta)^2}{2} \right] \simeq R_0 + r \left[1 - (1 + \delta)^2 \frac{(Z - Z_0)^2}{2\kappa^2 r^2} \right]. \quad (4.84)$$

Therefore, the inverse width of the resulting parabola $R = r - \alpha(Z - Z_0)^2$ depends less and less on κ when lowering δ , as shown in Fig.4.26. Therefore, the mildly stabilizing effect of

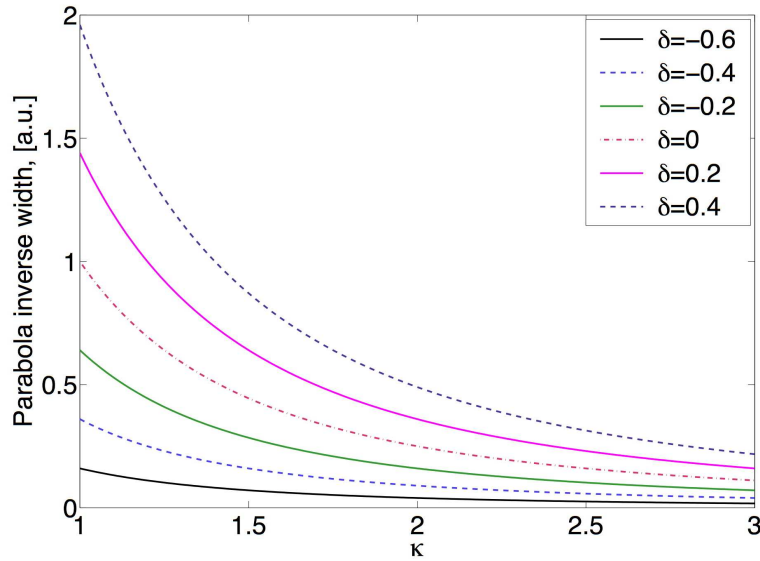


Figure 4.26: Inverse width of the approximate parabolic shape of a given flux surface around the lowest field region, as a function of elongation and triangularity.

deeply trapped electrons when triangularity is increased, due to the slight increase of the toroidal precession drift with triangularity (see Fig.4.16), becomes even more negligible as elongation is increased. We stress here that, being concerned with pure particle drifts, no effect on zonal flows through a q profile modification is considered by this analysis, in which the heat flux is estimated from a linear model only (Fig.4.7).

Let us now address a peculiarity in Fig.4.7 which was mentioned in Sec.4.6.4. For low values of elongation an increase in triangularity is first stabilizing and then destabilizing again, which, in other words, implies that a circular plasma is the most unstable equilibrium regarding TEM stability. Let us try to interpret this result by means of the toroidal precessional drift again. In Fig.4.27 we plot the toroidal precessional drift as a function of κ and δ in the region of interest, i.e. low values of elongation and triangularity. It can be seen how, contrary to the cases shown up to now, the toroidal drift is not a monotonic function of κ and/or δ for trapped particles bouncing in the high field side region, while the monotonic behavior in the deeply trapped region is maintained. Additionally, for

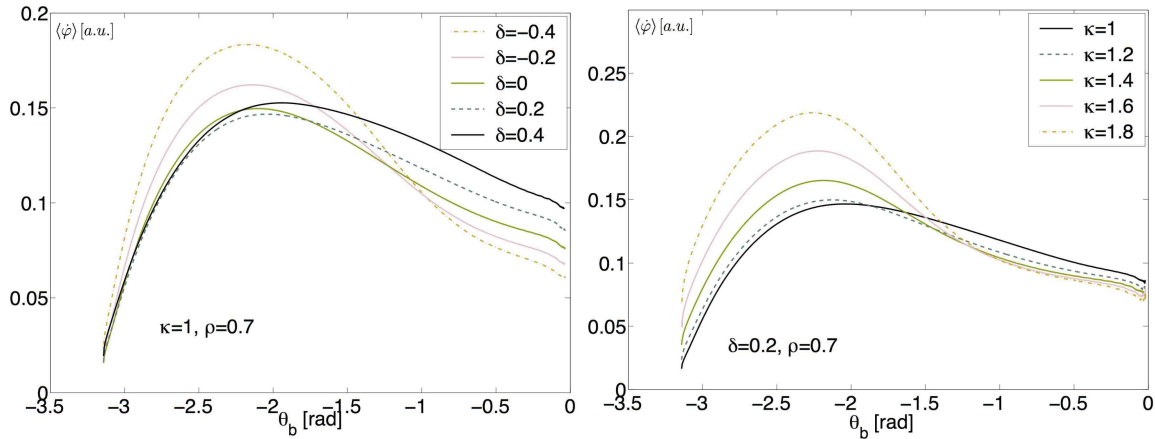


Figure 4.27: Toroidal precessional drift vs bouncing angle of trapped particles as a function of δ for $\kappa = 1$ (left) and as a function of κ for $\delta = 0.2$ (right)

positive δ the angle at which the consecutive curves cross each other shifts progressively towards the high field side. As a consequence, for low values of elongation and positive triangularities, when increasing δ we obtain a stabilizing effect on deeply trapped particles but no destabilizing effect on trapped particles bouncing in the high field side region, thus leading to a decreased overall quasi-linear transport. In Table 4.4 we estimate, in arbitrary units, the electron heat flux by calculating the full velocity integral, i.e. over energy and pitch angle from Eq.4.79. It can be seen how the non-monotonic behavior in δ for low κ is recovered even though the worst triangularity is shifted to -0.2 instead of 0. Furthermore, as in Fig.4.7, the calculated heat flux is not monotonically decreasing with κ at $\delta \simeq 0.4$.

	$\kappa = 1$	$\kappa = 1.2$	$\kappa = 1.4$	$\kappa = 1.6$
$\delta = 0.4$	4.1727	4.2409	4.1898	4.0584
$\delta = 0.2$	4.4982	4.3805	4.1961	3.9771
$\delta = 0$	4.7263	4.4173	4.1298	3.8566
$\delta = -0.2$	4.8085	4.3678	4.0072	3.6672
$\delta = -0.4$	4.7765	4.2554	3.8247	3.3047
$\delta = -0.6$	4.2120	4.1241	3.5561	2.6029

Table 4.4: Quasi-linear electron heat flux estimated from Eq.4.79 for a number of edge elongations and triangularities.

4.10 Conclusions

To summarize this chapter, negative edge triangularity stabilizes TEM modes mainly through perpendicular drifts and effective k_{\perp} modification. In particular the effective stabilization is a result of a competition between deeply and barely trapped particles which react in opposite ways to triangularity, the former acting to stabilize while the latter being destabilizing for increasing triangularity. This, in turn, is due to the electron toroidal precessional drift, which is larger with δ in the deeply trapped spectral region, while the opposite is true elsewhere in the pitch angle space. This mechanism is effective only close to the edge due to the finite triangularity penetration length; here, it indeed matches semi-quantitatively experimental results obtained in TCV on the effect of shape on confinement. However, the effect is experimentally seen much further into the core, where the present theoretical framework is unable to reproduce it.

A similar picture holds for plasma elongation with the difference that the destabilizing effect on deeply trapped particles can be neglected compared to the stabilizing effect on trapped particles bouncing in the high field side: the overall stabilizing effect of increasing elongation is therefore larger than the one obtained by decreasing triangularity.

Modeling also indicates that negative triangularity may lead to a different distribution of impurities which, in turn, can further stabilize TEM through increased collisionality in the plasma core. This effect, however, also appears insufficient to explain results. Additionally a possible difference in the $E \wedge B$ shear, again due to differences in ion temperature and density profiles, needs to be experimentally investigated. Moreover, even though global effects would ordinarily not be expected to play a major role, due to the small value of $\rho^* \simeq 1/80$, they might nevertheless be at play leading to additional differences in the TEM stabilization between the two equilibria.

These last three effects are indirect effects of the plasma edge influencing the core. Their assessment requires more accurate measurements of ion temperature, density and velocity, as well as turbulence diagnostics and a global collisional code able to handle equilibrium $E \wedge B$ flows.

4.11 Appendix 1: convergence studies

When solving the GK equation it is imperative to check whether the simulations converge in all the possible numerical parameters or, at least, the ones which most affect the numerical results. In general, convergence should be first checked in

- Real and imaginary parts of the linear frequency
- Heat and particle fluxes

- Energy of the perturbation

In a linear run performed with a local code such as GS2, it is needed to check convergence of the aforementioned quantities with respect to the following parameters

- Flux tube domain extent
- Velocity grid
- Number of parallel modes
- Confidence intervals on kinetic profiles

Since GS2 evolves linear modes implicitly, there are no problems of numerical stability; therefore there is no need to check for convergence in the time step provided that $\omega\Delta t \ll 1$, which is the criterion ensuring convergence. In our simulations $\max(\omega)\Delta t \simeq 10^{-3}$ which has then been chosen as the required precision in the calculation of the real frequency of each linear mode to stop the linear runs.

The flux tube extent is, for linear runs, equal to 7 poloidal turns; this value guarantees a drop in the energy of the fluctuations of several orders of magnitude at the ends of the flux tube with respect to the maximum value reached in the centre.

The number of grid points along the field line was normally set to 32 per poloidal turn, convergence was checked to 64.

The velocity grid is composed of the energy and pitch angle variables. Passing particles need 10 points in each parallel velocity direction, while trapped particles need at least 16 points, implying 32 points along the field line due to the GS2 numerical implementation. In Fig.4.28 we show a convergence study of the normalized linear heat flux as a function of the trapped particle pitch angle, to check that the maximum in the deeply trapped limit is not a numerical instability, as it looks at first sight, but rather a real physical effect.

Energy grids are usually made of 16 points between 0 and five times the temperature of each kinetic species in the simulation.

Since in linear runs there is no saturation, fluxes are to be normalized in such a way as to make them artificially saturate; one possibility is, for any mode, to divide each flux by the corresponding energy of the perturbation. In Fig.4.29 we show a typical temporal behavior.

Non-linear runs are of course much more demanding in terms of the computer time required by each simulation and in terms of convergence studies. Indeed, fluxes are to be considered as saturated after the Kelvin-Helmoltz instability saturated the linear phase of the simulation, over a time scale in general between five and ten times the time required for the linear fluxes to saturate. Moreover, additional checks must be performed, namely

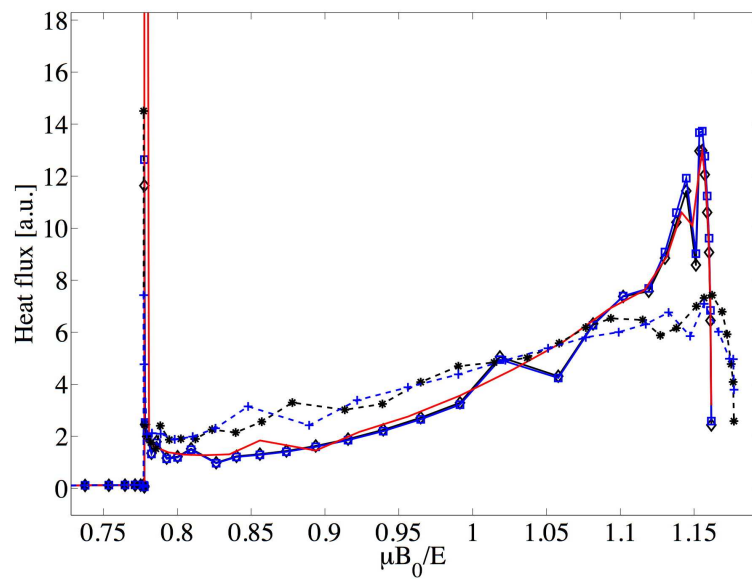


Figure 4.28: Normalized linear heat flux for TCV shots 28008 (full) and 28014 (dashed) as a function of pitch angle for a number of energy and trapped pitch angle points.

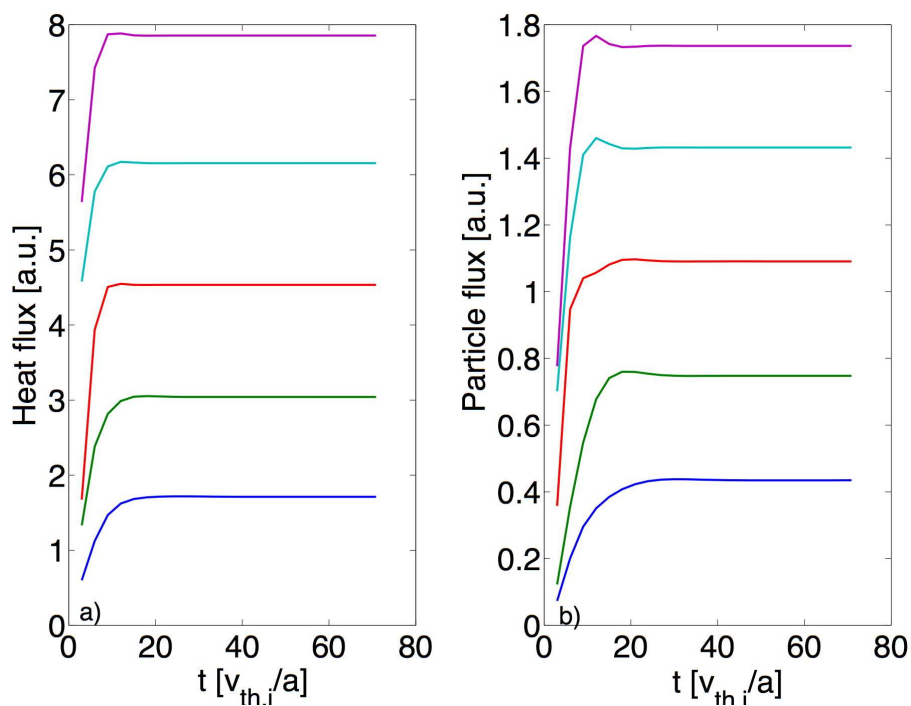


Figure 4.29: Temporal behavior of the quasi-linear energy flux (a) and of the particle flux (b) for a number of modes, normalized to the energy of the corresponding electrostatic perturbation, for a typical run. The relative accuracy is better than 10^{-5} .

- Poloidal extent of the evolved spectrum and its resolution
- Radial extent of the evolved spectrum and its resolution
- Relative dimensions (poloidal to radial) of the simulation box

each of these is necessary to make sure that the correct saturated regime has been attained in the simulation.

In particular it is imperative to show how the main saturating mechanism, i.e. zonal flows, are converged by changing the radial extent of the simulation box.

In Figs.4.30,4.31 we show a number of non-linear electrostatic simulations of pulse 28014 (positive triangularity), which is the most demanding in terms of numerical grids required, to prove convergence of our simulations in these last three points listed. In particular we performed simulations, presented below, with an increased number of radial modes such that $\Delta x/\rho_i = 2.4 - 1.7 - 1.2$ named Sim1-Sim2-Sim3, respectively. Additionally "sim2" is performed with an increased number of poloidal modes such that $k_y \rho_i \simeq 1$. Since these simulations do not show any major difference in saturated heat and particle fluxes, we can confirm that our original simulations indeed converged.

Let us summarise the numerical grids:

1. sim1 represents the grid used in the bulk of this study.
2. sim2 has 1.41 poloidal and 1.41 radial modes more than sim1 with the same k_x and k_y resolution.
3. sim3 has the same number of poloidal modes, with the same k_y resolution, and 3 times as many radial modes as sim1. The radial extent of the simulation domain in sim3 is 1.5 times the one in sim1 to assess convergence of zonal flows, so the maximum k_x evolved in sim3 is twice the one in sim1.
4. sim4 has an increased resolution in k_y to assess convergence with respect to this parameter. The remaining numerical parameters are chosen to be in between sim2 and sim3.

We summarise hereafter the evolved k-space for these three simulations:

Figures 4.30 and 4.31 show, as a function of the simulation evolution time normalized to the minor radius at the LCFS divided by the ion thermal velocity, the electron particle and heat fluxes for the Sim1, Sim2 and Sim3 numerical grids. The horizontal dashed line shows the time-averaged value in the saturated phase ($t > 180a/v_{th,i}$) adopted for case Sim1. Estimated saturated levels of sim2 and sim3 and sim4 are, respectively, within about 4%, 9% and 9% w.r.t. sim1, both for particle and heat fluxes. Finally Fig.4.31 proves that the two dimensional spectral region adopted in the simulation is sufficiently

	$k_y \rho_i$	$ k_x \rho_i $	$\Delta k_y \rho_i$	$\Delta k_x \rho_i$	$\Delta x / \rho_i$	L_x / ρ_i
sim1	0-0.67	0-1.27	0.05	0.03	2.4	207
sim2	0-0.94	0-1.79	0.05	0.03	1.7	207
sim3	0-0.67	0-2.61	0.05	0.02	1.2	303
sim4	0-0.68	0-1.82	0.03	0.03	1.7	207

Table 4.5: Table illustrating main numerical grids used to assess convergence of non-linear simulations

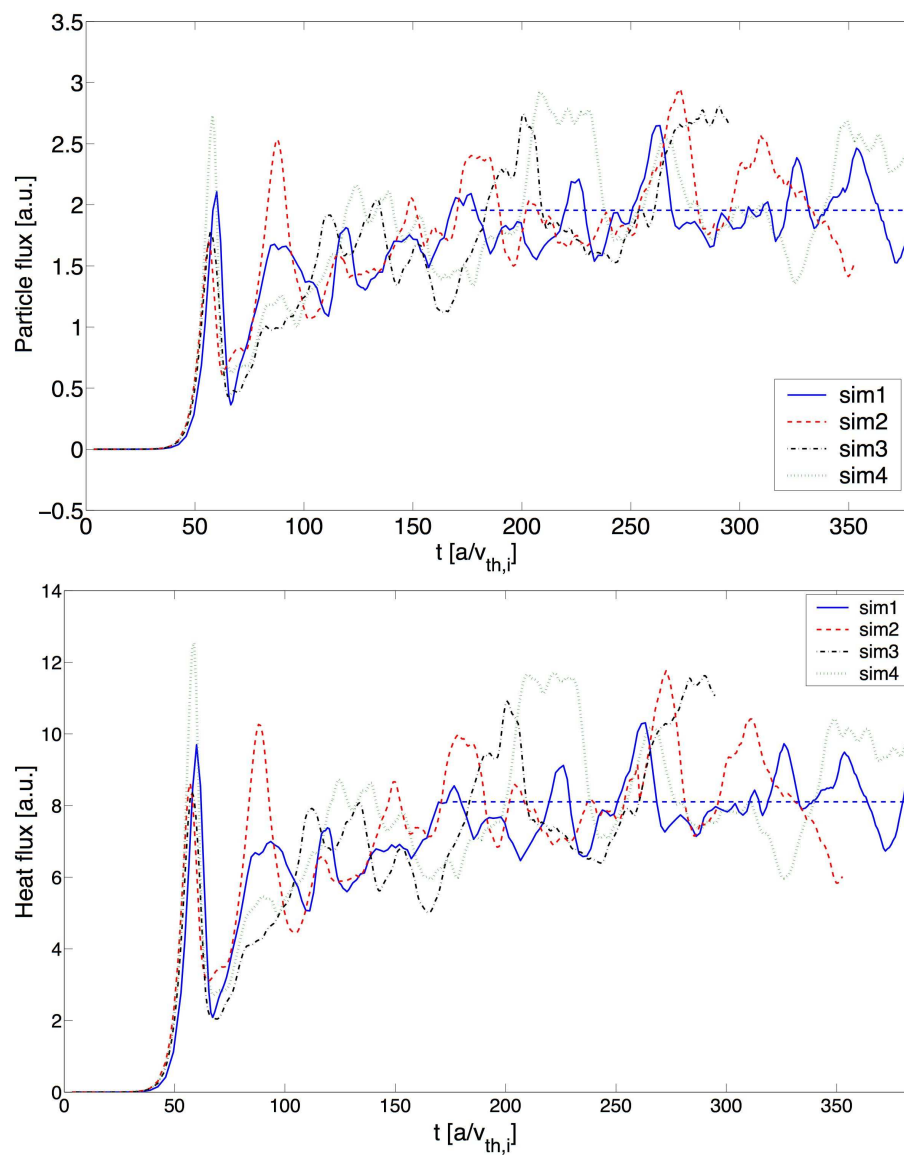


Figure 4.30: Temporal behavior of the non linear particle flux (top) and heat flux (bottom) for cases Sim1, Sim2 and Sim3.

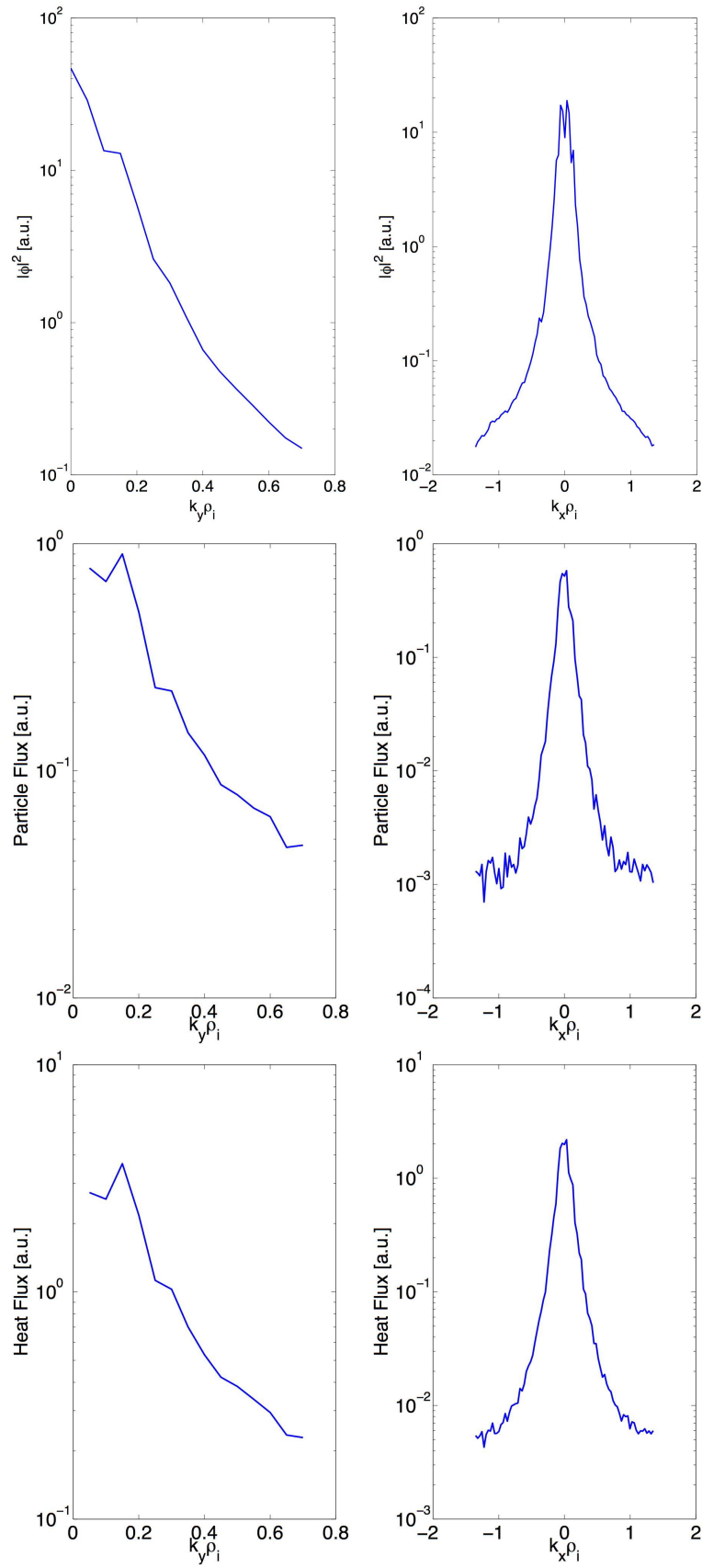


Figure 4.31: $|\phi(x, y)|^2$ (top), particle flux (middle) and heat flux (bottom) integrated over x (left) and over y (right) in logarithmic scale.

broad as the electrostatic potential and the heat and the particle fluxes decrease towards zero at the end of the grids.

4.12 Appendix 2: toroidal drift benchmark

In this section we will briefly give some additional information on the implementation of Eq.4.74 and how it was benchmarked.

A Fortran routine reads an EQDSK file and, for a given flux surface, fits the equilibrium to cubic splines and calculates the Jacobian and the magnetic field along the poloidal angle; the integral is then evaluated through a trapezoidal integration rule which, to converge, requires about 4000 equally spaced points. Non linear spacing does not lead to significant improvements in the evaluation of the integrals. The radial derivative in the numerator of Eq.4.74 is evaluated numerically by taking two neighboring flux surfaces. Convergence calculations led to choosing 0.01 as the relative flux difference between the two neighboring surfaces.

The numerical calculation was successfully benchmarked against the analytical derivation of Kadomtsev and Pogutse [45] in the appropriate limit, and against the Venus code [47] in the two TCV shots considered in Chapter 4 (see Fig.4.32).

An additional benchmark was performed against an analytical model developed by J.P.

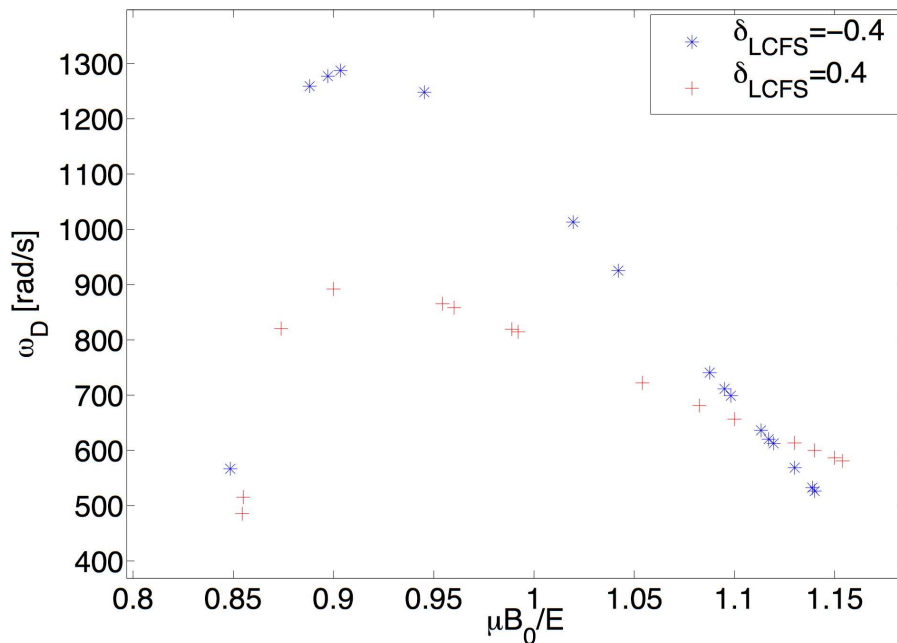


Figure 4.32: Toroidal precession drift calculated at $\rho_V = 0.65$ by the Venus code as the integral over the Maxwellian distribution. (courtesy of M. Jucker)

Graves [48] whose basic principle we report here. The plasma equilibrium is expanded

into harmonics of the poloidal angle θ according to the following formalism

$$\hat{R} = \hat{R}_{axis} + \hat{r} \cos(\theta) - \Delta(\hat{r}) + \sum_{m=2}^{\infty} S_m(\hat{r}) \cos[(m-1)\theta] \quad (4.85)$$

$$\hat{Z} = \hat{Z}_{axis} + \hat{r} \sin(\theta) - \sum_{m=2}^{\infty} S_m(\hat{r}) \sin[(m-1)\theta] \quad (4.86)$$

where R_{axis} is the radial position of the magnetic axis, Δ plays the role of the Shafranov shift and \hat{r} is the minor radius of the flux surface.

Considering only second order expansions, i.e. $m=3$, and imposing the same plasma boundary described at $\theta = \{0, \pm\pi/2, \pi\}$ by Eq.4.8 with $\lambda = 0$ (since λ is a higher order moment), the following mapping between the two models is recovered[48]

$$R_{mid} = R_{axis} - \Delta(\hat{r}) + S_3(\hat{r}) \quad (4.87)$$

$$r = \hat{r} + S_2 \quad (4.88)$$

$$\kappa = \frac{\hat{r} - S_2(\hat{r})}{\hat{r} + S_2(\hat{r})} \quad (4.89)$$

$$\delta = \frac{4S_3(\hat{r})}{\hat{r}} \quad (4.90)$$

The analytical expression of the toroidal drift is pretty long and complicated, we will report only the deeply trapped limit

$$\langle \dot{\varphi} \rangle = \frac{Tq}{eB_0 \hat{r} R} \left[1 - \frac{1}{2q^2} \left(\alpha - 2 \frac{\hat{r}}{R} \right) - \frac{\kappa - 1}{\kappa + 1} - 2 \frac{\hat{r} \kappa_{\hat{r}}}{(1 + \kappa)^2} - \frac{1}{4} (\delta + \hat{r} \delta_{\hat{r}}) - \Delta_{\hat{r}} - 2 \frac{\hat{r}}{R} \frac{1}{1 + \kappa} \right] \quad (4.91)$$

where the subscript \hat{r} stands for radial derivative, T is the particle temperature, q the safety factor and $\alpha = -Rq^2 \beta_{\hat{r}}$ the ballooning parameter.

By calculating its value for TCV shots 28008 and 28014 we obtain, in agreement with our calculations, a smaller value in the negative triangularity case.

The full pitch angle dependence is represented in Fig.4.33 confirming the same behavior found by Eq.4.74 and by the Venus code.

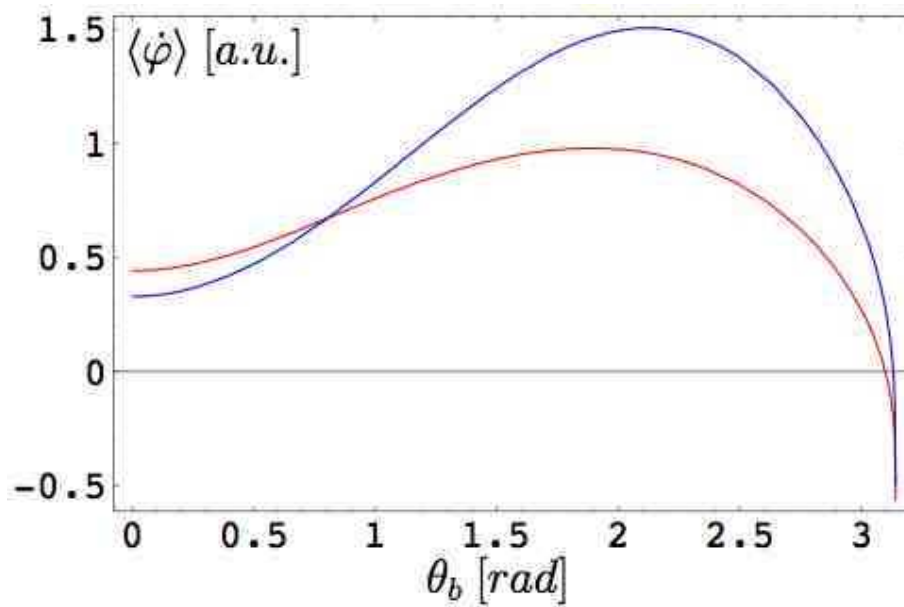


Figure 4.33: Toroidal precession drift, in arbitrary units, as function of the bounce angle for the two TCV shots 28008 (blue) and 28014 (red) calculated at $\rho = 0.7$ by the analytical model in [48] (Courtesy of Dr. Jonathan Graves)

Bibliography

- [1] H. Grad and H. Rubin, *Proceedings of the 2nd UN Conf. on the Peaceful Uses of Atomic Energy* **31** (1958), 190
- [2] V.D. Shafranov, *Reviews of Plasma Physics* **2** (1966) 103
- [3] Y. Camenen *et al.*, *Phys. Rev. Lett.* **102** (2009) 125001
- [4] T.G. Northrop and E. Teller, *Phys. Rev.* **117** (1960) 215
- [5] M. Rosenbluth and M.L. Sloan, *Phys. Fluids* **14** (1971) 1725
- [6] S. Brunner, *Ph.D. thesis*, Ecole Polytechnique Fédérale de Lausanne, 1997
- [7] M.N. Rosenbluth *et al.*, *Nuclear Fusion Supplement* **1** (1962) 143
- [8] C. Angioni *et al.*, *Phys. Rev. Lett.* **90** (2003) 205003
- [9] P. Catto, *Plasma Phys.* **20** (1978) 719
- [10] R.G. Littlejohn, *Journal of Plasma Physics* **29** (1983) 111
- [11] M.A. Beer, *Ph.D. thesis*, Princeton Plasma Physics Laboratory, 1995
- [12] T. Antonsen and B. Lane, *Phys. Fluids* **23** (1980) 1205
- [13] E.A. Frieman and L. Chen, *Phys. Fluids* **25** (1982) 502
- [14] A. Quarteroni and A. Valli, *Numerical approximation of partial differential equations*, Springer 1994
- [15] Y. Camenen *et al.*, *Nucl. Fusion* **47** (2007) 510
- [16] A. D. Turnbull *et al.*, *Nucl. Fusion* **28** (1988) 1379
- [17] F. Hofmann *et al.*, *Phys. Rev. Lett.* **81** (1998) 2918
- [18] E. A. Lazarus *et al.*, *Phys. Fluids B* **3** (1991) 2220
- [19] J. R. Ferron *et al.*, *Phys. Plasmas* **12** (2005) 056125

- [20] J. Ongena *et al.*, *Plasma Phys. Control. Fusion* **43** (2001) A11
- [21] F. Troyon *et al.*, *Plasma Phys. Control. Fusion* **26** (1984) 209
- [22] D. D. Hua *et al.*, *Phys. Fluids B* **4** (1992) 3216
- [23] R. E. Waltz and R. L. Miller, *Phys. Plasmas* **6** (1999) 4265
- [24] G. Rewoldt *et al.*, *Phys. Fluids* **25** (1982) 480
- [25] M. Kotschenreuther, G. Rewoldt, W.M. Tang, *Comput. Phys. Commun.* **88** (1995) 128
- [26] E. Belli *et al.*, *Phys. Plasmas* **15** (2008) 092303
- [27] S. Jolliet *et al.*, *Comput. Phys. Commun.* **177** (2007) 409
- [28] P. Angelino *et al.*, *Plasma Phys. Control. Fusion* **48** (2006) 557
- [29] J. E. Kinsey *et al.*, *Phys. Plasmas* **14** (2007) 102306
- [30] F. Hofmann *et al.*, *Fusion Technol.* **1** (1986) 687
- [31] J.-M. Moret *et al.*, *Phys. Rev. Lett.* **79** (1997) 2057
- [32] H. Weisen *et al.*, *Nucl. Fusion* **37** (1997) 1741
- [33] F. Hofmann *et al.*, *Plasma Phys. Control. Fusion* **43** (2001) A161
- [34] A. Pochelon *et al.*, *Nucl. Fusion* **39** (1999) 1807
- [35] K. Matsuda, *IEEE Trans. Plasma Sci.* **17** (1989) 6
- [36] Y. Camenen *et al.*, *Plasma Phys. Control. Fusion* **47** (2005) 1971
- [37] D. Boucher and P.H. Rebut, *Proc. IAEA Tech. Conf. on Advances in Simulation and Modeling in Thermonuclear Plasmas, Montreal* (1992) 142
- [38] H. Lütjens, A. Bondeson and O. Sauter, *Comput. Phys. Commun.* **97** (1996) 219
- [39] R. L. Miller, M. S. Chu, J. M. Greene *et al.*, *Phys. Plasmas* **5** (1998) 973
- [40] F. Hofmann and G. Tonetti, *Nucl. Fusion* **28** (1988) 1871
- [41] J. M. Greene and J. L. Johnson, *Phys. Fluids* **5** (1962) 510
- [42] F. Jenko *et al.*, *Plasma Phys. Control. Fusion* **47** (2005) B195

- [43] A. Bottino et al., *Phys. Plasmas* **11** (2004) 198
- [44] Y. Camenen, *Ph.D. thesis*, Ecole Polytechnique Fédérale de Lausanne, LRP 821/06
- [45] B. B. Kadomtsev and O.P. Pogutse, *Zh. Eksp. Teor. Fiz.* **51** (1966) 1734 [*Sov. Phys. JETP* **24** (1967) 1172]
- [46] F. Y. Gang and P. H. Diamond, *Phys. Fluids* **B2** (1990) 2976
- [47] O. Fischer *et al.*, *Nucl. Fusion* **42** (2002) 817
- [48] J.P. Graves, *Phys. Plasmas* **12** (2005) 090908

Chapter 5

Conclusions and future plans

This thesis can be roughly separated into two parts which, at a first sight, can appear as disjointed since the former is experimental while the latter is theoretical. However, in the opinion of the author, the two parts simply reflect two sides of the same, though extremely broad and complex, domain: turbulence in magnetized plasmas.

5.1 Summary

The thesis work focused, at first, on the feasibility study of a number of possible diagnostics for fluctuations measurements in the core of the TCV tokamak. Particular concern was given to the spatial localization of the measurement, un-ambiguity in the interpretation of the results, width and resolution of the spectral response, ease of comparison to theoretical models, number of target plasmas which can be used, portion of the plasma cross section accessible to measurements and capability to measure complicated, non-uniform plasma regions. Response properties are numerically evaluated for TCV main parameters. It is shown how, among the alternatives taken into considerations, only imaging techniques comply with all the required specifications, provided that they are employed in a configuration such that their lines of sight are tangent to flux surfaces. The final choice fell on the Phase Contrast technique, which proved to be superior to any other imaging technique.

The theoretical treatment of the Phase Contrast, including the approximations needed to validate the measurements and actual transfer functions of the system, is reviewed before describing in detail its practical realization on the TCV tokamak. Even though the Phase Contrast is intrinsically a line integrated measure, the tangential configuration and the use of an opportunely designed spatial filter allow excellent spatial localizations which, in selected configurations, can be of the order of 1% of the normalized minor radius. The extremely good localization is a consequence of a short integration length which validates

the Raman-Nath approximation even in the case of large fluctuating wave vectors. The diagnostic is therefore designed to capture long and short wavelength fluctuations, the former corresponding to the ion Larmor radius scale while the latter to the electron scale. The design of the spatial filter was also optimized to allow a uniform response in Fourier k space, thus avoiding distortions in the image reconstruction.

The system is translatable in the vacuum vessel, the reason being to allow one to measure the edge and the core of TCV, up to the magnetic axis in selected configurations.

A satellite project of the thesis was the installation of a single channel, homo-dyne, Doppler reflectometry, whose response properties were tested to assess the feasibility of a future, more complete, system. The prototype performed very well with an excellent signal to noise ratio, and is now routinely operated on TCV.

The second part of the thesis concerned linear and non-linear gyro-kinetic simulations of the impact of plasma shape, in particular of triangularity, on plasma micro-stability. Diverted L-mode TCV pulses, which experimentally indicated a stabilizing effect of negative triangularity, were analyzed with the GS2 code. The simulations identified the dominant instability as the Trapped Electron Mode, and were found in a fair agreement with the experiments, at least close to the plasma edge. Non-linear simulations are analyzed in phase space also to explain the effect of a finite collisionality on the experimentally observed transport coefficients. A linear, semi-analytical model successfully describes the relevant physical effects found in non-linear simulations in terms of a modification of the toroidal precession drift of trapped particles, exerted by triangularity. A number of additional effects is also discussed.

5.2 Future plans

Anomalous transport is one of the most difficult and important topics in plasma physics, both under the experimental and the theoretical point of view. It is therefore imperative to characterize micro-instabilities at our best, which is the main reason why the Tangential Phase Contrast Imaging diagnostic, described in this thesis, was developed.

The diagnostic must undergo an initial experimental benchmark with other existing diagnostics, in order to prove its sensitivity to, at least, main plasma events: viz. L-H transitions, Elms, disruptions, intensive power modulations, coherent and semicoherent modes. If this benchmarking phase will be successful, the diagnostic will be released as an operating tool to be fully exploited in all its characteristics.

In parallel, in order to assess our understanding of turbulent transport, it is necessary to model future PCI data with the most advanced gyro-kinetic codes available at the moment. This implies the development of a synthetic diagnostic to directly and quanti-

tatively compare experimental results to simulations. The simulations are, of course, to be performed with a physical model as more realistic as possible, meaning the inclusion of the actual plasma geometry, the Coriolis and bulk $E \wedge B$ drifts, and actual kinetic profiles. Only after a satisfying benchmark has been obtained, both the diagnostic and the gyrokinetic codes can be used to investigate physical peculiarities possibly captured in each tool. An ideal study of this kind is the experimental verification of the stabilizing effect of negative triangularity on plasma micro-instabilities, at least in low density L-mode plasmas, which would then bridge the two parts of this thesis.

It should be stressed that experimentalists and theoreticians should work in tight contact with each other, as the former group needs guidance from theory to be conscious of where their research is, and should be, heading; while the latter group needs experiments as it is the only way to validate their numerical models. In the opinion of the author, research in nuclear fusion is, nowadays, at such a level of complexity that it needs experimental mathematics to advance further.

5.3 Conclusions

Conclusions are usually meant to summarize and explain in a few sentences why the subject of the thesis is useful or interesting, I defer them to Werner Heisenberg and Horace Lamb.

When I meet God, I am going to ask him two questions: Why relativity? And why turbulence? I really believe he will have an answer for the first. (W. Heisenberg)

I am an old man now, and when I die and go to heaven there are two matters on which I hope for enlightenment. One is quantum electrodynamics, and the other is the turbulent motion of fluids. And about the former I am rather optimistic. (H. Lamb)

Acknowledgments

I would like to start my acknowledgments by thanking the direction of CRPP for giving me the possibility to be a Ph.D. student in their laboratory, in particular Dr. Kurt Appert who, at that time, was *de facto* leading the laboratory.

A special mention is deserved by my supervisor, Dr. Stefano Coda, who has always impressed me for his acuteness and deep knowledge and understanding of such a broad and heterogeneous domain as plasma physics. In a period where scientists tend to focus on a limited domain, his open-minded attitude was greatly beneficial for my academic formation. I additionally thank him for having been also a man to me and not only a supervisor.

Credits are also deserved by the experts, Dr. Stephan Brunner, Dr. Andreas Krämer-Flecken and Dr. Colin M. Roach, as well as, obviously, by Stefano Coda, for carefully examining this thesis.

During a Ph.D., i.e. in a period still, somehow, in between scholastic and working life, it is important to exploit the environment one lives and works in, to understand what direction is to be followed in the future: I was lucky enough to capture it.

These five years would have surely passed much more slowly if I had not met a few great people, most of them still friends of mine. In particular I wish to mention Elm, with whom I elaborated the definite theory, and IDE who, although I have never actually met most of them, share with me their spare time to work together on common ideals.

Last but not least my parents, who have never forced me to do anything I did not want to and, on the contrary, have always encouraged my to follow my ideas, even when these brought me abroad. If it had not been for them, I could have never done the studies I did. To them I dedicate this thesis.

This work was supported in part by the Swiss National Science Foundation.

Alessandro Marinoni - Curriculum Vitae

CITIZENSHIP Italian

PLACE AND DATE OF BIRTH Saronno (VA), Italy. March 16th 1979

EDUCATION **Ecole Polytechnique Fédérale de Lausanne**

Ph.D., Physics

- Thesis title: *Plasma fluctuation studies in the TCV tokamak: modeling of shaping effects and advanced diagnostic development*
- Advisor: Dr Stefano Coda
- Area of Study: Plasma turbulence, theoretical and experimental aspects

Politecnico di Milano

- Engineering license, July 2004
 - Professional practice examination 100/100
- Master thesis, Nuclear Engineering, February 2004
 - *Cum Laude*
 - Thesis title: *Study of Internal Transport Barriers in the JET tokamak by means of RF power*
 - Advisor: Professor Roberto Piazza
 - Co-Advisor: Dr Paola Mantica
 - Area of Study: Plasma transport

ACADEMIC EXPERIENCE **Ecole Polytechnique Fédérale de Lausanne**

Teaching Assistant

- **September 2006 to March 2009**
Assisted *Numerical Physics I+II*
- **September 2005 to June 2006**
Assisted *General Physics III+IV*
- **September 2004 to June 2005**
Assisted *Practical experiences, physics I+II*

Politecnico di Milano

Undergraduate Researcher

- **September 2003 to December 2003**
Winner of the London Italian embassy scholarship to participate in the JET Transport Task Force to plan, execute and analyze transport experiments on the JET tokamak

Carolus Magnus summer school

- **September 2003**

Took part in the third school on nuclear energy and fusion power.

PROFESSIONAL EXPERIENCE

National Council of Researches, Milan, Italy

- **April 2004 to July 2004**

Research on transport studies in tokamak plasmas with internal transport barriers

PUBLICATIONS REFEREED JOURNALS

First author

- A. Marinoni et al., *The effect of plasma triangularity on turbulent transport: modelling TCV experiments by linear and non linear gyrokinetic simulations*, Plasma Phys. Control. Fusion **51** (2009) 055016
- A. Marinoni et al., *Design of a tangential Phase Contrast diagnostic for the TCV tokamak*, Rev. Sci. Instr. **77** (2006) 10E929
- A. Marinoni et al., *Analysis and modelling of power modulation experiments in JET plasmas with Internal Transport Barriers*, Plasma Phys. Control. Fusion **48** (2006) 1469

Co-author

- X. Lapillonne et al., *Limitations of the $s - \alpha$ equilibrium model for gyrokinetic computations of turbulence*, Phys. Plasmas **16** (2009) 032308
- D. Van Eester et al., *JET (^3He)-D scenarios relying on RF heating: survey of selected recent experiments* Plasma Phys. Control. Fusion **51** (2009) 044007
- A. Casati et al., *Critical temperature gradient length signatures in heat wave propagation across internal transport barriers in the Joint European Torus*, Phys. Plasmas **14** (2007) 092303
- S. Coda et al., *The Physics of Electron Internal Transport Barriers in the TCV Tokamak*, Nucl. Fusion **47** (2007) 714
- P. Mantica et al., *Probing Internal Transport Barriers with Heat Pulses in JET*, Phys. Rev. Lett. **96** (2006) 095002
- T. P. Goodman et al., *Safety factor profile requirements for electron ITB formation in TCV*, Plasma Phys. Control. Fusion **47** 12B (2005) B107

CONFERENCE PUBLICATIONS

- A. Marinoni et al., *The effect of plasma triangularity on turbulent transport: modelling TCV experiments by linear and non linear gyrokinetic simulations*, 50th APS Conf. On Plasma Phys., Dallas (TX) USA, 2008
- A. Marinoni et al., *The TCV tangential Phase Contrast Imaging diagnostic*, 50th APS Conf. On Plasma Phys., Dallas (TX) USA, 2008
- A. Marinoni et al., *The impact of triangularity on plasma confinement: TCV experiments vs non-linear gyrokinetic modelling*, 34th EPS Conf. On Plasma Phys., Warsaw Poland, 2007

- A. Marinoni et al., *Design of a tangential Phase Contrast Imaging diagnostic for the TCV tokamak*, 16th topical conf. on High Temperature Plasma Diagnostic, Williamsburg (VA) USA, 2006

KNOWN
LANGUAGES

- Italian, mother tongue
- English, fluent
- French, fluent
- Swedish, scholastic knowledge

INFORMATICS

- Operating Systems: Linux, Apple OS X, AIX, Solaris and other UNIX variants, Microsoft Windows XP and basics of VMS.
- Programming: MATLAB, C, C++, Mathematica, Pascal, basics of IDL, Fortran and SQL.
- Applications: $\text{T}_{\text{E}}\text{X}$, $\text{L}^{\text{A}}\text{T}_{\text{E}}\text{X}$, Office, and other common productivity packages for Windows, OS X, and Linux platforms.